Machine-learning-enabled Synthesis & Characterization of Epitaxial Perovskite Oxide Films

by

Patrick Thomas Gemperline

A dissertation submitted to the Graduate Faculty of
Auburn University
in partial fulfillment of the
requirements for the Degree of
Doctor of Philosophy

Auburn, Alabama
August, 3 2024

Keywords: hMBE, SHO, RHEED, XPS, Machine Learning, Artificial Intelligence

Approved by

Ryan Comes, Chair, Associate Professor, Department of Physics
Marcelo Kuroda, Associate Professor, Department of Physics
Wencan Jin, Assistant Professor, Department of Physics
Stuart Loch, Alumni Professor, Department of Physics
Byron Farnum, Associate Professor, Department of Chemistry and Biochemistry

Abstract

Perovskite oxides are a well studied family of materials that possess a wide range of useful properties and novel properties. $SrHfO_3$ (SHO) is a perovskite oxide with an orthorhombic Pnma structure and large band gap of 6.1 eV. Its large band gap and insulating behavior have made it a candidate for next-generation gate dielectrics in MOSFET devices. Previous studies utilizing density functional theory modeling have suggested that a ferroelectric P4mm phase of SHO may be possible to synthesize under strained conditions. A ferroelectric phase of SHO would be an ideal candidate for a gate dielectric in ferroelectric random access memory (FRAM) devices. In order to investigate the possibility of a ferroelectric SHO phase, SHO thin film samples were synthesized on $GdScO_3$ (GSO), $TbScO_3$ (TSO), and $SrTiO_3$ (STO) using hybrid molecular beam epitaxy (hMBE). Due to the refractory nature of Hf metal, it is highly difficult to synthesize thin films containing Hf using the effusion cells in traditional molecular beam epitaxy (MBE). hMBE has emerged as a leading alternative that blends the highly tunable precision of MBE with the ability of atomic layer deposition (ALD), to easily synthesize refractory metals by introducing Hf through the metal organic precursor tetrakis(ethylmethylamino)hafnium(IV) (TEMAH).

In perovskite oxides heterostructures and devices, samples must be highly crystalline with sharp interfaces in order to exhibit the desired electrical properties and function correctly. Successfully synthesizing perovskite oxide samples usually requires significant numbers of growth attempts and detailed film characterization on each sample to find the optimal growth window of a material. The most common real time *in-situ* diagnostic technique available during MBE synthesis is reflection high energy electron diffraction (RHEED). Conventional use of RHEED allows a highly experienced operator to make some qualitative observations during growth, such as recognizing the sample has become amorphous or recognizing the large islands have formed on the surface. However, due to a lack of theoretical understanding of the diffraction patterns, finer, more precise levels of observations are challenging. To address these limitations, new

programs were created that utilize the modern data science techniques including component analysis (PCA) and k-means clustering to analyze the recordings of the RHEED patterns taken during growth.

Although hMBE growth allows for highly tunable control of film synthesis, the down side is that there is a very large parameter space that needs to be explored to find the optimal growth conditions. Common variables include the oxygen pressure, substrate temperature, substrate material, effusion cell temperatures, and metal organic precursor pressures. As a consequence of having this many variables and the limitation of growing only a few samples a day, fully searching the parameter space is not feasible. As a result, growths need to be carefully monitored and adjusted during synthesis to obtain the desired results. However, the only real time feedback that is available is RHEED; thus successfully finding the optimal conditions in a reasonable amount of time and growths requires the operator to possess significant expertise in film growth. Convolutional neural networks (CNNs) have been demonstrated to be capable of identifying patterns in data at a level that human operators are unable to. To investigate the ability of CNNs to make useful predictions that can provide more advanced and detailed information than traditional monitoring systems, a CNN was trained to predict film stoichiometry by learning from X-ray photoelectron spectroscopy (XPS) and RHEED data.

Acknowledgments

This work and everything that has led up to it would not have been possible without tremendous support, encouragement, and guidance of all those who I've had the pleasure to know and work with. I'd like to start by thanking my research advisor and mentor, Prof. Ryan Comes for his years of guidance and continued support. Ryan has been an outstanding advisor who supported my desire to research machine learning and branch out beyond his expertise. He demonstrated sincere compassion and empathy in helping myself and his other students during difficult times, and especially during the pandemic. He has pushed me to become a better researcher and physicist, and I will always be grateful to him.

It takes a whole team to keep the FINO lab in working order and it would not have been possible without the help of my colleagues. I want to thank Dr. Miles Blanchet, Dr. Suresh Thapa, Dr. Rajendra Paudel, Mr. Jibril Ahammad, Mr. Brian Opatosky, Ms. Tanzila Tasnim, and Mr. Bhavesh Ramkorun for their help and camaraderie throughout our years together in the lab. I want to thank my committee members Prof. Marcelo Kuroda, Prof. Wencan Jin, Prof. Stuart Loch, and Prof. Byron Farnum for their time and feedback.

These results would not be possible without the expertise and contributions of my collaborators. I would like to thank Dr. Sumner Harris and Dr. Rama Vasudevan from the Center for Nanophase Materials Sciences at Oak Ridge National Lab for collaborating on the convolutional neural network study. I am grateful to Prof. Robert Klie and Dr. Arashdeep Thind from University of Illinois Chicago for their STEM analysis of SHO. I would like to thank Prof. Wencan Jin and his graduate student Chunli Tang from Auburn University for their SHG measurements. I extend my appreciation to Prof. Boris Kiefer from New Mexico State University for his DFT modeling. I want to acknowledge Dr. George Sterbinsky from Argonne National Laborator for performing XAS on SHO samples. I am grateful to Dr. Sydney Provence for her work on the PCA

and k-means clustering study. I would like to thank Dr. Eren Suyolcu for sharing his LCO and LSCO RHEED data.

I gratefully acknowledge support for synthesis and characterization of samples from the National Science Foundation (NSF) under Award No. DMR-2045993. I acknowledge the Auburn University Easley Cluster for support of this work. I would like to acknowledge the Center for Nanophase Materials Sciences at Oak Ridge National Lab for time and resources provided under proposals CNMS2023-A-01807 and CNMS2023-B-02047. I respectfully acknowledge the U.S. Department of Energy, Office of Science, Office of Workforce Development for Teachers and Scientists, Office of Science Graduate Student Research (SCGSR) program, administered by the Oak Ridge Institute for Science and Education (ORISE) for the DOE under contract number DE-SC0014664.

I wish to express my heartfelt gratitude to all the friends who have supported and helped me over the years. In particular, I am deeply thankful to my close friends Alban, Julia, Joe, and Eduardo for the countless laughs and wonderful times we've shared.

I want to thank all of the professors at St. X High School, Xavier University, and Auburn University from whom I've learned so much over the years. I am profoundly grateful to Dr. Jonathan Morris for introducing me to the fascinating realm of research and condensed matter physics. His exceptional mentorship and unwavering friendship over the years have been invaluable.

My entire family, particularly my parents, Don and Kathy, and my sister, Kate, have always been extraordinarily supportive and profoundly encouraging. They have all consistently pushed me to pursue my dreams and challenged me to become the best version of myself. From a young age, my grandfather Tom Clayton instilled in me a sense of wonder and curiosity about the world, teaching me to observe my surroundings and question how everything works. From building birdhouses to restoring vintage record players and tube radios, he has imparted invaluable knowledge and continuously

fueled my scientific curiosity. To my grandfather Tom and my grandmother Gayle, who has graciously put up with our antics, I am eternally grateful.

Lastly, I extend my deepest gratitude to the love of my life, Ana Maria. From our shared endeavors in the optics lab to our countless late-night study sessions in the physics lounge, your unwavering support and boundless encouragement have been my guiding light. Your presence has been a source of inspiration, helping me to grow, overcome challenges, and achieve what I once thought impossible. I could not have accomplished all of this without you.

Table of Contents

List of Figures

List of Abbreviations

CNN Convolutional Neural Network

GSO $GdScO_3$

MBE Molecular Beam Epitaxy

PCA Principal Component Analysis

RHEED Reflection High Energy Electron Diffraction

SHO $SrHfO_3$

TSO $TbScO_3$

XPS X-Ray Photoelectron Spectroscopy

XRD X-Ray Diffraction

Chapter 1

Introduction

1.1 Introduction to Perovskite Oxides

Oxides are one of the most common materials in existence and form when oxygen bonds with any other element or elements. The majority of minerals in the earth's crust are oxides and they are integral to many industrial applications and to electronic device manufacturing. Polycrystalline SiO_2 is widely used as construction materials, as a dielectric in capacitors, and as a gate dielectric in transistors. Since computer manufactures discovered the power wall in 2007, HfO_2 has also become a common oxide used in the electronics industry and has been a key piece in the creation of high-κ gate dielectrics for computer chip semiconductors [1]. Perovskite oxides are a subclass of oxides that possess a high symmetry crystal structure and follow the formula ABO_3. The A-site atom is most commonly an Alkaline metal, Alkaline earth metal, rare earth metal, or lanthanide while the B-site is most commonly a transition metal. Figure 1.1 shows the cubic perovskite structure where the A-site atoms sit on the vertices of the cube and the B-site atoms are centered in the oxygen octahedra [2, 3]. The structure takes its name from the naturally occurring $CaTiO_3$ mineral. Given the wide array of elements that are possible constituents of perovskite oxide compounds, there is a wide range of material properties that perovskite oxides can possess. This breadth of behavior has made the perovskite oxide family a significant focus of researchers for decades. Some of the interesting phenomena are found at interfaces, such as 2DEGs at $LaAlO_3/SrTiO_3$ interfaces [4] and superconductivity at $LaAlO_3/KTaO_3$ interfaces [5]. Perovskite oxides, such as STO and BTO, possess ferroelectric phases and have been investigated as possible materials for ferroelectric field effect transistors (FeFET) and ferroelectric random access memory (FRAM) devices [6, 7].

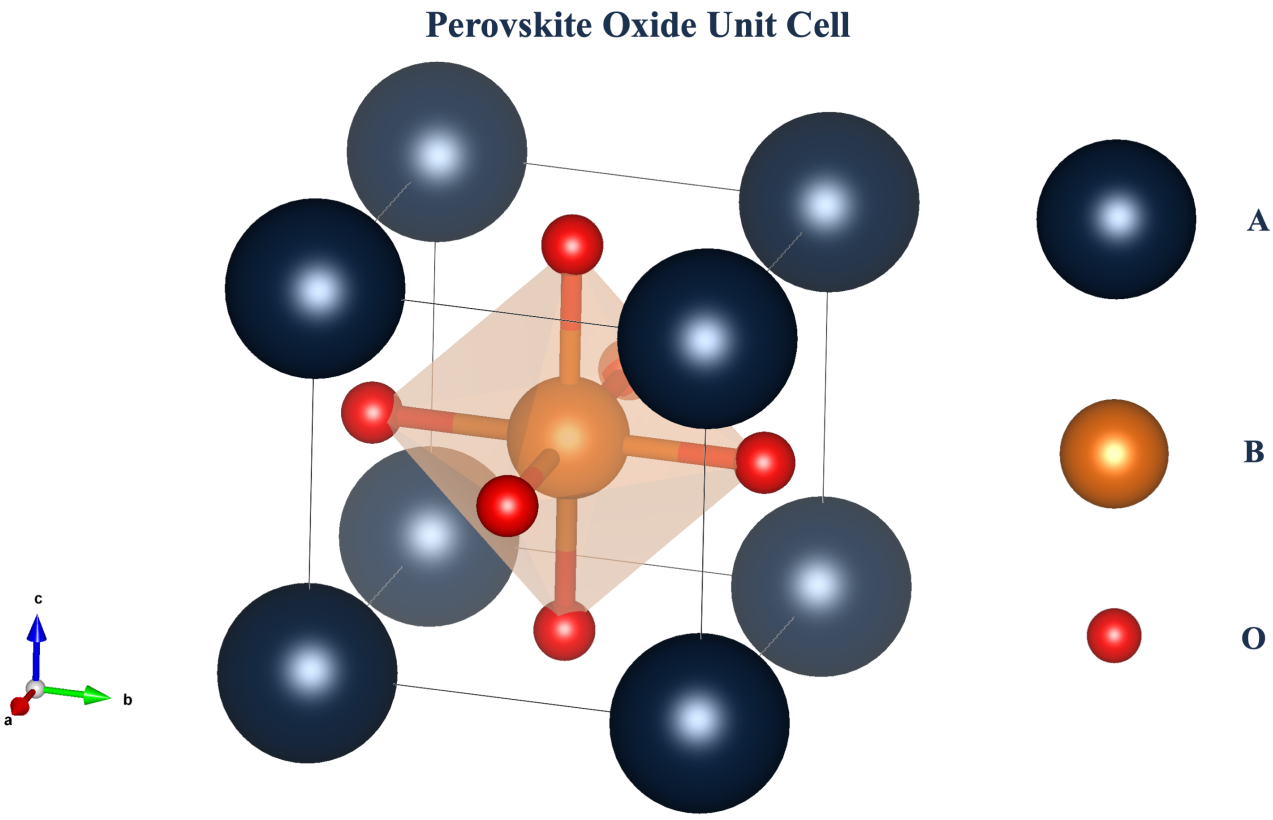

Figure 1.1: Cubic Perovskite Oxide Unit Cell.

1.1.1 Thin Films

In bulk materials, defects and boundary conditions play different roles compared to at the nano scale. The physical behavior of thin films is driven to a large extend by defects and boundary conditions. Thin films are often $<$ 50 nm thick and the applications of these materials are primarily pseudo 2D. As a result, small scale deformities, such as point defects and grain boundaries, can strongly affect the crystal structure. For example, defects in the structure of the layered perovskite Sr_2RuO_4 were found to result in the material not being superconducting [8]. The most common types of defects in thin film perovskite oxides are point defects, grain boundaries, and stacking faults. Point defects occur at a single point in the crystal and are the most common type of defect. An example are atomic vacancies, which occur where either a cation or anion is missing from the crystal structure. Impurities are another type of point defect in which an atomic species that should not be present in a material takes the place of species that

should be present at lattice site [9]. Impurities of small atomic species can also result in interstitial defects where the dopant atom does not rest on a lattice site and does not replace a constituent species. An anti-site defect occurs when a constituent atom occupies the lattice site of another constituent species. In thin film materials, multiple domains with different orientations and the grain boundaries can significantly increase electrical resistance and result in other issues [10]. Another issue that can occur is stacking faults, which is when, during epitaxial growth, there is a vertical mismatch in the layering of the material [11]. Misfit defects are a type of defect that are well studied in thin films and occur when a film is growing under strained conditions and the lattice forces a misfit dislocation to relax the strain.

Termination of the surface generally has little effect in bulk samples. However, in thin film materials, surface termination can have a profound effect on a film's characteristics. The surface of a thin film, the top 2-3 unit cells, strongly correlates to the electrical properties of some films [12]. For example, when a perovskite oxide surface is terminated in the (100) direction, the surface will terminate on either an AO or BO_2 half unit cell step. By changing the axis of termination to the (111) direction, the film now terminates in either an AO_3 or B layer. While this difference may seem trivial, the change from synthesizing $BaTiO_3$ on (110) $SrTiO_3$ (STO) and (001) STO resulted in an increase of the ferroelectric curie temperature from 550 $^{\circ}\mathrm{C}$ to 770 $^{\circ}\mathrm{C}$ [13]. 2-dimensinoal superconductivity was only found in $LaAlO_3$/$KTaO_3$ samples grown on (111) oriented $KTaO_3$ [5]. These studies demonstrate the profound effect crystal orientation and surface termination have on the electrical properties of thin films.

1.1.2 Heterostructures

The $LaAlO_3$/$KTaO_3$ [5] and $BaTiO_3$/STO [13] films are examples of thin film heterostructures, which are thin films that have been synthesized to contain sharp interfaces between materials. These interfaces have been the focus of much research due to their

ability to possess interesting phenomena and characteristics, such as 2D electron gases (2DEGs) [14] and superconductivity, that are not present in either individual material.

Metal-oxide-semiconductor field-effect transistors (MOSFETs) are the most common example of thin film heterostructures used in industry [15]. MOSFETs utilize multiple layers of semiconductors and insulators to create a transistor where the amount of current passed through the semiconductor-oxide interface is controlled by an external voltage applied to the oxide. Although the physics of MOSFETs is well known, there are many more interesting phenomena that occur at interfaces that are have not been fully explained. Thus, developing a better understanding of the links between the structural properties of the films and the electrical and optical characteristics of the heterostructures has been a major focus for researchers [16, 17].

Epitaxy is a type of crystal growth where the deposited materials are well ordered and their orientations are influenced primarily by crystal structure and orientation of the substrate [18]. Depending on the materials used, epitaxial growth is characterized as either homoepitaxy or heteroepitaxy. Homoepitaxy involves the growth of a material on a substrate or seed of the same material. This is commonly used in the semiconductor industry to grow Si wafers [19]. Heteroepitaxy occurs when the deposited material and seed material are different, such as when GaAs is synthesized on single crystal Si [20]. There are many different methods for epitaxy; however, they can be categorized by the phase of matter used. Vapor phase epitaxy methods utilize gaseous materials and includes methods such as MBE [21], PLD [22], CVD [23], and ALD [24]. Liquid phase epitaxy utilizes liquid materials and includes the Czochralski method, which utilizes molten metal and is commonly used to create single crystal Si ingots by the semiconductor industry [25]. Solid phase epitaxy is performed by depositing amorphous layers of materials on a crystal substrate and then annealing the layers until they form a single crystal [26].

In addition to the plethora of interesting phenomena that occur at the interfaces of heterostructures, there are those that occur within the material layers themselves.

While some of these phenomena occur as a result of the thin vertical dimension of the films, many occur as the result of stress and strain applied to the epitaxial films from the substrates they are synthesised on [7]. In bulk samples, the majority of the material is far from the nearest boundary with another material and thus strain is not being applied to majority of the sample and the crystal is in a fully relaxed state. However, as the samples are synthesized thinner and approach the thickness of thin films, the effects of stress and strain from the substrate begin to play a significant role in the materials structure. When films are grown epitaxially under strain, the crystal structure is distorted from the bulk phase to match the in-plane lattice parameters of the substrate [27]. Under compressive strain a lattice parameter along the axis of strain will shrink, while under tensile strain it will increase. This effect can be used to break or modify the symmetry of the film. The in-plane strain experienced by the film will result in a change in unit cell energy. Naturally, the crystal structure will react to minimize this energy in the presence of the new structural constraints. When a film is grown with compressive in-plane strain, the out of plane lattice constant will usually increase such that the new unit cell volume is nearly the same as the bulk, in a phenomenon called volume conservation [28].

In more complex crystal structures, such as perovskite oxides, there are additional structural changes that can take place. Perovskites possess oxygen octahedra at the center of the unit cell that is aligned with all three axis. Under compressive or tensile strain these octahedra will tilt, resulting in a change of symmetry [29]. STO is a cubic perovskite oxide that possesses octahedra with no tilts in the bulk. But when STO is synthesized on (110) $DyScO_3$, with tensile strain, and on (100) $(LaAlO_3)_{0.29}(SrAl_{0.5}Ta_{0.503})_{0.71}$ (LSAT), with compressive strain, the crystal structure changes from cubic to tetragonal phases [30]. The result of applying tensile vs. compressive strain to STO is that each of these samples also results in the STO phases being ferroelectric, but with the polarizations in different directions depending on the type of strain [30].

The amount of strain on an epitaxial film is derived from the lattice mismatch between the film and the substrate on which it was synthesized. The formula for lattice mismatch is [31]:

$$f = \frac{2(a_f - a_s)}{a_f + a_s} \approx \frac{a_f - a_s}{a_f}. \tag{1.1}$$

When the lattice mismatch is < 0.1, it is possible for a film to be synthesized epitaxially and strained to the substrate. If the mismatch is > 0.1, then it is unlikely that a strained film can be synthesized. Although a sufficiently small lattice mismatch may allow for a film to begin growing epitaxially and strained, the film may not stay strained as growth continues. The strain energy of the film is dependent on both the lattice mismatch and the thickness of the film [32]. As the film thickness continues to increase, the strain energy will grow beyond a level sustainable by the lattice and eventually misfit dislocations will begin to form. These misfit dislocations allow the film to relax from the strain. The thickness at which these defects begin to occur is called the critical thickness and depends heavily on the materials of the film and substrate as well as the lattice mismatch between them [33]. Beyond the critical thickness, more and more misfit dislocations will occur until the film is fully relaxed [34].

1.1.3 Surface Oxidation

As shown previously, many additional interactions need to be considered when dealing with thin films as compared to bulk materials. Surface oxidation is another important behavior that needs to be considered to fully explain the measured characteristics of a film [35]. The oxidation state of an atom is a representation of the charge on an atom in an ionically bonded material. For the purpose of determining the oxidation state, every bond is assumed to be ionic. Cations possess positive charges while anions are the oxidizing agents which possess negative charge. Oxygen is the cation of interest and typically possess a -2 charge [36]. Due to the number of elements that can fill the A and B sites of a perovskite oxide, there is a large range in oxidation states. The A site can

range from +1 to +3 while the B site can range from +3 to +5. The oxidation state of an atom plays an important role in the material's electrical and optical properties [37]. Oxidation state can also have strong effect on crystal structure. The cobalt atoms in $SrCoO_3$ (SCO) are particularly difficult to fully oxidize to its 4+ state and many works have looked for ways to increase the oxidation state [38]. If the 4+ oxidation state is not reached then the $Sr_2Co_2O_5$ phase becomes energetically favorable and samples are likely to end up with both phases in the sample [39].

For materials that are not as difficult to oxidize, oxidation of the sample does not just happen during synthesis. Most thin film perovskite oxides are synthesized under vacuum at high temperatures to prevent impurities and create highly crystalline samples. However, the majority of characterization techniques are not performed under vacuum. Once samples begin to cool down and are exposed to atmosphere many materials that were metastable in vacuum will begin to oxidize. This begins with oxygen adsorbing onto the surface and bonding to the atoms in the top couple of unit cells, which are exposed. But as these layers begin to oxidize, the more oxygen will begin to diffuse into the sample. This oxidation of the surface and film can result in a deterioration of the samples [40]. Surface oxidation will also affect any electrical measurements that utilize contacts or wires bonded to the surface of the material. There are several ways to tell if a material has suffered surface over oxidation, including the use of angle resolved x-ray photoelectron spectroscopy [41]. XPS extracts valence information from atomic species near the surface and may allow for the oxidation state to be determined [42]. In many cases, surface over oxidation will structurally deform the surface allowing for it to be diagnosed using atomic force microscopy. There are several methods for preventing surface over oxidation; however, the effectiveness of these techniques depends on materials propensity for over oxidation. For materials that can exist for some amount of time in atmosphere, keeping the samples in a nitrogen purged glove box should protect them. For materials that are highly reactive in atmosphere or begin to over oxidize

when cooled in vacuum, depositing a capping layer of a more stable material may protect them [37].

1.1.4 Superconductivity

Superconductivity is the phenomenon where a material's electrical resistivity drops to 0 Ω·m [43]. This effect occurs only at low temperatures and was first observed in solid mercury at $\approx$ 4 K [44]. In addition to no electrical resistance, superconducting materials also experience the Meissner effect, which expels all magnetic fields from the material [45]. This behavior has led to many interesting results including the ability to make objects supported by magnets levitate. Traditionally, superconductors have been separated into two types. Type 1 are superconductors that have a temperature transition directly from a non superconducting state to a superconducting state, while type 2 materials, also called hard superconductors, are ones where an intermediate state exists [46]. This intermediate states does not fully expel the magnetic field, resulting in magnetic vortexes forming within the material.

Classically, every material's electric resistance decreases as the material approaches 0 K. However, classically, it is never possible to reduce it 0 Ω [43]. Superconductivity is a quantum phenomenon that occurs as the result of coupling between phonon and electrons. In this system 2 electrons of opposite spin form a pair, called a cooper pair [47], which exchange phonons and result in the pair having energy lower than the Fermi level. This type of superconductivity was first described by Bardeen, Cooper, and Schrieffer in 1957 and thus materials of this type are referred to as BCS superconductors [48]. BCS superconductors are also referred to as conventional superconductors and are primarily pure metals with the highest known transition temperature being 39 K [49].

Unconventional superconductors are essentially all superconductors where the phonon exchange is not the mechanism utilized in electron pairing [50]. All of the materials referred to as "high temperature" superconductors are of this type. The cuprate family falls into the category of unconventional super conductors and is the group

of superconductors that currently have the highest transition temperatures under standard pressure [51]. These high temperature cuprates are made of layers of perovskite oxides alternated with Ruddlesden-Popper layers of alkali earth metals and layers of CuO_2 [52]. The number and order of layers varies between materials. Examples of superconducting cuprates include $Sr_{1-X}La_XCuO_2$ [53], YBa_2CuO_3, $PbBaSrYCu_3O_8$, and $Bi_4Sr_4CaCu_3O_{14+X}$ [52]. While much research has focused on oxides that possess superconductivity in the bulk phase [54], recently superconductivity has also been found in perovskite oxide interfaces [5], opening up interesting new paths for device and materials research. The exact mechanisms that precipitates high temperature superconductivity in perovskite oxides are still not fully understood and remain the focus of significant research.

1.1.5 Ferroelectricity

Dielectric behavior is another interesting and useful trait found in perovskite oxides [55]. When exposed to electric fields, dielectric materials will develop a polarization proportional to the strength of the electric field, as shown in Figure 1.2(a). Dielectric materials are insulators, so no charge flows through them under most conditions. By applying an electric field, such as in the charging of a capacitor, the electric moments of the dielectric will align with the electric field [56]. This effect allows capacitors with stronger dielectric materials to store more electrical energy.

Rather than a linear response to electric fields indicative of dielectrics, paraelectric materials show a strong response to weak electric fields and then above some field strength, show a linear response [57]. This behavior can be seen in Figure 1.2(b). The strong response occurs when the material begins to exhibit a polarization in response to the electric field, and the linear response occurs once that polarization medium has reached saturation. Several perovskite oxides are paraelectric, including STO which is an example of a high-κ dielectric [58]. When the external electric field is removed from the material, the polarization induced returns to zero.

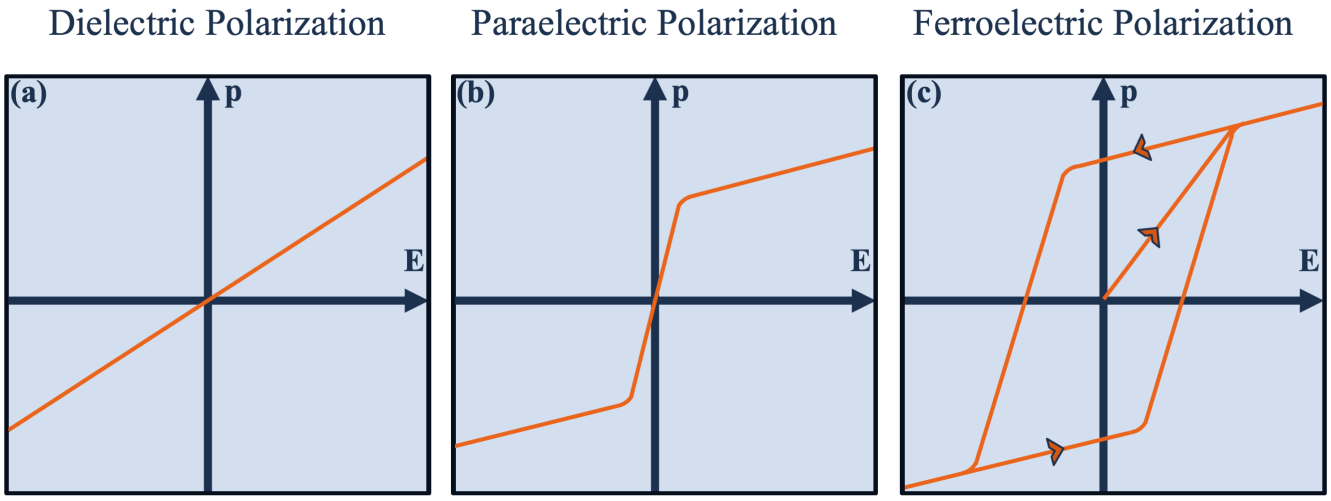

Figure 1.2: Polarization responses to external electric fields in dielectric, paraelectric, and ferreoelectric materials.

Ferroelectric materials exhibit similar behavior to the paraelectric materials when first exposed to an electric field. Like paraelectric materials, the external electric field induces a polarization in the ferroelectric material [59]. However, unlike paraelectric materials, ferroelectric materials will not return to an unpolarized state when the electric field is removed. Instead, these materials will maintain a spontaneous polarization at zero external field [60], as seen in Figure 1.2(c).

This spontaneous polarization can be forced to switch directions by a sufficiently large magnetic field in the opposite direction. This switchable nature and the presence of a spontaneous polarization are very similar in behavior to that of ferromagnetic materials. This switchable polarization has resulted in ferroelectrics being integrated into many types of devices. Radio frequency identification (RFID) chips use ferroelectric materials to power the antennas [61]. Ferroelectric oxides have also been investigated for possible use as gate dielectrics in MOSFETs [62, 63]. Traditional MOSFETs require a constant voltage to be applied for current to flow, and is thus the reason traditional random access memory (RAM) is volatile. If the gate oxide was a ferroelectric, an electric field would only need to be activated for a moment to switch the polarization of the

ferroelectric, thus requiring less energy during operation. Additionally, since the polarization is spontaneous, the memory is no longer volatile [64]. This new type of RAM is called ferroelectric RAM (FRAM).

1.1.6 Density Functional Theory

Density functional theory (DFT) is a highly useful method for predicting crystal structures in physics and materials science. In mathematics, a functional is a function that maps from one space to the real numbers or complex numbers [65, 66]. In computer science, this concept is simplified to a function that takes other functions as inputs. These concepts are used to solve the total electronic state of the crystal structure by approximating the exchange-correlations [67]. Exchange-correlations are approximations of the electron-electron effects that cannot be determined by the Hartree-Frock approximations.

There are several versions of these exchange correlations, with the local density approximation being among the most common. Several software packages, including Vasp [68–70] and Quantum Espresso [71–73], are open source and well maintained, resulting in the wide spread used of DFT. DFT allows researchers to model materials, predicting the material's structure and characteristics before synthesizing. This has resulted in a streamlined process, when searching for materials with specific qualities. With DFT, many material candidates can be ruled out quickly, resulting in quicker development and research. Although DFT is often useful, there are several situations where the results are not reliable. In many oxide semiconductors, DFT struggles with making accurate predictions of the band gap [74]. This has led to several specialized correlation functionals that attempt to correct this issue.

1.2 Introduction to Data Science, Artificial Intelligence, and Machine Learning

Traditional sciences seek to control nearly all variables to create a stable environment and test specific hypotheses. However, this approach is not always feasible due to high

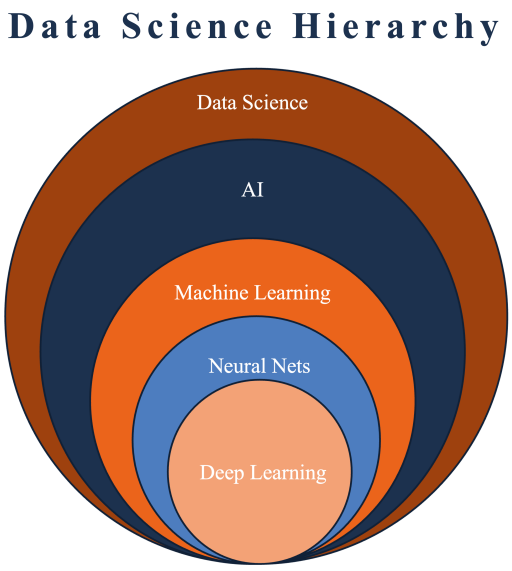

Figure 1.3: Euler diagram showing the relationships between data science, artificial intelligence, and machine learning.

numbers of degrees of freedom that cannot be directly manipulated. It is in these cases that data science has emerged as the predominant way of conducting research. Data science takes concepts from computer science, statistics, mathematics, physics, and other fields and combines them to identify trends and patterns in complex datasets [75]. As data science draws from a wide variety of other fields, it possesses an equally wide variety of techniques and algorithms. Regression analysis, dimensionality reduction, classification, and clustering are just some of the most common uses [76]. Within data science there are many distinctions that can be made to classify the many techniques. Figure 1.3 is an Euler diagram that shows the relationship between data science, artificial intelligence (AI), and machine learning (ML).

Artificial intelligence is a broad field covering any and all algorithms and programs where a computer is able to perform complex tasks that humans can perform [77]. The distinguishing characteristic between artificial intelligence and data science as a whole is the focus on constructing systems that approach or exceed the complexity of tasks of which humans are capable. Artificial intelligence algorithms are typically broken down into three major categories: supervised learning, unsupervised learning, and reinforcement learning. Supervised learning focuses on problems where there is an abundance

of labeled training data used to make predictions. Common examples include support vector machines and decision trees. Unsupervised learning uses unlabeled data and focuses on creating relationships or observing patterns in that data. Common examples include k-means clustering [78], principal component analysis [79], and Gaussian mixture models [80]. Reinforcement learning creates a system and allows it to train by taking actions and then adjusting it's future behavior based on the results. Most reinforcement learning models are based on Markov decision processes [81]. Artificial intelligence programs are already commercially implemented and are responsible for defect detection in manufacturing, traffic management in city planning, and warehouse optimization in supply chain logistics, among other things.

Machine learning (ML) is a subclass of artificial intelligence that encompasses any algorithm that is trained on data to complete a task without being explicitly programmed to do so [77]. As a subclass of AI, ML also focuses on completing complex tasks that traditionally require human intelligence; however, ML algorithms distinguishes themselves from AI by being more abstract and adaptable than other AI solutions. Machine learning algorithms are also often broken up into the same three categories as artificial intelligence algorithms: supervised learning, unsupervised learning, and reinforcement learning. The most widely used ML algorithms and the source of the ML explosion of the 2020s are neural networks [82]. Neural networks have many sub classes including convolutional neural networks (CNNs), recurrent neural networks, feed forward neural networks, physics informed neural networks, and others. Neural networks can be used for either regression or classification problems, and are able to be used in either supervised or unsupervised formats. For instance, feed forward neural networks are commonly used in commercial applications for facial recognition, computer vision, and natural language processing.

1.3 Overview of Thesis

This dissertation seeks to investigate the existence and characteristics of the P4mm phase of SHO and to develop improved characterization techniques using data science and machine learning algorithms that aid in materials characterization. Chapter 2 introduces perovskite oxide thin films and molecular beam epitaxy, a common and highly precicse technique to synthesize epitaxial thin films, and the method used in this work. Chapter 3 explores the thin film characterization methods used in this work to investigate the SHO films while chapter 4 delves into data science, artificial intelligence, and machine learning, along with the techniques from them that will be used to characterize thin films. Chapter 5 demonstrates the use of the big data processes of principal component analysis and k-means clustering to enhance understanding of RHEED data and evolution of sample surfaces during growth. Chapter 6 analyzes the structural, optical, and electrical characteristics of thin film SHO samples synthesized epitaxially with in-plane strain. Chapter 7 studies the ability of the random forest and neural network machine learning techniques to generate useful predictions in real time from RHEED patters. Finally, chapter 8 summarizes the results of this dissertation and highlights routes for possible future work.

Chapter 2

Thin Film Synthesis

2.1 Thin Films

Many previous studies of oxides have focused on polycrystalline samples, which are easy to grow using sputtering and chemical vapor deposition. As a result of this cheap and reliable synthesis, materials like SiO_2 and ZnO are wide spread in the electronics industry [83]. However, the effects of impurities, grain boundaries, and mixed orientation in polycrystalline materials often result in diminished effectiveness of the synthesized materials. Single crystalline samples do not have these issues and also allow for more detailed investigations of the materials properties.

Thin films crystals are samples whose thickness ranges from a couple of unit cells to a few hundred nanometers. The synthesis techniques for epitaxial thin film samples result in higher purity, larger crystal domains, lower amounts of defects, and single crystalline samples [84]. These higher quality samples allow for more accurate and precise measurements of structural, optical, electric, and magnetic properties. Thin film samples often have sharper interfaces, allowing for deposition of heterostructures and the study of 2D phenomena, such as 2D electron gases at $LaAlO_3/SrTiO_3$ interfaces [4] and 2D superconductivity at $LaAlO_3/KTaO_3$ interfaces [5]. Devices such as MOSFETS can also be synthesised in single crystal thin film form [85].

2.2 Molecular Beam Epitaxy

2.2.1 History

Molecular beam epitaxy (MBE) is a thin film synthesis technique that is able to achieve highly crystalline epitaxial growth of single crystal samples. MBE systems use cylindrical crucibles called effusion cells to evaporate pure elements. Due to the cylindrical shape of the effusion cell, the evaporated material escapes the cell in beam shape that

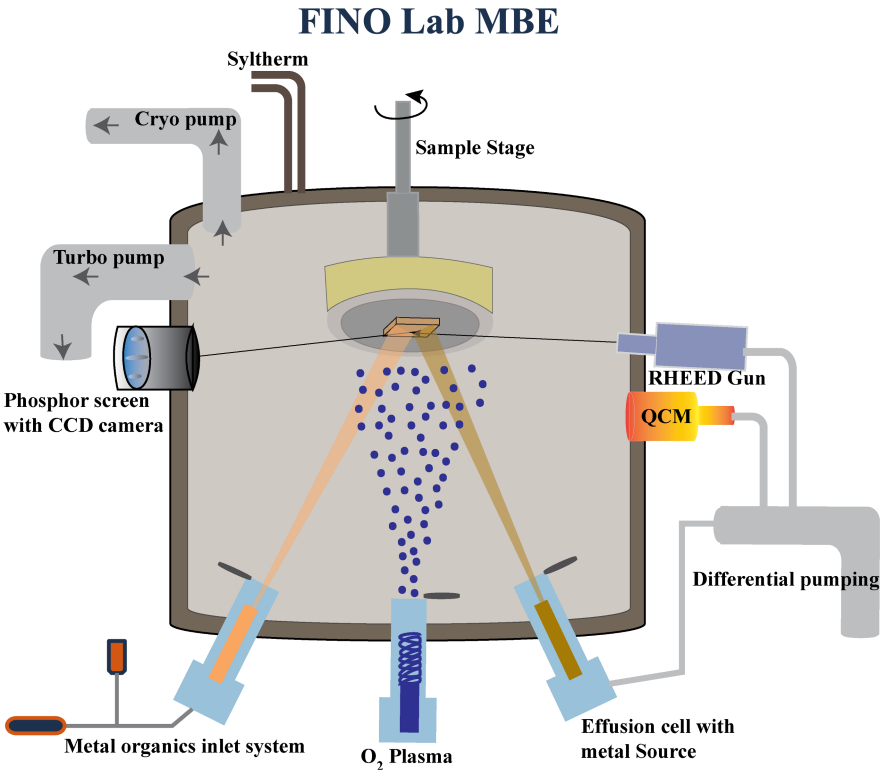

Figure 2.1: Schematic of hybrid molecular beam epitaxy chamber in the Films, Interfaces, and Nanostructures of Oxides (FINO) Lab. Adapted from [88].

is aligned with the sample stage of the chamber [86], as seen in Figure 2.1. In order to reduce the rate of collision between the metal atoms and ensure consistent growth, MBE chambers are kept at pressures in the range of 1.0×10^{-8} to 1.0×10^{-10} Torr. In this ultra high vacuum (UHV), the mean free paths of the metal atoms are over 5 m [87] while the distance from the effusion cells to the sample stage is around 20-40 cm. This ensures that the metal atoms do not react or bond to any atmospheric elements and are able to deposit on the substrate.

MBE was first used to study the nucleation of Si in 1968 [89]. In 1969 the *in-situ* characterization methods of Auger electron spectroscopy and low energy electron diffraction (LEED) were added [90]. Shortly after several groups began to utilize MBE to synthesize GaAs and other III-V materials [91]. In 1970 the first works were published that showed RHEED can be used to obtain real time feedback on sample quality [92, 93]. As a result, RHEED became the primary system used for *in-situ* film

characterization in MBE chambers. This setup has remained as the core design behind contemporary MBE chambers. This setup for MBE chambers was a significant advancement over previous synthesis methods; however, it provided no system to synthesize oxides, the most common materials in the world [91]. The first results of oxide MBE were published in 1979 on the synthesis of Al_2O_3 on GaAs substrates [94]. The aluminum metal was introduced by an effusion cell while oxygen was introduced by molecular O_2 gas.

2.2.2 Oxide Molecular Beam Epitaxy

Initially, oxygen gas was supplied in it's molecular form [95]; however, this required samples to be grown at temperatures high enough to react the O_2 with the sample. This greatly restricted the growth of materials that require low temperatures deposition. However, by passing O_2 through a radio frequency plasma generator, an oxygen plasma is created that is far more reactive than molecular oxygen [96]. This setup can be seen in Figure 2.1. Alternatively, oxygen can be introduced in the form of ozone, O_3, which is also more reactive than molecular oxygen. This change not only allowed for increased range of growth conditions, but it was also found that atomic oxygen, O^- served to clean carbonaceous material from the chamber and the surface of substrates [97]. Reducing sample surface contamination is critical for the growth of oxide heterostructures as the interfaces of these heterostructures is where much of the interesting physics takes place [4, 5].

In order to achieve the desired material, careful calculations are used to determine the appropriate effusion cell temperature for each growth. A quartz crystal microbalance (QCM) can be mounted inside the vacuum chamber and used to measure the deposition rate of the metal oxides [98]. The QCM crystal is placed directly in front of the sample stage while an effusion cell. The depositing material changes the mass of the crystal resonator resulting in a change in frequency that is measured and used to calculate the deposition rate of the metal.

Despite the advantages of using oxygen plasma, there are several downsides. The radio frequency (RF) generator used to create an oxygen plasma can give off radio signals that cause signal interference for other instruments, including thermocouples that are not RF shielded. The highly reactive oxygen that is critical to the successful oxidation of some materials is also rather effective at oxidizing equipment as well. Unfortunately, everything in the chamber is subjected to the same reactive oxygen. If anything in the chamber begins to oxidize, then it can become a source of contamination in the chamber. Additionally, any equipment that oxidizes will wear out quicker and need to be replaced more frequently. Any piece of equipment that is heated during growth, such as the sample heater, sample stage, and effusion cells, needs to be made of materials that will not oxidize easily or needs to have sufficient cooling systems that reduce its reactivity. Tantalum is stable at high temperatures making it a common choice for sample holders and stages [99].

Unfortunately, the materials in the effusion cells are also exposed to oxygen consistently, causing them to oxidize. For some materials, this is not much of an issue as the thin layer of oxide that forms can be blasted off the surface before calibration. However, for materials that are highly reactive like Sr, constant oxygen exposure would result in the majority of the source being oxidized and rendered useless. One solution to this is to have a valve that can be closed to separate the highly reactive sources from the main chamber when not in use [100]. But the materials still need to be under constant vacuum, so an additional valve that is connected directly to a differential pump must be present. This setup, seen in the bottom right of Figure 2.1, is highly effective but is also costly, so it is reserved only for the most reactive metals. Despite these issues, oxide MBE has been used to synthesize several of the most important materials discovered in the last 50 years and is still one of the best options for synthesizing single crystal thin films.

2.2.3 Hybrid Molecular Beam Epitaxy

Traditional oxide MBE uses effusion cells capable of operating at up to ≈1600 °C, while selected high temperature cells are able to operate at up to 2500 °C, but are not in common use. While this setup is effective for supplying a wide variety of metals for synthesis, there are several metals for which this does not work. V, Zr, Ti, Nb, Hf, Ir, and Ta are all refractory metals which have extremely low vapor pressures even at high temperatures [101]. As a result, deposition of these refractory metals via traditional MBE ranges from challenging to impossible. Atomic layer deposition (ALD) is another common synthesis method. ALD solved the problem of depositing refractory metals by introducing them via metal organic precursors [24]. The exact chemical structures of the precursors vary; however, they are all similar to the ones shown in Figure 2.2. The precursors consist of a refractory metal atom bonded to several ligands, some of which contain oxygen. These precursors allow for refractory metals to be evaporated and deposited at much higher and more consistent rates than if high temperature effusion cells were used. The precursors are stable enough to be evaporated at low temperatures, 100 °C, but reactive enough that when exposed to reactive oxygen and higher temperature substrates, $>$ 400 °C, they will break down, depositing the metal atom.

Gases as sources in MBE were first used in 1980 when arsine was used to grow GaAs and when phosphine was used to grow InP [102], but these precursors left much to be desired since they are both toxic. In 1981 and 1982, the first metal organic precursors were used [103, 104], though it wasn't until 1986 that a metal organic precursor was used in conjunction with an effusion cell for the first time [105]. In 2009 a renewed interest was given to hMBE and the first growths of a perovskite oxide, STO, using hMBE were performed with highly reactive oxygen [106, 107]. In this study, the metal organic titanium tetraisopropoxide (TTIP) was used to supply Ti atoms. Since then, hMBE has need been adopted by many groups as a way to supply refractory metals in MBE [108]. Figure 2.1 shows a version of the metal organic injection system used

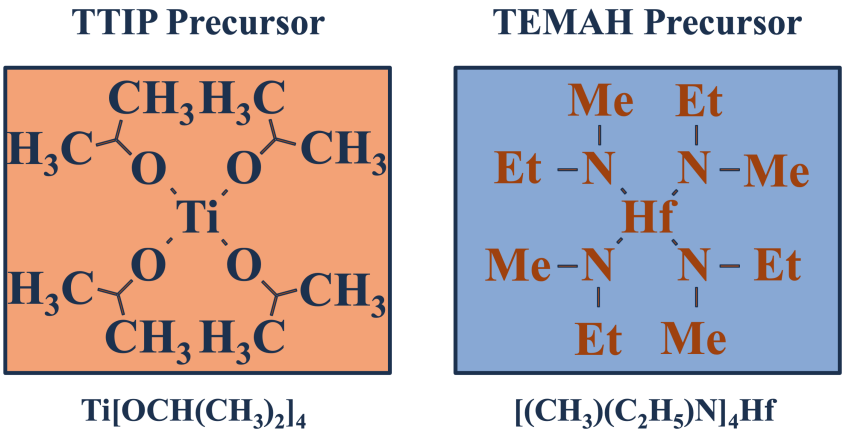

Figure 2.2: (Left) Molecular structure of the metal organic precursor Titanium(IV) isopropoxide (TTIP).(Right) Molecular structure of the metal organic precursor tetrakis(ethylmethylamino)hafnium(IV) (TEMAH).

in hMBE. In this setup, the metal organic precursor used was contained in a stainless steel bubbler that was heated to evaporate the precursor. The gaseous precursor is then sent through a gas injector, which is heated to prevent the precursor from recondensing. When the precursor is at low pressures, < 100 mTorr, the gas injection system functions much like an effusion cell, supplying the metal organic directly to the sample in a beam shape.

Due to the additional source of gas being used during growth, the chamber pressure will increase. Additionally, the metal organic molecules will not necessarily stick to the first surface they find as the metal atoms would. Instead, those molecules that do not collide with something that has sufficient thermal energy to cause the molecule to react will scatter. For this reason, covering the walls of the chamber in Figure 2.1 is a low temperature shroud that is constantly being cooled by syltherm [109] pumped from a low temperature chiller. The syltherm and shroud are chilled to -60 °C, resulting in the scattered metal organic molecules getting stuck to it. This improves purity of the chamber, where the effusion cell sources will still operate as expected, and prevents contamination of the chamber [100]. Some precursors may contain oxygen that may add to the oxygen environment of the growth. If the materials being synthesized tend to over oxidize or requires a low oxygen environment to grow, then a precursor without

oxygen should be used. When selecting a precursor, another thing that must be considered is the substrates surface chemistry [110]. As mentioned, there are often several commercially available precursors for a single metal and each of these precursors will have different vapor pressures and decomposition temperatures. Thus, careful consideration is required to ensure a precursor will fit the growth window for the sample being synthesized.

2.3 Thin Film Growth Modes

Epitaxial thin film synthesis can be divided into two categories depending on the materials being grown. If the thin film is grown on a substrate of the same material, the synthesis is called homoepitaxy [19]. If the film material is different than the substrate it is called heteroepitaxy. Heteroepitaxy is more common as many of the interesting phenomena in oxides occur in heterostructures [20]. Within epitaxial growth there are several possible growth modes by which films are deposited. The growth mode describes the behavior of the deposited atoms on the surface of the sample and is highly dependent on surface structure, chemistry, and kinetics. In layer by layer growth, the adsorbed atoms fill an entire layer of the crystal before starting to form the next layer [111], illustrated in Figure 2.3. Layer by layer growth is the preferred growth mode for samples in MBE as it results in uniform surfaces and interfaces. Additionally, since the film completes an entire layer before continuing, it allows for precise control of film thickness and termination, both of which are important for obtaining the properties desired in heterostructures. Samples synthesized with layer by layer growth will also have very low roughness, meaning characterization techniques that require smooth surfaces will work well. In order to achieve layer by layer growth, the lattice mismatch between the film and the substrate must be quite small, otherwise the strain energy will cause defects that prevent such growth. Complex oxide films must also be near stoichiometric for layer by layer growth to occur. If the film has an overabundance of one element, the layers will not be able to fully form before excess material begins to form the next layer. Layer

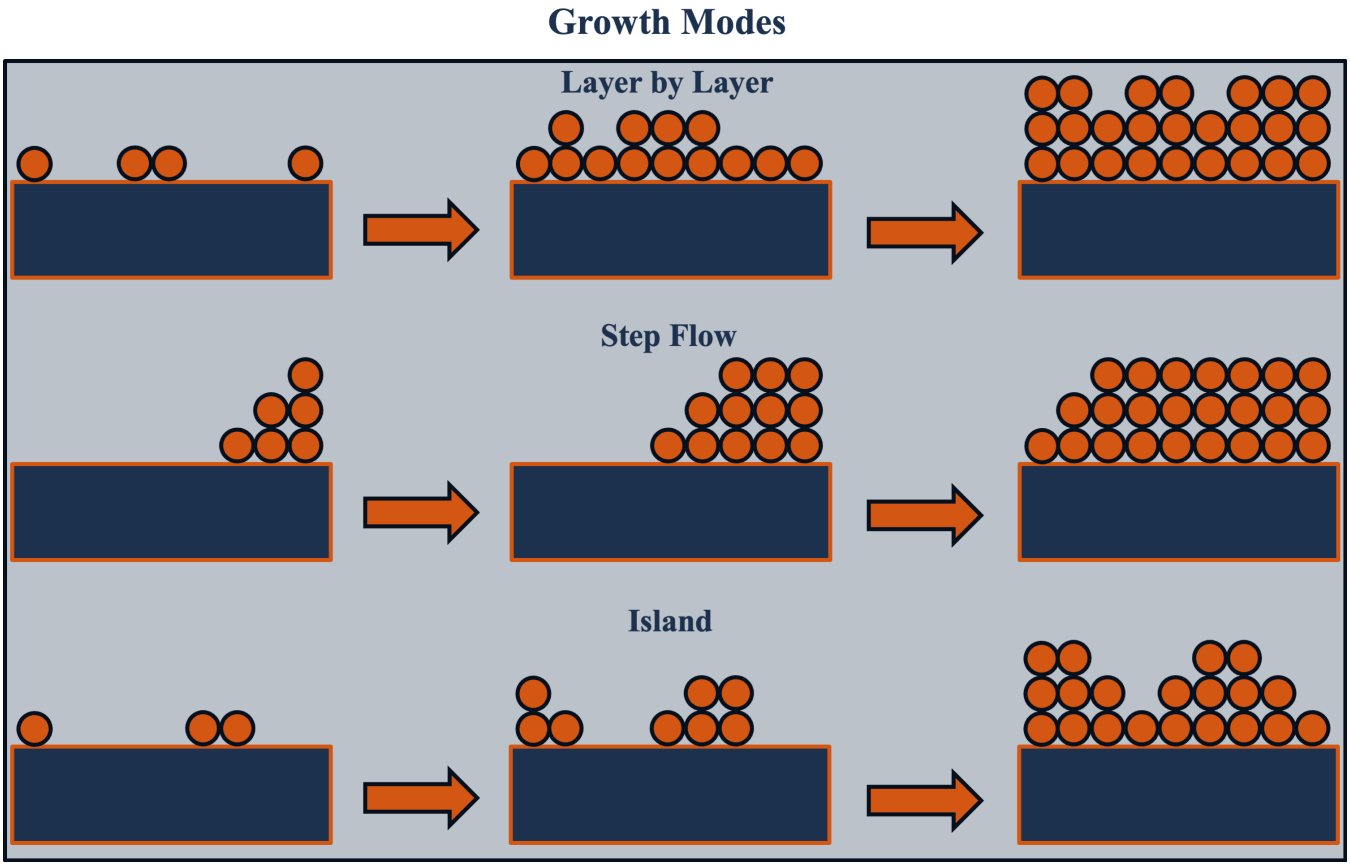

Figure 2.3: Diagram of growth modes common in molecular beam epitaxy.

by layer growth also requires a high substrate temperature. This temperature range will provide the adsorbed atoms enough mobility to move along the surface and slot into place.

Step flow growth is another growth mode possible in MBE thin film synthesis. In step flow growth, the adsorbed atoms will continue to move across the surface of the film until they become bound to a step edge [112], as depicted in Figure 2.3. This mode of growth requires even higher temperatures than layer by layer growth to allow for the adsorbed atoms to remain mobile until they encounter a step edge. This process utilizes the few degree miss-cut of the substrate that results in step edges. If the surface of the substrate does not have a smooth surface and fairly sharp step edges, then this growth mode will not be achieved. Like layer by layer growth, step flow growth also requires an very low lattice mismatch and near stoichiometric film deposition. Step flow growth

is able to achieve very low defect rates like layer by layer; however, the deposition rates possible are lower than those possible with layer by layer growth.

Island growth is non-ideal growth mode that results in islands of atoms forming rather than smooth layers [113], as seen in the last line of Figure 2.3. Island growth is usually the result when layer by layer or step flow growth are not achieved. This mode can result from the substrate temperature being too low, thus resulting in adsorbed atoms not being able to move across the surface. It can also occur when the lattice mismatch between a film and substrate is too high or a surface is too rough. When films are grown in an island growth mode, strain effects will likely not be present in the film. Instead the layers will relax causing defects in the sample. As a result, most films synthesized with an island growth mode will not be single crystalline and will have a very rough surface. This will make growing additional layers of a heterostructure difficult and will negatively effect the results of characterization techniques that rely on smooth film surfaces. Once island growth begins, the size of the islands will continue to increase as deposition continues. It is also possible to obtain film to begin growing in a step flow or layer by layer mode and then switch to island growth once the film has reached the critical thickness [114].

Chapter 3

Thin Film Characterization Methods

In order to determine the underlying structure and properties of thin films synthesized using MBE, several different characterization techniques are used. During film growth, *in-situ* reflection high energy electron diffraction patterns are obtained in order to monitor the evolution of the sample. X-ray photoelectron spectroscopy is performed *in-vacuo* on samples post growth to determine the stoichiometry, film surface termination, and valance band features. *Ex-situ* X-ray diffraction, X-ray absorption spectroscopy, scanning transmission electron microscopy, and second harmonic generation are employed to further characterize the structure and properties of films.

3.1 Reflection High Energy Electron Diffraction

Reflection high energy electron diffraction (RHEED) is a common characterization technique used in pulsed laser deposition and MBE [115]. In most systems, due to the geometry of the chambers and the temperature and pressure conditions, RHEED is the only *in-situ* characterization technique possible. Being *in-situ*, RHEED is able to provide information about a sample in real time rather than post growth [116]. This provides opportunities for the operator to adjust growth conditions during growth to obtain a better sample. RHEED patterns result when a focused high energy electron beam hits a crystalline sample at a very shallow angle, $< 1^{\circ}$. Figure 3.1 shows the geometry of electron diffraction. The electrons that diffract off of the crystalline sample then fly through the vacuum chamber until they hit a phosphorous screen. As a result of the electron bombardment, the phosphorescent screen emits light proportional to the number of electrons hitting the screen.

The diffraction patterns are governed by Bragg's law, $n\lambda = 2d\sin(\theta)$, where d is the spacing between crystal planes and the wavelength is the de Broglie wavelength of the electron [115]. In reciprocal space, the crystal structure forms rods; and when

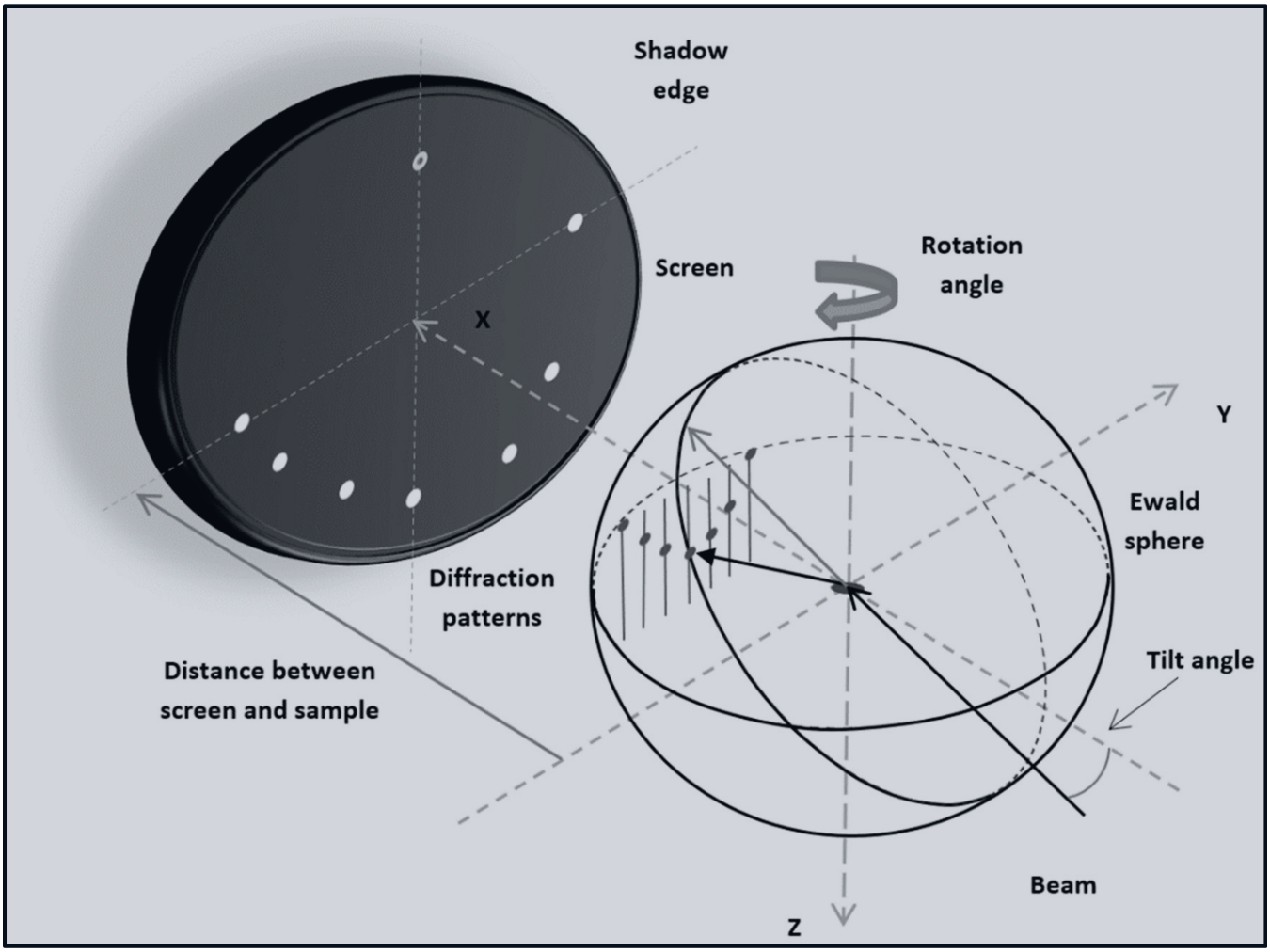

Figure 3.1: Schematic of reflection high energy electron diffraction. Reproduced from [117] under CC BY 4.0 [118].

these rods align with the Ewald sphere the Laue condition is satisfied and a maxima is observed. Under ideal circumstances, the intersection of the Ewald sphere and the reciprocal lattice rods yield perfect points. However, due to the nonidealities in the crystal structure and experimental setup, the spots are sometimes observed as streaks [119]. This becomes the case when the average length of the domains in the crystal become shorter than the coherence length of the electron beam [120]. Since n in Bragg's law can be any positive integer, there are infinitely many Laue rings that result from RHEED. However, in many practical conditions only the 0^{th} order and 1^{st} order rings are usually observable. Each Laue ring will also have several spots corresponding to different rods

in the reciprocal lattice. RHEED can be collected along several crystallographic axes, but it is common for (001) oriented perovskites that the axis chosen is either the (100) or the (110) axis. The intensity of RHEED spots also depends on the atomic number of the atoms causing the diffraction. Heavier atoms result in brighter spots and streaks than lighter atoms. Although RHEED is much less sensitive to the lighter elements such as carbon and nitrogen, significant surface contamination will still result in a drastic decrease in pattern intensity [115].

A standard RHEED system consists of several important pieces. The electrons are generated when a voltage of $10 - 20$ kV is applied across a tungsten filament anode and a cathode. The voltage results in the electron being pulled toward the anode and thus the voltage controls both the amount and velocity of electrons [115]. The voltage is usually kept at the lowest sustainable level to avoid burning out the filament. The resulting electrons then pass through a series of electron optics that focus the beam. The electron beam is focused onto the phosphorous screen rather than the sample in order to maximize the resolution of the diffraction pattern. The electron beam then exists the electron gun, where the filament and optics are housed. The electron optics are controlled by the power supply and a small control box that sit on the power rack. The pattern that results on the phosphor screen from the electron bombardment is recorded and transmitted to a computer from a camera placed just behind the screen in a blacked out enclosure. Another way to improve the lifetime of a RHEED gun is to connect a differential pump to the gun, see Figure 2.1. This lowers the pressure of the gun, resulting in less buildup of material and preventing the electrons from being absorbed prematurely. A RHEED system from STAIB instruments, visualization software from KSA, and screen recording software from Flashback Express were used in this work.

Due to the propensity of electrons to be absorbed or scattered easily, RHEED is a surface sensitive characterization that probes only the top one to two unit cells of a sample [115]. From RHEED we are able to observe changes in the surface sample in real time and some important changes in the sample can be observed. The simplest

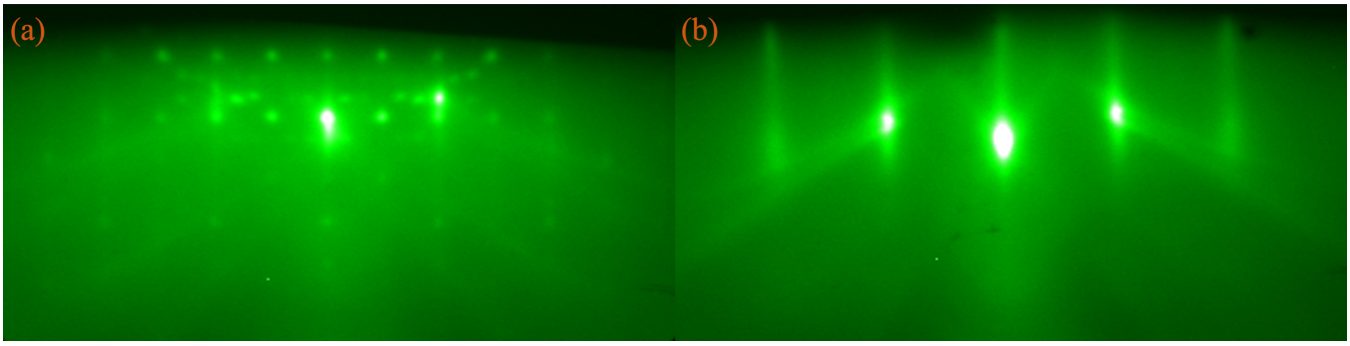

Figure 3.2: (a) RHEED image of an STaO film that has both the $SrTaO_3$ and $Sr_2Ta_2O_7$ phases present. (b) A RHEED image from an SHO film grown on GSO showing a high quality film with domains smaller than the decoherence length of the electron beam.

change to observe through RHEED is a change of the diffraction pattern. If the pattern remains sharp but changes pattern, the sample is likely undergoing a phase change or possibly developing a second phase. This can be seen in Figure 3.2(a), where a $SrTaO_3$ film is developing a $Sr_2Ta_2O_7$ phase over part of the surface [121]. Since the screen shows a mixing of the diffraction pattern expected for the 113 phase and the diffraction pattern for the 227 phase, it can be determined that both phases are present on the surface of the sample. Figure 3.2(b) shows a RHEED image from a high quality SHO-GSO sample which shows no signs of other phase or islands present.

Since the Bragg condition is dependent on the spacing of the crystal lattice, changes in the spacing between RHEED spots indicate a change of the in-plane lattice constants of the film [115]. In heteroepitaxy, the film will have the same lattice spacing of the substrate if the film remains fully strained. As a result, the spacing between the RHEED spots of the film should line up exactly with the RHEED spots of the substrate. Thus by comparing the current RHEED pattern to an image take of the substrate RHEED pattern prior to growth makes it possible to identify if the film has significantly relaxed. The diagram of RHEED in Figure 3.1 assumes an atomically flat crystal surface, which is most often not the case. When the surface begins to become multilayered or covered in islands, the electrons will be subjected to additional scattering effects. This results in the RHEED pattern becoming diffused at first, and eventually becoming an array of increasingly large spots. So long as the surface is still crystalline, some diffraction pattern

should be observed. However, if the sample was becoming amorphous, no diffraction pattern would be observed at all.

In addition to monitoring the RHEED pattern of the film, there is information that can be gained by monitoring the intensity of RHEED spots themselves. It is common to use a program to sum the intensity within a certain region, a single spot, and plot this over time [115], resulting in a graph like the one in Figure 3.3. From this monitoring, it becomes possible to easily observe the change in the film quality over time. If the film is starting to become rough, amorphous, or covered in islands, the intensity will begin decreasing. If a change to the growth conditions is made, then the surface may begin to recover and an increase in intensity will result. If the intensity remains constant over time, then it can be inferred that the sample is maintaining quality. In Figure 3.3, oscillations can be observed in the intensity of specular spot, with these oscillations resulting from the sample undergoing layer by layer growth [115, 122]. Starting with a complete layer, the intensity is at a maximum; and, as the surface begins to have adsorbed atoms partially cover the surface, the intensity begins to decline. At the point when the layer is beyond 50% filled, the pattern begins to increase and reaches another maximum when full. Since this cycle corresponds to the deposition of a single unit cell, it is possible to precisely tune a growth to be a desired thickness or even end in a particular termination.

Although RHEED is highly useful during film synthesis, there are several downsides and limitations. The results extracted from the RHEED patterns are limited to primarily qualitative observations rather than quantitative ones. Thus the first and foremost limitation is that it requires a well trained expert to comprehend and interpret the patterns. Without sufficient experience, recognizing the patterns and the subtle changes during growth renders the technique much less useful. This experience takes many growths over several years to acquire. Significant experience is needed to analyze RHEED images because there are few advanced analytical tools that can be used to analyze the images. The theory is able to successfully explain the location of the Laue

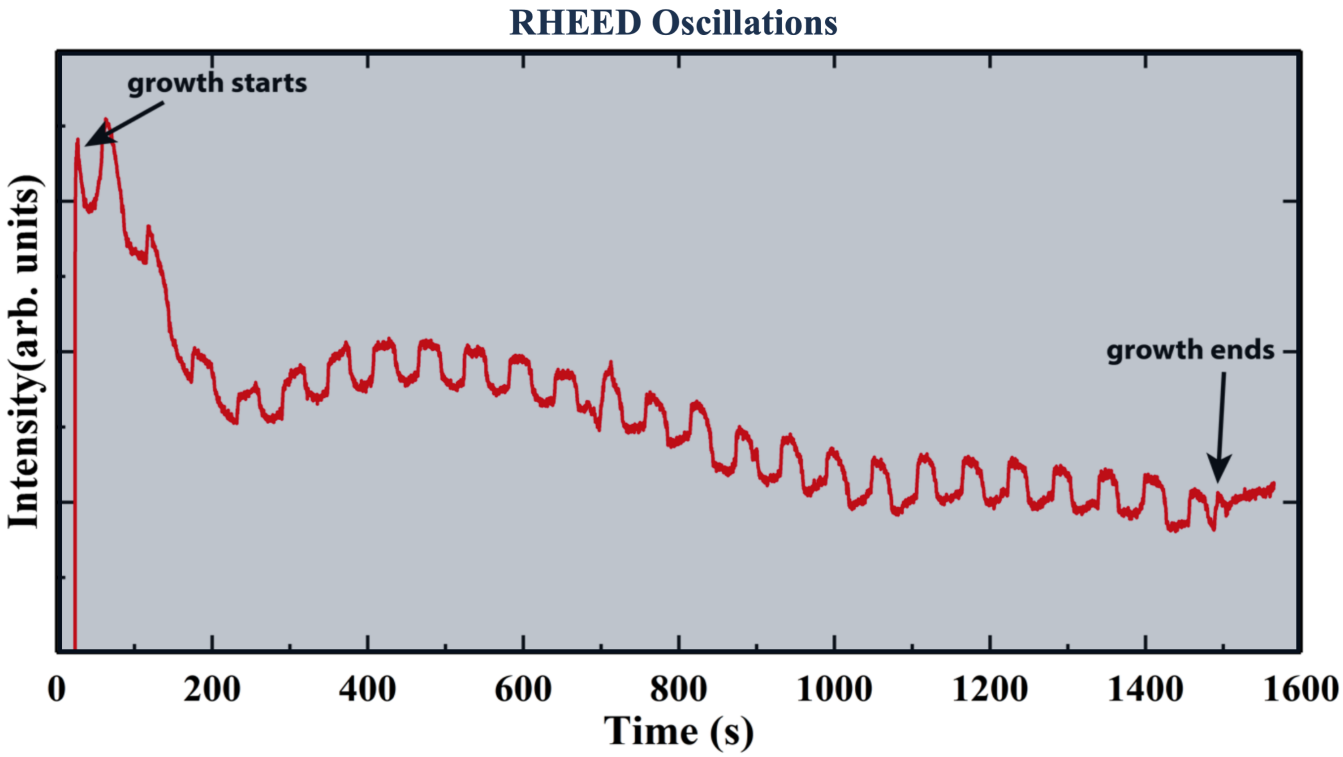

Figure 3.3: Plot of the average specular spot intensity over the duration of the growth of an LFO by MBE. Reproduced from [122].

rings and RHEED spots [123]; however, this is limited to ideal circumstances and ignores the other effects present in real samples. In some cases it is not possible to use RHEED at all due to the properties of the materials being synthesized. In $CoMn_2O_4$, the cobalt is difficult to fully oxidize and tends to reduce. When the RHEED beam is incident on a portion of the sample during growth, a discoloration is observable, which is the result of that section of the sample being reduced [124].

3.2 X-ray Photoelectron Spectroscopy

X-ray photoelectron spectroscopy (XPS) is a well studied surface sensitive technique for characterizing the atomic composition of thin film samples. XPS spectra can be used to investigate a plethora of film characteristics, including the atomic species present in samples, identify different bonding environments, and inform on the oxidation state. XPS is based on the photoelectric effect, where high energy photons incident on a sample cause electrons to be ejected [125]. In a monochromatic XPS system, X-rays are

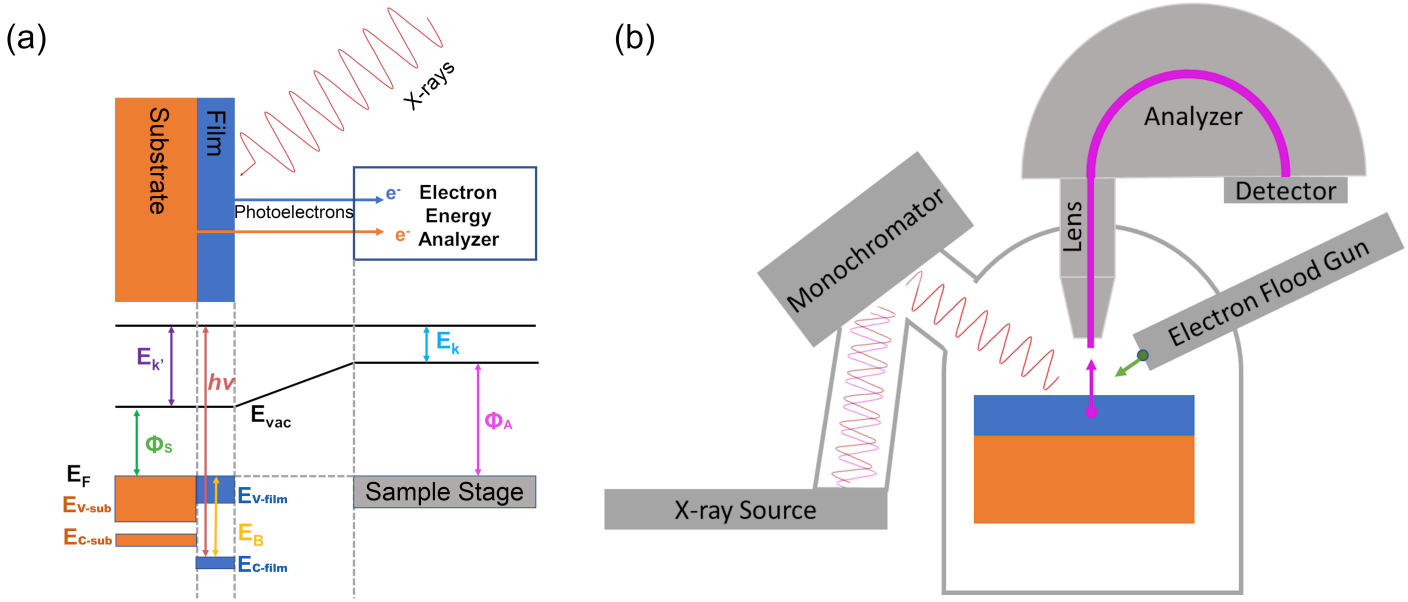

Figure 3.4: (a) The energy band diagram of a thin film sample in XPS. (b) Schematic of an XPS system. Reproduced from [41].

generated by an elemental source, such Mg Kα X-ray (1253.6 eV) or Al Kα X-ray (1486.6 eV) [41]. Before reaching the sample, incident X-rays are passed through a Rowland circle monochromator to ensure only one wavelength of X-rays is present. The electrons ejected by these X-rays are referred to as photoelectrons and emitted in every direction. Since electrons are easily absorbed or scattered, XPS measurements take place in UHV at pressures below 5×10^{-9} Torr. Figure 3.4(b) shows a diagram of an XPS system.

Some of the photoelectrons coming off the sample will happen to be aligned with and pass through the collection lens. Behind this lens are a set of electron optics that retard the electron's speed. These electrons are then sent through a hemispherical electron analyzer that selects for specific electron velocities. Finally, all of the electrons with the selected velocity encounter an electron detector and are counted [41]. In newer XPS systems, it is possible to count electrons over a small range of energies simultaneously, significantly decreasing data collection time [126–128]. In the XPS chamber a sample sits on a metal conducting stage that is electrically grounded. This grounding allows conducting samples to constantly replace the vacancies created by the emitted

photoelectrons. However, if the sample is semiconducting or insulating, the surface of the sample will become depleted of electrons and positively charged. This results in an effective electric field that affects the exit velocity of the remaining electrons [41]. In order to replace the electrons and fill the vacancies, an electron neutralizer, or flood gun, is used. This subsystem showers the sample in a constant ray of low energy electrons. These electrons are captured by the sample and fill the missing core levels, neutralizing the electric field created by the vacancies.

Figure 3.4(a) shows the band diagram of a sample undergoing XPS. From the diagram, the energy of a photoelectron is given by:

$$E_{photon} = h\nu = E_B + \Phi_S + E_{k'}, \tag{3.1}$$

where the binding energy, E_B, is the energy needed to bring the electron to the Fermi level, the material's work function, Φ_S, is the energy needed to free an electron at the Fermi level from the sample and into vacuum, and the vacuum kinetic energy is $E_{k'}$. This kinetic energy is not the same kinetic energy selected by the XPS analyzer. The observed kinetic energy, E_k, depends on the work function of the XPS, Φ_A, and is related to the vacuum kinetic energy by:

$$E_{k'} = E_k + \Phi_A - \Phi_S. \tag{3.2}$$

Substituting equation 3.2 into equation 3.1 for $E_{k'}$ results in:

$$E_B = h\nu - E_k + \Phi_A. \tag{3.3}$$

The photon energy, $h\nu$, is determined by the X-ray source used. In this work, an Al Kα X-ray source was used, which has an energy of 1486.6 eV. The XPS work function, Φ_A, can be determined experimentally, and is fixed for a given system. Thus the kinetic energy observed by the XPS can be used to directly calculate the binding energy

of the core levels from which the photoelectrons originated. The energies of the valence electrons in the core levels are effectively unique. Thus by consulting a reference catalog that comes with the XPS system, the particular valence shell and element the photoelectrons were ejected from can be determined.

While the X-rays incident on the sample will fully penetrate the sample and excite electrons from the film and substrate, the photoelectrons observed by the analyzer will be from the top ≈ 10 nm of the sample. This can be understood by examining the inelastic mean free path of the electrons, which is calculated by [129]:

$$\lambda(\text{nm}) = \frac{143}{E_{k'}^2(\text{eV}^2)} + 0.054\sqrt{E_{k'}(\text{eV})}. \tag{3.4}$$

For an Al Kα source, the mean free path will range from $\approx 1-2$ nm, and more than 50% of the signal observed will be from the top 2 nm [41]. As a consequence, XPS is inherently a surface sensitive characterization technique. It is possible to make the results even more surface sensitive. The estimate that 50% of the signal coming from the top 2 nm is under the assumption that the analyzer is situated normal to the surface of the sample, where the photoelectrons reaching the analyzer took the shortest path out of the sample. However, by tilting the stage at some angle, the path the photoelectrons take through the sample becomes longer. This results in a decrease of the average depth at which observed photoelectrons originate. At an angle of 70°, the majority of the signal will come from the top two unit cells [41]. However, tilting the stage in this way will result in longer collection times need to observe the signal over the background noise.

Figure 3.5 shows an example of the Hf 4d peak from an SHO-GSO sample. This type of high resolution narrow binding energy scan is called a multiplex or core level scan. A low pass energy of 35.5 eV is used and the energy range is scanned dozens of times. The data is aggregated and used to compile plots like that in Figure 3.5. The shape of these peaks is most accurately described by a Voigt function, which is a convolution of a Gaussian and Lorentzian and is given by:

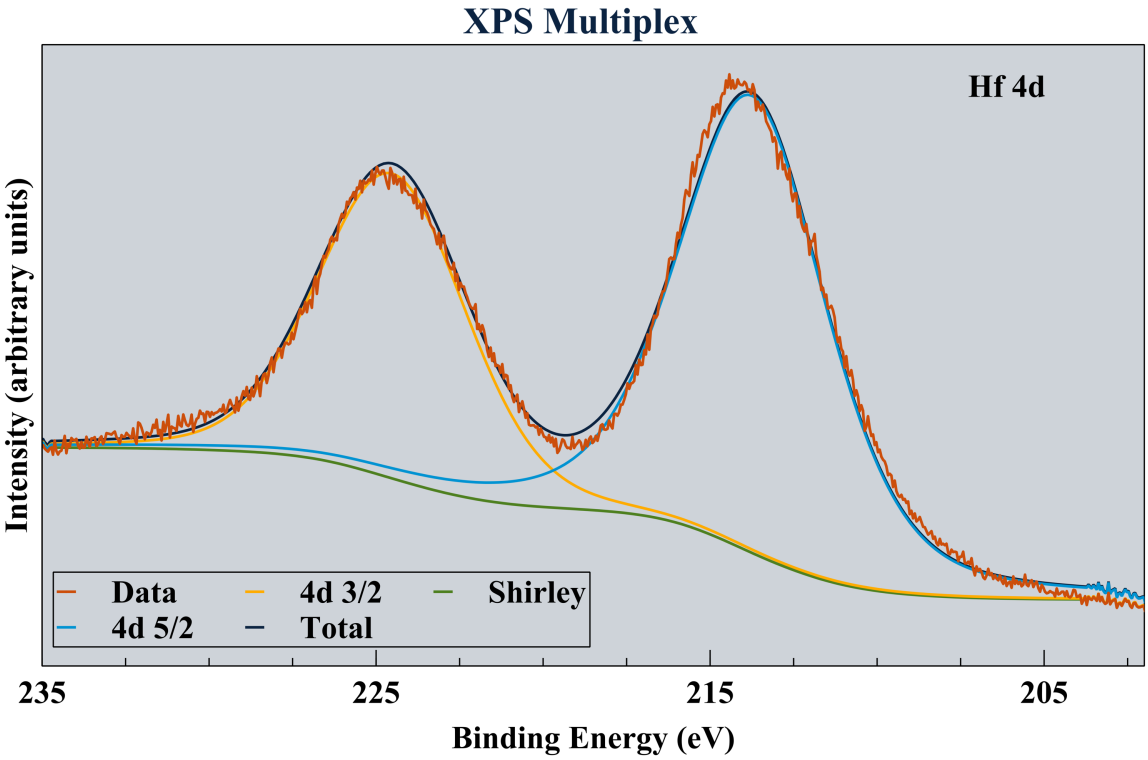

Figure 3.5: XPS multiplex spectra of the Hf 4d transition of an SHO-GSO sample.

$$V(x', y) = \frac{y}{\pi} \int_{-\infty}^{+\infty} \frac{e^{-t^2}}{(x' - t)^2 + y^2} dt \tag{3.5}$$

$$x' = 2\sqrt{\ln 2} \frac{x - x_0}{g_{fwmh}} \qquad y = \sqrt{\ln 2} \frac{l_{fwhm}}{g_{fwmh}}$$

where g_{fwmh} and l_{fwhm} are the full width at half maximums of the Gaussian and Lorentzian functions, respectively [130]. The Voigt function has no known analytical solution, and thus must be solved computationally for each data set. Solving and optimizing the solution possesses a computationally expensive cost and as a result, several pseudo-Voigt functions are used to approximate the solution [131]. The two most common approximations are the Gaussian-Lorentzian sum (GLS) and Gaussian-Lorentzian product (GLP), given by:

$$GLS(x, F, E, m, h) = h \times (1 - m) e^{-4 \ln 2 \frac{(x-E)^2}{F^2}} + \frac{h \times m}{1 + 4 \frac{(x-E)^2}{F^2}} \tag{3.6}$$

$$GLP(x, F, E, m, h) = h \times e^{-4\ln 2(1-m)\frac{(x-E)^2}{F^2}} \times \frac{1}{1+4\frac{(x-E)^2}{F^2}} \tag{3.7}$$

where F is the full width at half max of the XPS peak, E is the energy at which the peak lies, m is mixing coefficient, for which 0 results in a pure Gaussian and 1 results in a pure Lorentzian, and h is the height of the XPS peak. In most spectra fitting software, the mixing coefficient is fixed and defaults to a value of 0.3 [131]. In this work, the Gaussian-Lorentzian sum approximation was used and the mixing coefficient was allowed to vary during fitting, in order to minimize the error between the fit and the observed spectra. Before the data was fit with the Gaussian-Lorentzian sum, a Shirley background was fit to the spectra. This background is shown in black in Figure 3.5.

In order to compute the binding energy of a photoelectron using Equation 3.1, the work function of the XPS must be measured. While this is possible, in practice a different method is used to correctly ensure the correct positioning of the peaks. In XPS systems where samples have already been exposed to vacuum, there is always carbonaceous material on the surface. The carbon 1s peak is strong and well known to occur at 285 eV binding energy. Thus rather than shift the data by the experimentally determined work function of the XPS system, the spectra can be shifted to align the carbon peak at 285 eV. In the system used in this work, samples are kept in vacuum between growth and XPS analysis, so the oxygen 1s peak at 530 eV binding energy is used to align the spectrum. The software Casa XPS was used to fit the XPS spectra in this work [132, 133].

In Figure 3.5, two peaks are present that correspond to the Hf 4d core level. This is due to the effects of spin orbit coupling [41]. For electrons not in the *s* orbital, the total angular momentum is not the same for spin-up and spin-down electrons. This difference in momentum results in an energy shift that goes as $L \cdot S$, where L and S are the orbital and spin angular moment operators, respectively. Thus a splitting in the binding energy of spin-up and spin-down photoelectrons occurs when electrons are in any orbital where $l \neq 0$. The two peaks correspond to the two possible values of the total angular moment

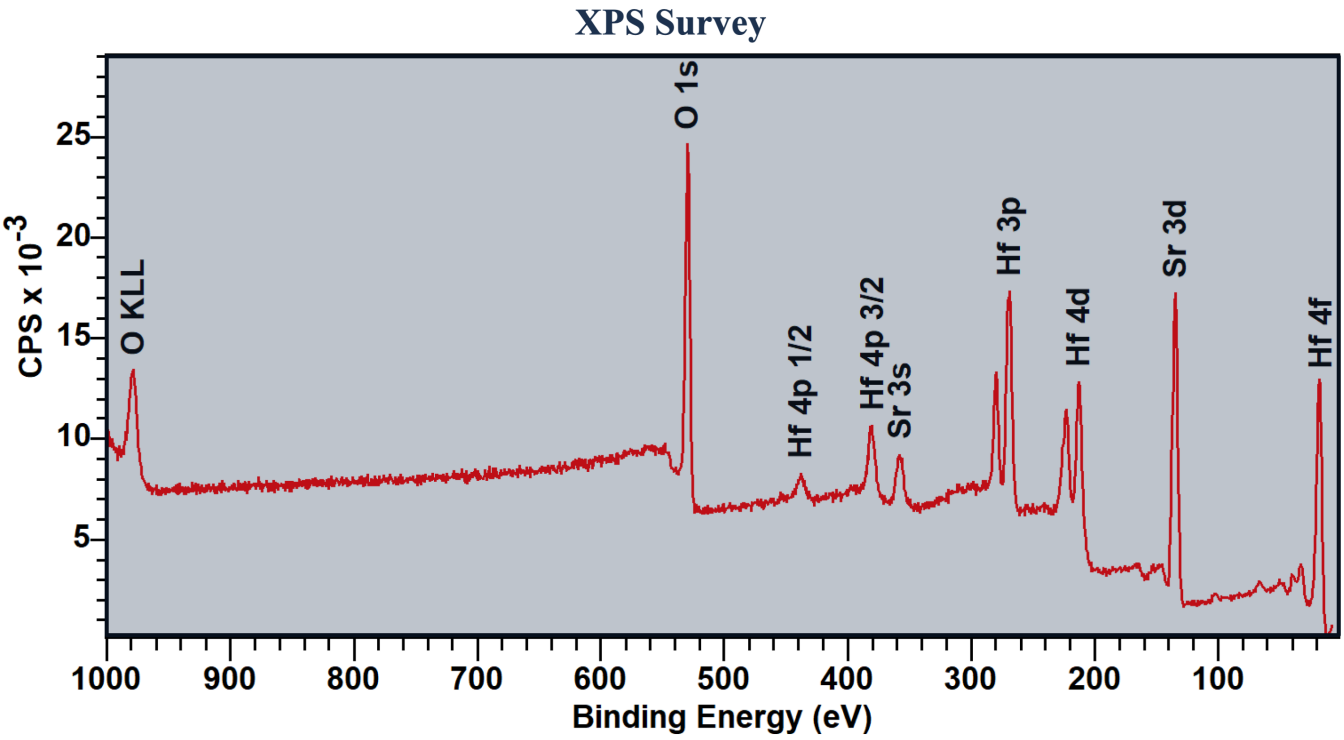

Figure 3.6: XPS survey spectra of the of an SHO-GSO sample.

of the photoelectrons, $j = l \pm s$. For a 4d electron, the total angular momentum can take either a value of $j = 2 + \frac{1}{2} = \frac{5}{2}$ or $j = 2 - \frac{1}{2} = \frac{3}{2}$. The effect of this splitting results in the two peaks in Figure 3.5. The ratio of the areas of these two peaks is not equal, but instead is 3:2. This is because the relative intensities are determined by the number of magnetic sub-state configurations, $2j + 1$, that correspond to each j value [41].

A quick, high pass energy XPS scan over the full range of binding energies is called a survey and an example is shown in Figure 3.6. Each peak on the spectra represents a different core level in the atomic species present in the sample. In Figure 3.6 the binding energy of each peak was compared to the reference catalog for the XPS and the corresponding core level was identified and annotated. The wide range and speed of survey spectra make them highly effective for identifying atomic species present in the surface of a sample. As a result, if an unexpected element were present, it would have a peak that could be easily identified. In Figure 3.6, the peak labeled O KLL is generated by a more complex process than the core level peaks. When photoelectrons are

ejected from the sample, vacancies are left behind. Since these are core level vacancies, electrons in higher energy shells will drop down to fill them and a photon with energy equal to the difference in energy of the two shells will be emitted. In the event that this photon is absorbed by another core level electron and imbues enough energy for the electron to escape the sample, the result is an Auger electron [134]. Auger electrons are denoted by the element from which they originate, and a 3 letter set that indicates the core level of the vacancy left by the photoelectron, the core level of the electron that transitioned to the vacant core level, and the core level of the Auger electron emitted. In the case of some elements, these Auger electron peaks are more intense than core level photoelectron peaks, making them useful for identifying atomic species present.

It is also possible to extract stoichiometry of a film from XPS spectra. Using the Gaussian-Lorentzian sum fits for a core level peak from each constituent element, the ratios of the areas can be calculated. These ratios can the be modified by the relative sensitivity factors found in the XPS reference catalog. The relative sensitivity factors correct for effects such as the different photoionization cross-sections and different inelastic mean free paths for the different core levels. Stoichiometry measurements are consistent between samples on the same system; however, the precision and accuracy are limited. Typically XPS stoichiometry measurements are accurate within $\approx 10\%$ when compared to results on the same sample from Rutherford back scattering (RBS). Using the same principles, XPS can be used to identify surface termination in stoichiometric films. This process requires that two measurements be taken with the sample stage oriented to the detector at different angles. The first is a steep angle, ideally $< 45^{\circ}$, which will inform on the stoichiometry in the top $5-8$ nm of the film, while the second is at a shallower angle, ideally $> 60^{\circ}$, which utilizes the short mean free path of the photoelectrons to obtain information from only the top 2 unit cells. By observing the change in stoichiometry from the steep angle spectra to shallow angle spectra, it is possible to determine on which element the film is terminated.

Oxidation states play an important role in determining the electronic properties of a material; luckily, XPS is capable of extracting oxidation states information from multiplex spectra. When atoms possess different oxidation states, there results a splitting in the XPS spectra, and an additional Gaussian-Lorentzian sum will need to be fitted to ensure a correct fit [37]. The peak with the lower binding energy will correspond to a lower oxidation state. By comparing the areas of these two peaks, a ratio or an average of the oxidation states can be calculated. To investigate if the oxidation state is uniformly distributed in the film or segregated between the surface and the bulk of the film, the same method for identifying the surface termination can be used [135]. This process is unlikely to work in the event that a sample has been exposed to atmosphere and allowed to oxidize the surface.

3.3 X-ray Diffraction

The high degree of symmetry in a perovskite oxide is one of the signature features of the family of materials and plays a major role in the properties of thin films. Thus it is imperative to confirm that the structure of synthesized films are exactly as expected. X-ray diffraction (XRD) uses x-rays to probe the structure of thin film samples in several different modes [136]. XRD requires highly crystalline samples, and is applicable to single crystalline, polycrystalline, bulk, and powder samples. The three processes of XRD used in this work to characterize thin film samples are x-ray reflectivity, high resolution XRD, and reciprocal space mappings. A Rigaku SmartLab diffractometer system with a four-circle goniometer was used in this work. The x-rays were generated from a Cu Kα source with a wavelength of 1.54 Å. To filter out the Cu Kα_2 line, A two-bounce Ge(220) monochromator was used, resulting in only the Cu Kα_1 x-rays reaching the samples. Figure 3.7 shows the geometry of XRD measurements with a thin film sample.

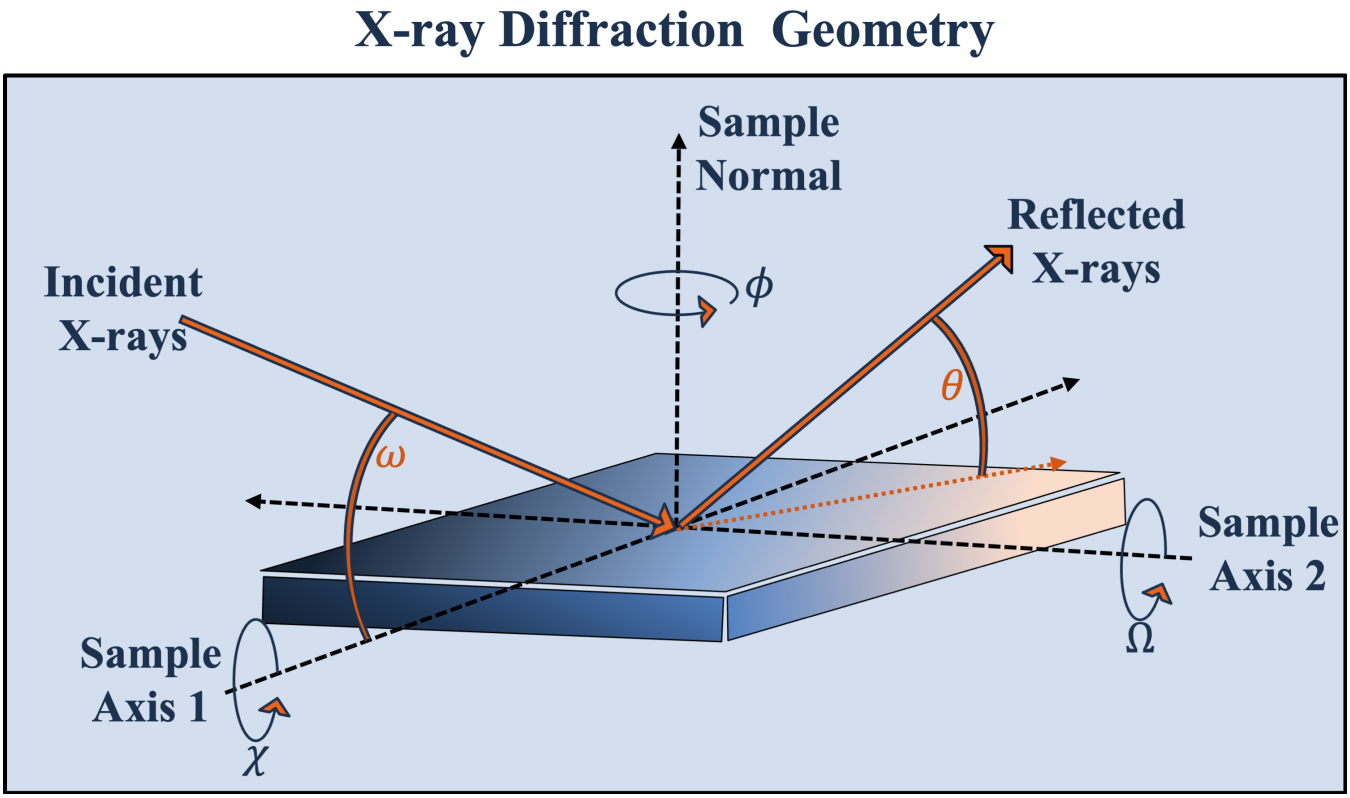

Figure 3.7: Schematic of the geometry in an XRD system. Adapted from [137] under CC BY 4.0 [118].

3.3.1 X-ray Reflectivity

X-ray reflectivity (XRR) is a quick and accurate way to use XRD to determine the thickness of thin films. XRR is setup in a glancing configuration where the incident angle, ω, and reflection angle, θ, are equal. A $2\theta/\omega$ scan is collected in this configuration, where the detector and source move while maintaining the condition $\omega = \theta$. Instead of the primary structural peaks, fringes are observed at low values of 2θ, like those seen in Figure 3.8. These fringes occur when there is a sharp interface between the film and substrate and diffracted X-rays constructively and destructively interfere [138]. These fringes are governed by the Fresnel equations and are highly dependent on the thickness of the film, density of the film, roughness of the film surface, and roughness of the film-substrate interface. The frequency of the fringes is primarily dependent on thickness of the film, with thicker films having a higher frequency [138].

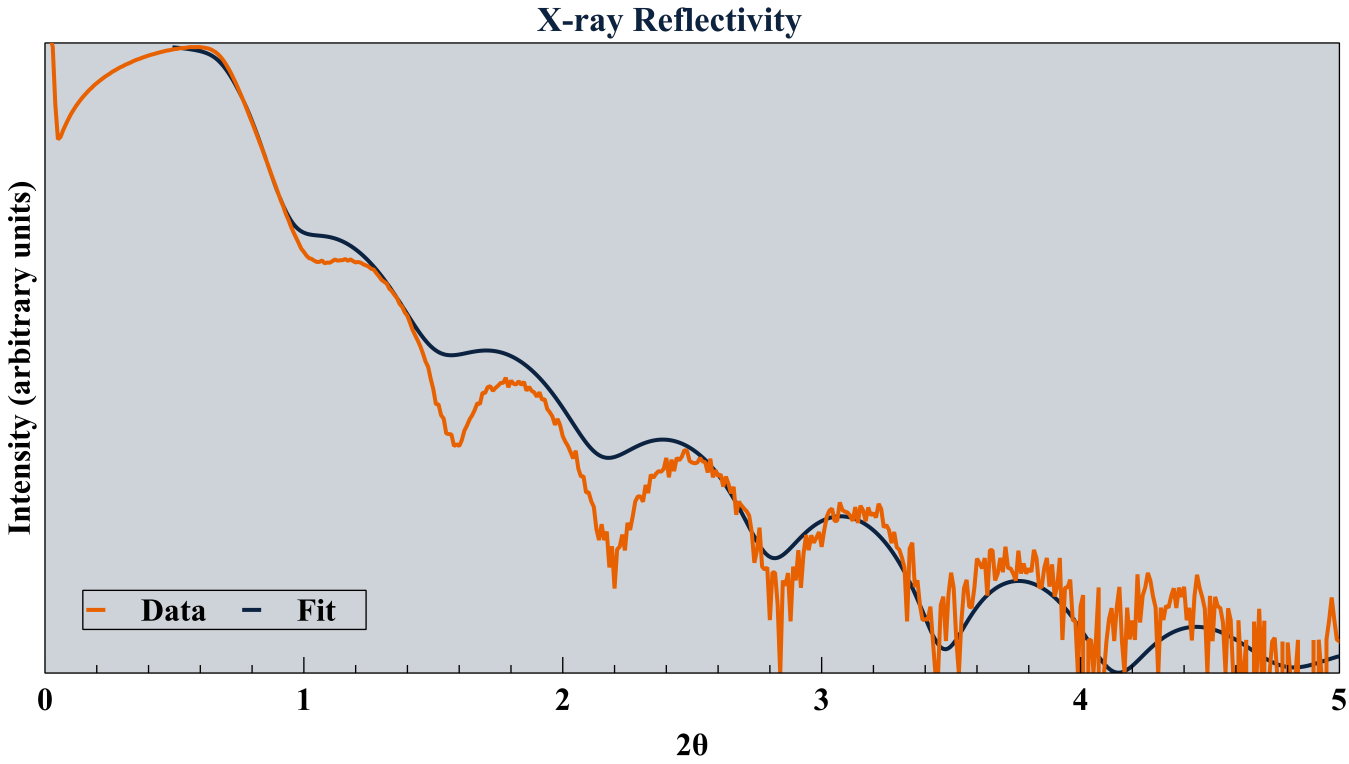

Figure 3.8: XRR spectrum (orange) with a theoretical fit (black) from an SHO-GSO sample.

From modeling the SHO-STO interface studied in Figure 3.8, a thickness of 12.4 nm was determined. In order to observe these thickness fringes, the film must usually be at least 5 nm thick. Since the interference of the X-rays that diffract off the crystal lattice are what create the fringes, it is necessary for the film to have sharp surfaces. If the surfaces of the films become too rough or island covered, the thickness fringes will not occur and XRR will be unable to measure the thickness. Using the measured thickness of the thin film sample, the deposition rate can also be calculated. This is highly useful when creating heterostructures or super lattices, where precise thicknesses are needed. Since XRR is performed after samples have been exposed to atmosphere, it is common for the top one or two unit cells to over oxidize. If this occurs, it is still possible to obtain thickness measurements; however, a more complex model is needed that incorporates multiple alyers with different densities.

3.3.2 High Resolution X-ray Diffraction

High resolution X-ray diffraction (HRXRD) is an XRD method that is bulk sensitive and used to analyze out-of-plane structural information of the crystal. HRXRD is setup similar to XRR, where the angle of the detector and the incident X-ray beam are the same. In this method, the line bisecting the angle between the detector and source is always normal to the sample. However, where XRR uses glancing angles, $2\theta < 10°$, HRXRD will use larger angles, typically $10° < 2\theta < 70°$. The locations of the diffraction peaks in HRXRD are governed by Bragg's law:

$$n\lambda = 2d_{hkl}\sin(\theta) \tag{3.8}$$

where λ is the wavelength of the Cu Kα_1 X-rays and d_{hkl} is the diffraction grating made of the crystal planes of the film and substrate [139]. The diffraction grating spacing, d_{hkl}, is given by:

$$d_{hkl} = \frac{c}{\sqrt{h^2 + k^2 + l^2}} \tag{3.9}$$

where c is the out of plane lattice parameter of the film or substrate. Unless the film and sample have the same c lattice parameter, which is the case in homoepitaxy, d_{hkl} will be different for the substrate and film and result in different 2θ positions of the peaks. For perovskite oxides, the (001) and (002) peaks are typically the ones measured. Figure 3.9 shows HRXRD spectra for several SHO-GSO samples and that contain both the (001) and (002) peaks. Since HRXRD is bulk sensitive, the peaks for both the film and substrate can be observed. Due to the thickness of the substrate, the substrate peaks are sharp and the most intense [140]. In Figure 3.9 the GSO substrate peaks are located at $2\theta = 22.5°$ and $2\theta = 46°$. Since these films are thin, the (001) and (002) film peaks are broad. The film peaks are located at lower values of 2θ than the corresponding peaks for the substrate since the c lattice parameter is greater for the SHO films. In addition to the primary film peaks that are a result of the Bragg condition, some samples

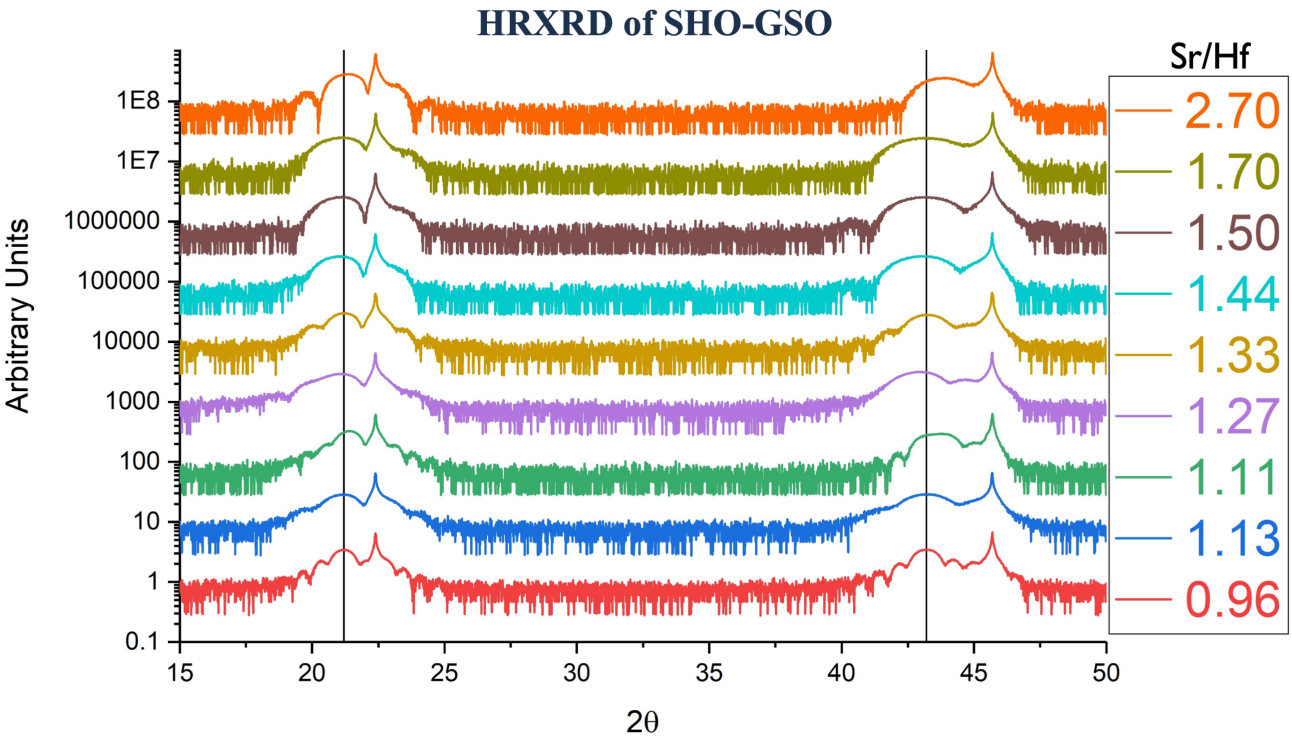

Figure 3.9: HRXRD spectra of several SHO-GSO samples ordered from top to bottom by the ratio of Sr:1 Hf.

possess Kiessig fringes [141]. These are analogous to the thickness fringes observed in XRR and occur in sufficiently thick, highly crystalline samples. When present, these fringes can be modeled to calculate the thickness of the sample. In Figure 3.9, it can be seen that the positions of the SHO (001) and (002) peaks vary slightly from sample to sample. This is due to the films having different out of plane lattice constants, resulting in different values of 2θ that satisfy the Bragg condition. This can be used to infer which samples have relaxed and are no longer strained, and which are still epitaxially strained to the substrate.

3.3.3 Reciprocal Space Mapping

While HRXRD is only able to provide information about the out-of-plane structure of the thin film samples, reciprocal space mapping (RSM) is able to provide information about the in-plane and out-of-plane structure simultaneously [142]. Unlike in HRXRD and XRR, in RSM a motorized sample stage is needed that can rotate about the surface

normal, ϕ, and about one of the axes parallel to the surface, Ψ, as shown in Figure 3.7. These additional degrees of rotation allow for peaks that are not normally in the plane of the detector to be measured. In perovskite oxides, the cubic (103) peak is traditionally used and corresponds to the (204) peak in perovskites with an orthorhombic Pnma structure. In RSM, 2D composite images are constructed by rastering over the θ and ω [143]. Originally, many 1-dimensional scans were needed to raster this space; however, the use of a 1-dimensional X-ray detector allows for a range of θ values to be recorded concurrently and results in a significant decrease in data collection time. Though the data is collected in θ vs ω space, results are commonly presented in the $\frac{\mathrm{Q}_x}{2\pi}$ vs $\frac{\mathrm{Q}_z}{2\pi}$ space, where the transformations into $\frac{\mathrm{Q}_x}{2\pi}$ and $\frac{\mathrm{Q}_z}{2\pi}$ from θ and ω are given by [143]:

$$\frac{\mathrm{Q}_x}{2\pi} = \frac{1}{\lambda}(\cos\omega - \cos(2\theta - \omega)) \tag{3.10}$$

$$\frac{\mathrm{Q}_z}{2\pi} = \frac{1}{\lambda}(\sin\omega - \sin(2\theta - \omega)). \tag{3.11}$$

Figure 3.10 shows two RSMs for SHO films, with one grown on GSO and one grown on STO. The spots corresponding to the substrates are small and sharp due to their thickness and highly crystalline nature, while the films are thinner resulting in more broad peaks. The narrow range in $\frac{\mathrm{Q}_x}{2\pi}$ values of the SHO-GSO film spot indicate the film has a small range of in-plane lattice parameters. For the SHO-STO sample, the opposite is true and the values are very broad. From the SHO-GSO sample, it can be observed that the film spot and substrate spot are vertically aligned, possessing a similar range of $\frac{\mathrm{Q}_x}{2\pi}$ values. This indicates that the film is epitaxially strained to the substrate in-plane. However, the film spot for the SHO-STO film is diffuse and most of the $\frac{\mathrm{Q}_x}{2\pi}$ of the film peak are not aligned with the substrate spot in $\frac{\mathrm{Q}_z}{2\pi}$. Since this is true of the majority of the film peak, it can be inferred that most of the film is not epitaxially strained in-plane with the STO substrate. However, there is a small stripe of intense response that suggests some of the film is strained. Given the large lattice mismatch for

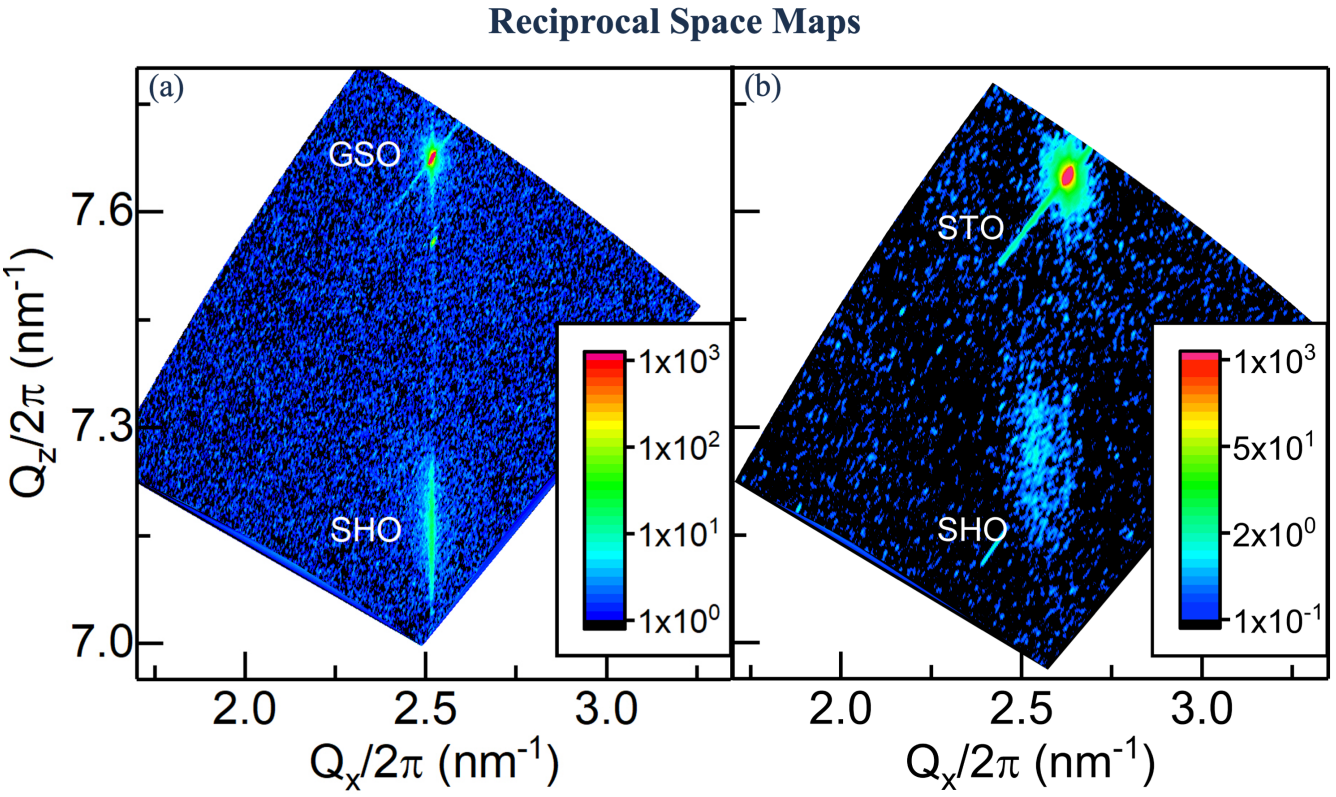

Figure 3.10: (a) RSM of the 103 peak of an SHO-GSO sample showing the film is epitaxially strained to the substrate. (b) An RSM of the 103 peak of an SHO-STO sample showing partial relaxation of the film.

SHO and STO, this most likely corresponds to a couple of unit cells at the interface that formed epitaxially strained, while the bulk passes through a range of in-plane lattice values as it relaxes. In this way, RSMs are highly effective at identifying the in-plane lattice parameters of films and if the film is epitaxially strained to the substrate.

3.4 X-ray Absorption Spectroscopy

X-ray absorption spectroscopy (XAS) is a well known technique for characterizing the chemical states of materials. XAS is bulk sensitive and can be used to determine the atomic valence, atomic coordination, and bond lengths in a sample [144]. In XAS systems, samples are bombard with monochromatic X-rays. The incident X-rays are absorbed by core level electrons and possess sufficient energy to excite the electrons into unoccupied states. The core level holes left by this process are filled by electrons

of higher energy levels dropping down. This transition gives off a photon with energy equal to the difference in energies between the initial state and core level hole. This type of photon excitation is called fluorescence and is the signal measured in XAS [144]. In XAS, a range of incident photon energies are scanned while the fluorescence is measured. In order to generate the continuous range of high energy X-rays needed in XAS, a synchrotron at one of the national labs is used.

XAS spectra are broken up into two distinct regions, the XAS near edge (XANES) and the extended XAS fine structure (EXAFS). The XAS edge is the result of electrons in a core level being excited to an unoccupied state. In Hf, the lowest unoccupied state is the 5d shell. However, not all electrons can transition into this shell from core levels. Selection rules require that the angular momentum of an electron change by 1 ($\Delta l = \pm 1$), the spin remain unchained ($\Delta s = 0$), and as a result the total angular moment change by 1 ($\Delta j = \pm 1$) [145]. Thus only an electron initially in a p-orbital or f-orbital can transition to the 5d shell. Similarly, an electron initially in a p-orbital can only transition to an s-orbital or d-orbital; however, since Hf has a filled 6s shell, the lowest possible energy transition is into the 5d shell. Thus by selecting an X-ray energy corresponding to the energy difference between the Hf 2p $\frac{3}{2}$ and Hf 5d $\frac{5}{2}$ shells, an electron from the 2p $\frac{3}{2}$ state will be excited into the 5d $\frac{5}{2}$ state. Additionally, polarization of the incoming X-rays in either an in-plane or out-of-plane configuration restricts which of the 5d orbitals an electron will transition to, with in-plane allowing transitions to the d_{xy} and $d_{x^2-y^2}$ orbitals and out-of-plane allowing transitions to the d_{xz}, d_{yz}, and d_{z^2} orbitals.

Figure 3.11 shows the in-plane and out-of-plane XANES and EXAFS spectra of an SHO-TSO sample, panels (a) and (b). Panels (b) and (d) show the dichroism between the in-plane and out-of-plane spectra for the XANES and EXAFS, respectively. The analysis of XANES data focuses on the initial peak and its features, such as pre-edge peaks. Pre-edge features can indicate specific properties such as the cation coordination [146]. In this work the Hf L_3-edge is used investigate the electronic density of

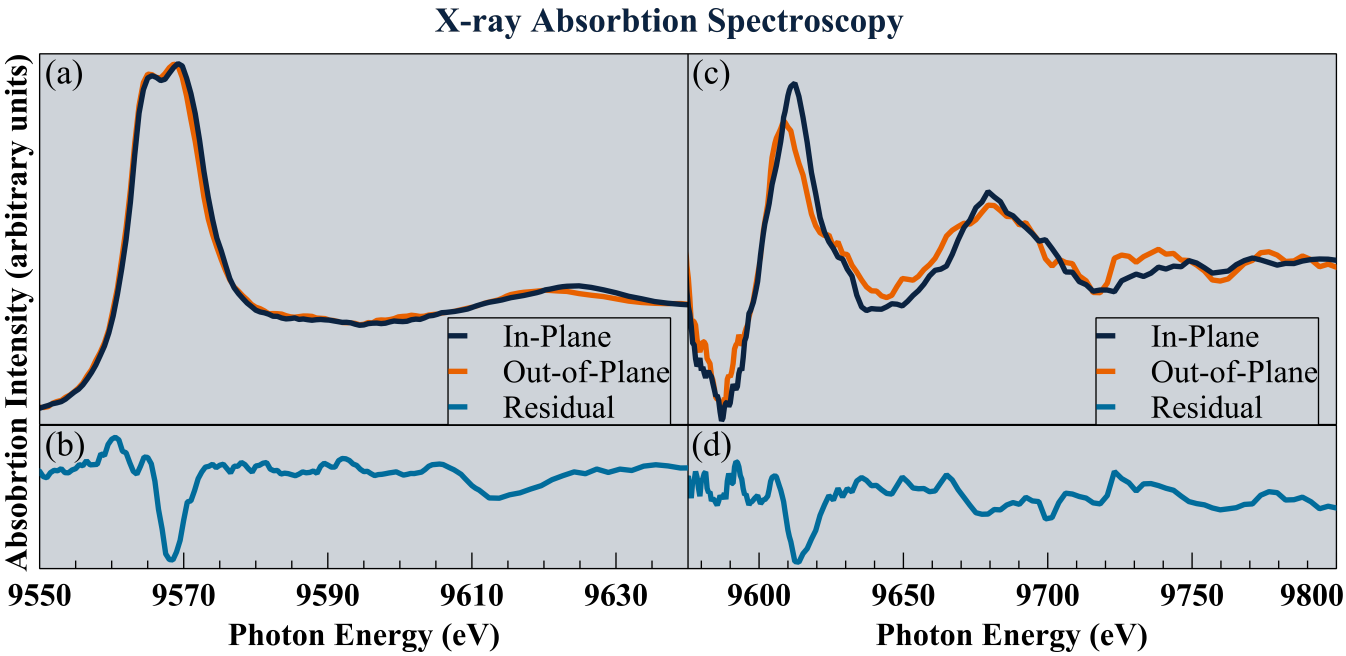

Figure 3.11: (a)XANES and (c) EXAFS spectra collected from an SHO-TSO sample.(b) and (d) are the residuals of the in-plane and out-of-plane responses in the XANES and EXAFS, respectively.

states of the Hf 5d orbitals. EXAFS data is located in the energies after the initial peak has died down and is indicative of the oscillations seen in Figure 3.11(c). Using careful modeling of this region, it is possible to calculate the bond lengths present in the material. In this work the Hf L_3-edge x-ray absorption spectroscopy was carried out at beamline 20-BM of the Advanced Photon Source at Argonne National Laboratory.

3.5 Second Harmonic Generation

Second harmonic generation (SHG) is an optical characterization technique that utilizes a nonlinear optical process to determine symmetry in the crystal structure of thin films. SHG is a second order optical process that occurs when two photons with the same frequency are combined in a medium into a single photon with half the energy and twice the wavelength. SHG's efficiency is dependent on the second order non linear susceptibility tensor of the film material. Since the only materials for which this tensor is nonzero are non-centrosymmetric, an SHG response indicates the sample possess no

centrosymmetry [147]. In this work, an ultrafast light source with 800 nm wavelength, 50 fs pulse duration, and 200 kHz repetition rate was used in conjunction with a single photon counting electron multiplying charge coupled device (EMCCD) camera to record the SHG response of thin film SHO and rule out the presence of possible phases.

3.6 Scanning Transmission Electron Microscopy

Scanning transmission electron microscopy (STEM) is a high resolution imaging technique used to characterize materials. STEM provides atomic level resolution of cross sectional samples of thin films and reveals important structural information about the film. Before STEM images can be collected, a thin slice of the sample, called a lamella, must be collected. This lamella is created in a process called a lift out, where a focused ion beam (FIB) is used to mill away material surrounding a cross sectional slice of the sample [148]. Afterwards, the FIB is used to thin the lamella down until it is < 100 nm thick, which is needed for the electron beam to penetrate the sample. Once the lamella is prepared, it is placed in the STEM system such that the electron beam is normal to the lamella's surface.

Figure 3.12 illustrates the relative geometry of the STEM system. During measurements, a convergent electron beam is focused onto the lamella, while the stage is rastered so that data can be collected over a wider area and a composite image can be created. In STEM, the electrons that pass through the sample are detected using a series scintillators, photomultipliers, and photodetectors. The results are separated into three key regions, which are the bright field, annular dark field, and high angle annular dark field [149]. The primary transmitted cone of electrons are scattered as small angles and the resulting image is referred to as the bright field image. In this regime, variations in sample density and structure are easily observed. The annular dark field (ADF) region forms a ring around the bright field region and is primarily the result of scattered electrons. As a result, ADF images are sensitive to atomic number with atoms of higher atomic number being brighter than those with low atomic number. High angle annular

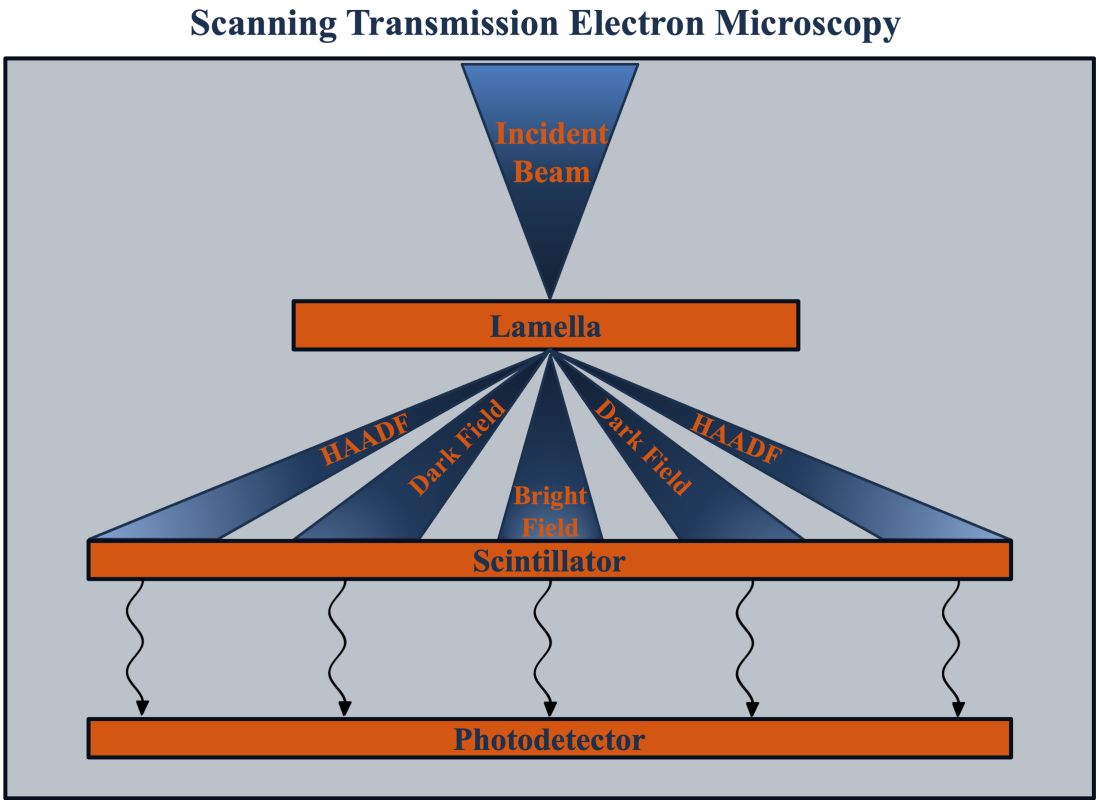

Figure 3.12: Schematic of the data collection process of STEM.

dark field (HAADF) is similar to ADF, but occurs at higher angles due to scattering of heavier elements [150]. This region forms a ring around the ADF region and is ideal for imaging heavy species such as Hf. Since STEM generates atomically resolved real space images, it is highly effective for identifying the crystal structure and observing lattice defects.

Convergent beam electron diffraction (CBED) replaces the scintillators and photodetectors from traditional STEM with direct electron detectors, which allows angle resolved information to be obtained. The diffracted electrons form circular disks patterns whose position is governed by Bragg diffracting (Equation 3.8) and the spacing of the crystallographic planes (Equation 3.9) [151], and whose diameter is determined by:

$$D = \frac{4\pi}{\lambda} \sin \alpha \tag{3.12}$$

where λ is the wavelength of the electrons and α is the convergence semi-angle of the electron beam[152]. When the convergence angle is sufficiently small, it is possible to resolve individual disks. By rastering the beam over the sample, a 4D data set is collected, resulting in the term 4D-STEM. Due to the additional angle resolved data present in 4D-STEM, it is possible to create strain mappings of thin films, as well as determine the crystal symmetry and orientation [153].

Chapter 4

Data Science, Artificial Intelligence, and Machine Learning Methods

4.1 Motivation

RHEED is a highly common form of real time analysis used during material synthesis in MBE and PLD; yet, due to an inability to theoretically model the many effects present in RHEED images, traditional RHEED analysis focuses only on the intensity and shape of diffraction pattern for a few still images taken during and after growth. While this is insightful, there is a wealth of unused information present in RHEED. Data science and machine learning are fields that are built on the ideas of extracting and coalescing complex trends from data into new usable forms to generate additional insight. Thus, data science and machine learning techniques offer a new way to improve understanding of and better utilize RHEED data over what has previously been possible.

Machine learning is already a common area of research and has been applied to a variety of tasks. Handwriting recognition [154] and image to image translation [155] are some of the most common. In materials research, machine learning techniques have been applied to a wide array of material characterization and analysis techniques, including STEM [156, 157], SPC [158], transport measurements [159], surface morphology [160], crystal structure determination [161], and RHEED [78, 79]. Several studies have also been conducted that focus on utilizing machine learning techniques such as neural networks and random forests to make predictive models that utilize various forms of data, including XANES spectra [162], materials structure databases [163], and MBE operation data [164], to extrapolate additional information on the structural and chemical qualities of materials.

In this work, principal component analysis and k-means clustering are used on recordings of RHEED patterns to provide quantitative feedback that informs on the evolution of the film surface during growth. The predictive machine learning algorithms

random forests and convolutional neural networks were used to create a model by which RHEED data can be transformed into a new data space so that real time analysis can be performed to identify film stoichiometry.

4.2 Data Preprocessing

Preprocessing of data is one of the most critical steps for any computational project. Data preprocessing involves filtering or modifying of raw data collected before utilizing it in any models. Raw data is data collected directly from a source; which for experimental work, is most often a measurement system or control system. Raw data can have many issues that would make it unsuitable to be used directly in computational research. Common issues include excessive noise in the data collected, large amounts of redundant data, excessive amounts of background signal, or an instrument bias [165]. Each of these could have profound impacts on the training and results of the computational models in which they are used. Excessive amounts of background information will drastically slow the training process and drown out the significant signals. An instrument bias may cause all of the data to be shifted by some constant or function resulting in different datasets being out of line from each other and decreasing the accuracy of any model results.

To address these issues many different types of preprocessing programs and algorithms can be used depending on the problem at hand. One of the simplest forms is mean subtraction, where the mean of a dataset is calculated and then removed. In machine learning and with neural networks in particular, datasets are often rescaled to have a standard deviation of 1 and shifted to have a mean of 0 [166]. This form of preprocessing is critical for algorithms like neural networks, where feature importance is directly related to the size of the inputs. A more complex version of data rescaling involves fitting data to a particular distribution, such as a Gaussian [166]. For data that is not numerical, models often require that the data be preprocessed by encoding the categorical labels into integers. While for many projects standard data preprocessing

tools may be sufficient, there are many instances where existing tools may need to be modified or custom tools may be needed. Examples of custom tools used in this work will be described in section 5.1 & section 7.3.2.

4.3 Principal Component Analysis

Principal component analysis (PCA) is a data processing algorithm that is used in a wide variety of ways. PCA works by taking a dataset and performing multiple matrix operations in order to construct a set of eigenvectors and eigenvalues that will operate as a new basis set for the data [167]. This process is done iteratively, and at each iteration the new eigenvector is chosen to maximize the variance in data along the new component and such that it is orthogonal to all eigenvectors that have already been chosen [168]. Figure 4.1 shows a two dimensional example of the PCA process. The orange ellipse contains a number of randomly chosen points and PC1 and PC2 are the two new principal components chosen by PCA for those points. PC1 was placed along the major axis of the ellipse as doing so maximized the variance of the component. Subsequently, the second component must be orthogonal to the first, and thus the second component had to be placed along the minor axis of the ellipse. These eigenvectors can now serve as the new axes and each data point I can now be expressed as:

$$\begin{aligned} I &= \lambda_1 a_1(x,y) + \lambda_2 a_2(x,y) + \cdots + \lambda_n a_n(x,y) \\ &= \sum_{m=1}^{n} \lambda_m a_m(x,y) \end{aligned} \tag{4.1}$$

Here, λ_i represents the ith eigenvalue, while $a_i(x,y)$ is the ith eigenvector which is a function of the original x, y space [169]. The number of new eigenvectors is the number of PCA components specified by the user. This number cannot be larger than the number of dimensions of the original dataset, i.e. 2 for this 2D case. However, by choosing a number of PCA components smaller than the original dimensions of the dataset, a dimensionality reduction is achieved. This reduction in dimensionality is highly useful in cases where the original dataset has a high number of dimensions,

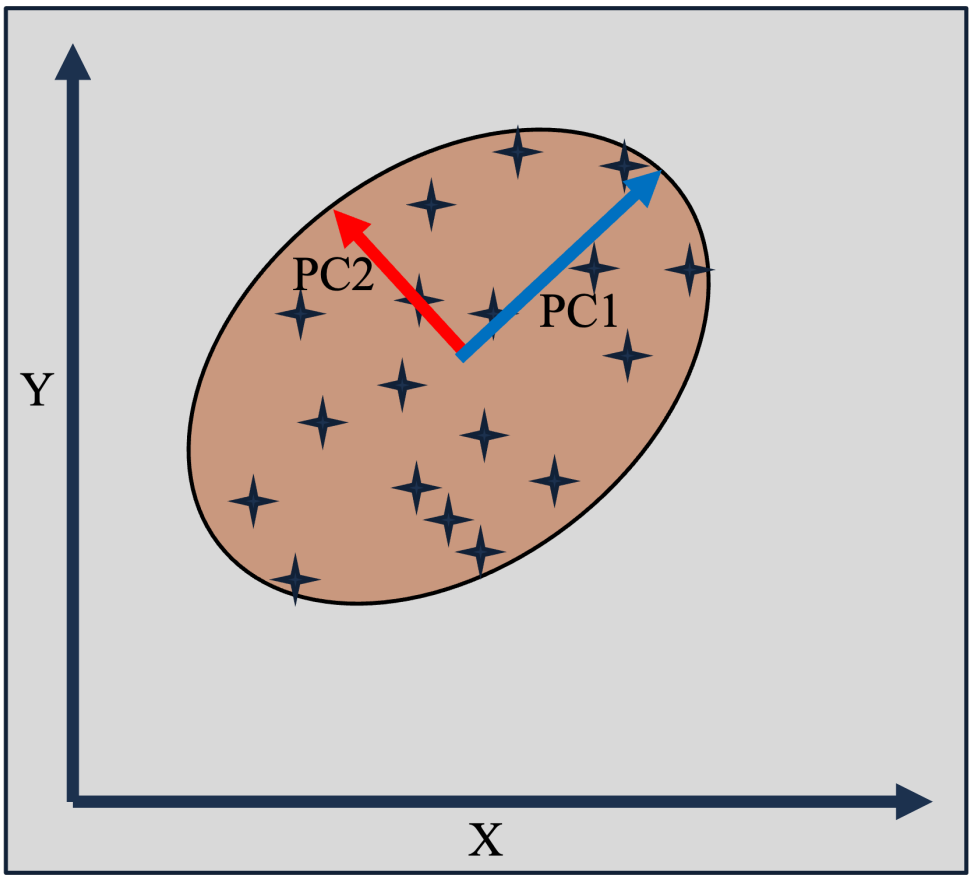

Figure 4.1: Diagram of a 2D example of principal component analysis.

but contains many redundant or non-linearly independent dimensions. If all points in the 2D dataset displayed in Figure 4.1 were given the same third dimension value, for example the plane of this page, then an additional PC3 could be constructed. However, since the variance in that dimension is 0, no information is lost by stopping the PCA process at 2 components. This is a trivial example; however, if there were hundreds of dimensions in a dataset this process could reduce the total greatly, making other computational operations on the data more feasible. Furthermore, since the variance of the data is maximized for each integration, each subsequent component will hold less information than the components preceding it and greater than those afterward. Thus truncating the process before the maximum number of components is reached will not result in significant loss of information.

Figure 4.2 shows the 6 component eigenvectors for a recording of RHEED patterns during an SHO growth. In this case, each of the eigenvectors is an image and the corresponding eigenvalues are plotted vs time in the (a), (c), and (e) panels. From the y-axis of the eigenvalue plots, the importance of each subsequent eigenvector is less than or equal to the preceding eigenvectors. To recreate the original image at any time, each eigenvector image must be multiplied by the corresponding eigenvalue at that time and summed together. Part of the PCA process requires that the median range of each component is zero, thus both the negative most values and positive most values are of equal though opposite weight [170].

One down side of PCA as a data analysis technique, is that the components constructed by PCA are not necessarily easy to interpret and it may not be easy to correlate each eigenvector to physical property. In Figure 4.2 the Eigenvector1 has extreme positive values where the specular and 1st order RHEED spots are located. This would suggest that the first eigenvector represents the overall intensity of the RHEED pattern and thus can be used as a quality indicator. However, in the same eigenvector there is a large dark area along the top side of the image. This dark area is due to the beam being blocked from the RHEED screen during data collection by the sample stage as a result of the design of the chamber. It is unclear why these two features ended up in the same eigenvector and thus interpreting its change over time is not trivial. Another limitation is that PCA works best for linear datasets. If a dataset is non-linear, the effectiveness of PCA declines, although this can be mitigated with coordinate transformations prior to PCA [170]. PCA results can also be biased by sampling errors, though this issue is most common with small numbers of data points [171]. Despite these limitations, PCA is highly effective at dimensionality reduction and enables additional algorithms to be utilized that are less effective or infeasible for datasets with larger dimensions.

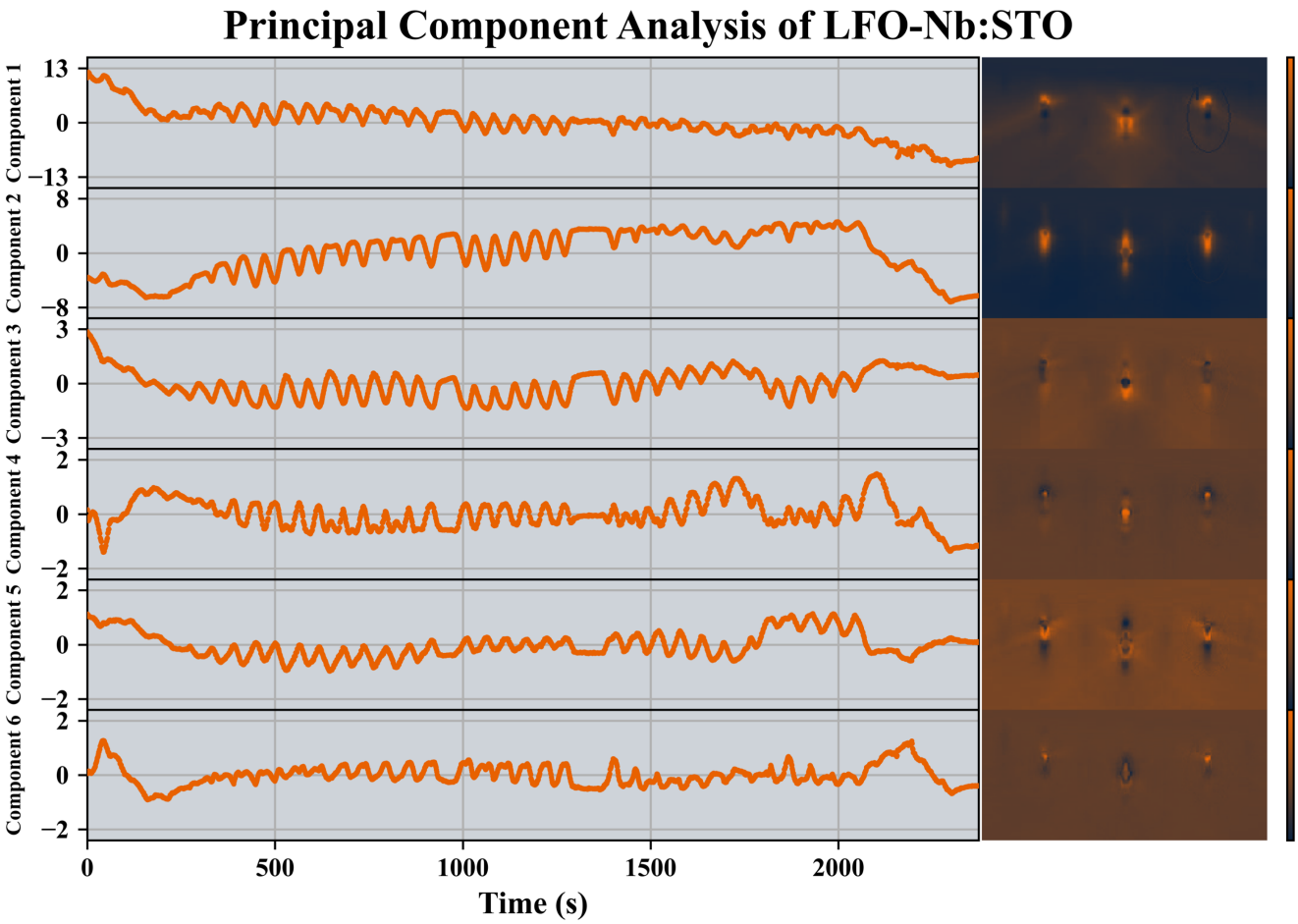

Figure 4.2: The principal components and the corresponding eigenvector images of an LFO film during synthesis by MBE.

4.4 k-means Clustering

k-means clustering is an algorithm that sorts data points into k different clusters. This process has its origin in signal processing, but can be used in many different applications. k-means can be defined as iteratively minimizing the loss function:

$$L = \frac{1}{m} \sum_{i=1}^{m} ||x_i - \mu_{k_i}|| \tag{4.2}$$

where m is the number of data points, and μ_{k_i} is the centroid of the cluster k that the point i is in [172]. The centroid is the geometric center of a cluster and each cluster is constructed such that each data point in that cluster is closer to the centroid of that cluster than the centroid of any other cluster. Initially, k centroids are chosen at random.

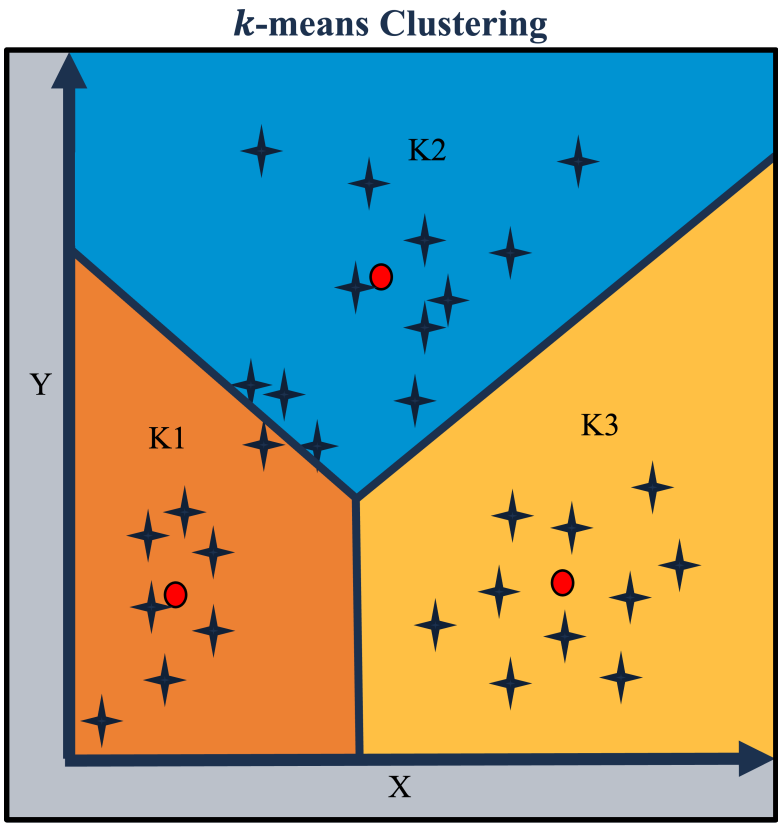

Figure 4.3: Diagram of a 2D example of k-means clustering.

Then the algorithm iterates over the following two steps. First, the algorithm places each data point into the cluster with the closest centroid. Second, the centroids of each cluster are recalculated. This process continues until a specified iteration limit is reached or the clusters cease to change [172]. k-means clustering is useful for classifying data into groups based on quantitative features rather than qualitative ones. Figure 4.3 shows the results of a 2D example of k-means clustering. In this example, there are $k = 3$ clusters and thus the 2D space has been divided into 3 regions. The red dots are the centroids and are located in the middle of each cluster of data.

k-means is not without its limitations. The four data points on the border of K1 and K2 highlight one of the limitations of k-means clustering; that is, the algorithm is not always able to identify the correct number of clusters. In the example in Figure 4.3, it appears that a 4^{th} cluster should have been added to make the 4 points on the boarder of K1 and K2 distinct. This is often the case for clusters of points that are substantially

smaller than the large ones [173]. This can be mitigated by the user specifying k based on some outside knowledge or by running the clustering for a range of k values and then having the user select the most informative. The latter solution is feasible due to the low computational cost of the algorithm. Another shortcoming of k-means is that it uses euclidean distance as the loss function [173]. Figure 4.3 represents the low dimension example where this is not an issue; however, with higher numbers of dimensions both the computational efficiency and the accuracy get worse. However, this issue can be mitigated by using a process like PCA that reduced the dimensionality of the data to a lower dimension space.

Figure 4.4 shows the k-means clustering results for the same dataset shown in 4.2. The graph in Figure 4.4 shows each frame of the RHEED recordings separated into clusters with the x axis being the timestamp of the frame during the growth. The numbering of the clusters is generally arbitrary, but in this case was chosen based off the order the clusters appear in the RHEED recording. With the exception of cluster 4, the clusters are nearly continuous with some sections of alternating at the beginning or end of each cluster. From these periods of alternation it can be determined that the surface of the sample was undergoing some cyclic change consistent with layer by layer growth. The 6 RHEED images in Figure 4.4 are the mean images created by averaging every frame in the respective clusters. Comparing these images reveals useful information about the evolution of the surface that would normally go unnoticed. Comparing the k-means results to the RHEED oscillations observed in Figure 3.3, it is clear in both cases that the surface oscillates between different states. While the traditional interpretation of the RHEED spot oscillations in Figure 3.3 would suggest that the surface was switching between two states, from the k-means clustering it is clear that the surface is continuously developing through different surface reconstructions, with the oscillations being present at the transition between groups and oscillating between 3 states around the 1200 second mark.

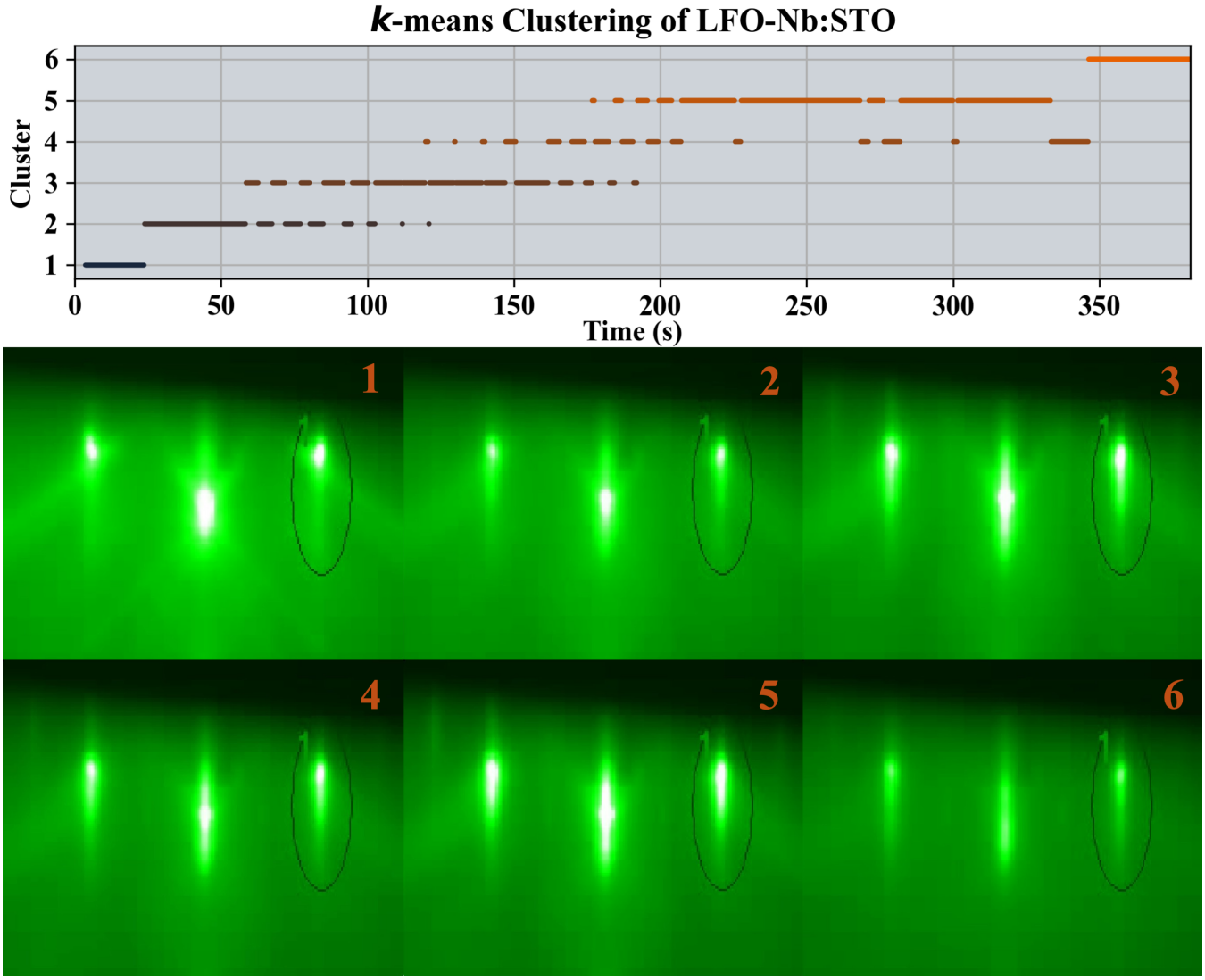

Figure 4.4: The k-means clustering results and the corresponding mean images of the PCA analysis of the LFO film growth shown in Figure 4.2.

4.5 Random Forests

Random forests are predictive models that are computationally cheap to build and train, yet are quite good at classification problems. Random forests are made by creating and training decision trees on subsets of the data [174]. Decision trees are very simple predictive models that take an array of data as an input and perform a series of comparisons to select a result. They are usually illustrated as flow charts for ease of understanding. These trees are primarily used for classification where data is sorted into a number of

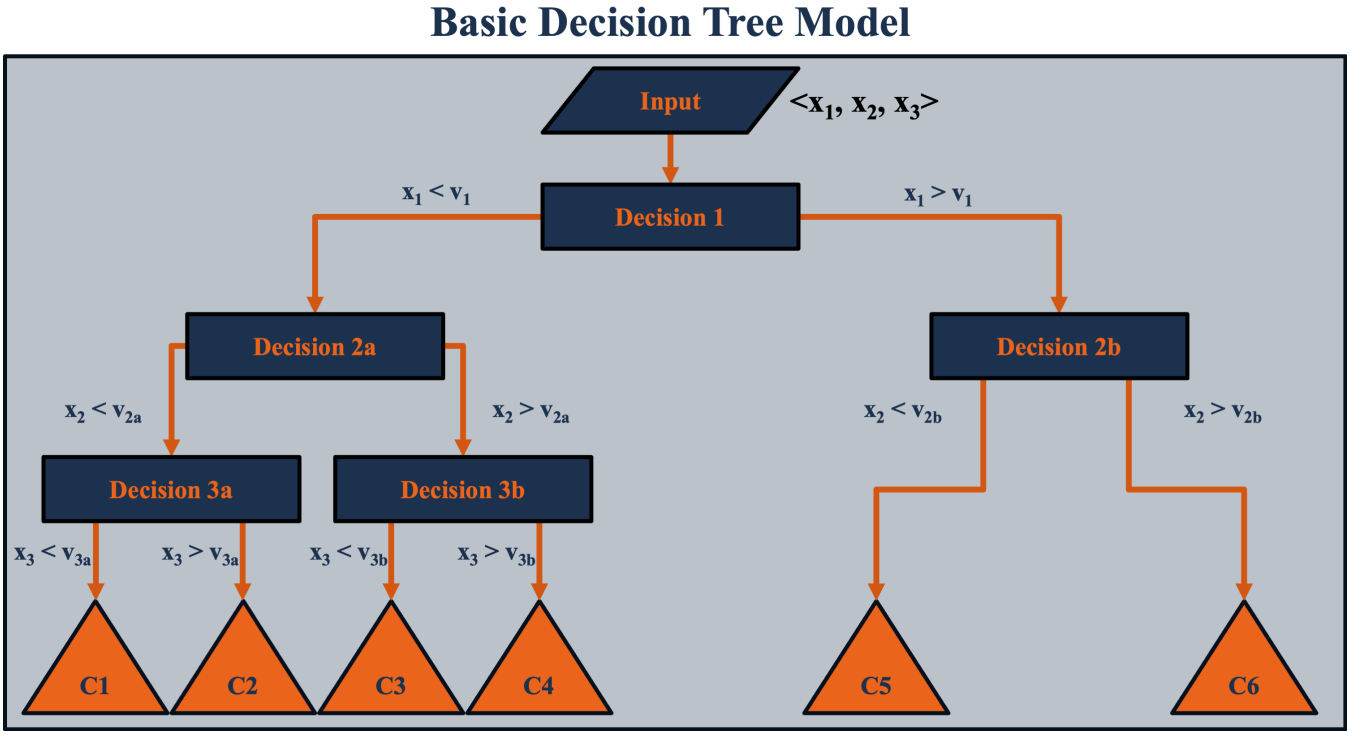

Figure 4.5: Diagram of a decision tree classifier with with an input array of size 3.

categories specified by the user; however, there are versions that can be used for regression problems, where the output is a numerical value.

Figure 4.5 shows an example model of a decision tree. In this example, the input array contains 3 values and there are 6 possible output categories. At each each node in the tree, one of the inputs is compared to that node's variable and then the appropriate path is taken. The node variables are determined by iteratively passing inputs through the tree and optimizing the variables to improve accuracy and minimize the loss function. The categorical cross entropy loss is used for classification models and is given by:

$$L_{cce} = -\frac{1}{M}\sum_{k=1}^{K}\sum_{m=1}^{M} y_m^k x \log(h_\theta, k), \tag{4.3}$$

where M is the number of training examples, K is the number of possible classifications, y_m^k is the correct label of data point m for class k, x is the input of data point m,

and h_θ are the model weights [175]. For regression models, the mean squared error loss is most commonly used and is given by:

$$L_{mse} = -\frac{1}{N}\sum_{i=1}^{N}(x_i - y_i)^2, \tag{4.4}$$

where N is the number of training samples, x_i is the result predicted by the model for sample i, and y_i is the true value for sample i [176]. Additionally, some variants of the variable optimization algorithm force the earlier decision nodes to be the most significant, thus providing the user with information on the relative importance of each value in the input array. Although decision trees have a few benefits, such as being trainable with minimal data and are easy to use and understand, there are several limitations. The accuracy decreases rapidly as the dimensions of the input increase. They are unstable, meaning small changes in the training dataset can cause large changes in the tree structure and accuracy. And they are less accurate than many other computational models. However, by utilizing many decision trees in parallel, these issues can be mitigated.

Random forests create a number of decision trees that are each trained independently and whose results are averaged to make the final prediction [174]. Figure 4.6 shows a diagram of a random forest model comprised of n trees with the same inputs and output categories as the decision tree in Figure 4.5. Rather than train each tree on the complete training dataset, each tree is given a unique randomly chosen subset of the training dataset. This results in each tree being able to focus on different features of the dataset and reduces the chance of many trees being identical. By selecting the most commonly chosen result in the case of classification or the average result in the case of regression, the random forest results in a substantial increase in accuracy compared to an individual decision tree. Additionally, the decision to train each tree on a subset improves stability in the model and thus small changes in the training set do not result in large changes of the output as was the case with the decision tree [174]. This also allows for more stability at higher dimensions of inputs compared to the decision tree. Even though many decision trees are trained in a random forest, the computational

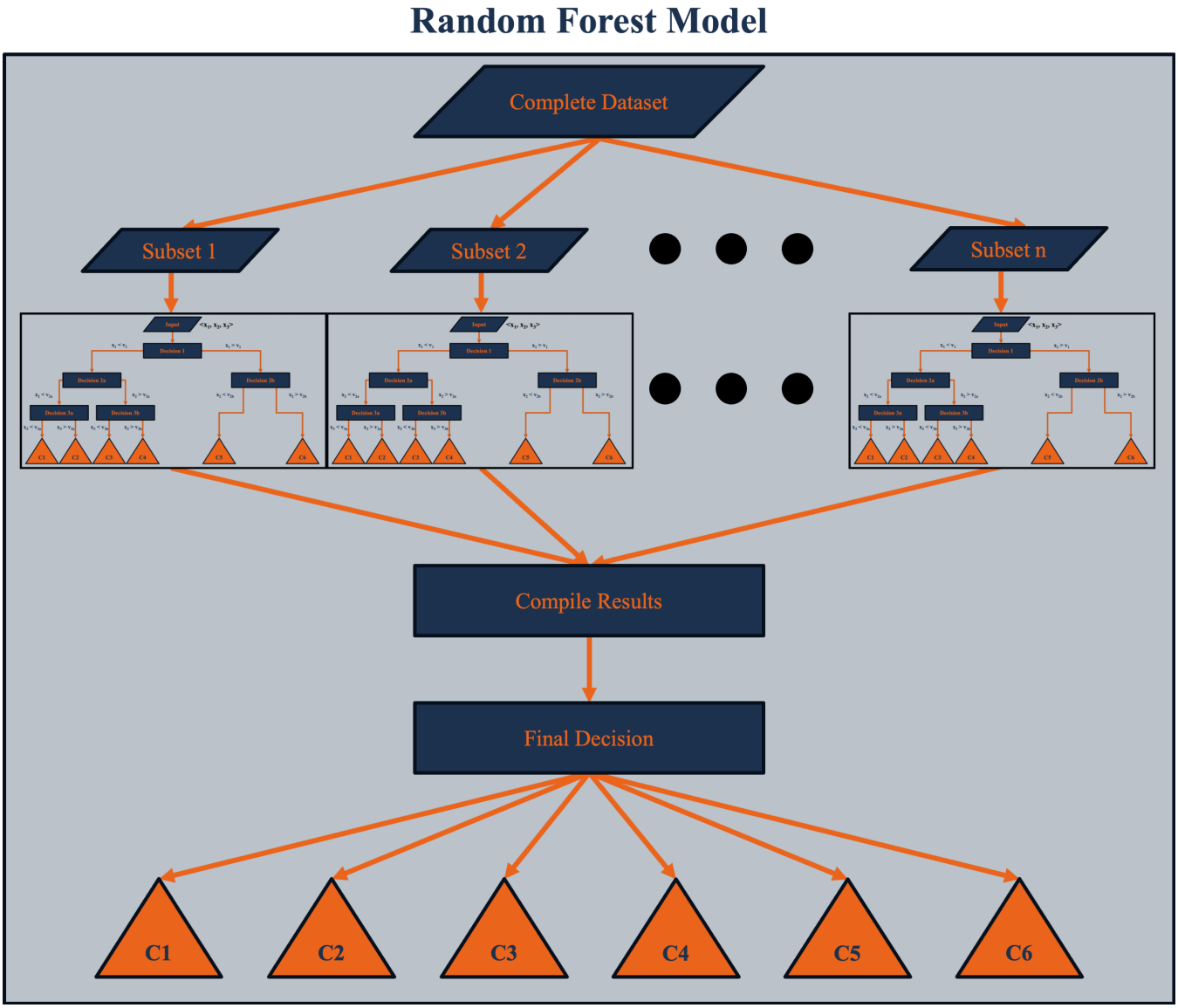

Figure 4.6: Diagram of a random forest classifier model and it's constituent decision trees.

costs are still so low that training can still be run on most laptops. And just as the feature importances can be determined for the individual decision trees, they can also be calculated for the random forest as a whole. These feature importances can provide a quantitative measure of significance of the input features and be used to gain additional insight into what most strongly correlates between the input and output data sets [177].

Despite all these advancements over decision trees, random forests are still unable to effectively handle image data directly [178]. The input array for a simple 256x256 gray scale image would be 65,536 long, thus a single complete binary decision tree

would need 2,147,516,416 variables. The work around to this is to utilize dimensionality reduction of some kind to reduce the data space to a level random forests can utilize. PCA is one possible choice; however, it would be computationally expensive to perform PCA on all the image data needed for training; and as discussed prior, the components are not inherently interpretable meaning the usefulness of the feature importances would be completely lost. An option that is computationally efficient and would maintain the usefulness of the feature importances are feature descriptors. Feature descriptors are the results of fitting some kind of function or functions to the input data [179]. In 2D this is often done with cubic splines or other polynomial interpolations. In 3D, more complex interpolations are often used; however, the core concept remains the same. The constants from the data fits are then used as the input array for the random forest. Since the features passed to the model are not values of individual pixels, but rather information about the curvature at a point, additional information can now be extracted from the feature importances [162].

4.6 Neural Networks

The vast majority of computing programs have historically been built on the concept of the Von Neumaann architecture where information is stored in one location, called memory, and calculations are performed in another, called the processor. However, from studies of neurons in the brains of animals, it was observed that this not how animals think. Neurons form large networks where both the information and calculations take place; this model is called neuromorphic [180]. Artificial neural networks (ANN), usually referred to simply as neural networks (NN), were developed on the basis of creating models that could mimic the behavior of neurological processes. Figure 4.7 shows a basic diagram of a neural network. Each circle of the diagram represents a node called a neuron. In each neuron there are three steps [181]. (1) Inputs are received from either an initial input or another neuron and are multiplied by the weights of the

neuron. (2) The results are summed and added to the bias value of the neuron. (3) The result is passed to an activation function. The output can be expressed as:

$$O(\boldsymbol{z}) = I(\boldsymbol{w}^T \boldsymbol{z} + b), \tag{4.5}$$

where $\boldsymbol{z}$ is the array of input values to the neuron, $\boldsymbol{w}$ is the array of weights of the neuron, b the bias value of the neuron, and $I()$ is the activation function [181]. The weights are real numbers that are initially random but are modified during training. An activation function can be any function that takes a single real input and returns the like. However, most neural networks now use a leaky rectified linear (ReLu) activation function defined by [182]:

$$f(x) = \begin{cases} -0.1x & \text{if } x \leq 0 \\ x & \text{if } x > 0 \end{cases} \tag{4.6}$$

Neurons are organized into layers and in Figure 4.7 there are 5 layers separated into 3 categories. Neurons in the input layer receive a single value of the input array, thus the size of the input layer must be the same size as an individual data sample. In the case of a 256x256 image that would be 65,536 neurons. Neurons in the middle three layers are regarded as hidden layers since they are not interacted with directly from the input or output. The number and size of hidden layers is specified by the user and varies greatly depending on the complexity of the problem and size of the data set. In this example, each of the hidden layers are fully connected layers, also known as dense layers, since each neuron provides its output to each neuron in the next layer. The output layer is always a dense layer and its size is determined by the problem being modeled. For a classification model, the number of neurons in the output layer is equal to the number of classification categories. For a regression or predictive model, the number of neurons will be the dimensionality of the data being predicted. Output layers will also have a different activation function from the other layers [183]. For binary classification models the result should either be 0 or 1, so a sigmoid function is used:

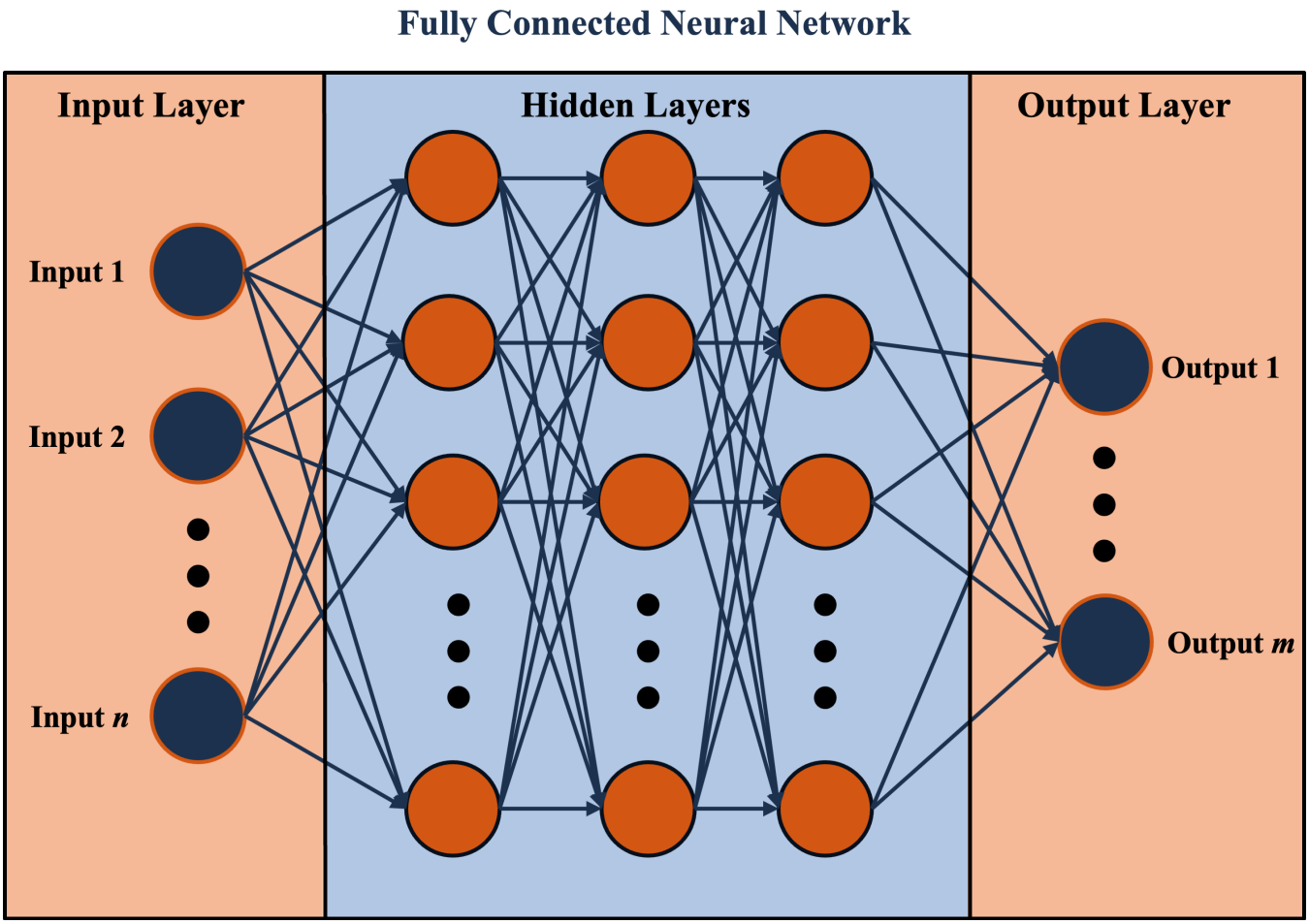

Figure 4.7: Diagram of a fully interconnected neural network with 3 hidden layers.

$$f(x) = \frac{1}{1 + e^{-x}}. \tag{4.7}$$

Here the closer the result to 0 or 1, the more confident network is in the result. For categorical classification models, a soft max activation fiction is used:

$$\sigma(\boldsymbol{z})_j = \frac{e^{z_j}}{\sum_{k=1}^{K} e^{z_k}} \tag{4.8}$$

Here $\boldsymbol{z} = (z_1, ..., z_K)$ is the input vector and K is the number of categories. The result is a vector where each entry is the probability that the input belongs to that class. And for regression models, a linear activation model is used:

$$f(x) = x. \tag{4.9}$$

Before training, the weights and biases of the model are assigned random values between -1 and 1. This helps prevent models from getting stuck in local minima and improves diversity in the model outputs. Training a model consists of 3 steps [182] (1) A data point from the training data set is passed through the network and the result extracted. (2) The loss associated with the result is calculated. (3) Backpropagation is performed to adjust the weights and biases to minimize the loss. This process is performed iteratively for each sample in the training data set. Each complete cycle using the training data is called an epoch and the number of epochs to train for can either be user specified or determined by a function of the change in the loss through each cycle. Backpropagation is the process by which the derivatives of the loss function are calculated and the weights and biases are updated to minimize the loss. This process goes layer by layer starting with the last layer and moving toward the first layer of the network. The most common backpropagation algorithm used in neural networks is gradient descent, although many variants of this are used in practice depending on the problem at hand [184].

Rather than perform backpropagation after each sample in the training data set, steps (1) and (2) are performed for multiple samples and then backpropagation is performed. This prevents individual samples that might be outliers from having undue influence on the performance of the network and reduces the number of times backpropagation needs to be performed [185]. If these batches are randomly created each epoch, then the result is stochastic gradient descent which offers slightly better results than regular gradient descent. Gradient descent requires that derivatives of the activation functions exist for it to work efficiently [184]. If the derivatives do not exist or are 0, backpropagation fails and the weights of that neuron will remain unchanged. Originally, a non-leaky ReLu activation function, where $f(x) = 0$ for $x < 0$, was common as it would ”turn off” the neuron if a negative value was input and ”turn on” for a positive

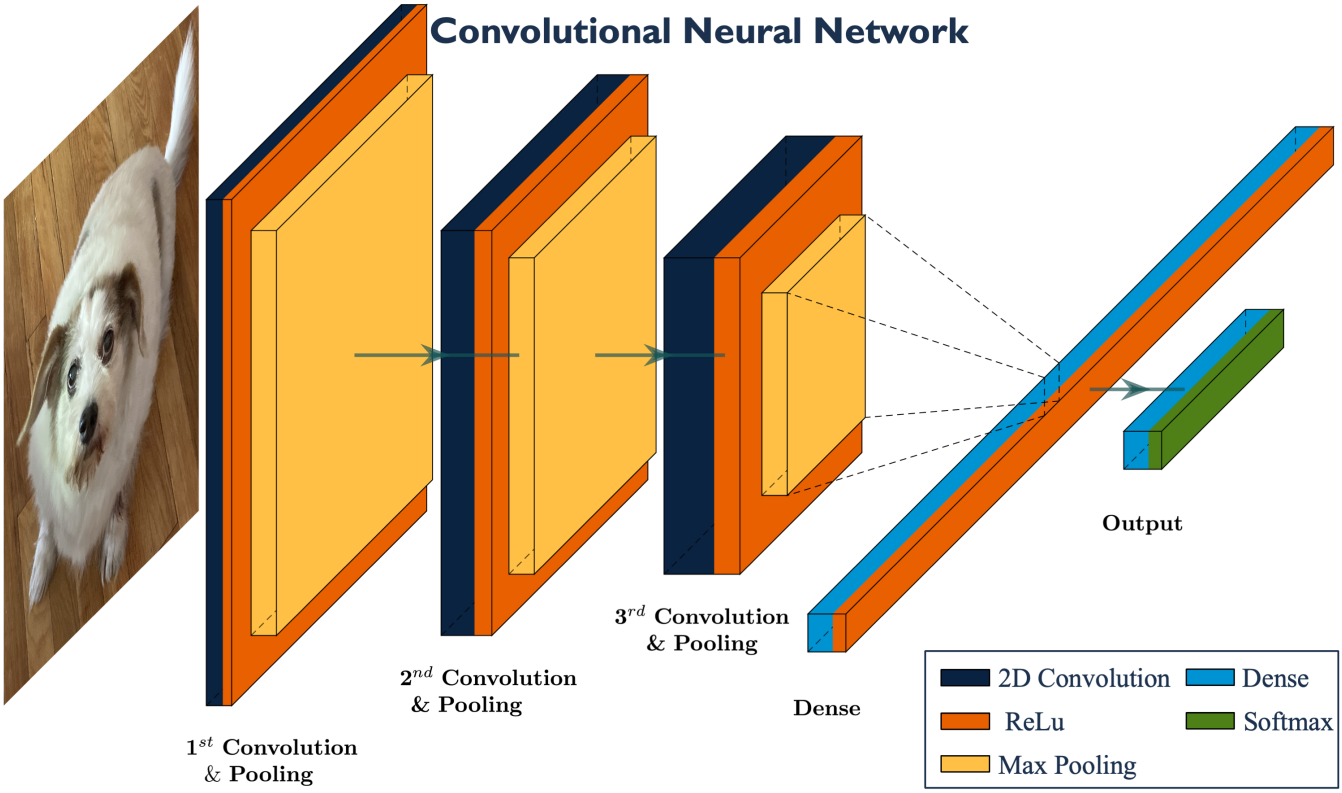

Figure 4.8: A diagram of a convolutional neural network that classifies images based on the animals present [188].

value [186]. However, if the weights of the neuron caused the input to be negative, the gradient would be 0. Thus leaky Relu is used now instead, as the gradient in the case where the input is negative will still have a derivative but the ”on” and ”off” nature is retained. Once the training is complete, the network can be fed new inputs to to test the accuracy or to obtain new results [186].

The neural network model in Figure 4.7 represents the most basic level of networks. For most problems, more complex network architectures are used. If that model was used to process gray scale images of size 256x256, each neuron in each dense layer would need 65,536 weights, making it far too computationally expensive to train. Convolutional neural networks (CNNs) are networks that are specialized for dealing with image or 2D data. One of the first successful works on CNNs was used to identify handwritten digits [187] and highlights the practical uses. Figure 4.8 shows a basic structure of a CNN.

This model represents a classifier CNN that is designed to identify the type of animal in the image. This kind of application of CNNs is very common, with one commercially available example being the app *PictureThis - Plant Identifier*, which identifies plants from photos by utilizing a CNN based on the same principals [189]. The network in Figure 4.8 takes an image, in this case a dog, as input and first passes it through three sets of convolution and pooling layers. Convolution layers take the input and pass it through a 2D filter. Each filter is essentially a matrix of weights ranging from 0 to 1. Just as with the weights in the dense layers of the past example, they are randomly initialized before training and are optimized during the backpropagation portion of training. These filters are most often of size 3x3 pixels. Each filter is rastered across the image to calculate the resulting matrix called a feature map. Convolution layers include multiple filters in each layer with the individual feature maps being combined into a single 3D matrix as an output. The dimensions of the resulting feature map can be determined by:

$$L \times W_F \times H_F = \left[\frac{W_I - F}{S} + 1\right] \times \left[\frac{H_I - F}{S} + 1\right] \times K \tag{4.10}$$

where H_I and W_I are the height and width of the input, the filter has size $(F \times F)$ and stride S, and K is the number of filters [190]. Each of these feature maps is then passed to a pooling layer. Local pooling rasters a pooling window, often 3x3 pixels, across each feature map and performs an operation. Taking the max value in the pooling window is called max pooling and often used, though average pooling, where the average is calculated, and other options exist. Pooling is used to reduce the dimensionality of the feature maps before they undergo additional convolutions. By combing these convolution and pooling layers, the network is able to extract broader features of the image. After the last of the feature sampling concludes in the convolution and pooling layers, the data is flattened and passed to a series of dense layers. Lastly the data arrives at the output layer whose dimension is the number of output categories of the classifier. Rather than

use stochastic gradient descent, CNNs are often trained using a variant called adam that uses unique learning rates for different parameters rather than using a single learning rate for all parameters [191].

Although CNNs are capable of succeeding with complex tasks such as image identification, there are many common issues that arise during training. The most common issues are overfitting and underfitting. Overfitting occurs when the model trains too well to the training data set and as a result has comparatively poor performance on samples from outside the training set. This issue plagues many deep CNNs, though there are ways to prevent it. Weight regularization adds an additional loss function at each layer that penalizes nodes with values significantly more intense than others. This works to prevent any one feature from gaining to much importance and dominating the results [192]. Another solution is to observe when the accuracy of a test set begins to decline or ceases to improve and stop training then. There is also a learning rate that affects how aggressively gradient descent modifies weights. Reducing this learning rate will slow the training but should reduce overfitting.

Underfitting is the opposite of overfitting and is where the model is unable to fit to the features in the training set, resulting in poor model performance [193]. The solutions are the opposite of those for overfitting. Increasing the learning rate and training for more time may solve the issue. If weight regularization is present, its effect on the total loss should be decreased. If after all of these changes, underfitting is still present, then it is likely the model design is not complex enough. Adding more layers of convolutions or more dense layers may be needed for the features of the data set to be fit by the model. If the model is still unable to learn, then the cause is most likely a lack of training data.

Mode collapse is another common issue, and is when the model's predictions begin to collapse to a small range of values. For example, if the model in Figure 4.8 always predicted the input image was a cat regardless of input. The primary limitation of neural networks is that due to their complexity, a larger amount of training data is needed than for simpler models, such as random forests. Without sufficient amounts

of training data, a model will not converge regardless of how or how long it is trained. But when sufficient data is available, the ability of CNNs to solve new problems is very useful. Previous studies have utilized CNNs to successfully transform data from one domain to another [155]. In physics, CNNs have been used to find solutions to scattering problems [194] and predict XANES spectra [162]. A subclass of CNNs called physics informed neural networks (PINNs) utilize an additional loss function that penalize non-physical behavior. PINNs have been used to find solutions to fluid flow [195] and heat transfer problems [196].

Chapter 5

Principal Component Analysis and k-means Clustering

RHEED has been standard equipment on MBE chambers since the 1980s [91] because it provides real time, *in-situ* feedback on the surface evolution of thin film samples during synthesis. And while many studies have resulted in increased understanding of RHEED or developed new techniques to utilize RHEED [197], due to the complexity and effectiveness of these techniques, most film growers still opt for simple, qualitative analysis methods of RHEED. However, there is certainly much more information that can be extracted from RHEED, and advances in the fields of data science and machine learning have yielded algorithms and tools that can serve to augment existing data analysis and provide new paths to unlock deeper understanding of RHEED data. This dissertation focuses on the synthesis of SHO thin films by MBE and the development of two machine learning tools that can be used to better understand and control the synthesis of films.

This chapter focuses on the results of the application of PCA and k-means clustering on recordings of RHEED patterns collected on a variety of samples as well as the effects of different preprocessing techniques on the resulting eigenvectors and clustering. I was responsible for the synthesis of $SrTaO_3$, while the synthesis of the other samples and their corresponding RHEED recordings were performed by former members of the Auburn University FINO Lab (AU FINO) Suresh Thapa and Rajendra Paudel, as well as Eren Suyolcu from Max Planck Institute for Solid State Research. The code used for PCA and k-means was written by former member of the AU FINO Lab Sydney Provence and myself, while I am responsible for the results and analysis shown here.

5.1 Data Preprocessing

Several different methods of preprocessing were used to prepare RHEED videos to be used in the PCA and k-means algorithms. PCA is a computationally intensive algorithm that scales with the number of samples n and the dimensions of the samples p as $O(n^2p+n^3)$ [198]. For a RHEED video with resolution of 1080x1080 pixels, frame rate of 5 frames per second, and a duration of 25 mins, the time needed for PCA to be completed on a single node of the Auburn University Easley cluster would be over a week. Thus, it is important to reduce both the number of frames sampled from a video and the dimensions of the video used in order to obtain a feasible run time. For the dimensionality, this is achieved by cropping the RHEED patterns down to a smaller subset of the recorded frame. Figures 5.1(a) and (b) show the raw image of a RHEED pattern and the cropped version used in PCA, respectively. During this process, a balance must be struck such that a sufficient amount of the pattern is retained and as much background as possible is excluded. The number of sample frames is reduced uniformly throughout the video by reducing the frame rate. The specific frame rate used is varied from growth to growth and is selected based on the growth rate of the material. For materials synthesised using only metals evaporated out of effusion cells, the deposition rate is considerably higher than those that utilize hBME. If too low a frame rate is selected, information such as RHEED spot oscillations can be lost. In practice, it was found that for faster growths, a frame rate of 1 fps was sufficient while for slower growths, such as SNO, a frame rate of 0.2 was sufficient. Additionally, blank frames at the beginning and end of growth were removed, as well as any frames that were partially obstructed during recording. With these modifications, the execution time for PCA was reduced to less than 2 hours.

In addition to the changes made to improve execution time, there are several image preprocessing algorithms that can improve image quality. The quality and sharpness of RHEED images are determined by not only the quality and structure of the film surface, but also the chamber geometry, chamber pressure, the quality of the phosphorous

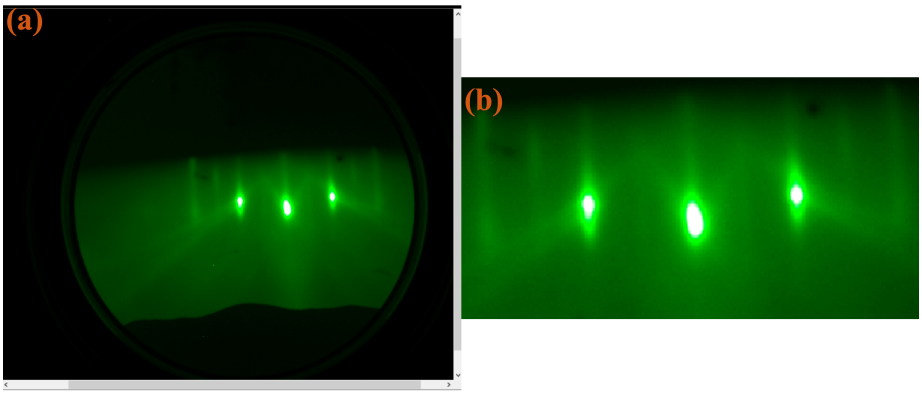

Figure 5.1: (Left) An uncropped RHEED image of SHO. Right The cropped RHEED image used for PCA and k-means

screen, and the quality of the RHEED camera. These additional effects do not reflect the quality of the film and can result in RHEED patterns that are not as clear as other samples, resulting in fainter features being obscured. Since the primary use of RHEED patterns is to be visually interpreted by a researcher, it is critical that these effects be mitigated as much as possible. In order to achieve this mitigation, three different intensity transformation functions are investigated.

Figure 5.2 shows the three intensity transform functions and the identity function for reference. The piecewise intensity function is given by:

$$I_{out} = \begin{cases} 0 & \text{if } I_{in} \leq T \\ \frac{I_{in}-T}{1-T} & \text{if } I_{in} > T \end{cases} \tag{5.1}$$

where I_{in} and I_{out} are the input and output intensities, respectively, and T is the cutoff threshold. This piecewise function maps all pixel values below some specified background value to 0 and rescales the remaining pixel values between 0 and 255. In practice, the cutoff threshold is determined by calculating the distribution of pixel intensities for a given RHEED image and then determining a threshold pixel intensity from that distribution. This results in a large area of the image becoming black while the remaining parts of the image have linearly increased contrast. The power intensity function is given by:

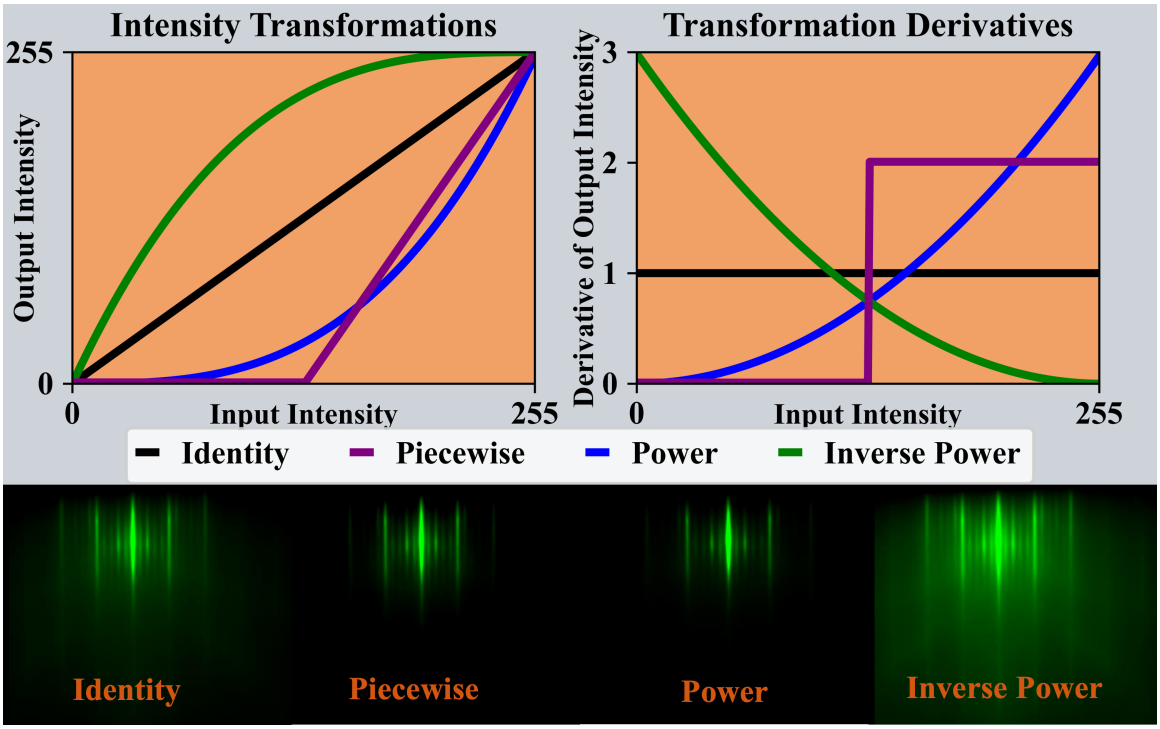

Figure 5.2: (Top Left) The intensity transformation functions used on RHEED images. (Top Right) The first derivatives of the intensity transformation functions. Bottom: An example LSCO RHEED image and the effects of the identity function and 3 transformation functions.

$$I_{out} = I_{in}^{\gamma} \tag{5.2}$$

where γ is a positive real number. This method uses a power function to rescale the pixel intensities rather than a linear one, resulting in reduced contrast between low intensity values and greater contrast between high intensity values. This is ideal for when the RHEED screen is heavily saturated, making it difficult to distinguish bright features from the background. The inverse power function results in the opposite effect, where low intensity values are increased in contrast while high intensity spots experience decreased contrast. The function is given by:

$$I_{out} = |1 - (1 - I_{in})^{\gamma}|. \tag{5.3}$$

This transformation is ideal for when there are weak features like Kikuchi bands and higher order spots that need to be enhanced to become visible. Figure 5.2 shows an example RHEED image from an LSCO sample grown at the Max Planck Institute for Solid State Research and the results of the three transformation functions applied to it.

Due to the geometry of the chamber, it is nearly impossible to align samples the same way each time. Additionally, due to vibrations, magnetic interference, and mechanical noise present during growth, the alignment can shift during the course of a sample growth, either suddenly due to an instantaneous event such as the opening of a shutter or gradually due to sample drift on the stage. This causes a translation of the image during a RHEED recording and poses a problem for PCA and k-means as the different locations of the pattern on the screen will be interpreted as a feature. In order to mitigate this, a system for identifying the specular spot of RHEED images and aligning them to the center of frame was devised. For a given RHEED image, the image is mirrored across the vertical axis and the difference between the mirror image and the original is calculated using a residual sum of squares. The mirror image is then translated 1 pixel horizontally and the residual sum of squares is calculated again. This is

repeated for each possible horizontal alignment of the image and its mirror. As can be seen in Figure 3.1, RHEED patterns exhibit bilateral symmetry across the vertical axis and thus the difference between an image and its mirror will be minimized when aligned along the vertical axis of the specular RHEED spot. This method is highly effective at finding the horizontal center of a RHEED pattern and allows for different patterns to be aligned horizontally. This method will be referred to as the residual sum of squares (RSS) alignment.

While RHEED images possess vertical mirror symmetry, RHEED images are not symmetric about the horizontal axis; however, the individual spots or streaks are symmetric about a horizontal axis. Thus in order to align the images vertically, the image is cropped and only the specular RHEED spot is used. First, an approximate center is found for the spot using a geometric mean of the pixel intensity. Using this approximated center, the image is cropped to the specular spot. Finally, the RSS alignment algorithm is used to find the vertical center of the specular spot. In order to prevent background signal from dominating the RSS calculations, a low intensity filter is used that sets all values less than 90% of the maximum spot intensity to 0. Thus, only the high intensity spots are used in the RSS alignment algorithm to determine the symmetry. Without this filter, the accuracy of this method drops considerably. The preprocessing algorithms were implemented in Python 3.9.16.

5.2 PCA & *k*-means Implementation

PCA was implemented in Octave version 1.5.0 using single value decomposition [199]. The number of PCA components is specified by the user, but for this work it is set at 6, which retains $> 99.98\%$ of the variance in the raw data. The resulting eigenvalues and eigenvectors are stored in binary text and binary MATLAB files for post processing. The k-means clustering is performed on the results of the PCA and is also written in Octave 1.5.0. The clustering is performed from 1 to k where k is specified by the user and in this work is 10. Once k gets beyond 10, the differences between clusters

decreases and several clusters containing only a few frames begin to appear, making it hard to interpret the results. For each value of k, the clustering is run 100 times with different random starting configurations, in order to ensure an absolute ground state is found. Each clustering attempt is limited to 20 iterations, with the results being saved in binary text and binary MATLAB files for post processing. Graphs of the eigenvectors, eigenvalues, clustering distributions, and centroid images are created during post processing which is written in Matlab 2020b.

5.3 Results

5.3.1 Intensity Rescaling

Figures 5.3 and 5.4 show the PCA and k-means clustering results, respectively, for an LCO sample grown by MBE at the Max Planck Institute for Solid State Research. The top 3 components of Figure 5.3 and the tiles on the left of Figure 5.4 correspond to the raw video collected during growth, while the bottom 3 components in Figure 5.3 and the tiles on the right in Figure 5.4 correspond to the same video after it has undergone the piecewise rescaling described in section 5.1. The eigenvalue plots show no difference between the raw and transformed videos, with the exception of component 3. However, this change is not significant, as it can be easily seen the eigenvalues and eigenvectors are both inverted in the transformed video. Multiplying both the eigenvalues and eigenvectors by -1 will result in no change to the video, thus this is not a significant change. The difference between these two videos is easiest to observe from the centroid images in Figure 4.4, where we see the contrast of the transformed video is higher and results in clearer separations between the reconstructions spots. The primary limitation to this transform is that any information that is present in the darker regions is lost; however, from the k-means clustering graphs, it can be seen that the results have not been significantly effected by the transformation and thus this method for artificial contrast can be used without distorting the understanding of the videos.

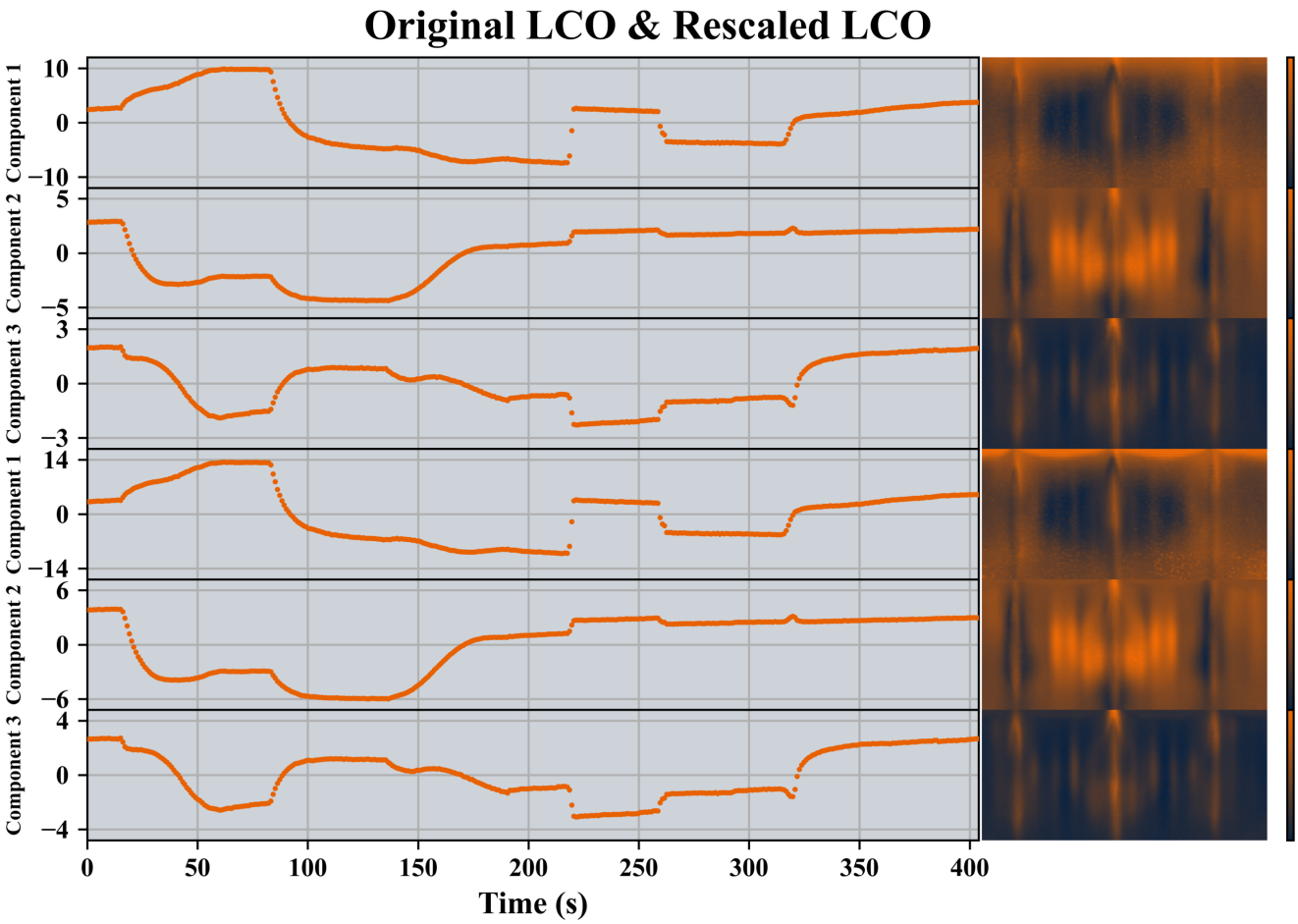

Figure 5.3: Results from the PCA of a sample containing a RHEED recording of an LCO sample and a copy of the same recording after undergoing a piecewise intensity transformation. (Top Left) The first three eigenvalues of the original recording plotted over the course of the growth. (Top Right) The corresponding eigenvectors from the original recording. (Bottom Left) The first three eigenvalues of the transformed recording plotted over the course of the growth. (Bottom Right) The corresponding eigenvectors of the transformed recording.

Figures 5.5 and 5.6 show the results of PCA and k-means, respectively, for an LFO sample grown using MBE in the Auburn University FINO lab. The top 3 components of Figure 5.5 and the A tiles of Figure 5.6 correspond to the raw video collected during growth, while the bottom 3 components in Figure 5.5 and the B tiles in Figure 5.6 correspond to the same video after it has undergone the power rescaling described in section 5.1 with $\gamma = 2.0$. As was the case with the LCO video that underwent piecewise rescaling, there is no discernible difference between the original and transformed eigenvalues and eigenvectors. Due to the power recalling function, the contrast is toned

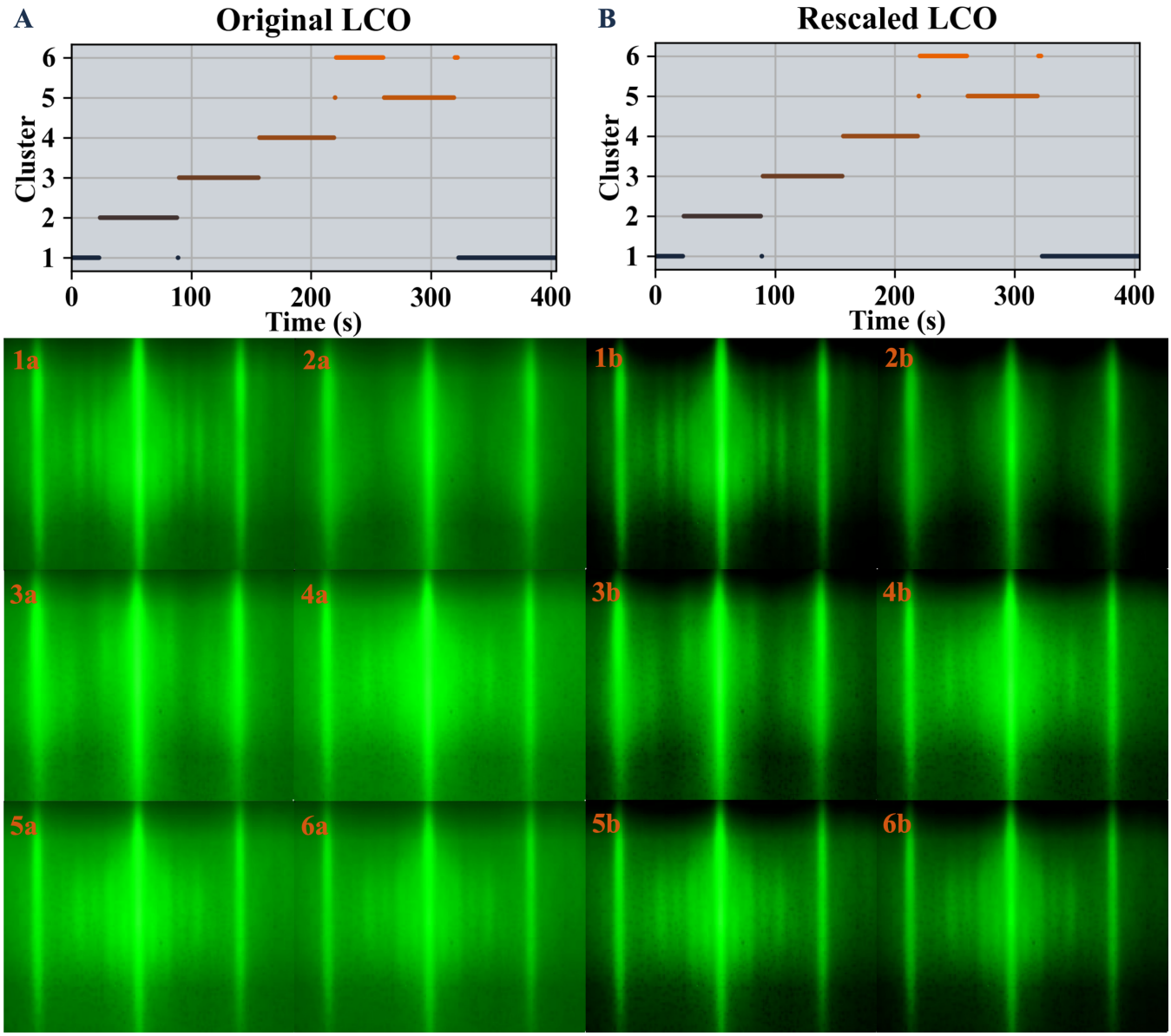

Figure 5.4: Results from the PCA of a recording containing the original RHEED recording of an LCO sample and the same recording after undergoing a piecewise intensity transformation. (A),(B) Graphs of the clusters over the course of the growth for the original and transformed recordings, respectively. (1a)-(6a) The centroid images for the clusters plotted in (A). (1b)-(6b) The centroid images for the clusters plotted in (B).

down for lower intensity values and increased for higher intensity. As can be seen in the HDR LFO centroid clusters, this improves the distinction between the Kikuchi bands, spots, and background. From the clustering plots we see there is no change in the first 6 clusters, with the exception of the very first frame being swapped between clusters 1 and 2, resulting in the ordering being switched. However, in clusters 7 and 8, there

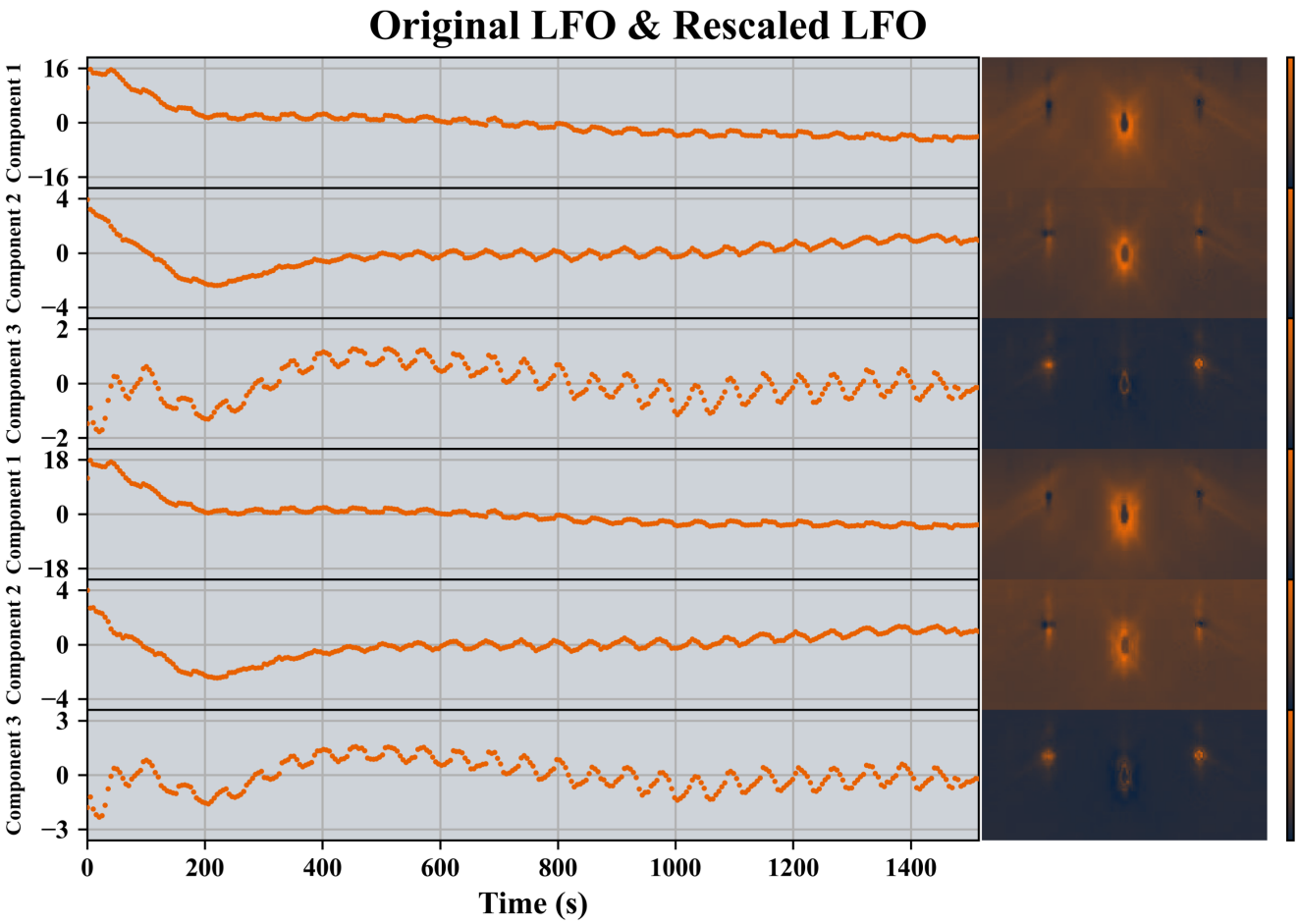

Figure 5.5: Results from the PCA of a recording containing the original RHEED recording of an LFO sample and the same recording after undergoing a power intensity transformation. (Left) The eigenvalues plotted over the course of the growth. (Right) The corresponding eigenvectors.

is an increase in the alternating pattern between the two clusters that matches the frequency of the specular spot oscillations and the frequency observed in the eigenvalues. In this case, the improved contrast between the background and RHEED pattern features results in an improved analysis and demonstrates the positive effects of careful data preprocessing.

5.3.2 RSS Alignment

One of the common issues encountered during an extended growth is drifting or shifting of the RHEED pattern over time. This can be caused by mechanical vibrations

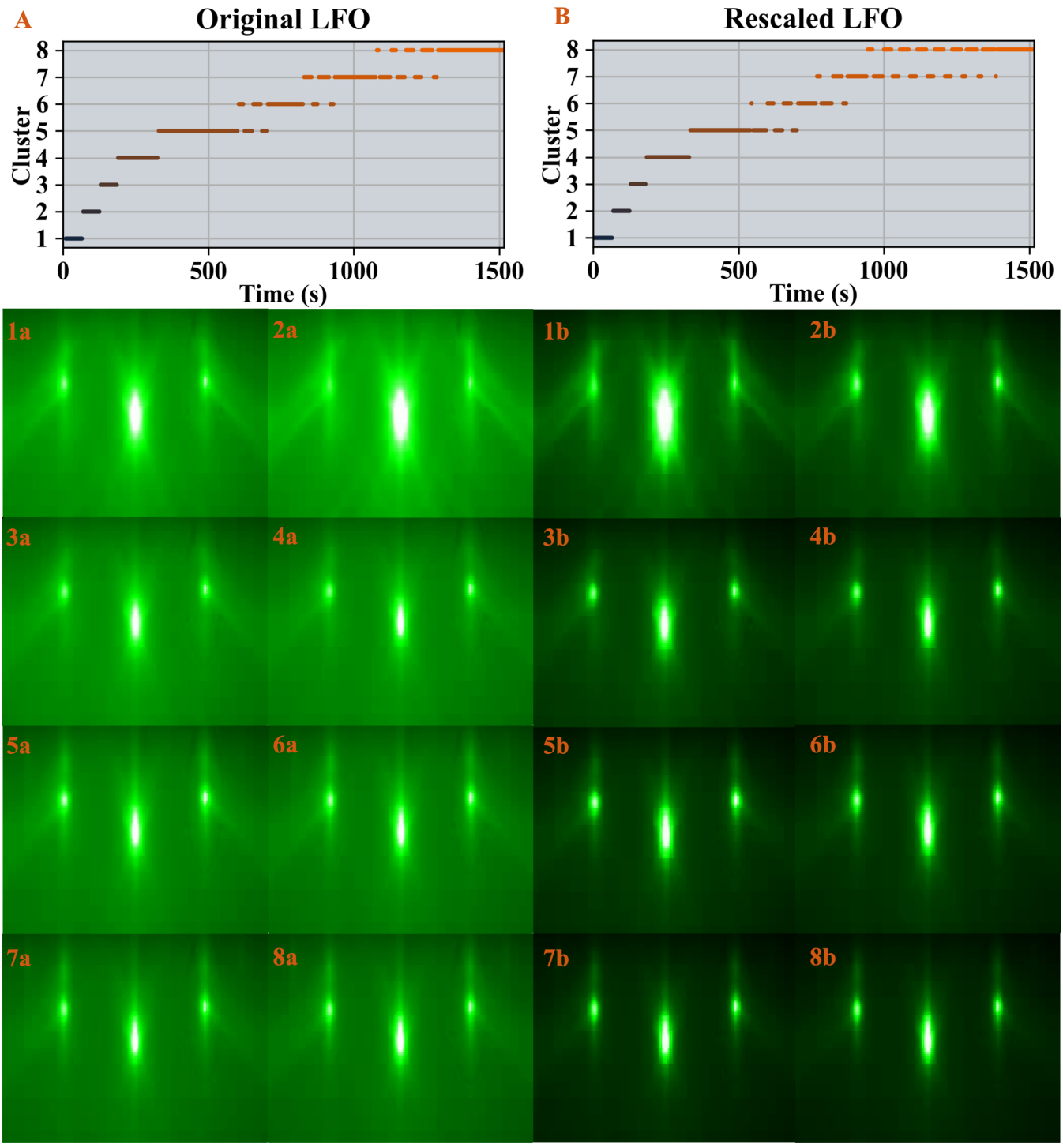

Figure 5.6: Results from the PCA of a recording containing the original RHEED recording of an LFO sample and the same recording after undergoing a power intensity transformation. (A),(B) Graphs of the clusters over the course of the growth for the original and transformed recordings, respectively. (1a)-(6a) The centroid images for the clusters plotted in (A). (1b)-(6b) The centroid images for the clusters plotted in (B).

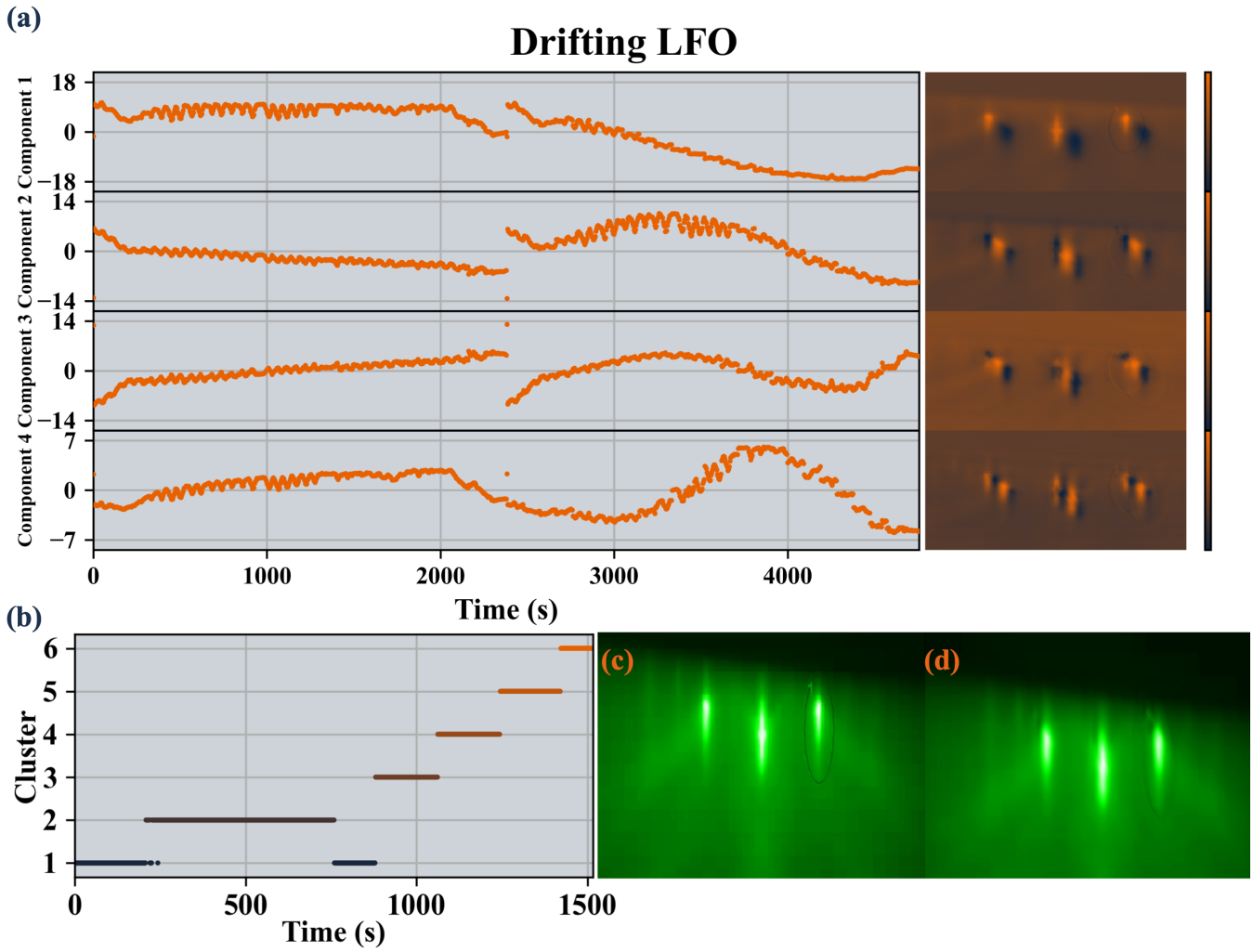

Figure 5.7: Results from PCA and k-menas clustering of a recording containing the original RHEED recording of an LFO sample and the same recording with an artificial drift applied. (a) The first four eigenvalues plotted over the course of the growths and their corresponding eigenvectros. (b) A graph of the clusters over the course of the recordings. (c),(d) The centroid images of clusters 3 and 5, respectively.

present in the lab or can be the result of charging effects causing minor deflections in the electron beam. For the purpose of traditional RHEED interpretation, this issue is easily rectified by adjusting the alignment of the RHEED system; however, for numerical analysis such as specular intensity monitoring, PCA, and k-means, this is not the case. In PCA and k-means, small translations in the pattern result in different components and changes to the clustering that obscure the physical information present. This is seen clearly in Figure 5.7, which show the PCA and k-means results of an LFO sample grown using MBE at the Auburn FINO lab. The first half of the graph corresponds

to the original recording, while the second half of the graph corresponds to the same video that was translated 25 pixels right and 25 pixels down at a constant rate over the length of the video. From the clustering in Figure 5.7(a), it is clear that the drifting of the RHEED pattern causes the corresponding frames of the first and second half to vary greatly. The eigenvalues of the first 3 components shown in Figure 5.7(b-e) shows that PCA focuses on this translation and constructs eigenvectors that produce this translation. The eigenvalues in the drifting recording are periodic while the eigenvectors display bright and dark spots that correspond to the drift. The eigenvectors also exhibit little to no finer structures indicating the important details are being blurred out as compared to the primary spot intensity.

In order to correct for drift or sudden shifts in the pattern, the RSS alignment algorithm described in section 5.1 is used. Figure 5.8 shows the PCA and k-means results for the same recording in Figure 5.7 after it the RSS alignment was applied. The clustering graph now shows nearly identical clustering for the original and drift recordings. The RHEED images in 5.8(f) and (g) show that the centroid images of clusters 2 and 5 are now aligned with each other. The eigenvalue plots of the first 4 components show that the PCA now yields the same results for both recordings and as a result the eigenvectors now show features like the Kukuchi bands that correspond to the sample surface rather than focusing on the translation. From these results it is clear that the RSS alignment algorithm is able to successfully mitigate the effects of pattern translation and works to ensure PCA and k-means results are focused on significant features that inform on the film surface quality.

In addition to correcting drift and sudden shifts in alignment, RSS alignment is also able to align recordings from different samples with accuracy within a couple of pixels. This works best for videos that begin with clean substrates that possess high quality RHEED patterns, as they will have the sharpest features. Figures 5.9 and 5.10 show the PCA and k-means results for the combined recordings of two LFO-Nb:STO

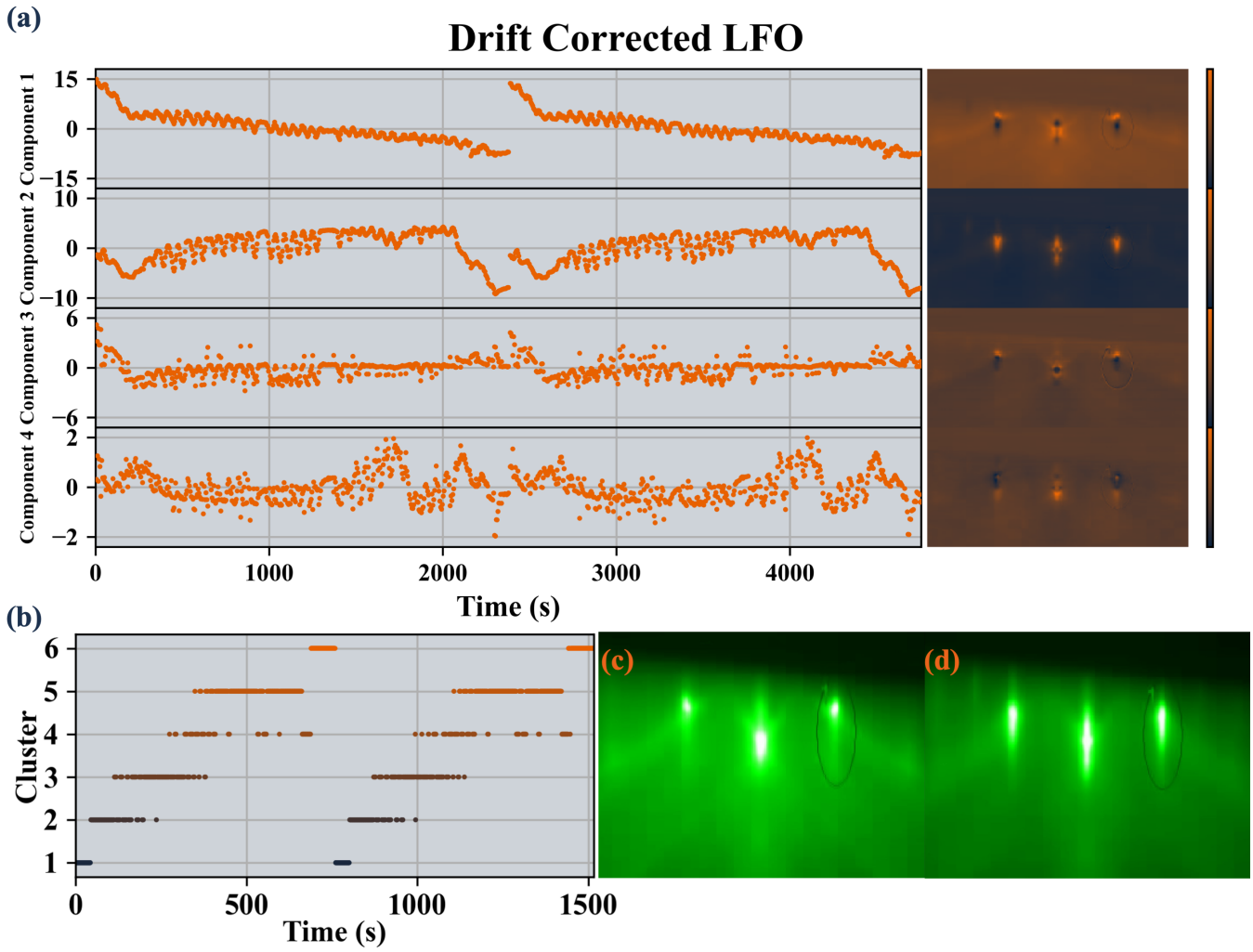

Figure 5.8: Results from PCA and k-menas clustering of the same recording in Figure 5.7 after the RSS alignment algorithm was applied. (a) The first four eigenvalues plotted over the course of the growths and their corresponding eigenvectros. (b) A graph of the clusters over the course of the recordings. (c),(d) The centroid images of clusters 3 and 5, respectively.

samples grown in the FINO lab at Auburn University. The samples were grown at identical conditions on the same day, with the first lasting 1500 s and the second lasting 1900 s. As expected, the eigenvalues are not the same for the two growths, though for a few components, such as 1, 3, and 5, the beginning of each growth is similar. The eigenvalues of the first component possess very similar values and follow the same progression. The corresponding eigenvector appears to represent the primary spot intensity and a change in the first order spot location. The clustering graph in Figure 5.10 shows that the growths proceed through the same two clusters initially, but diverge afterwards.

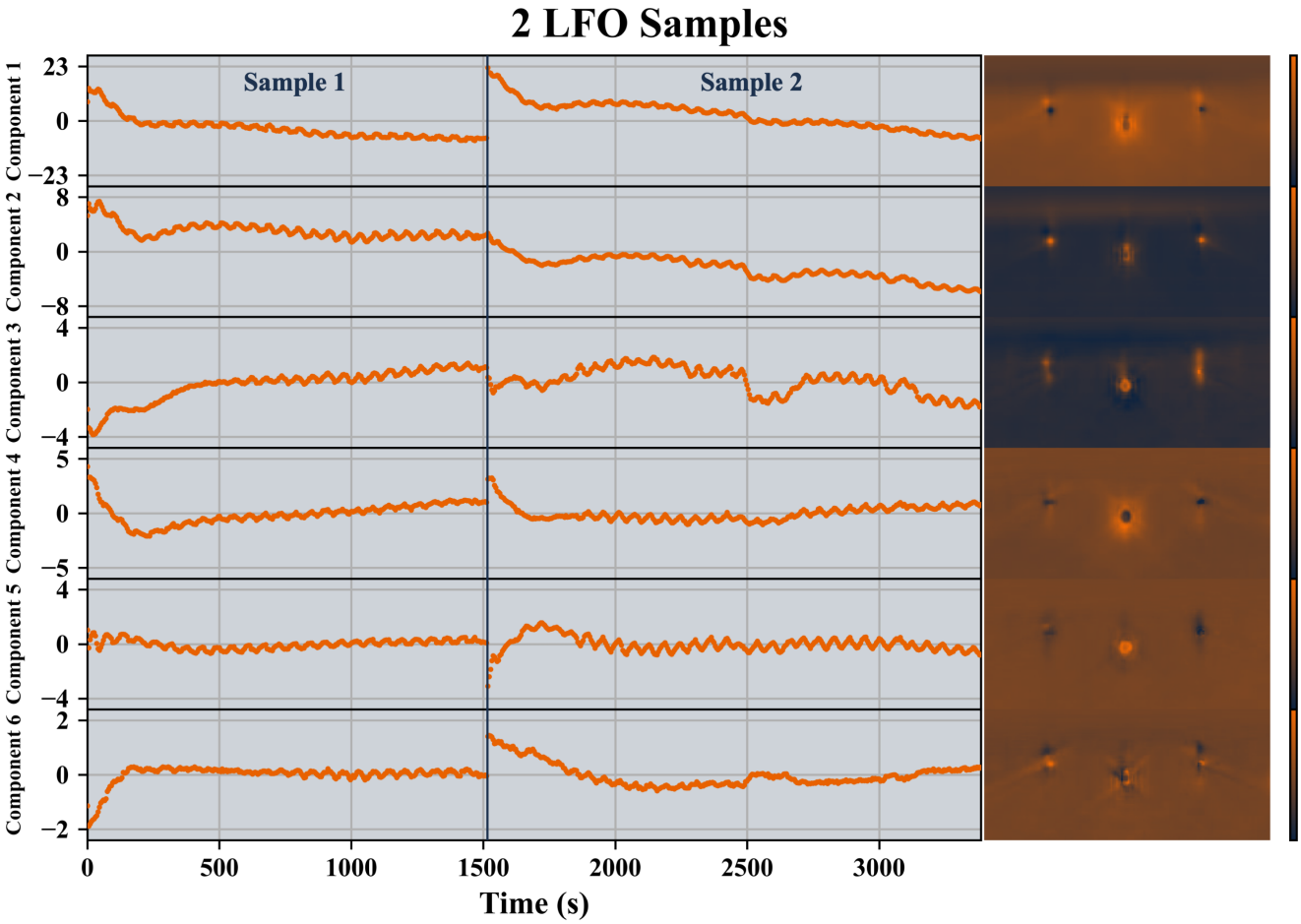

Figure 5.9: Results from the PCA of a recording containing 2 LFO samples. (Left) The eigenvalues plotted over the course of the growths. (Right) The corresponding eigenvectors.

The first cluster is highlighting the pattern of the Nb:STO substrate, which is replaced after ≈ 100 seconds by the second cluster which shows a fainter pattern with less sharp Kikuchi bands. LFO 1 then proceeds through clusters 3 and 4 which show clear bands and distinct spots with minimal streaking. However, LFO 2 remains in cluster 2 for ≈ 800 seconds before transitioning to cluster 5 where the RHEED is softer and no Kikuchi bands are present. This softening along with less distinct spots suggest that islands have begun to form or parts of the film have begun to lose their structure and become amorphous. While in this instance the two growths diverge into different results, without the RSS alignment, the direct comparison of the development the films

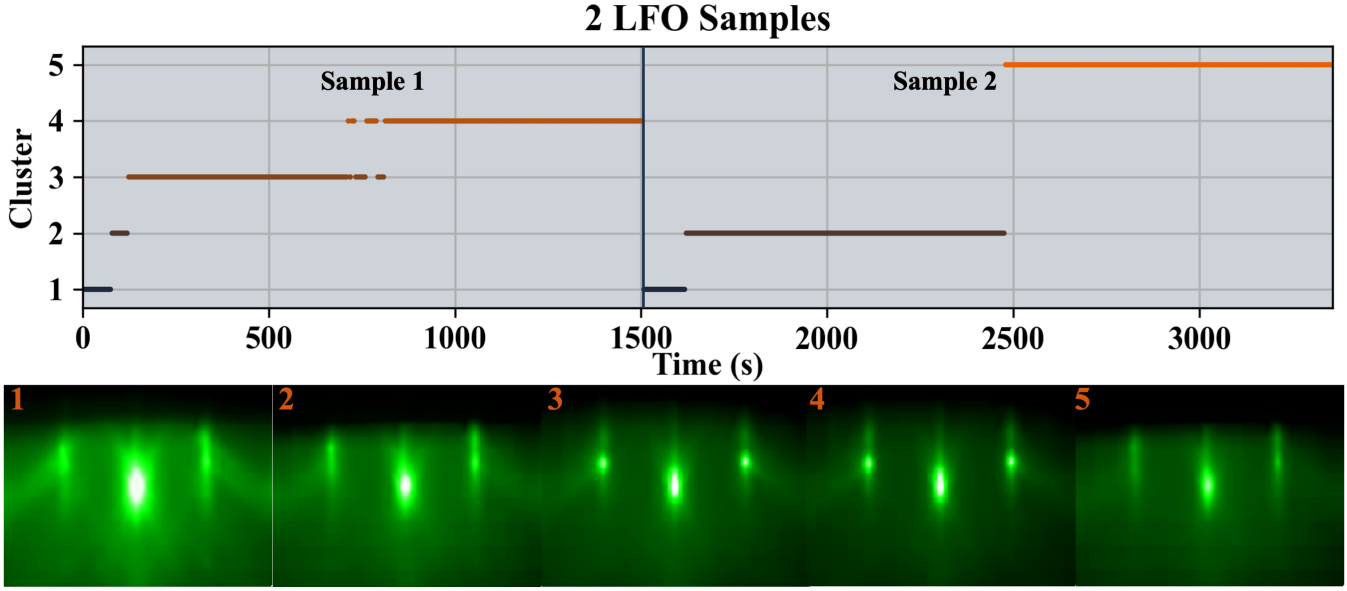

Figure 5.10: Results from the k-means clustering of a recording containing 2 LFO samples. (Top) A graph of the clusters over the course of the growths. (Bottom) The centroid images corresponding to the clusters in the graph.

surface would not be possible, as the PCA and k-means would have split the growths in the same manner observed in Figure 5.7.

5.3.3 $SrNbO_3$

Figures 5.11 and 5.12 show the PCA and k-means clustering results, respectively, of a SNO-GSO sample grown by MBE at the Auburn University FINO Lab. The clustering graph shows a slow progression through the first two clusters, whose centroid images contain the intermediate reconstruction spots from the GSO substrate. Clusters 3 and 4 show weak Kikuchi bands and dimmer 1^{st} order spots, which is consistent with the first unit cells of growth. Clusters 5 and 6 show an increasing brightness and sharpening Kikuchi bands as the growth approaches ≈ 3 nm that indicate the film has achieved a highly crystalline surface [37]. From the eigenvalue plots, it is clear that no RHEED oscillations are present. This suggests that the growth mode for this sample was not layer by layer growth, but possibly step flow growth or a mix of growth modes. In clusters 1, 3, 5, and 6, there is a sharp change observed that aligns with the end of the second cluster, and delineates between smooth evolution observed in the first half of

the growth from the sharper more intense changes observed in the second half. This indicates that the deposition of the film begins slow and takes ≈1700 seconds to cover the substrate with the first 1-2 unit cells while the second half of the growth produces 5-7 unit cells in the same time. This may be due to changes in the surface chemistry between the substrate and film or could be caused by changes in the metal sources or oxygen environment during growth.

Figure 5.13 shows the k-means clustering results of a SHO-SNO-GSO sample grown by MBE at the Auburn University FINO Lab. The clustering graph shows the timings of the SNO and SHO growths, along with the cool down phase. As was the case for the SNO-GSO growth in Figure 5.12, the first cluster is the largest and the

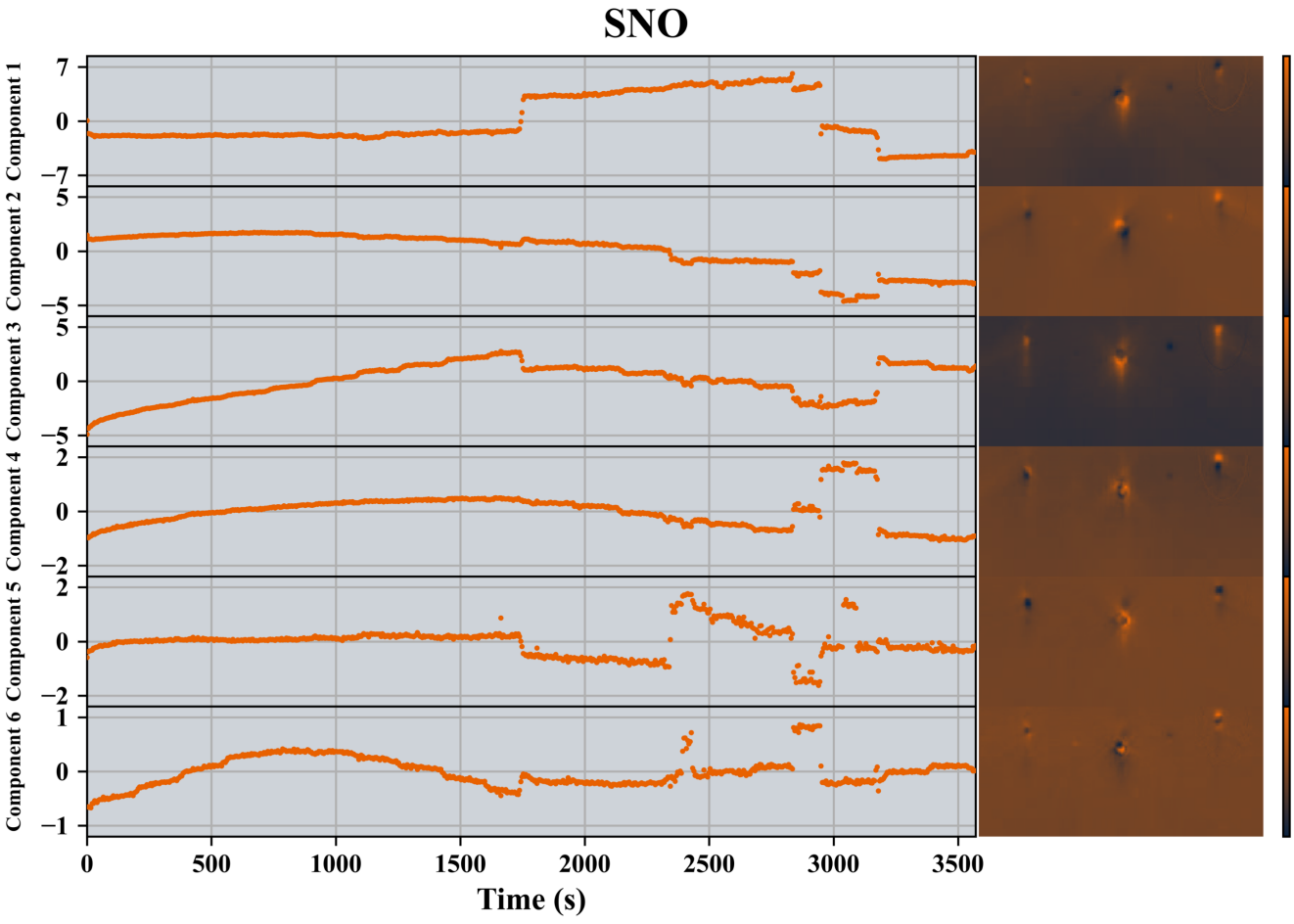

Figure 5.11: Results from the PCA of an SNO sample. (Left) The eigenvalues plotted over the course of the growth. (Right) The corresponding eigenvectors.

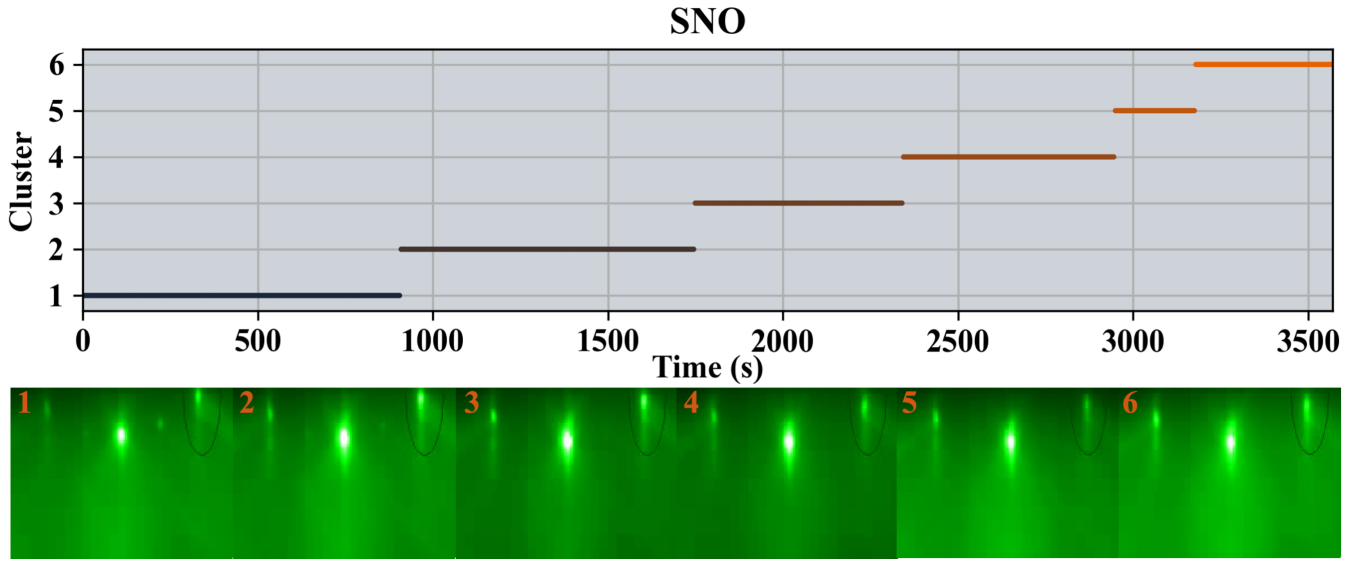

Figure 5.12: Results from the k-means of an SNO sample. (Top) A graph of the clusters over the course of the growth. (Bottom) The centroid images corresponding to the clusters in the graph.

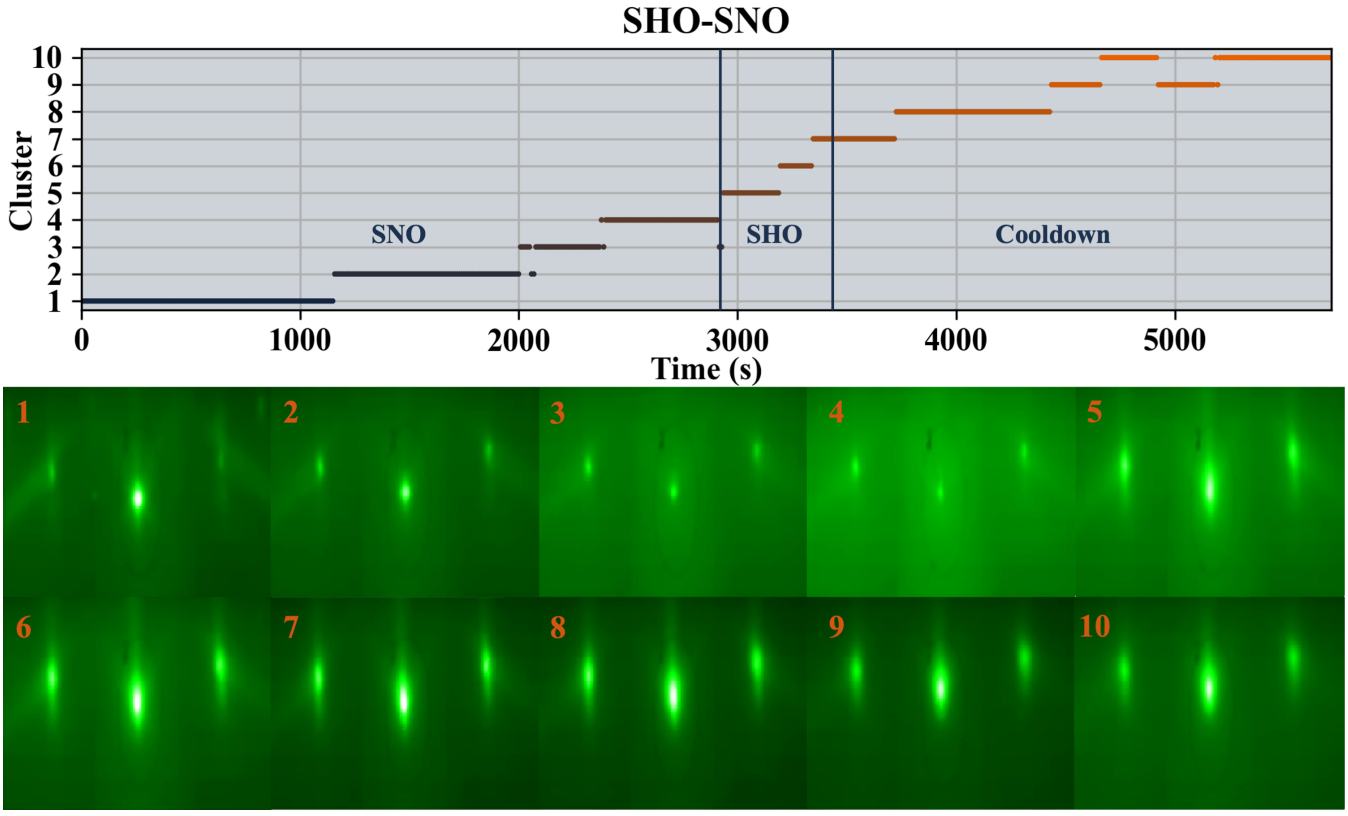

Figure 5.13: Results from the k-means of an SHO-SNO-GSO sample. (Top) A graph of the clusters over the course of the growths and cool down. (Bottom) The centroid images corresponding to the clusters in the graph.

corresponding centroid image shows reconstruction spots that result from the substrate. Clusters 2, 3, and 4 show softening of the spots and Kikuchi bands that indicate the SNO film contain defects or lacks proper ordering. However, the sharp increase in spot intensity observed in clusters 5, 6, and 7 indicate a recovery by the SHO film and suggest it is highly crystalline. From the timing of the clusters, it is clear that the SHO film maintains a high quality surface even once cooling down begins. This stands in sharp contrast to SNO, which is metastable and tends to over oxidize during cooling. Clusters 8, 9, and 10 show no major changes to the surface structure, indicating that the SHO has succeeded as a capping layer and prevented over oxidization of the underlying film. This was confirmed by XPS, which also showed that the oxidation state of Nb was lower in films covered with SHO capping layers [37].

5.3.4 $SrTaO_3$

During growth, there is a possibility for unexpected features to appear in a film. Surface islands and additional phases are prime examples, which both result in changes to the RHEED pattern. Figures 5.14 and 5.15 show the PCA and k-means clustering results, respectively, for an STaO sample grown by hMBE in the FINO lab at Auburn University. From the centroid images, it is clear that the film begins growing as expected in the perovskite phase; however, clusters 5, 6, and 7 show an additional 227 phase appearing like the one observed in Figure 3.2. This 227 phase is represented by the small faint spots between and above the primary spots perovskite RHEED spots. With traditional RHEED interpretation by a user, there is not a quantitative way to denote exactly when a second phase becomes observable, but since k-means clustering defines boundaries between clusters based on the principal components, it is possible to conclusively say that the secondary phase appears in cluster 5, at the ≈ 500 second mark and remains consistently starting at the ≈ 600 second mark. The 1^{st} and 4^{th} components in Figure 5.14 show dark spots consistent with the secondary phase pattern and the eigenvalues show similar responses during the second half of the growth. Components 4, 5, and

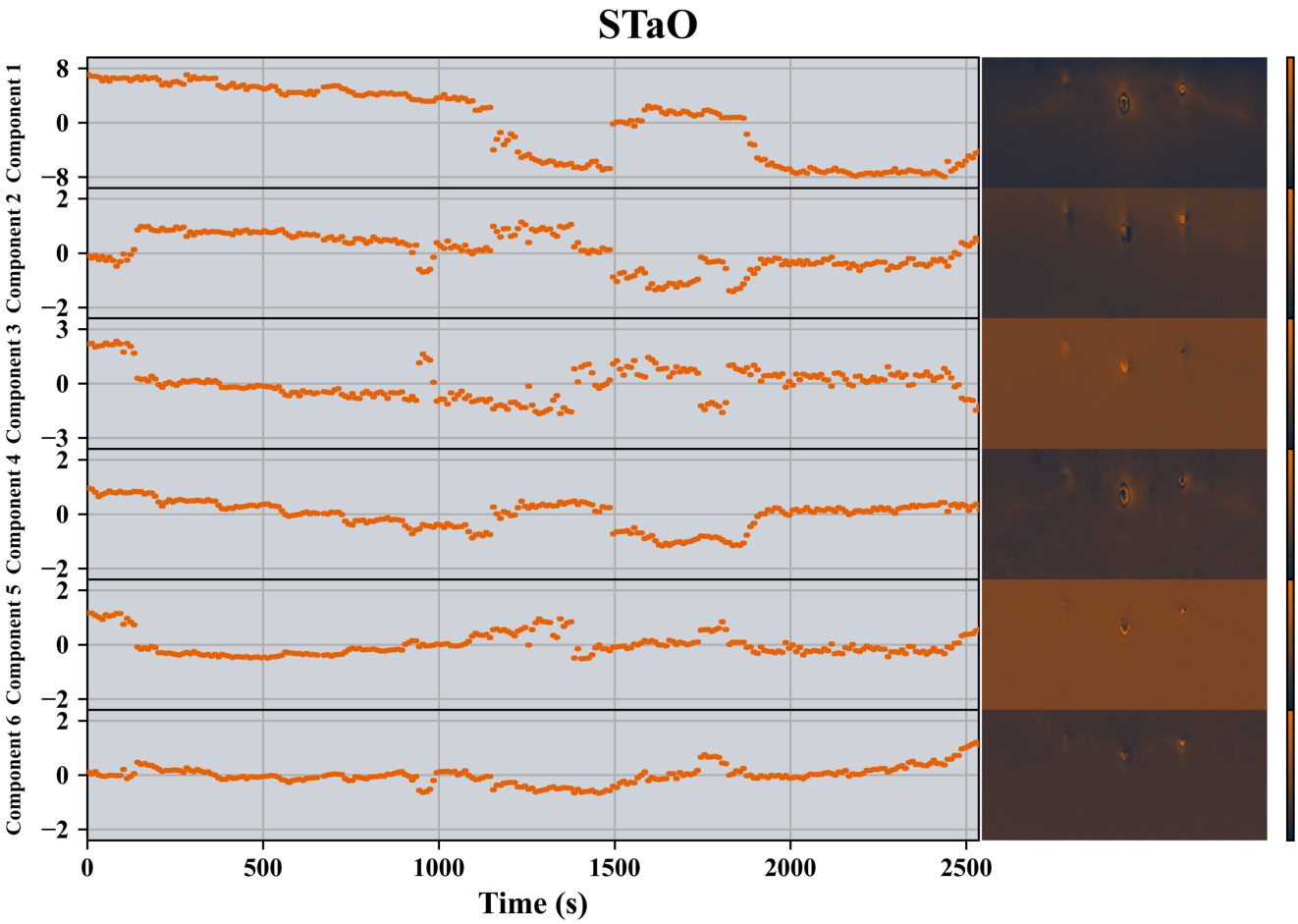

Figure 5.14: Results from the PCA of an STaO sample. (Left) The eigenvalues plotted over the course of the growth. (Right) The corresponding eigenvectors.

6 all show signs of oscillations or periodic behavior in the first 1200 seconds consistent with layer by layer growth. These oscillations are not observed strongly in the specular spot monitoring or the k-means clustering, since they are of smaller strength than the other components. Thus in this instance, looking directly at the eigenvalue evaluations provides the ability to extract a growth rate when normally it would not be possible.

5.3.5 $La_{1.84}Sr_{.16}CuO_4$

Figures 5.16 and 5.17 show the PCA and k-means clustering results, respectively, for an LSCO sample grown by MBE at the Max Planck Institute for Solid State Research. The clustering graph and eigenvalue plots have been overlaid with the shuttering times and

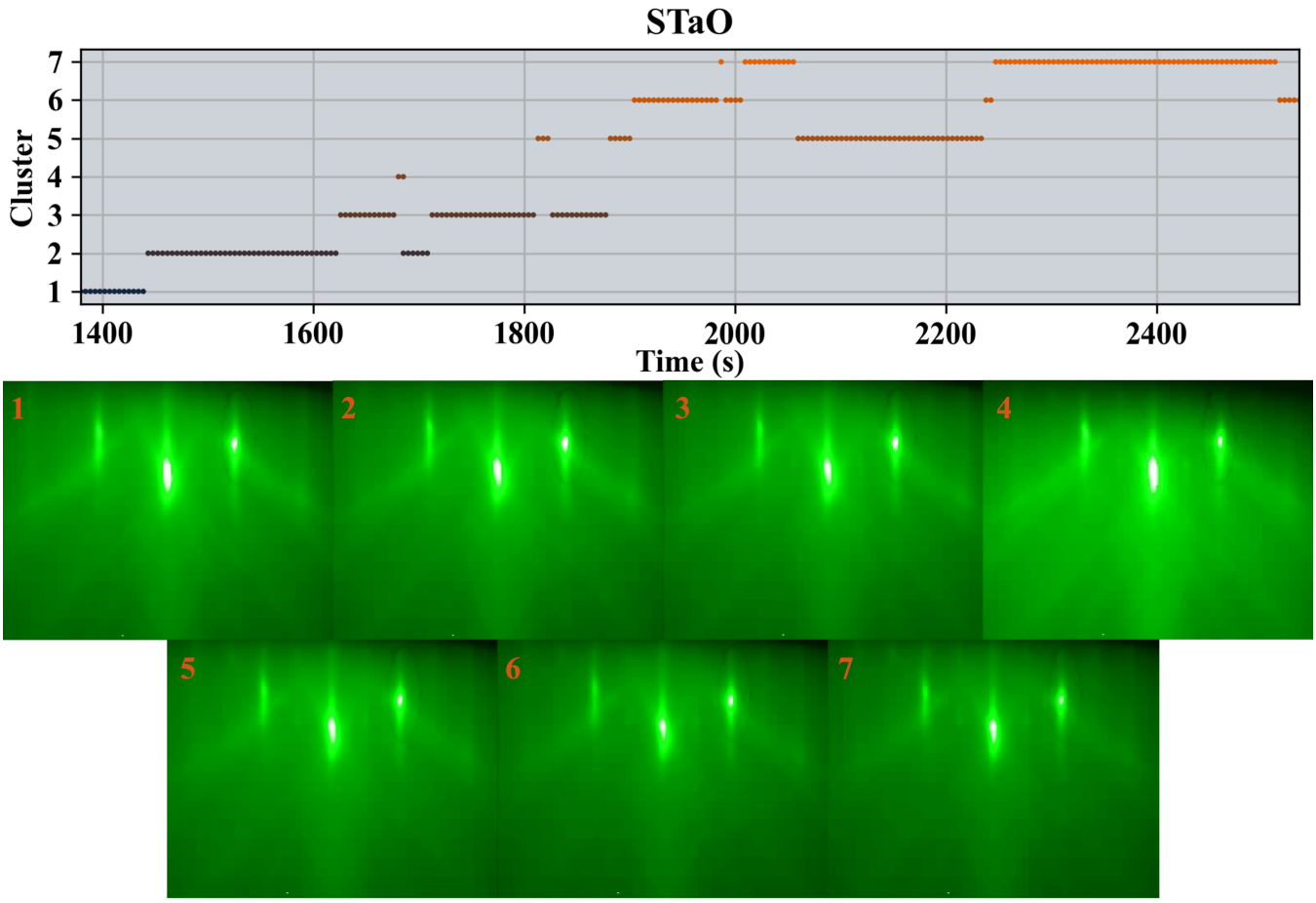

Figure 5.15: Results from the k-means of an STaO sample. (Top) A graph of the clusters over the course of the growth. (Bottom) The centroid images corresponding to the clusters in the graph.

oxygen environment to highlight the correlation between the cluster durations, eigenvalue changes, and the growth conditions. Components 4, 5, and 6 show strong responses to the change in oxygen environment at 170 seconds, while every component reflects a change when ozone is reintroduced at 300 seconds. All of the components also show a response when the Cu shutter is closed and the La & Sr shutters are opened at 40 seconds. In each of the centroid images, there are intermediate streaks resulting from surface reconstruction. Cluster 1 possesses a 5a reconstruction, which is the result of the Cu ordering in the CuO layer, while cluster 4 possess a 4a reconstruction, which is caused by ordering of oxygen vacancies on the surface [200]. The k-means clustering provides quantitatively significant boundaries for the different clusters, resulting in

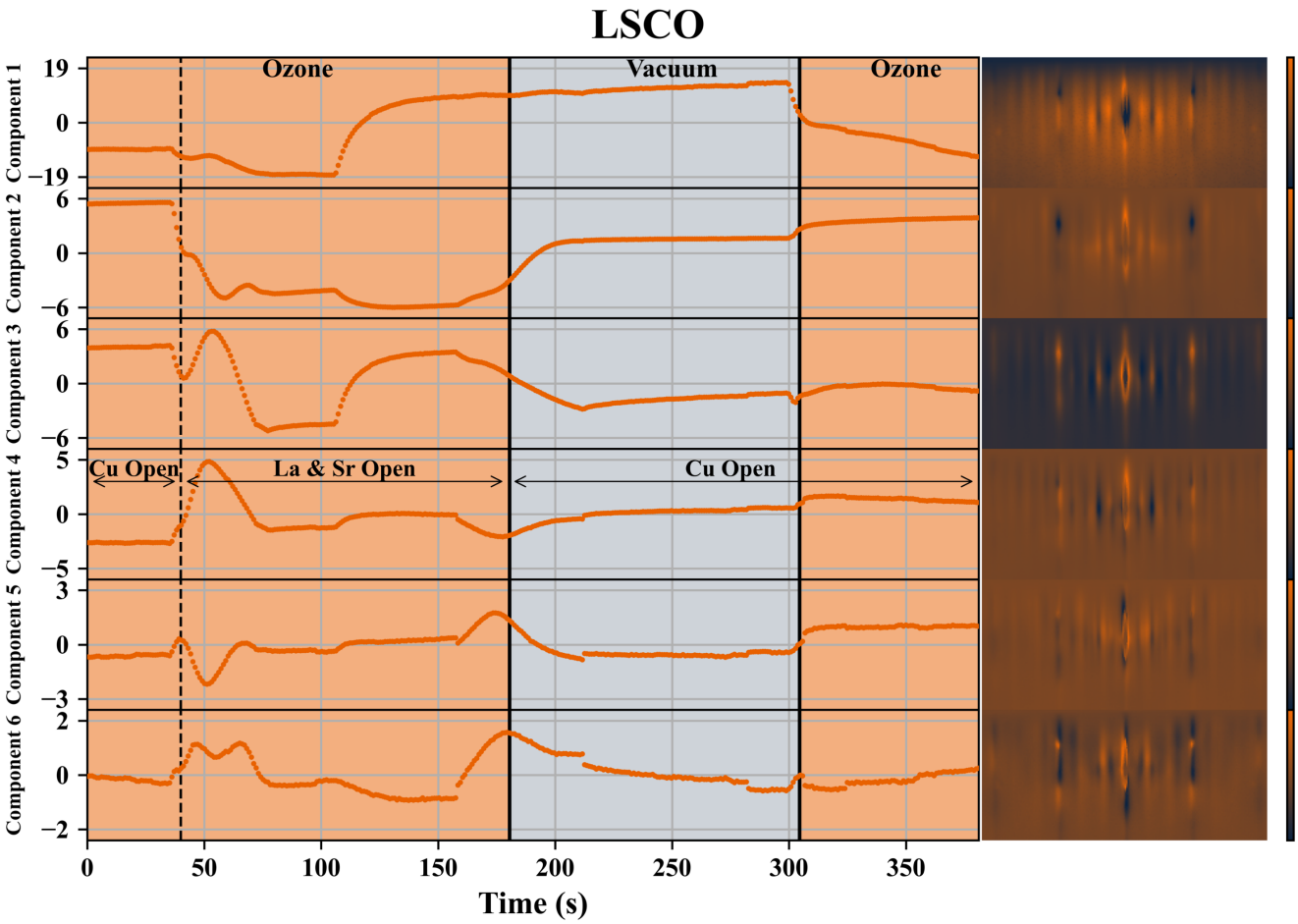

Figure 5.16: Results from the PCA of an LSCO sample. (Left) The eigenvalues plotted over the course of the growth overlaid with information on the oxygen environment and shuttering cycle. (Right) The corresponding eigenvectors.

centroid images that are strongly coupled to the shuttering times and allow for clear understanding of the surface morphology during each phase of growth.

5.4 Conclusion

Traditional RHEED analysis is primarily limited to specular spot intensity monitoring and qualitative analysis of the RHEED pattern. While this has served film growers well for decades, there is far more information contained in RHEED that can be teased out with the right tools. Here we have shown that PCA is able to construct a set of eigenvector and eigenvalue pairs that provide useful information about the evolution of the film. By analyzing the change in eigenvalues over the growth, new patterns, such

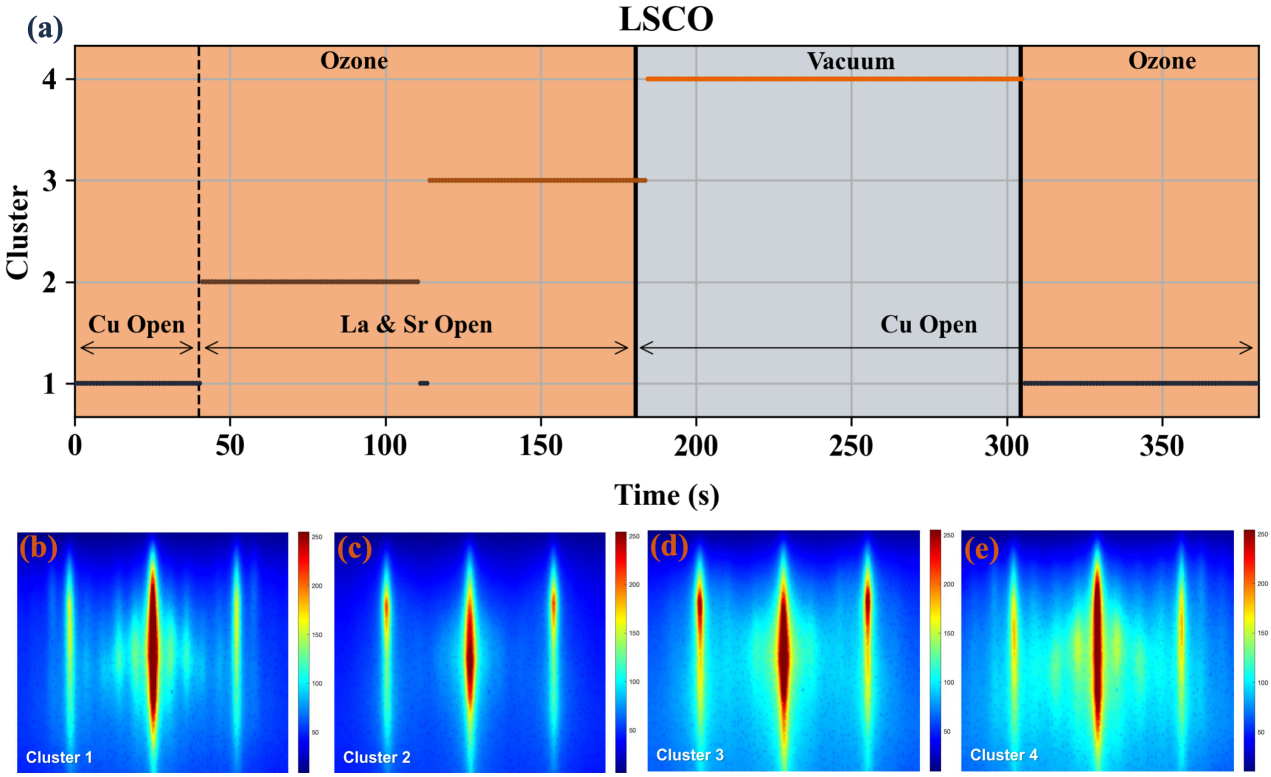

Figure 5.17: Results from the k-means of an LSCO sample. (Top) A graph of the clusters over the course of the growth. (Bottom) The centroid images corresponding to the clusters in the graph.

as weak spot oscillations, are observed that were previously too weak to recognize. k-means clustering is able to utilize the eigenvalues to create mathematically significant clusters that distinguish between segments of the growth. The centroid images that result from these clusters highlight the changes in the film and provide a film grower with clear timeline of the evolution of the film's surface.

Chapter 6

Epitaxial Strain Effects in $SrHfO_3$ Films Grown by Hybrid Molecular Beam Epitaxy

This chapter is adapted from my paper bearing the identical name. In this work, I was responsible for synthesizing the $SrHfO_3$ samples, collecting and analyzing the RHEED, XPS, XRD, and RSM data, analyzing the XAS data, and creating the Gaussian convolutions of the density of states. The remaining characterization techniques were conducted by Boris Kiefer of New Mexico State University (DFT), Chunli Tang & Wencan Jin of Auburn University (SHG), George Sterbinsky of Argonne National Laboratory (XAS), and Arashdeep Thind & Robert Klie of University of Illinois Chicago (STEM).S

6.1 Introduction

6.1.1 Interest in Perovskite Oxides

Complex metal perovskite oxides possess a wide range of electrical properties that have made them the focus of many works. They show promise as lead-free piezoelectrics, thermoelectrics, high κ gate dielectrics in MOSFETs, etc. Some of the interesting phenomena are found at interfaces such as 2DEGs at $LaAlO_3$ (LAO)/$SrTiO_3$ (STO) interfaces [4] and superconductivity at LAO/$KTaO_3$ interfaces [5]. Perovskite oxides, such as STO and $BaTiO_3$, possess ferroelectric phases and have been investigated as possible materials for ferroelectric field effect transistors (FeFET) and ferroelectric random access memory (FRAM) devices [6, 7]. Good FeFET gate oxide candidates need to be ferroelectric, possess large band gaps, and have high dielectric constants. This has made Hf-based materials such as HfO_2 intriguing, due to the unusually weak ferroelectricity observed in the material and the large band gap and dielectric constant that are well known [201]. A hafnate material with a larger ferroelectric response would be noteworthy and has generated interest in the study of hafnate perovskite thin films.

6.1.2 Material Properties and P4mm Phase

$SrHfO_3$ (SHO) is a perovskite oxide, similar to STO, where corner-connected HfO_6 octahedra form the building blocks of the three-dimensional framework. The cuboctahedral cavities thus formed by these corner-connected HfO_6 octahedra are filled by Sr cations. SHO exhibits polymorphism and has various energetically competing phases. These phases correspond to space-group symmetries of Pnma, I4/mcm, P4/mbm, P4mm, $Pm\bar{3}m$, where Pnma is the ground state structure. SHO is a large band gap (6.1 eV) [202] perovskite oxide that is orthorhombic (Pmna) [203] in the bulk with a pseudocubic lattice constant of 4.08 Å [202]. Temperature-dependent studies have found that SHO can also take on Cmcm, I4/mcm, and $Pm\bar{3}m$ phases at higher temperatures [203]. Due to its high band gap and high dielectric constant (21) [204], SHO has been investigated as a high-κ gate dielectric for MOSFETs [24, 62]. It has also been considered as a possible lead-free piezoelectric material [205, 206].

Unlike other phases of SHO P4mm is non-centrosymmetric, which results primarily from the off-centering of Hf atoms with respect to the center of the HfO_6 octahedra. There have been several theoretical works about the possible existence of this polar P4mm phase, with several predicting it does not exist [207, 208] , while others predicting its stability [205]. If synthesized, these works predict the P4mm phase to be ferroelectric [207], with a spontaneous polarization of 0.52 C/m^2 along the c axis [205]. In the last few years, there have been attempts to synthesize this P4mm phase with pulsed laser deposition [206, 209]. One study reported the successful synthesis of $\sim$35 nm thick P4mm SHO films on $SrTiO_3$ (STO) substrates using PLD and found evidence of ferroelectric behavior [206]. However, another study synthesized SHO thin films on STO by PLD and found them to be cubic $Pm\bar{3}m$ and paraelectric [209]. Most previous reports have utilized PLD or ALD to synthesize SHO thin films; however, neither of these works nor those that utilize MBE were able to achieve coherently strained SHO films on STO, where the lattice mismatch is $\sim$-3%.

A key structural characteristic of a perovskite framework is for the BO_6 octahedra to undergo cooperative rotations or tilts. These octahedral tilts are denoted by Glazer's notation [210, 211]. Using Glazer's notation, an octahedral tilt pattern can be described as $a^x b^y c^z$, where a, b, and c correspond to the magnitude of the octahedral tilts along those respective crystallographic directions for a pseudocubic unit cell. If the magnitude of the octahedral tilts along two crystallographic directions is equal, then those tilts are denoted by the same symbol. The superscript (x, y, and z) denotes the type of octahedral tilts, where (+) denotes in-phases octahedral tilts for the top and bottom neighboring octahedra, while (-) denotes out-of-phase octahedral tilts. The absence of octahedral tilts along a specific crystallographic direction is denoted by (0). The Pnma phase of SHO has an octahedral tilt pattern of $a^+b^-b^-$, which is the same for the GSO and TSO substrates as well. The tetragonal phases I4/mcm and P4/mbm have tilt patterns of $a^0a^0c^-$and $a^0a^0c^+$, respectively. The P4mm and the cubic $Pm\bar{3}m$ phases do not exhibit octahedral tilts ($a^0a^0a^0$).

6.1.3 SHO as a Capping Layer

In addition to the possibility of possessing a ferroelectric phase, SHO also shows promise as a capping layer for perovskite oxides. Many perovskite oxides are unstable in the atmosphere or meta-stable for short periods of time, with exposure causing oxidation of the samples and sample degradation [37]. This problem can be eliminated by adding a capping layer that buries the interfaces; however, this usually involves careful selection of a material based on its electronic and magnetic properties so that it will not affect the samples of interest [212, 213]. Density functional theory calculations for SHO have predicted that SHO's insulating behavior will prevent it from accepting donor electrons from any other transition metal perovskite oxide [214]. This makes SHO an excellent candidate for capping atmospherically unstable and meta-stable perovskite oxides, as they would preserve the structure of the films while not changing the electrical properties of the films and interfaces. Theory also predicts that charge transfer through thin

layers of SHO would still be possible, allowing for modulation doping of samples and the formation of 2DEGs at heterostructure interfaces [214].

6.1.4 hMBE

The primary reason epitaxial SHO has not been synthesized much using MBE is likely due to the refractory nature of Hf. Refractory metals, such as Hf and Nb, have low vapor pressures even at temperatures approaching 2000°C. Thus, it is not practical to evaporate these elements in an effusion cell and an electron-beam evaporation source is needed instead. However, over the past few years, hMBE has made significant progress in repeatably and reliably utilizing such refractory metals to synthesize perovskite oxides [37, 108, 110, 215]. hMBE achieves this by utilizing metal organic precursors commonly employed in ALD as source material rather than pure metallic sources. Others have proposed the use of oxide sources in effusion cells that may evaporate as suboxide metal-oxide molecules and have proposed HfO as one possible source [216], but this has not yet been demonstrated and would still require evaporation from sources above 2000°C. Thus, metalorganic precursors high vapor pressures at considerably lower temperatures offer the most promising avenue for consistent and well controlled deposition of Hf by MBE. Several Hf precursors are commercially available, but Tetrakis(ethylmethylamino)hafnium(IV) [217] was chosen in this work due to it's high vapor pressure, common use in atomic layer deposition, and thermal stability.

6.1.5 This Work

In this work, thin film samples of SHO were grown on STO, $TbScO_3$ (TSO), and $GdScO_3$ (GSO) using hMBE. In situ RHEED was used to monitor the film surface during the growth process and *in vacuo* XPS [218] was used to investigate film composition and stoichiometry. HRXRD and RSM maps were used to determine film relaxation, while STEM was used to determine the film's atomic structure. Total energy calculations using DFT were carried out over a wide range of compressive strain to

determine the thermodynamic stability of various phases of SHO. The electronic structure of the film and its dependence on the compressive strain was measured using XAS and compared with the electronic density of states calculations. The presence of polar distortions was investigated using SHG.

6.2 First-principles Modeling

To predict phase-stability as a function of epitaxial strain, the thermodynamic ground state for 5 phases of SHO with with differing octahedral distortions was calculated using density functional theory (DFT). The computations were performed with the Vienna ab-initio Simulation Package [219, 220] accounting for electronic exchange and correlations within the Perdew–Burke-Ernzerhof (PBE) parametrization of the Generalized-Gradient-Approximation (GGA) [221]. Electrons are treated within the projector augmented-wave framework (PAW) [222, 223]. We followed Material Project recommendations, and adopted a plane wave energy cutoff of E_{cut} = 520 eV [3] and a Γ-centered k-point grid with a k-spacing of 0.3 $Å^{-1}$. We examined the phases: Pnma, I4/mcm, P4/mbm, $Pm\bar{3}m$, and P4mm. The equilibrium structures were subjected to in-plane strain ranging from -5% to +5% in steps of 0.5% for each phase. The out-of-plane lattice parameter was calculated using the equation $\epsilon_{33} = \frac{-\nu}{1-\nu}(\epsilon_{11} + \epsilon_{22})$. The value of Poisson's ratio (ν) of 0.3 for SHO was determined using lattice parameters obtained from XRD measurements of the samples described below. This value is consistent with the computed Poisson ratio of 0.25 for the $Pm\bar{3}m$ phase. In order to determine the e_g and t_{2g} ordering, we computed the electronic density of states with energy bins of < 15 meV. The site projected eDOS d-orbital angular momentum channels in the d-orbital manifold were computed and normalized to arbitrary units (for phases with more than 1 Hf per u.c.), providing phase resolved t_{2g} (d_{xy}, d_{xz}, and d_{yz}) and e_g (d_{z^2} and $d_{x^2-y^2}$) ordering.

Figure 6.1 shows the crystal structure and electronic density of states for the Pnma, P4mm, and I4/mcm phase of SHO with -3% compressive in plane strain. For P4mm

we find a small lattice distortion of c/a=1.002, and that Hf is located above the equatorial plane of the HfO_6 octahedron by 0.08 Å, consistent with a ferroelectric phase. However we find that the P4mm phase is not the ground state. The energies for each phase as a function of in-plane strain are plotted in Figure 6.2. The strain was calculated using $f = \frac{a_{substrate} - a_{film}}{a_{film}}$, where the pseudo cubic lattice constant and bulk lattice constant were used for the substrate and film respectively. From this figure we see that Pnma structured SHO is the thermodynamic ground state, consistent with previous computations [206] and experiment [203]. Pnma remains the structural ground state for compressive and tensile strain in the range from -5% to +5%, covering the range of feasible strain values and experimental values. We find that phase stability decreases in the order Pnma (0 eV/fu) $<$ I4/mcm (30 meV/fu) $<$ P4/mbm (62 meV/fu) $<$ P4mm (160 meV/fu) $\sim$ Pm$\bar{3}$m (160 meV/fu) at 0% strain, consistent with previous work [206]. We note, that the P4mm and Pm$\bar{3}$m equilibrium structures are energetically degenerate but structurally distinct. At -3% compressive strain we find that phase stability decreases in the order Pnma (127 meV/fu) $<$ I4/mcm (158 meV/fu) $<$ P4/mbm (189 meV/fu) $<$ P4mm (303 meV/fu) $\sim$ Pm$\bar{3}$m (340 meV/fu).

6.3 Experimental Methods

6.3.1 Hybrid MBE

SHO films were grown in a (001) orientation on (110) oriented GSO and TSO with pseudocubic lattice parameters of 3.96 Å and 3.95 Å, respectively and on STO with lattice parameter 3.905 Å. Substrates were obtained from MTI Crystal and sonicated in acetone and then isopropanol before being dried with nitrogen. GSO and TSO substrates were annealed for 6 hours at 1,100°C in a Lindberg Blue M tube furnace from Thermo Scientific. A Park Systems Atomic Force Microscope (AFM) was used to confirm this treatment resulted in a single termination with step edges $\sim$200 nm in width. All samples were grown in a Mantis MBE. The substrates were heated to 1,000°C over

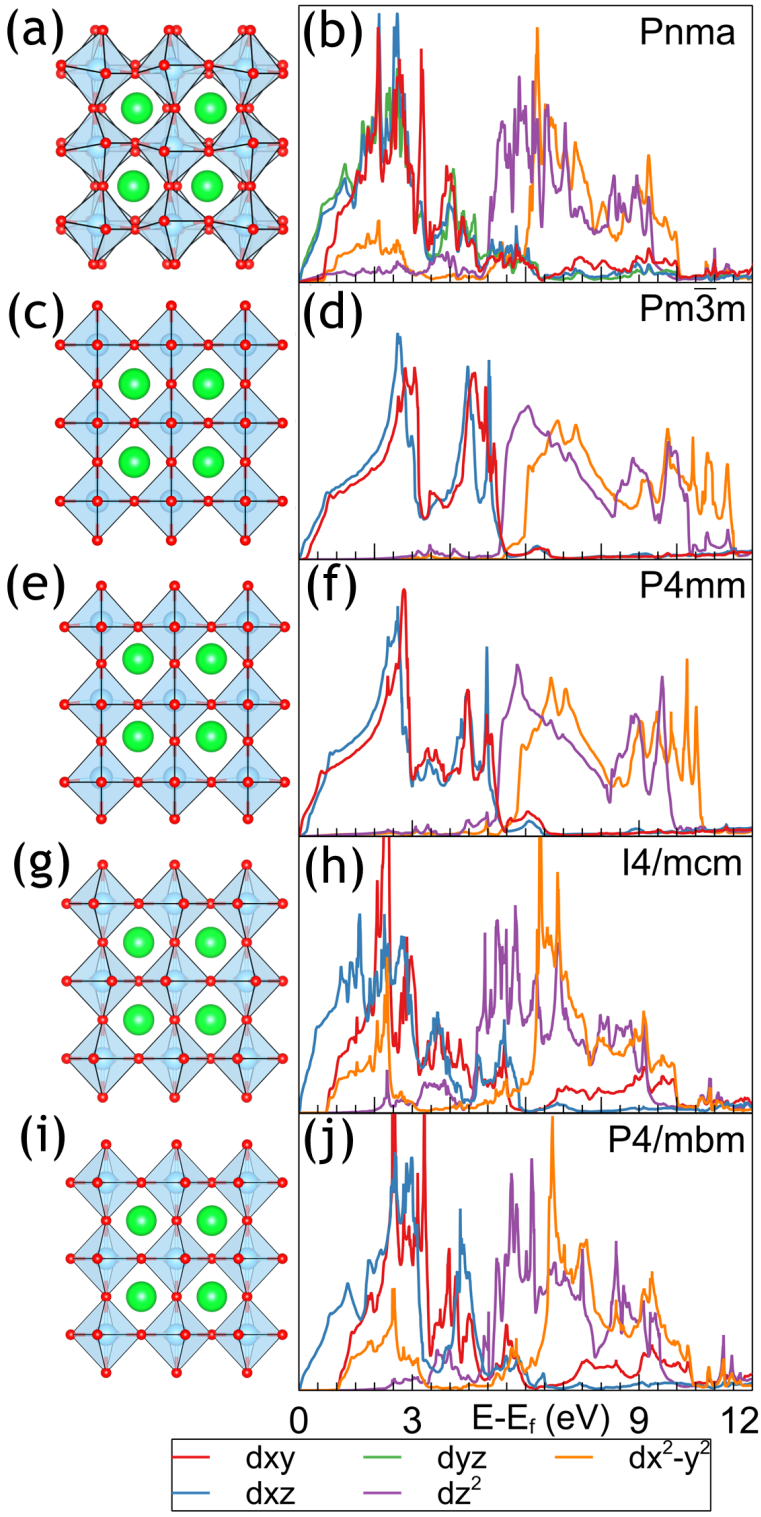

Figure 6.1: (a), (c), (e), (g), & (i) Show the crystal structure of SHO for -3% in-plane strain for the Pnma, Pm$\bar{3}$m, P4mm, I4/mcm, & P4/mbm, respectively. (b), (d), (f), (h), & (j) Show the eDOS results of our DFT results for the Pnma, Pm$\bar{3}$m, P4mm, I4/mcm, & P4/mbm, respectively. The d_{xz} and d_{yz} states are degenerate for all phases but Pnma.

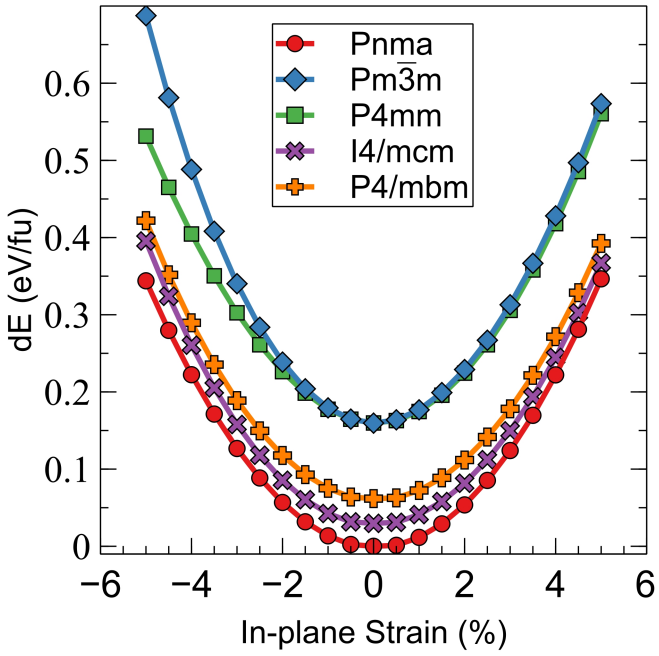

Figure 6.2: Plot of the change in energy from the ground state for the different SHO phases as a function of in-plane strain.

1hr in an oxygen plasma with pressure 2 x 10^{-6} Torr to prevent the surface of the substrate from reducing before growth.

Strontium (99.99%, Sigma-Aldrich, USA) was supplied using a low-temperature effusion cell and the flux was calibrated with a quartz crystal micro-balance (QCM). An oxygen environment of 2 x 10^{-6} Torr was used for calibration. Hf was supplied using the metal-organic precursor tetrakis(ethylmethylamino)hafnium (TEMAH, 99.99%, Sigma-Aldrich). TEMAH was stored in a bubbler and connected to the chamber by an ALD pneumatic valve (Swagelok 316L) and a heated gas injector (E-Science, USA). A capacitance manometer (Baratron) was attached to the gas line to monitor the Hf partial pressure. The temperature of the bubbler was maintained by a heating tape controlled by a PID controller. Hf was calibrated by changing the bubbler temperature and observing the change in partial pressure. In order to reduce scattering of TEMAH and its constituent molecules during growth, the chamber shroud was cooled to -60°C using an SP Scientific RC210 pump and Syltherm XLT as coolant.

Samples were grown using co-deposition of Sr and Hf at 1,000°C in an oxygen plasma with chamber pressure 2 x 10^{-6} Torr. Upon opening the Hf source, the chamber pressure increases to 7 x 10^{-6} Torr and remains there for the duration of growth. After deposition, the samples were cooled from 1,000 to 400°C over 400 seconds in an oxygen plasma of 2 x 10^{-6} Torr. Once the samples reached 200°C, they were transferred *in vacuo* to the XPS.

During growth and cool down, *in situ* RHEED (Staib Instruments) was used to monitor the sample surface and growth quality. Videos of the RHEED were collected using Flashback Express Recorder. After the growth, principal component analysis and k-means clustering were performed on the RHEED using software previously developed by our group [79].

6.3.2 Characterization

XPS spectra were collected for each sample using a PHI 5400 XPS with a base pressure of 8 x 10^{-10} Torr. Low resolution spectra were taken over from 0 to 1400 Binding Energy(eV) with a pass energy of 178.95 eV and high resolution spectra were take over core level peaks with pass energies of 35.75 eV. The ratio of cations can be determined through XPS by comparing the areas under the fit curves and adjusting by the ratio of the relative sensitivity factors (RSF). In this way, the stoichiometry of each film was determined. The x-rays were generated by an Al-kα source and an electron flood gun was used during data collection to prevent electron depletion since the film is not conducting. XPS spectra analysis and curve fitting was done using Casa XPS.

A Rigaku Smartlab XRD with a four-circle goniometer was used to collect 2θ-ω scans over the (002) peak of each sample. This system utilizes the Cu Kα1 line isolated with a double bounce Ge (220) monochromator. Reciprocal space maps were captured using a 2D detector and were used to determine film strain.

Hafnium L_3-edge X-ray absorption spectroscopy was carried out at beamline 20-BM of the Advanced Photon Source at Argonne National Laboratory. The incident

x-ray energy was controlled by a Si(111) double crystal monochromator, and the x-ray beam was focused by a Pt/alumina bilayer coated toroidal mirror. The Hf $L\alpha$ partial fluorescence yield was collected using a seven element Ge solid state detector. All samples were spun about an axis normal to the film surface during measurement to mitigate Bragg peaks. Angles of incidence were maintained under ten degrees, and the x-ray polarization was oriented either in-plane or out-of-plane.

Rotational anisotropy second harmonic generation measurements were performed using an ultrafast light source with 800 nm wavelength, 50 fs pulse duration, and 200 kHz repetition rate. In the normal incidence geometry, the incident and reflected light were fixed as p or s polarization, and the reflected SHG intensity is recorded as a function of the azimuthal angle ϕ between the scattering plane (electric polarization) and the in-plane crystalline axis. The incident light was focused onto a 50 μm diameter spot on the sample with a fluence of $\sim$0.25 mJ/cm^2. The second harmonic signal is collected by a single photon counting EMCCD camera.

6.3.3 Electron Microscopy

The cross-section lift-out samples of $SrHfO_3$/$TbScO_3$ (SHO-TSO) and $SrHfO_3$/$GdScO_3$ (SHO-GSO) films were prepared using a Thermo Fischer Scientific Helios 5 CX focused-ion beam (FIB)/ scanning electron microscope (SEM) DualBeam system at University of Illinois Chicago. Samples were prepared such that the SHO-TSO sample would have a zone axis of [010] for the orthorhombic TSO substrate, while the SHO-GSO sample had a $[10\bar{1}]$ zone axis for the GSO substrate. This allowed for the observation of cation sublattice and octahedral tilts along both axes to determine the space group of the SHO films under strain. The SHO-TSO and SHO-GSO thin films were sputter-coated with a 10 nm thick layer of Pt/Pd to avoid charging during FIB lamellae preparation. To protect against the ion-beam induced surface damage to the SHO films, a protective coating of W was deposited. The final lamellae thinning was performed using a 1 kV

ion beam energy to minimize the amorphization of the lamellae cross-section and to obtain electron-transparent samples.

Scanning transmission electron microscopy (STEM) experiments were carried out at University of Illinois Chicago using an aberration-corrected JEOL JEM-ARM200CF microscope. The microscope is equipped with a cold-field emission gun and a CEOS aberration corrector, and was operated at 200 kV. The electron energy loss spectroscopy (EELS) experiments were performed using a dual-range Gatan Continuum spectrometer. A spectrometer entrance aperture of 5 mm was used, resulting in a collection semi-angle of 53.4 mrad. A dispersion of 0.75 eV per channel was used to acquire the core-loss edges in the low-loss (Sc L and O K) and high-loss (Tb M, Gd M, Hf M, and Sr L) energy range with an acquisition time of 0.25 seconds per spectrum. The background signal before core-loss edges was modeled using a power law. To improve EELS signal quality, principal component analysis (PCA) was performed to remove random noise components. An Oxford X-Max 100TLE windowless silicon drift detector was used to perform energy-dispersive X-ray spectroscopy (EDS).

A probe convergence semi-angle of 30 mrad was used to perform atomic-resolution high-angle annular dark-field (HAADF), low-angle annular dark-field (LAADF) and annular bright-field (ABF) imaging. The collection angles used for HAADF, LAADF and ABF imaging were set to 90 mrad to 370 mrad, 40 mrad to 160 mrad, and 11 mrad to 23 mrad, respectively. The atomic-resolution images were acquired sequentially (10-15 frames). The images were subsequently aligned and integrated to improve signal-to-noise ratio. For bond-distance analysis, the atomic positions in the HAADF images were initially estimated using relative intensity. Subsequently, these atomic positions were refined using 2D Gaussian fitting.

Four-dimensional scanning transmission electron microscopy (4D-STEM) experiments were carried out using a Gatan ClearView CMOS detector. The microscope was operated at 200 kV with a probe convergence semi-angle of 2 mrad. The 4D-STEM datasets were acquired with a pixel size of 0.8 nm to 1 nm and the diffraction patterns

were collected using an exposure time of 50 ms to 75 ms. A combination of hardware and software binning was used to limit the size of each diffraction pattern to 256 × 256 pixels. The 4D-STEM data analysis was performed using the py4DSTEM python package [224].

6.4 Experimental Results

6.4.1 Film Synthesis and Characterization/ RHEED and k-means

6.4.1.1 RHEED

Figure 6.3(a) shows the high temperature RHEED image of SHO-TSO along the [110] azimuth immediately following the conclusion of growth, while Figure 6.3(b) shows the ambient temperature RHEED image. The bright spots and streaks with clear Kikuchi

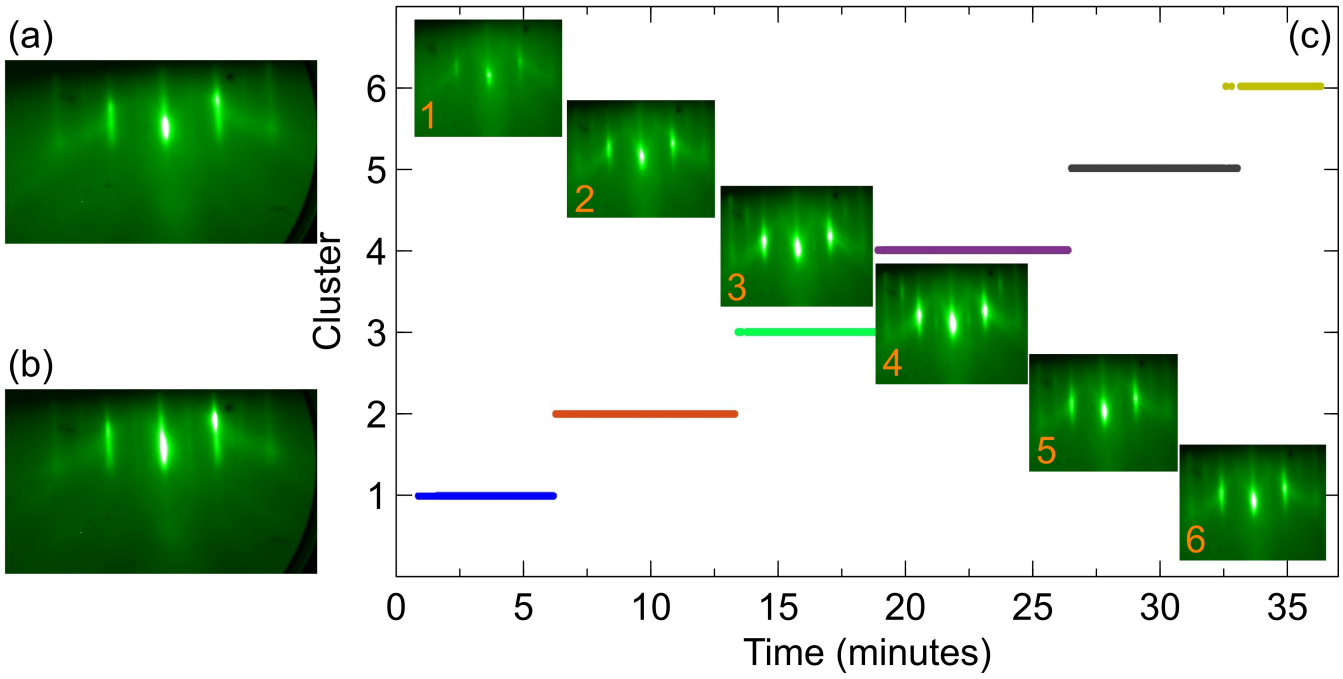

Figure 6.3: (a) RHEED image of SHO-TSO film after growth at 1000°C. (b) RHEED image of SHO-TSO film after growth at room temperature. (c) k-means clustering of SHO-TSO film. The mean RHEED image for each group is vertically aligned with the group and have the group number inlaid.

bands indicate a smooth and highly crystalline surface. The intermediate streaks indicate a weak surface reconstruction is present. From the k-means clustering in Figure 6.3(c), we can see how the surface evolves throughout the 37 minute long growth of SHO-TSO. Each cluster is constructed by minimizing the difference between each frame and the mean frame of the cluster. As a result, each frame in the cluster is most similar to the mean of that cluster than the mean of any other cluster. Cluster 1 encompasses the TSO RHEED pattern and shows a decrease in intensity and softening Kikuchi bands, which is may be attributed to the polar-non-polar interface and disorder in the early stages of growth. The intensity increases in clusters 2, 3, & 4, with 3 & 4 showing a weak surface reconstruction between the primary spots. This indicates the surface was improving and was highly crystalline and well ordered. The presence of Kikuchi bands in Figure 6.3(b) indicate the surface retains its fairly smooth and retains high crystallinity even after cooling down to ambient temperature.

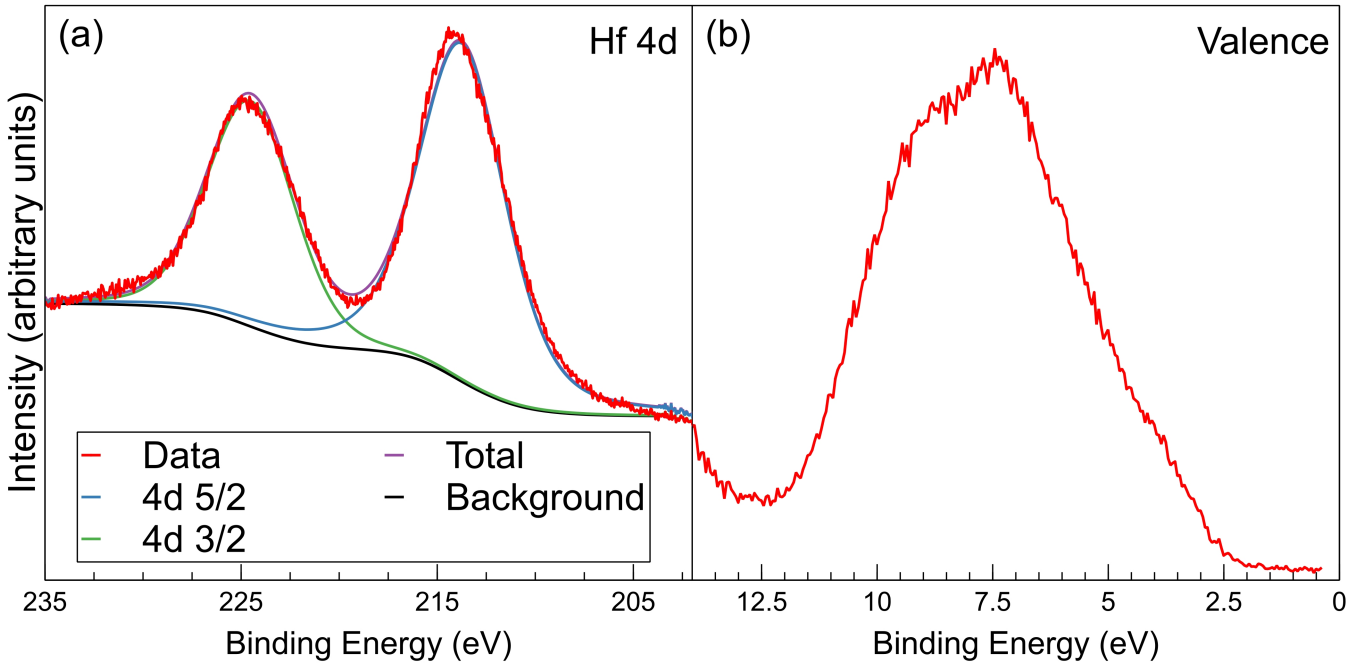

Figure 6.4: (a) XPS spectra of the Hf 4d peak from SHO-TSO film. (b) XPS spectra of the valence band of SHO-TSO film.

6.4.1.2 XPS

Figure 6.4(a) shows the Hf 4d peak convolutions for SHO-TSO and Figure 6.4(b) shows the valence band spectra collected at the same time. Peak fits for O 1s and Sr 3d can be found in the appendix. From the Hf 4d and Sr 3d peaks, the cation ratio of the SHO-TSO sample was calculated to be approximately 1:1, indicating the film is nearly stoichiometric. Since strontium has a significantly lower atomic mass than terbium, RBS would not provide accurate stoichiometry.

6.4.1.3 XRD

Figure 6.5(a) shows the HRXRD spectra of SHO films grown on TSO and GSO substrates. In both samples we observe a film peak at lower 2θ values than the TSO and GSO substrate peaks indicating the films have larger out of plane lattice constants. There are no peaks indicating other phases are present. Figure 6.5(b) shows the reciprocal space map for the 103 pseudo-cubic peak for the SHO-TSO film. The sharpness of the SHO film peak in the $Q_x/2\pi$ axis indicates the samples possess a very small

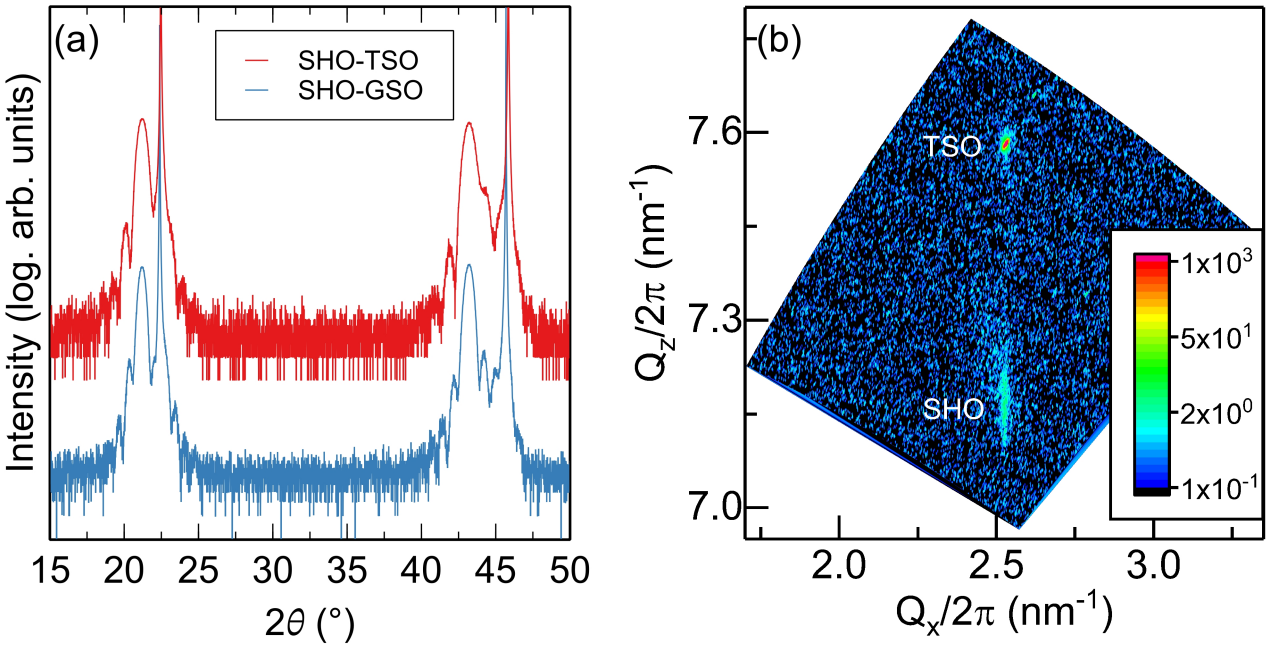

Figure 6.5: (a) HRXRD of SHO-TSO and SHO-GSO samples. (b) RSM of SHO-TSO film showing the SHO film is epitaxially strained with TSO.

range of in plane lattice constants. Since the SHO film spot and the TSO substrate spot are aligned at the same value on the $Q_x/2\pi$ axis, we know the film possesses the same in-plane lattice constant as the substrate and thus has a compressive strain of $\sim$-3%.

6.4.2 Characterization of Perovskite Phase

6.4.2.1 SHG

Figure 6.6 shows the results of SHG measurements for SHO-TSO and SHO-GSO samples. The results show no sign of a SHG response indicating that the SHO films are centrosymmetric. Of the 5 phases expected for SHO, only the P4mm phase is polar and non-centrosymmetric. Thus, this result is consistent with the Pnma, $Pm\bar{3}m$, I4/mcm, and P4/mbm phases of SHO and inconsistent with the emergence of a strain-stabilized P4mm phase. The lack of SHG response also supports the absence of a ferroelectric distortion in strained SHO predicted by previous works [205, 207].

The absence of a P4mm phase is consistent with the DFT modeling presented above which finds that there is a 160 meV/fu difference between the P4mm and ground state Pnma phases. The absence of a polar phase matches the results found by [209],

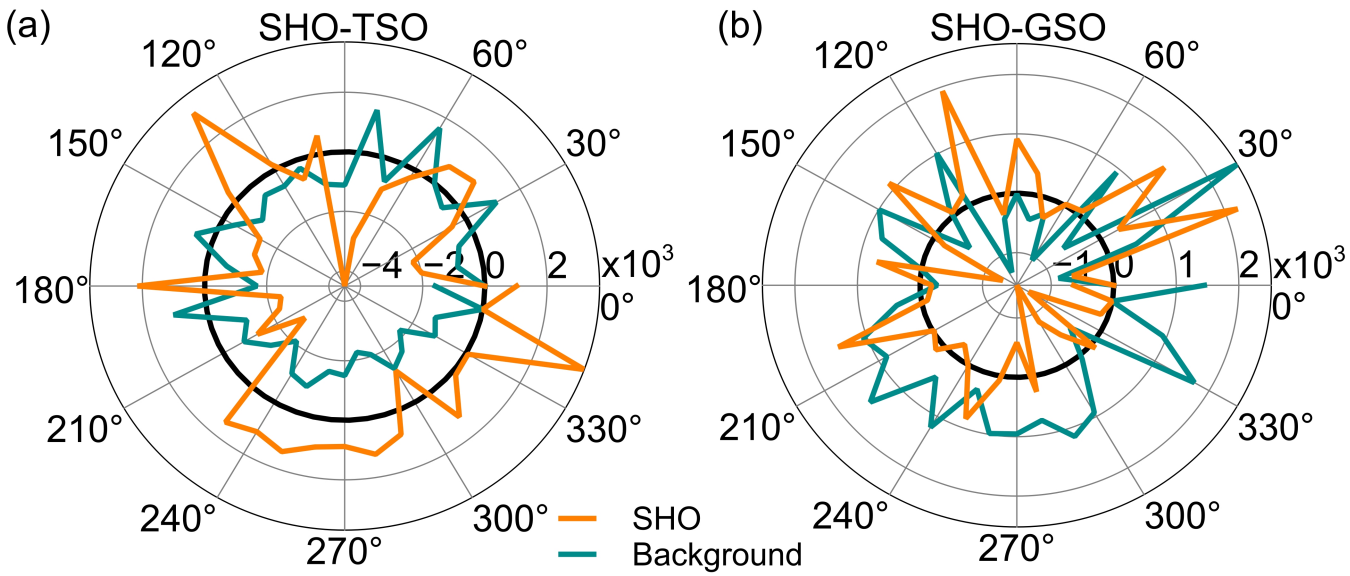

Figure 6.6: SHG measurements of SHO-TSO (a) and SHO-GSO(b). The lack of significant signal shows neither film is centrosymmetric.

which observed a $Pm\bar{3}m$ phase in SHO films grown on STO by PLD. However, other work [206] found that 35 nm thick SHO-STO films grown by PLD possessed a P4mm phase and observed a SHG response. The samples synthesized in these works shown by RSM appeared to be relaxed, as compared to the films presented here which are compressively strained to the GSO and TSO substrates.

6.4.2.2 XAS, DFT

Figure 6.7 (a) & (b) depict the Hf L_3-edge for an SHO-TSO film and SHO-GSO film respectively. These measurements were performed to probe splitting of the energy levels for unoccupied Hf $5d$ states under strain and to the best of our knowledge are the first reported spectra Hf L_3 spectra for perovskite hafnates. The absorption spectra show clear splitting of the t_{2g} and e_g levels in the absorption, which generally has not been observed in measurements of HfO_2 samples previously [225]. The X-ray linear dichroism (XLD)is calculated by XLD$= I_{ab} - I_c$. In both samples, the t_{2g} peaks are nearly degenerate between the in-plane and out-of-plane response, with the leading edge of the out-of-plane $\sim$100 meV. However, the samples exhibit a significantly larger splitting of $\sim$700 meV between the the in-plane and out-of-plane spectra at the e_g peaks.

As result of crystal field splitting, the Hf unoccupied $5d$-orbitals are broken into the t_{2g} and e_g bands where $d_{xz} = d_{yz} = d_{xy} < d_{z^2} = d_{x^2-y^2}$. As observed from the RSM and XRD, these samples are compressively strained from the substrate and possess increased c-lattice parameters as compared to the bulk. This causes at elastic response should induce additional crystal field splitting that breaks the degeneracy of the t_{2g} and e_g bands resulting in $d_{xz} = d_{yz} < d_{xy} < d_{z^2} < d_{x^2-y^2}$. This can be observed in the SHO samples by the presence of the weak dichroism in the leading edge and t_{2g} band peak and a more substantial dichroism at the e_g peak. This result is consistent with past study on BTO-$DyScO_3$ (DSO) films, which observed a splitting of $\approx$1 eV was observed in the e_g band peak, similar to the splitting observed here [146]. While the SHO films exhibit a slight dichroism in the t_{2g} band, the BTO-DSO films observed

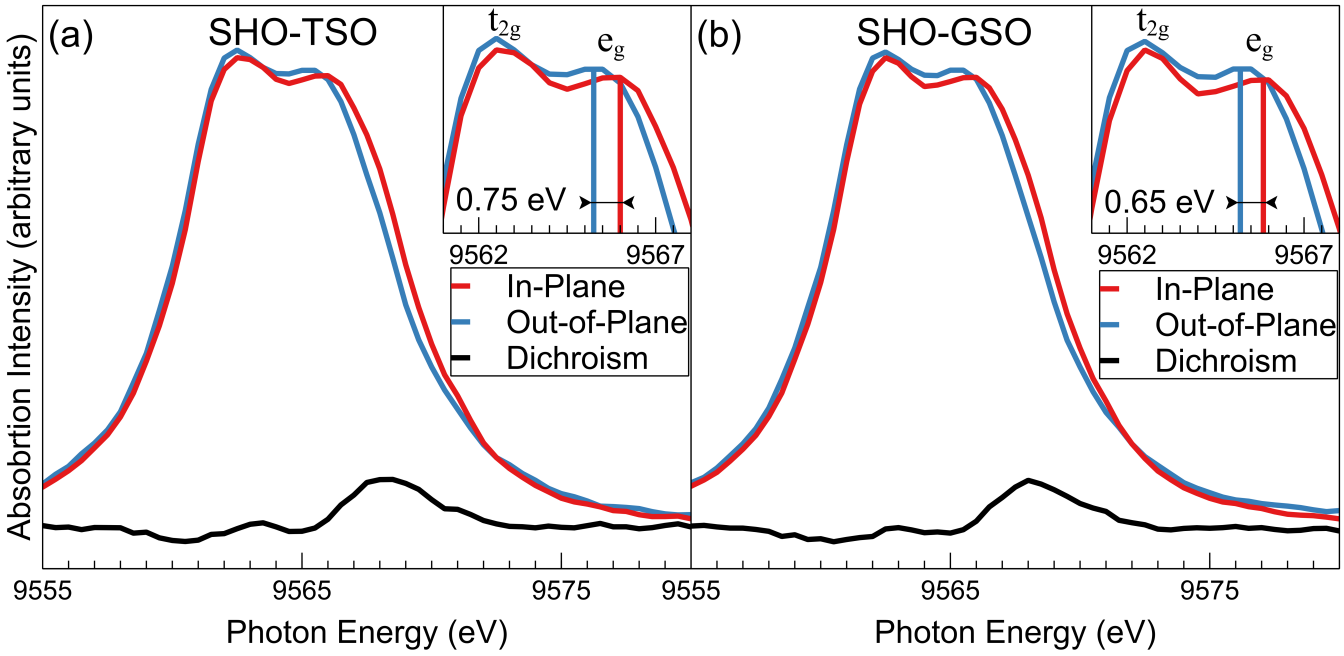

Figure 6.7: XAS data for SHO-TSO (a) and SHO-GSO (b). Insets show the splitting between in-plane and out-of-plane signal for the e_g band.

a triply degenerate t_{2g} band. This degeneracy in the t_{2g} was attributed to the presence of polar distortions, which offset the effect of the crystal field splitting in BTO.

To compare our results with theory, we applied a Gaussian convolution to the eDOS predicted by our DFT calculations to match the XAS instrumental resolution. The resulting convolutions for all 5 phases at -3% compressive strain can be found in the appendix, with the Pnma phase shown in Figure 6.8. As can bee seen in Figure A.A.9, all phases except the P4mm exhibit a dichroism on the L_3-edge. This dichroism is also exhibited by both SHO samples in Figure 6.7. This result is in agreement with the SHG measurements and effectively rule out the presence of the P4mm phase. As can be seen in Figure A.A.9, the $Pm\bar{3}m$ phase possesses an additional feature on the high energy side of the L-edge, not present in the other modeled phases or the SHO XANES spectra. In Figure 6.8 (b-c) the dichroisms and their derivatives for each phase possess similar features, with exception of the additional peak on the $Pm\bar{3}m$ phase at 10 eV. These features along with the significant decrease in phase stability predicted for by DFT, rule out the presence of the $Pm\bar{3}m$ phase. Determination of the stable octahedral

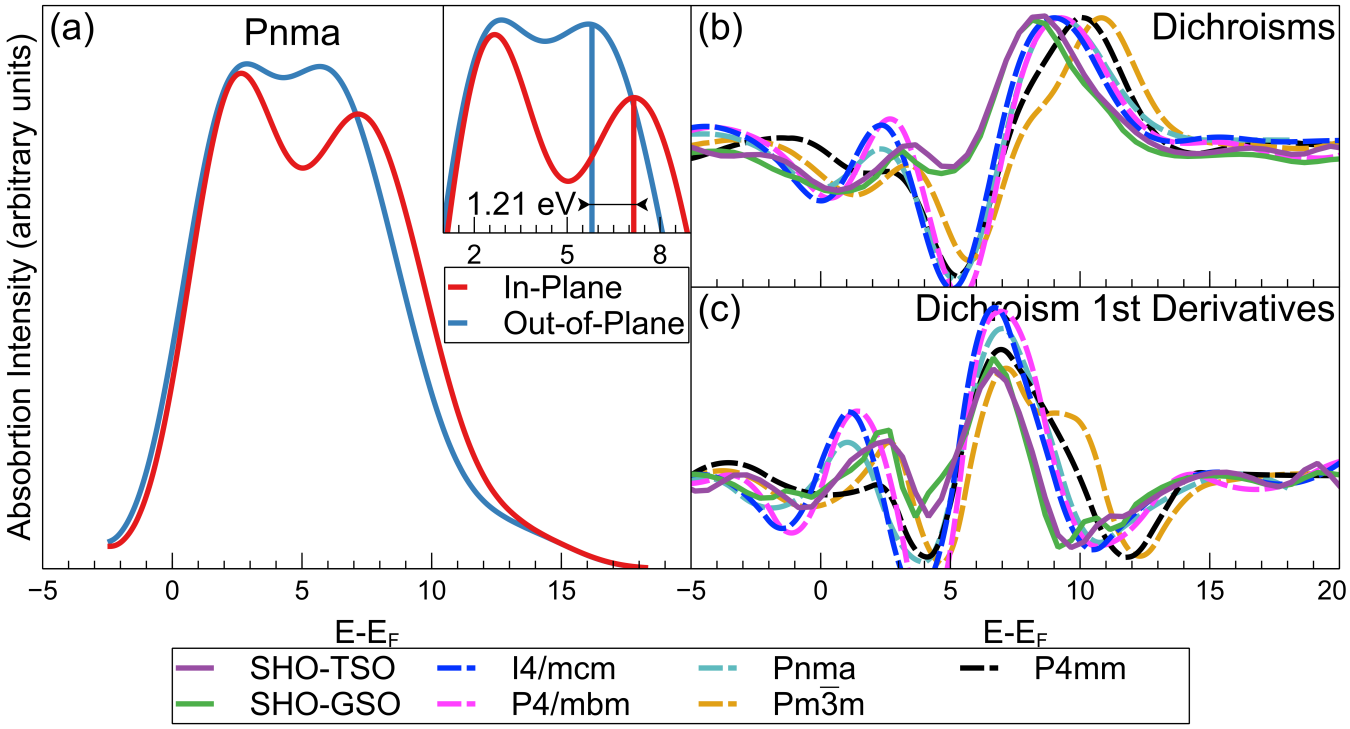

Figure 6.8: (a) The Gaussian convolution of the eDOS from DFT results for the Pnma phase of SHO. (b) & (c) The dichroism and it's derivative, respectively, for the XAS data of SHO-TSO, SHO-GSO, and the 5 phases of SHO modeled by DFT with -3% in-plane strain.

tilt pattern from XAS was not possible due to the very similar XLD predictions for the Pnma, I4/mcm, and P4/mbm phases.

6.4.2.3 STEM

To investigate the atomic and chemical structure of the SHO-TSO and SHO-GSO films along with the interfacial strain effects in the samples, we have performed STEM imaging experiments combined with EELS and EDS. Figure 6.9 shows the STEM-EELS results for the SHO-TSO and SHO-GSO films. Figure 6.9(a) and 6.9(d) show the atomic resolution HAADF images of the SHO-TSO[010] and SHO-GSO[10$\bar{1}$] films along with their respective crystallographic orientations. We have performed EELS experiments to understand the chemical distribution of elements across the cross-section of the SHO-TSO and SHO-GSO. The Sr *L*, Hf *M*, Tb *M*, Gd *M*, Sc *L*, and O *K* edge maps are shown in Figures 6.9(b) and 6.9(e) for the SHO-TSO and SHO-GSO thin film samples,

respectively. We observe the interface to be chemically diffused for both SHO-TSO and SHO-GSO samples. For instance, on comparing the EELS chemical maps for Tb *M* and Hf *M* edges (SHO-TSO) as well as Gd *M* and Hf *M* edges (SHO-GSO), we observe the interface is not chemically sharp but diffused. There is formation of a chemically intermixed layer, which is about ≈2-4 u.c. thick. To emphasize this point, the extracted EEL spectra for different regions of the film and substrate of the SHO-TSO and SHO-GSO samples are shown in Figures 6.9(c) and 6.9(f), respectively. We ascribe this chemical heterogeneity at the interface to non-uniform morphology and surface terminations of the TSO and GSO substrates. Moreover, we also observe the SHO-TSO and SHO-GSO interfaces to be oxygen deficient, as shown in O K edge maps in Figures 6.9(b) and 6.9(e), respectively. The impact of the chemical heterogeneities at the surface of TSO and GSO substrates on the atomic structure of the SHO films is discussed later in the manuscript. Additionally, the EDS chemical maps for Sr $K\alpha$, Hf $L\alpha$, Tb $L\alpha$, Gd $L\alpha$, Sc $K\alpha$, and O $K\alpha$ edges are shown in the supplementary information Figure A.A.14.

Our DFT calculations (see Figure 6.2) show that SHO has various energetically competing phases for a range of compressive strains. These phases correspond to Pnma, I4/mcm, P4/mbm, P4mm, $Pm\bar{3}m$, where Pnma is the calculated ground state for a wide range of compressive and tensile strain as shown in Figure 6.2. The atomic models of the SHO with in-plane compressive strain of 3% are shown in Figure A.A.1. Both TSO and GSO also adopt the same space-group symmetry of Pnma as the calculated ground state of SHO. The atomic models showing the TSO and GSO substrate orientations used for SHO film growth are shown in Figure A.A.2.

To understand the experimental epitaxial relationships between SHO-GSO/SHO-TSO, and evaluate the microstructure of the SHO film, we have performed 4D-STEM experiments. 4D-STEM provides a unique capability of elucidating the space-group symmetry of the sample in the reciprocal space with a sufficient real-space resolution to clearly distinguish between the film and the substrate. Figure 6.10 shows the 4D-STEM results for SHO-GSO[$10\bar{1}$] and SHO-TSO[010]. Figures 6.10(a) and 6.10(e)

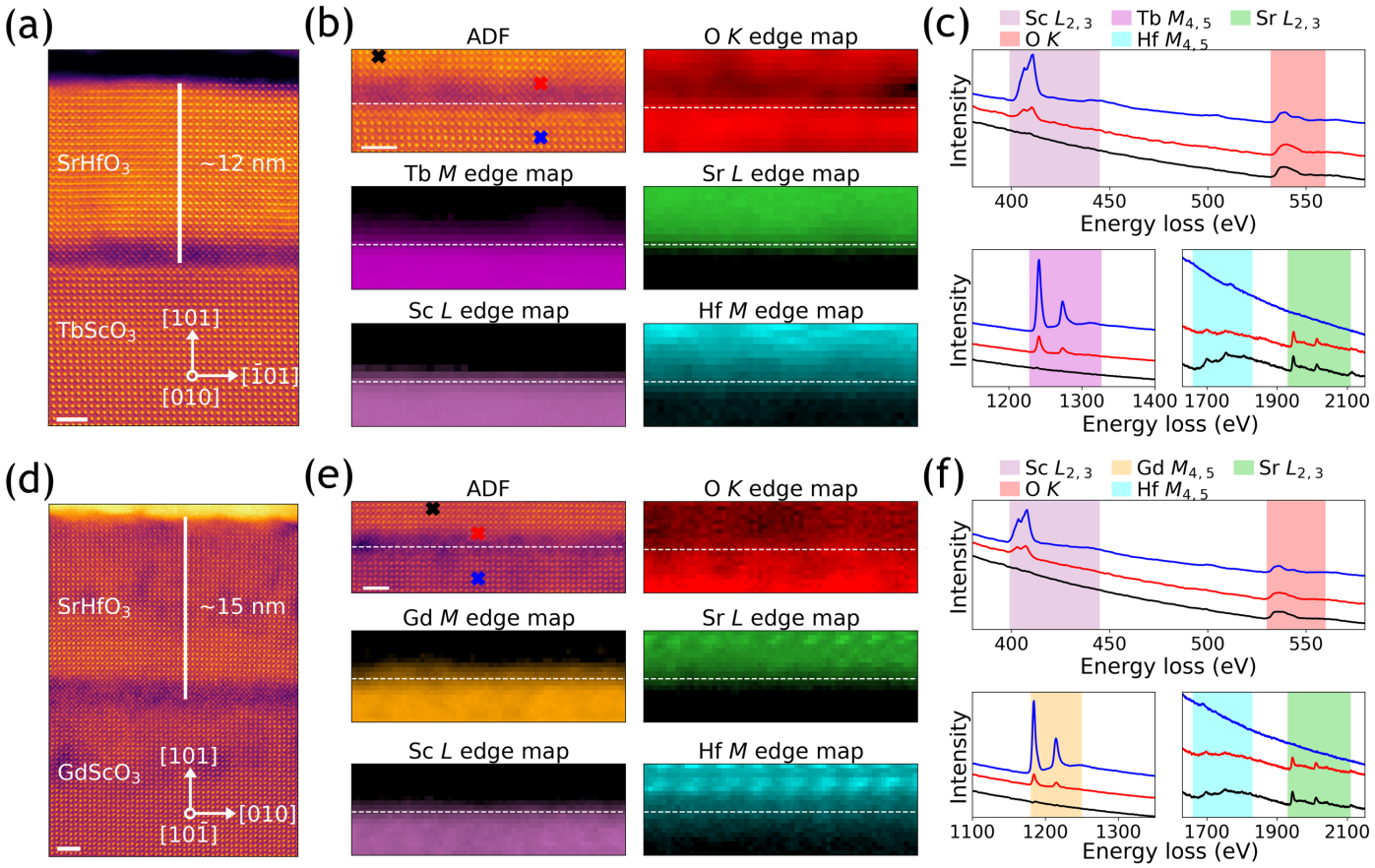

Figure 6.9: (a) Atomic resolution HAADF image showing the cross-section of the SHO-TSO film along [010]. (b) ADF image along with EELS chemical maps of Tb *M*, Sc *L*, O *K*, Sr *L*, and Hf *M* edges across the SHO-TSO interface showing the chemical distribution of elements. (c) Extracted EEL spectra for Tb *M*, Sc *L*, O *K*, Sr *L* and Hf *M* edges. The EEL spectra were extracted from the probe positions marked with the same color in the ADF image shown in (b). (d) Atomic resolution HAADF image showing the cross-section of the SHO-GSO film along [10$\bar{1}$]. (e) ADF image along with EELS chemical maps of Gd *M*, Sc *L*, O *K*, Sr *L*, and Hf *M* edges across the SHO-GSO interface showing the chemical distribution of elements. (f) Extracted EEL spectra for Gd *M*, Sc *L*, O *K*, Sr *L* and Hf *M* edges. The EEL spectra were extracted from the probe positions marked with the same color in the ADF image shown in (e). Scale bars in (a), (b), (d) and (e) correspond to 2 nm.

show the ADF images simultaneously acquired during the 4D-STEM dataset collection for SHO-GSO and SHO-TSO respectively. The extracted convergent-beam electron diffraction (CBED) patterns for the SHO film and GSO/TSO substrates are shown in Figures 6.10(b) and 6.10(f). Figures 6.10(c) and 6.10(g) show the simulated CBED patterns for the SHO-Pnma, SHO-I4mcm, SHO-P4mbm and GSO-Pnma/TSO-Pnma

phases, along the GSO[$10\bar{1}$] and TSO[010] respectively. By comparing the CBED patterns for the SHO film and the corresponding substrates (GSO and TSO), we can clearly see that the SHO film does not adopt the expected Pnma phase. For the SHO film, we find that the simulated CBED patterns for SHO-I4mcm and SHO-P4mbm show a good match with the experimental CBED patterns along both GSO[$10\bar{1}$] and TSO[010] crystallographic orientations. Moreover, simulated kinematical diffraction patterns for a parallel electron beam condition are shown in Figure A.A.16 for all potential SHO phases along with the GSO and TSO substrates.

The diffraction patterns for the P4mm phase are also within the measurement limits. However, based on the SHG data shown previously, we can rule out the presence of the non-centrosymmetric P4mm phase. Additionally, we also observe non-orthogonality in CBED patterns between the in-plane and out-of-plane Bragg vectors as well as some very weak reflections, which correspond to small domains with Pnma phase in the SHO films, which may be due to strain relaxation and other structural defects in the material. This phase impurity is also consistent with atomic-resolution imaging described later in Figure 6.11.

To better understand the microstructure and epitaxy of the SHO films, we have further calculated strain for the SHO film using 4D-STEM CMED data. The strain maps for SHO-GSO[10-1] and TSO [010] are shown in Figures 6.10(d) and 6.10(h) respectively. The green circles in Figures 6.10(b) and 6.10(f) mark the Bragg disks selected for in-plane and out-of-plane strain calculation. Given that SHO has a larger unit cell volume than the GSO and TSO substrates, and the films are grown under a compressive in-plane strain, $\approx$-3%, we expect a high out-of-plane tensile strain. This can be clearly observed in the out-of-plane strain maps for SHO-GSO and SHO-TSO as shown in Figures 6.10(d) and 6.10(h). The strain maps show non-uniform strain for the in-plane lattice directions for both SHO-GSO and SHO-TSO samples. For a perfect epitaxy, the strain along the in-plane direction should be minimal. However, we find that for both samples, there are regions that correspond to good epitaxy, but

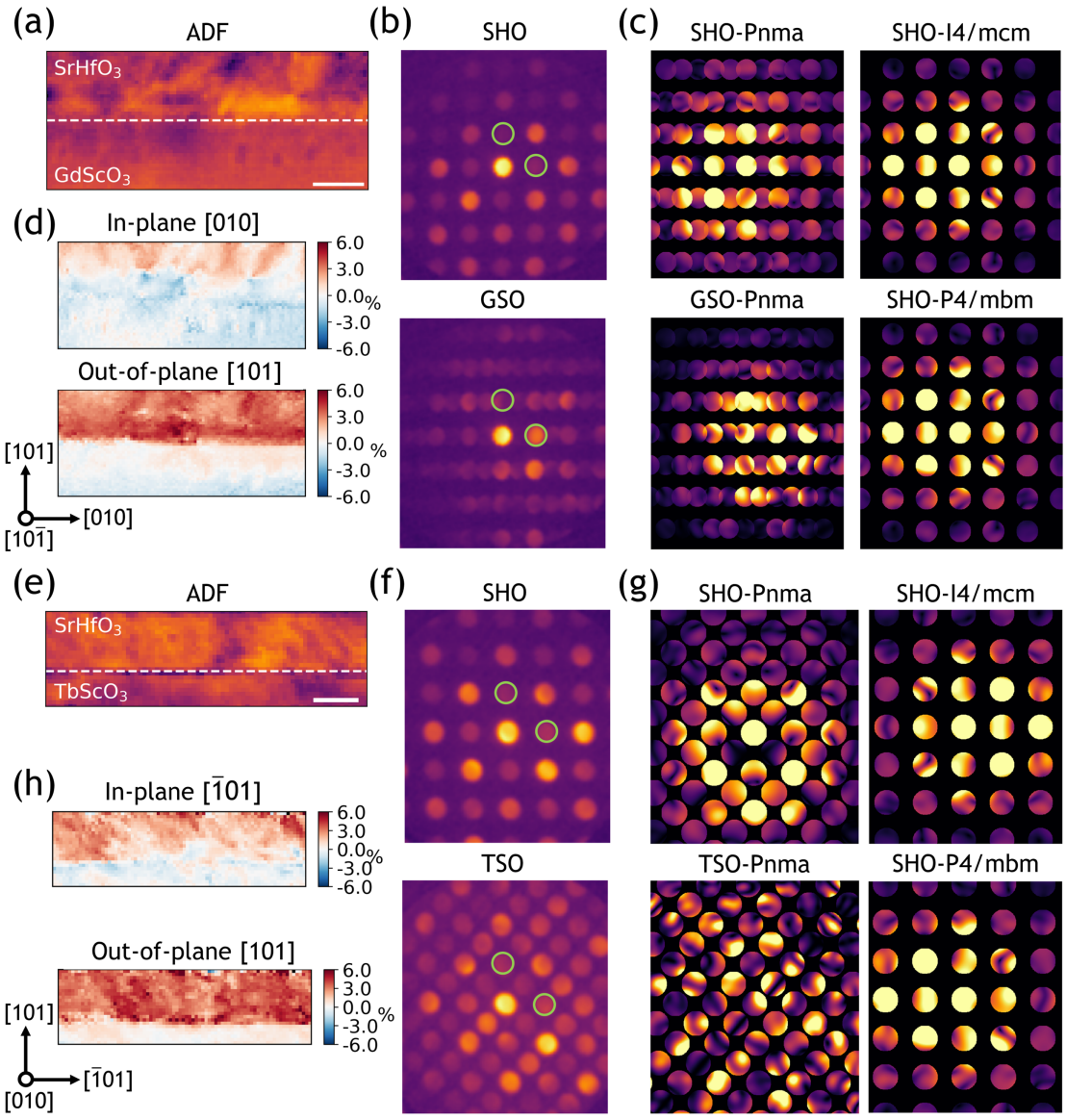

Figure 6.10: ADF image simultaneously acquired during 4D-STEM data collection for (a) SHO-GSO and (e) SHO-TSO samples. The dashed white lines mark the SHO-GSO/TSO interface. CBED patterns for (b) SHO-GSO and (f) SHO-TSO integrated over the area of the film and substrate respectively. Simulated CBED patterns for (c) SHO-GSO and (g) SHO-TSO. The crystallographic orientations corresponding to the experimental and simulated data are provided in (d) and (h) for SHO-GSO and SHO-TSO samples respectively. Strain maps for (d) SHO-GSO and (h) SHO-TSO samples, where strain is calculated with respect to the substrate. Bragg disks used for strain mapping are marked as green circles in (b) and (f) for SHO-GSO and SHO-TSO respectively. The CBED patterns have been rotated post acquisition to match the real-space substrate orientation. Scale bars in (a) and (e) correspond to 10 nm.

a large fraction of the SHO film shows various degrees of tensile strain along the in-plane direction. The observation of tensile strain along the in-plane direction means

that some interfacial strain relaxation has occurred due to misfit dislocations, which can be observed in HAADF measurements as well. This non-uniformity in strain maps can also be observed in LAADF imaging mode. The LAADF imaging mode is sensitive to strain contrast, where non-uniform image contrast reveals non-uniform epitaxy and a high density of defects, as shown in Figure A.A.15. Therefore, the non-uniform strain in the SHO films can be directly attributed to phase impurities and a high density of defects arising from the epitaxial mismatch between the film and substrates.

We have further performed atomic-resolution HAADF and ABF imaging to identify the changes in bond distances (Figure 6.11(a)), BO_6 octahedral tilt patterns (Figure 6.11(b)) and structural defects (Figure 6.11(c)) for the SHO-TSO and SHO-GSO samples. Figure 6.11(a) shows atomic-resolution HAADF images for the SHO-TSO (top) and SHO-GSO (bottom) samples. Since, intensity in a HAADF image is approximately proportional to the squared atomic number ($\tilde{Z}^2$) of the atomic column [226] each atomic column in the substrate and the film can be clearly distinguished. For the HAADF images shown in Figure 6.11(a), we have labeled the B-site cations (Sc (Z = 21) for TSO/GSO and Hf (Z = 72) for SHO). The HAADF images for the TSO and GSO substrates match well with the expected Pnma phase for the substrates along their respective crystallographic orientations. The atomic models for the TSO and GSO substrates are shown in Figure A.A.2. Consistent with the substrate crystallographic orientation (as marked in Figure 6.11(a)), we have calculated the in-plane and out-plane B-site cation bond distances (Sc-Sc for TSO/GSO and Hf-Hf for SHO) using the extracted Sc and Hf atomic positions from the corresponding SHO-TSO and SHO-GSO HAADF images. For the projections shown in Figure 6.11(a), the expected in-plane [$\bar{1}$01] and out-of-plane [101] Sc-Sc bond distance for TSO is 3.95 Å. While for GSO, the expected in-plane [010] and out-of-plane [101] Sc-Sc bond distance is 3.98 Å. These expected Sc-Sc bond distances are marked as vertical dashed lines in the bond distance profiles (Figure 6.11(a)).

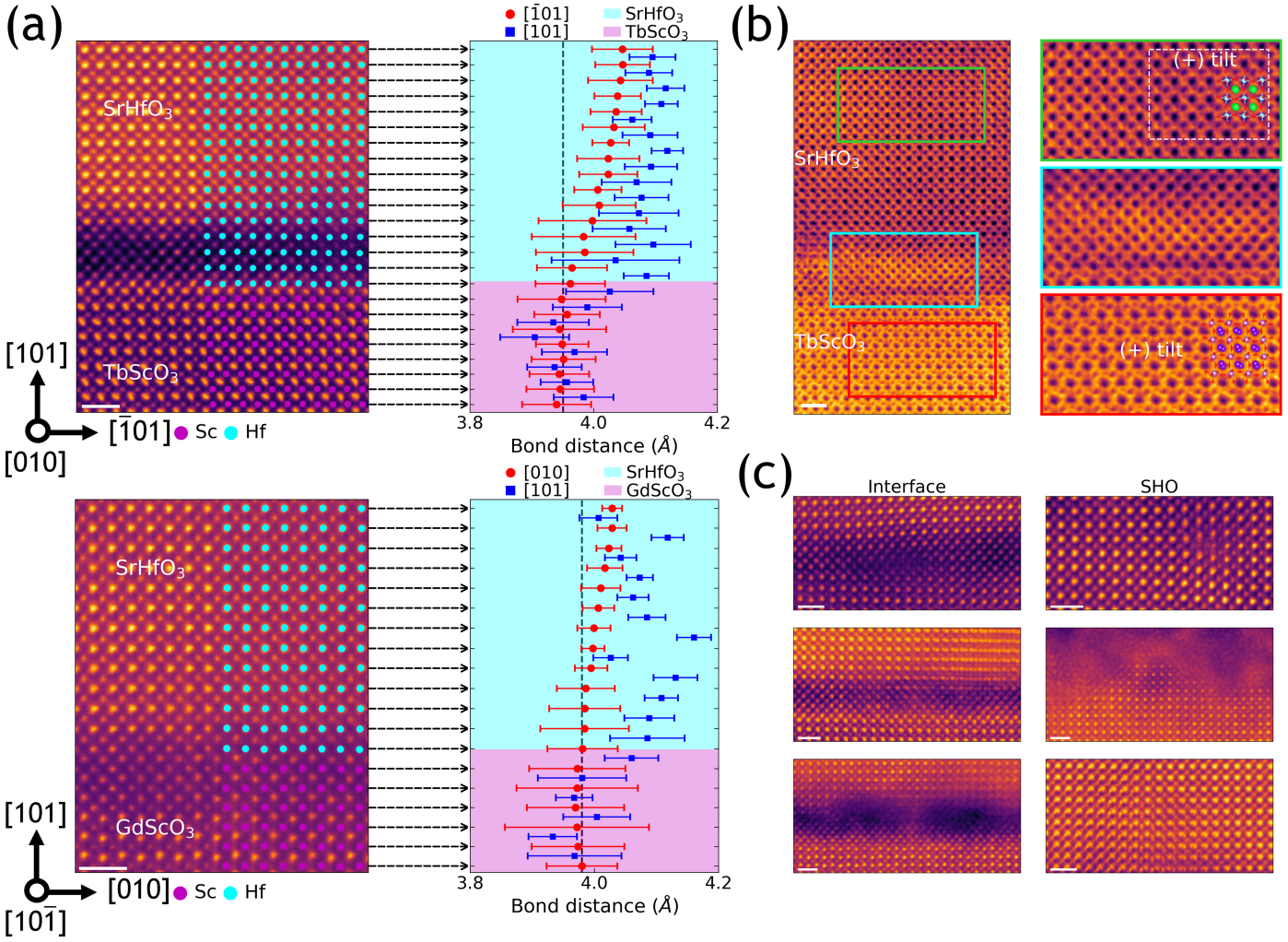

Figure 6.11: (a) Atomic resolution HAADF image showing the cross-section of the SHO-TSO (top) and SHO-GSO (bottom) with labeled B-site cations and the corresponding in-plane and out-of-plane bond distance profiles. The arrows mark the respective atomic-planes in the image and the bond-distance plot. The error bars in the bond distance profiles correspond to the standard deviation. The vertical dashed lines mark the in-plane and out-of-plane Sc-Sc bond distances for TSO and GSO respectively. The crystallographic orientations correspond to that of the TSO and GSO substrates. (b) Atomic-resolution ABF image (left) for an SHO-TSO sample. The higher-resolution ABF images (right) are extracted from the regions marked in same colors as the borders on the left ABF image. (c) Atomic-resolution HAADF images showing defects at the SHO-TSO/GSO interfaces and in the bulk of the SHO films. Scale bars in (a), (b) and (c) correspond to 1 nm.

For an ideal epitaxial relationship, the in-plane bond distances for the film (Hf-Hf) should be constrained to that of the substrate (Sc-Sc) for the entirety of the film thickness, while the out-of-plane bond distance should undergo relaxation (tensile for SHO) as we move further away from the substrate. As shown in Figure 6.11(a), we

observe that the calculated in-plane and out-of-plane Sc-Sc bond distances show a good match for both TSO and GSO. We find that the out-of-plane Hf-Hf bond distance are larger compared to that of Sc-Sc, which is expected for the SHO film because of the application of compressive strain by both TSO and GSO substrates. However, for both SHO-TSO and SHO-GSO, we observe that the Hf-Hf in-plane bond distance is not constrained to that of the substrate, i.e. the Sc-Sc in-plane bond distance. This continued relaxation of the in-plane bond distances as we move away from the substrate results in the inability to achieve phase control for the SHO film growth. Moreover, the lack of epitaxial growth constraints results in the growth of SHO films that have a non-uniform interface with a high density of defects (as shown in Figures 6.11(c) and A.A.15). We also observe higher error bars in the bond distance profiles close to the interface, which is caused by chemical diffusion at the interface resulting in the formation of an intermixed layer, as also revealed by STEM-EELS data in Figure 6.9. The diffused interface along with the high-density of defects results in non-uniform strain accommodation as shown by atomic-resolution imaging (Figure 6.11(a)) as well as 4D-STEM analysis (Figure 6.10).

As is the case with most perovskite structures, the BO_6 octahedra can exhibit a variety of tilt patterns, which forms a key basis of polymorphism in SHO. To ascertain the HfO_6 octahedral tilt patterns, we have performed atomic-resolution ABF imaging as shown in Figure 6.11(b). We observe that for the TSO substrate, ScO_6 octahedra show the expected (+) tilt pattern along [010] consistent with the TSO Pnma phase. However, for the SHO film, we observe non-uniform octahedral tilt patterns, where some regions exhibit (+) tilt patterns, as shown in Figure 6.11(b), which corresponds to a Pnma phase. While some regions don't show any octahedral tilting, which corresponds to pseudocubic [100] and [010] orientations of I4/mcm and P4/mbm phases. Consistent with STEM-EELS data as shown Figure 6.9, we are unable to resolve the oxygen sublattice in the SHO film at the interface, because of a high concentration of oxygen vacancies at the SHO-TSO interface. Moreover, apart from a chemically diffused

interface, we also observe a high density of structural defects at the SHO-TSO/GSO interface as shown in Figure 6.11(c). These defects include dislocations, stacking faults, misorientations and polycrystalline domains. Additionally, we also observe amorphous domains at the interface as well as at the SHO film surface. This confirms that it is unfeasible for the SHO films to accommodate a high compressive strain beyond a few unit cells. Figure A.A.15 shows wide field-of-view HAADF and LAADF images, where non-uniform strain contrast is evident across the cross-section of the SHO-films. This further illustrates non-uniform epitaxy and a high density of defects in the SHO films.

Overall, using a combination of STEM-EELS, 4D-STEM CBED, and atomic-resolution imaging, we show that hMBE can yield highly crystalline SHO films on the TSO and GSO substrates. However, a high compressive strain results in a diffused interface with a high concentration of oxygen vacancies and structural defects, which makes phase control of the SHO film challenging.

6.5 Conclusion and Discussion

We have successfully demonstrated the epitaxial growth of SHO films grown on GSO and TSO substrates using the TEMAH metal organic precursor in hMBE. We have achieved the first synthesis of SHO with -3% biaxial in-plane strain, as confirmed by RSM measurements. SHO's ability to remain stained under compressive strain, along with its insulating properties, make SHO an ideal material for capping layers of perovskite oxides films and heterostructures. Previous DFT studies predicted that SHO films would exhibit the polar P4mm phase when synthesized under compressive strain; however, SHG measurements identified no SHG response, indicating the samples are not centrosymmetric and ruling out the presence of the P4mm phase. A absence of polar distortions is in agreement with previous first principal studies [207, 227] as well as a synthesis study [209]. However, this contradicts one previous study that found fully relaxed SHO-STO films exhibited the P4mm phase [206].

While DFT modeling showed a small range of structural energies between five possible phases of SHO, XAS measurements and 4D-STEM mapping of the samples rule out the presence of the Pnma, $Pm\bar{3}m$, and P4mm phases. The absence of the Pnma phase, which SHO, GSO, and TSO take in the bulk, supports previous first principal studies that predicted compressive strain could stabilize the octahedral tilting in SHO [207]. However, the absence of the cubic $Pm\bar{3}m$ phase contrasts with a synthesis study which found SHO-STO films took on a cubic phase [209]. 4D-STEM measurements showed that the SHO-GSO and SHO-TSO films exhibit either I4/mcm and P4/mbm phase. Based on the DFT modeling presented, we conclude that the films most likely take on the I4/mcm structure rather than the P4/mbm due the 31 meV/fu difference in energy between the two structures.

Chapter 7

Characterization of RHEED Patterns by Machine Learning Algorithms

As stated previously, one of the key goals of AI and ML is to achieve results that match or exceed the abilities of humans. If a machine learning solution is not as effective or as efficient, then an automated process holds little value. Thus, the first step of the investigation into CNNs is focused on whether or not a trained model can recognize the differences between different materials. Observing the differences between different patterns along different crystal axes or different phases is one of the first things a researcher will learn while using RHEED, and therefore it is a perfect starting place to test out CNNs capabilities before evaluating predictive models. The data used for this model were collected by former member of the AU FINO Lab Sydney Provence. The implementation of this model written by Sydney Provence and myself.

CNNs require a large amount of training data to be accurate, and even if they are effective at their task, they do not inherently provide any new understanding of the underlying physics. Random forests offer a few benefits over CNNs, including lower training data requirements and feature importance values. These are inherent to the training of the random forest and provide a quantitative metric of how influential each input is relative to the others. These importance features, along with the lower data prerequisites make random forest models good, inexpensive alternatives to CNNs under the right conditions. The LFO samples used as the data set for the random forest model were synthesized and characterized by former member of the AU FINO Lab Rajendra Paudel and the implementation of the model was programmed by me.

Although the large amount of labeled training data needed to construct effective CNNs can be a problem, when that data is available, the results tend to outperform random forests. Additionally, where a random forest relies on researcher specified data descriptors to reduce the dimensionality of the data set, CNNs utilize the full range of image data and have been shown to be successful at identifying complex and subtle

patterns in image data. Thus, CNNs are provided with all of the data and are able to determine which features are significant without the input of researchers. The STO samples used as the data set for the stoichiometry prediction and classification models were synthesized by Sumner Harris of the Center for Nanophase Materials Sciences at Oak Ridge National Lab, while the XPS characterization was performed by Sumner Harris and myself. I was responsible for the implementation of the stoichiometry classification model and Sumner Harris was responsible for the implementation of the stoichiometry prediction model.

7.1 Material Classification

Image classification is a supervised learning process that requires labeled images to train. This training set used in this work was created by loading samples into the MBE in the FINO lab and recording videos of the RHEED patterns as the samples were heated up, cooled down, and slightly rotated. These conditions replicate common changes during sample growth. The materials used include LAO, LFO, LNO, MAO, MGO, and STO, which are commercially available oxide samples that are frequently used as substrates in the MBE synthesis of perovskite oxides. These materials include a few different crystal structures, including perovskites and spinels, and the RHEED patterns were recorded along the 110 axis for all samples.

Figure 7.1 shows the architecture created to classify the images. The model consists of 4 convolutional layers with 8, 16, 24, and 32 filters, respectively. After each convolutional layer, a pooling layer with size 2×2 and a stride of 2 down samples the results to a fourth of the input size. After the convolution layers, the output is flattened and fed into 2 dense layers with output sizes 5000 and 2000, respectively. The output for this network is size 6, since there are 6 categories of materials used. The convolutional layers and dense layers utilize leaky Relu activation functions, while the output layer utilizes a soft max function. Since this is a classification network, a categorical

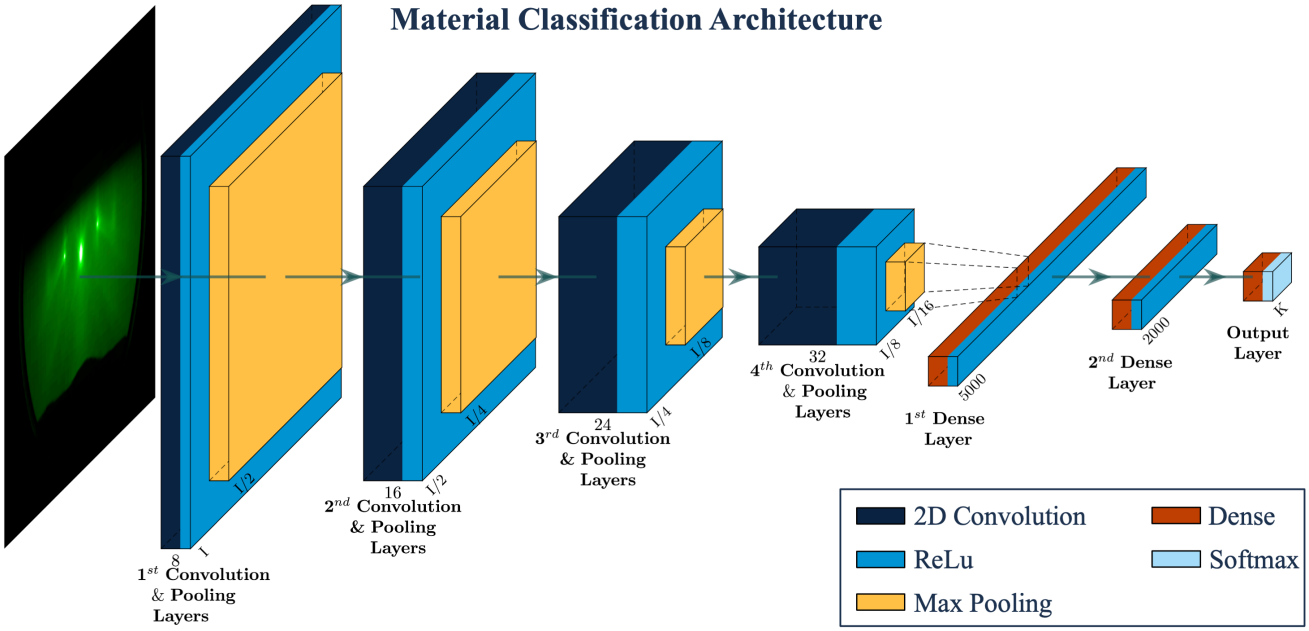

Figure 7.1: CNN model architecture for the classification of RHEED images into material categories.

cross entropy loss function was used to train. The model was programmed in Python 3.9.16 Keras 2.10.0.

Figure 7.2 shows the results of the classification network. The training set is able to achieve 99% accuracy after 18 epochs, while the validation set reaches an accuracy of 97%. The training and test confusion matrices show a breakdown of how samples were classified. The Y axis represents the material in the image, while the X axis shows into which category the image was classified. Elements along the diagonal indicate samples that were classified correctly, while samples off the diagonal were misclassified. The training data set and test data set both show remarkable accuracy, with the training data set only misclassifying 9 images out of over 25,000 images. Interestingly, the majority of misclassified images were of STO, and LFO. From the test matrix it is clear that the model struggled the most with differentiating between LFO and STO. This is likely due to both materials possessing a perovskite structure and having a very small lattice mismatch, of $\approx 0.6\%$ [122]. Despite being highly similar in crystal structure, the network was able to successfully classify all but 1% of the LFO and STO images correctly. This accuracy is certainly sufficient to show that machine learning and AI

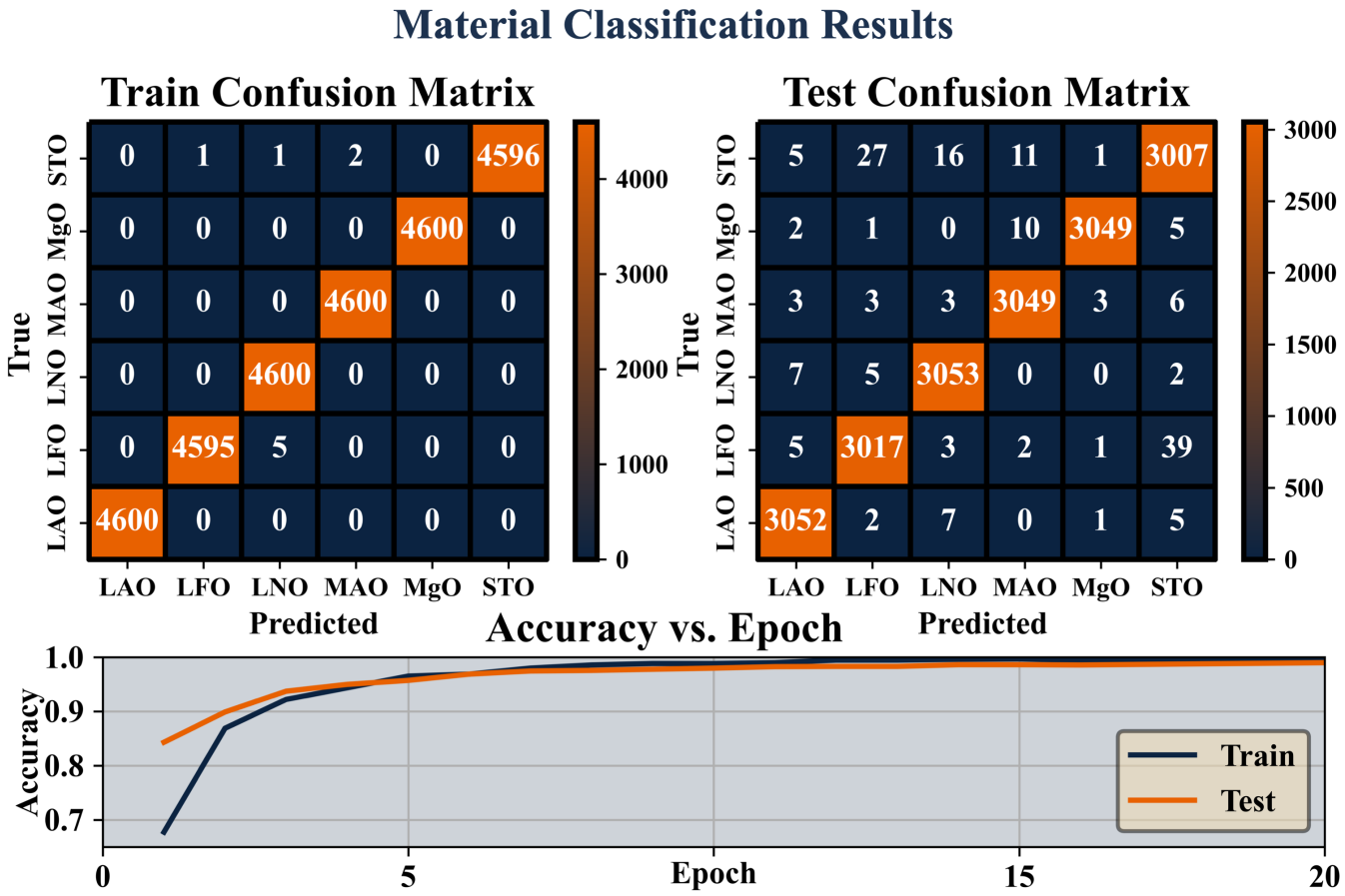

Figure 7.2: Results of the CNN classification model. (Left) Training confusion matrix at final epoch. (Right) Validation confusion matrix at final epoch. (Bottom) Model accuracy vs. Epoch.

models can identify and distinguish between the complex features of RHEED patterns. This result also supports the possibility that machine learning can be used to analyze RHEED patterns and make predictions about material composition.

7.2 Predictions of LFO Stoichiometry Using Random Forests

7.2.1 Data, Preprocessing, & Implementation

In order to train a random forests model to predict stoichiometry based off RHEED images, a labeled training data set is needed. RHEED recordings of LFO samples grown using MBE in the FINO lab were selected for this work. LFO is a perovskite oxide with space group Pnma that produces highly ordered samples even when grown slightly off

stoichiometry. Over 30 highly crystalline samples with clear RHEED patterns were chosen to serve as the data set. In order to minimize any effects of the screen recording process, each of the RHEED recordings was processed to have the same resolution and scaling. Similarly, the XPS survey spectra corresponding to each sample were also preprocessed to align the O 1s peak at 530 eV binding energy and to normalize the intensity to of the O 1s peak to 1. This will remove some of the variance between scans caused by the XPS system.

As mentioned prior, unlike CNNs, random forest models are not adept at interpreting image data directly. Thus, it is necessary to process the images into descriptors which describe the features of the images. This reduces the dimensionality of the data to a level that random forests are able to function well with. Ideally, this would be done using a theoretical model that is designed to accurately describe the images; however, as stated prior, RHEED spots are the result of several complex scatterings occurring simultaneously, and thus no model to precisely describe them currently exists. Thus, for RHEED images, the specular and 1st order RHEED spots were fit with a Gaussian oval function described by:

$$I(x,y) = h + Ae^{-\frac{(x-x_0)^2}{\sigma_x^2} - \frac{(y-y_0)^2}{\sigma_y^2}} \tag{7.1}$$

where A is the amplitude, (x_0, y_0) is the center, σ_x and σ_y are the standard deviations, and h is a constant offset. Due to the limitations of the camera on most RHEED systems, the specular and 1st order spots can become saturated. As a result, the intensity plateaus at 255, causing the spots to no longer fit a Gaussian oval. This is solved by clipping the Gaussian fit above the value A, such that:

$$I(x,y) = \begin{cases} I(x,y) & \text{if} I < A \\ A & \text{if} I \geq A \end{cases} \tag{7.2}$$

The fit parameters, A, (x_0, y_0), σ_x, σ_y, and h, for the specular and 1st order spots spots serve as the descriptors for the RHEED images. Figure 7.3 shows two RHEED spots

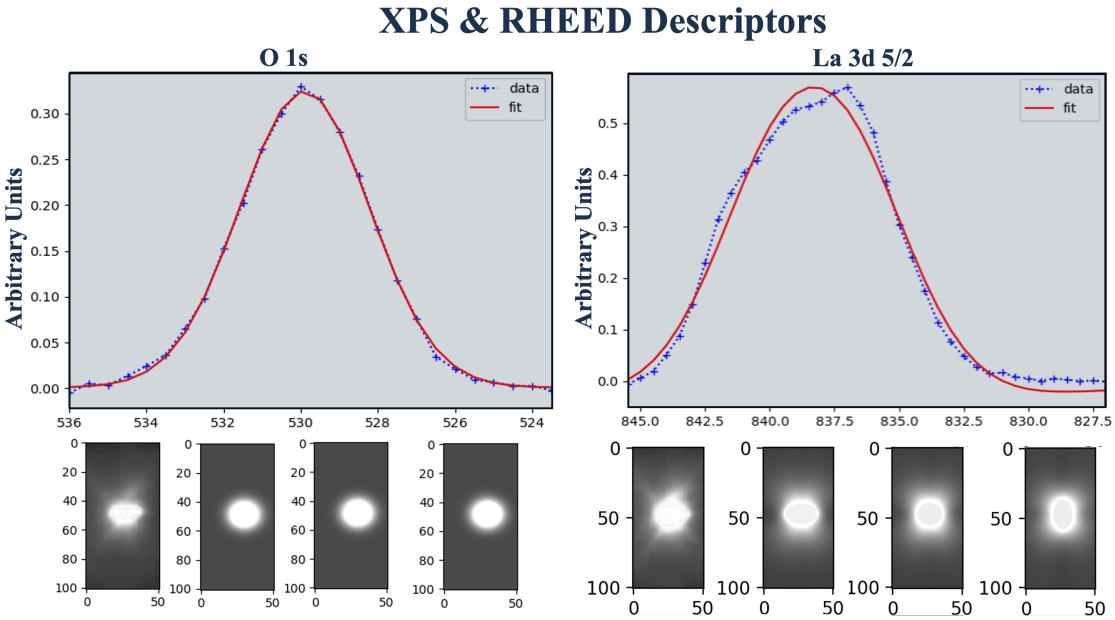

Figure 7.3: (Top) XPS survey spectra fit with Shirley backgrounds and GLS functions that were used as descriptors in the random forest prediction model. (Bottom) Two RHEED spots and three corresponding fits by clipped Gaussian oval used as descriptors in the random forest prediction model.

and three different fits for each one. These images show that the clipped Gaussian oval function is able to accurately adjust to the spot radii, intensity, and background; however, it is also clear that several effects such as the streaks jetting out from the spots are lost. Unlike the RHEED spots, XPS core level peaks are known to be fit using Voight functions, which can be approximated using a Gaussian-Lorentzian sum, as defined in equation 3.6. Each shell core level peak was fit using a single GLS function, while 2 GLS functions were used to fit p and d shell peaks, in order to account for spin orbit splitting. The E, F, m, and h values for each of the O 1s, La 3d 5/2, La 3d 3/2, Fe 2p 3/2, and Fe 2p 1/2 peaks serve as the descriptors to the XPS spectra. Figure 7.3 shows the fits and raw data for an O 1s and a La 3d 5/2 peak after a Shirley background had been subtracted. Both of the peaks are symmetric and thus are fit well by the GLS functions, resulting in little to no loss of information from the spectra. The random forest models were implemented with Python 3.9.16 using Scikit-learn's RandomForestRegressor model. Each random forest consisted of 1000 decision trees and were trained on the descriptors of the LFO RHEED and XPS data.

7.2.2 Results

The bottom row of Figure 7.4 shows some of the fits resulting from a model trained on 1000 images. The top row of Figure 7.4 shows the results of several random forests trained on different numbers of RHEED images. As expected, the error decreases as more data is provided to train the network. There is close alignment between error of the test and train sets, indicating that the model has not suffered from over fitting. The La 3d 5/2 and Fe 2p 3/2 results show that the error begins to plateau around 100 to 1000 images, indicating that the models reach peak accuracy rather quickly. However, while the training curve for La 3d 5/2 plateaus, the test curve becomes sporadic, indicating that the model has some instability in the peak fitting.

At around 10,000 images, the model results in errors in the range of 5-10%. While this uncertainty is low, it is still too high to provide a film grower with actionable information that could change the course of growth, as once a sample is off stoichiometry by 10% or more, it is highly unlikely that the structure will be able to recover even if adjustments are made. One possible explanation for the limitations in accuracy is that the descriptors are not capturing enough of the important information that is needed to predict the stoichiometry. It is clear from Figure 7.4, that the Gaussian oval fit does not capture the finer structure of the RHEED pattern. These fits also completely omit surface reconstruction spots, secondary phase spots, and Kikuchi bands.

One of the strongest benefits of random forest models and using descriptors to describe data is that the feature importances can provide valuable information about what is most influencing the results. However, the feature importance analysis of the model shows no major outliers among the descriptors. Although, notably, σ_x and σ_y were among the three most important features. This aligns with the idea that RHEED spot width can be used as an alternative to spot intensity averaging in RHEED monitoring. Since the model shows no major difference in the relative importance of the features, the greatest benefit of random forests was not realized, leaving the low amount of training data required as the only key benefit. Since the classification network was successful,

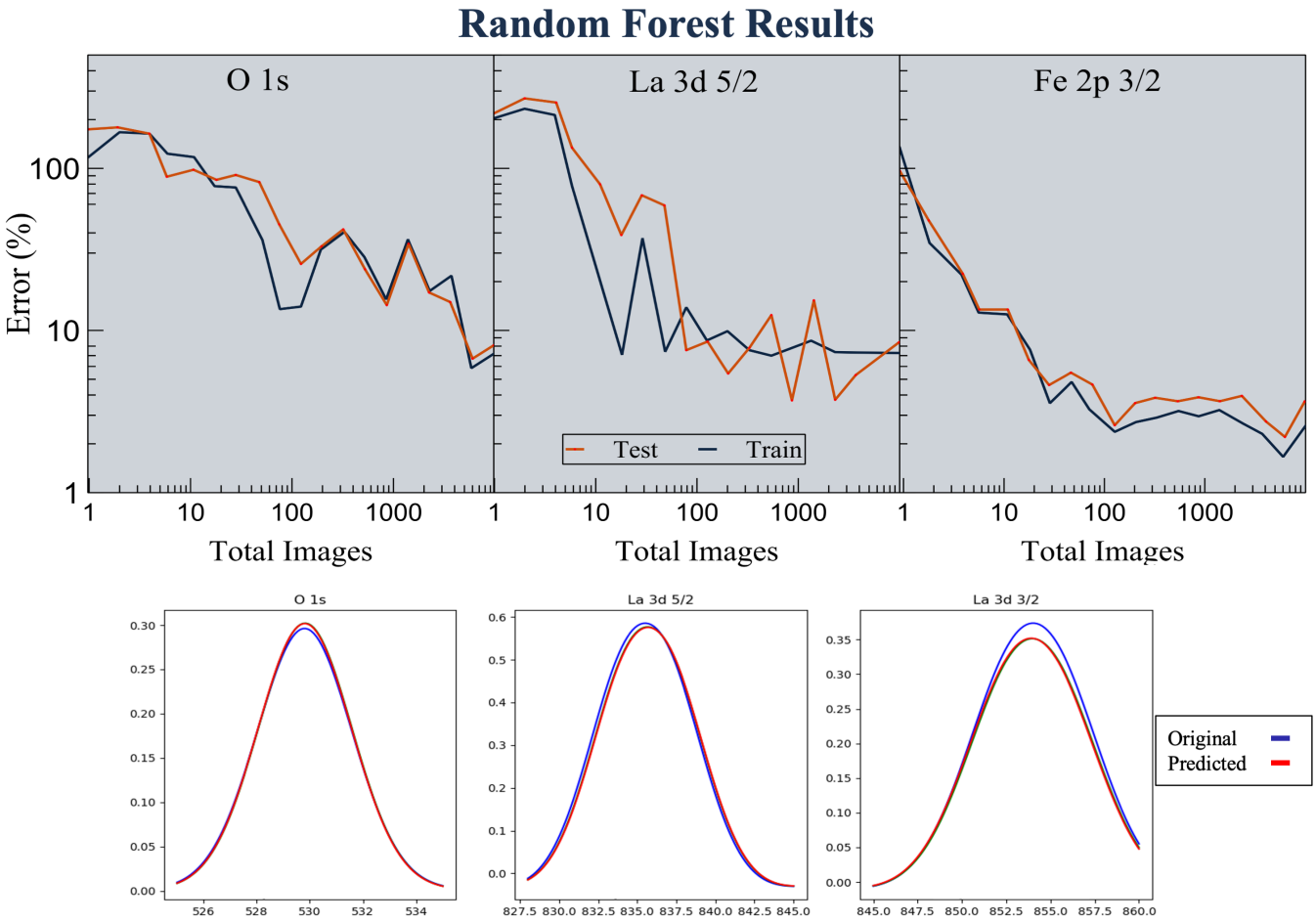

Figure 7.4: (Top) The peak area error in % vs the number of RHEED images on which the random forest was trained. (Bottom) Examples of the original descriptors and the predicted fits.

and the random forest showed only moderate accuracy, it is likely that the RHEED and XPS descriptors did not contain enough of the material information and that a CNN trained to predict stoichiometry may avoid this issue.

7.3 Classification and Prediction of STO Stoichiometry Using CNNs

7.3.1 Data Collection

In order to ensure that the CNN has a sufficient range of data on which to train, homoepitaxial STO samples were grown using PLD at the Center for Nanophase Materials Sciences (CNMS) at Oak Ridge National Lab (ORNL). Pulsed laser deposition is

a film synthesis technique similar to MBE. Both operate at UHV to grow high quality thin film samples, suspend samples on a heated stage, and use RHEED to monitor growth; however, where MBE uses effusion cells to evaporate metal onto a substrate, PLD achieves this by vaporizing metals and metal oxides with laser pulses. The metal targets are positioned ≈ 5 cm below the substrate and are hit by regular laser pulses during growth. These pulses cause rapid heating of the metal targets and the result is a plasma of metal ions called a plume. This plume has much higher density than the beam of metal ions in MBE and results in growth rates that are much higher MBE. Since this plasma pulse is moving rapidly, the system can sustain higher oxygen pressure without drastically affecting the growth rate.

For this work, STO films were grown on commercially available STO substrates. In order to achieve a Ti terminated surface prior to growth, each substrate was submerged in boiling water for 24 hours and then immediately annealed for 3 hours at 800°C. This recipe produces clear and regular step edges with a Ti terminated surface [228]. PLD systems typically have only one laser and rely on a movable target wheel to swap the targets during growth. This results in an alternating growth cycle similar to shuttered growth in MBE. In order to determine an appropriate recipe for homoepitaxial STO, SrO, and TiO_2 calibration samples were grown with a fixed number of pulses and then analyzed using XRR and XRD to identify film thickness. From this, it was determined that Sr was deposited at a rate of 0.79 Å/pulse, while TiO_2 was deposited at 0.1865 Å/pulse, which is a ratio of 4.2 Ti:1 Sr. Based off this information, and following the route of previous works [229, 230], a base recipe for stoichiometric homoepitaxial STO of 3 Sr pulses to 11 Ti pulses was selected, which should deposit approximately 1 u.c.. In order to maximize the operational range of the CNN, a set of training data with a wide range of stoichiometries is needed. To achieve this range, the number of Sr pulses will remain fixed at 3, while the number of Ti pulses will be given by the function:

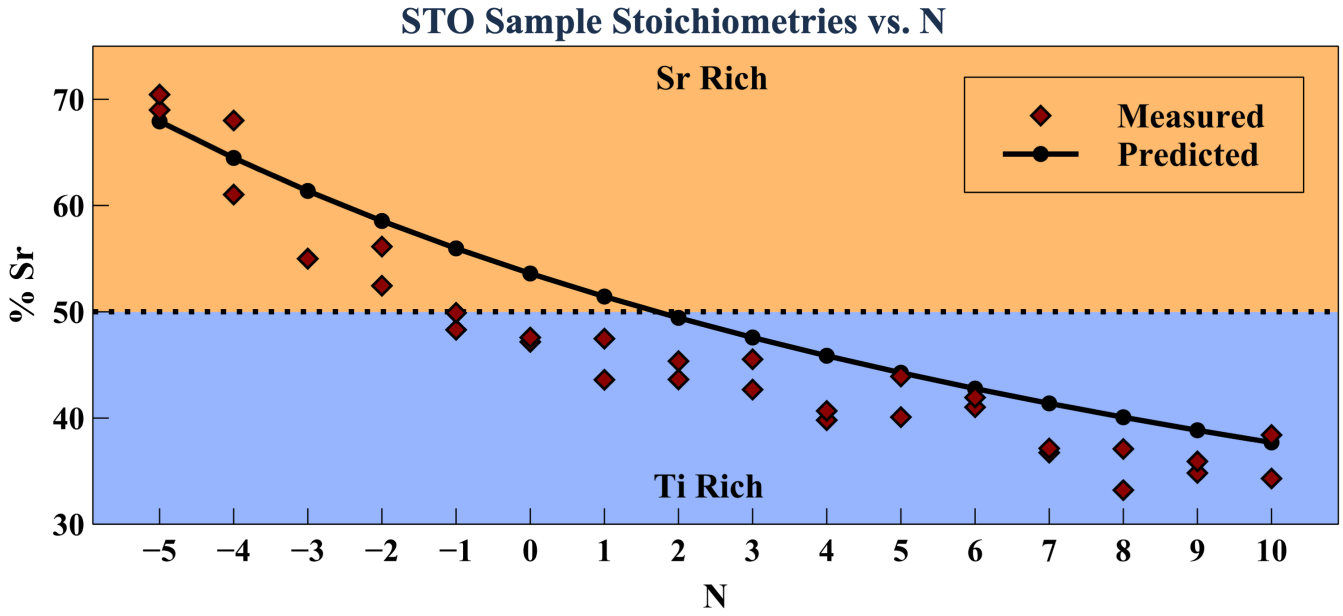

Figure 7.5: The % Sr of each homoepitaxy STO sample grown using PLD, along with a curve of the predicted values.

$$\text{Pulses}_{\text{Ti}} = 11 + N \tag{7.3}$$

where N can range from -5 to 10. For each value of N, two samples were grown at 700°C with molecular O_2 flowing at 5 sccm resulting in 20 mTorr of background pressure.

XPS survey and multiplex spectra were collected for each sample. The multiplex were taken over the regions of the O 1s, Ti 2p, Sr 3d, and Sr 3p peaks. A valence band spectra was also collected for each sample. These spectra were collected at the CNMS at ORNL. Figure 7.5 shows the stoichiometry of the STO samples as a function of N. The samples range from 70% Sr rich to 65% Ti rich. The black line represents the stoichiometry predicted by the recipe. Notably, the curve appears fairly accurate in the extremes; however, the curvature does not seem to match. This discrepancy highlights the kinds of problems that machine learning predictions may be able to address.

7.3.2 Network Architecture & Implementation

Two different model architectures were used for the classification and prediction of the STO film stoichiometries. Figure 7.6 shows the model architecture for the classification model, which takes as input a RHEED image from a sample and classifies the sample into a set range of stoichiometries. The model consists of three 2D convolution blocks each consisting of a 2D convolution layer, batch normalization layer, leaky ReLu layer, and max pooling layer. The number of convolutional filters doubles with each successive block, with the first block having 16 filters. Each pooling layer has a pool size of 2×2 and a stride of 2×2, resulting in the x and y dimensions of the image each being reduced by half during each block. After the three convolution blocks, the data is flattened and passed to a dense layer with a ReLu activation function. At this point the data has dimensions $\frac{I_X}{8} \times \frac{I_Y}{8} \times 256$, where I_X and I_Y are the initial width and height of the image, respectively. The dense layer has output size $\frac{I_X \times I_Y}{64}$ and is passed to a an output layer utilizing a softmax activation. The output is an array of K probabilities corresponding to the chance that the input image corresponds to each category. For this work, a value of $K = 7$ was chosen so that each bin would contain on average 4+ samples.

This model was programmed in Python 3.9.16 using Keras 2.10.0 and was run on the Easley cluster at Auburn University. The available samples were broken into training and test sets with sizes 26 and 5, respectively. For each sample, the last 100 frames, corresponding to the last 10 s of growth, were used. Prior to training, images were cropped to 512×512 in order to remove excess background and were then downscaled to 256×256 pixels. To minimize bias learned from the training set, data points were repeated as necessary in the training data to ensure each bin possessed the same number of data points. The model used a categorical cross entropy loss function and an Adam optimizer with learning rate 0.001.

Figure 7.7 shows the model architecture for the stoichiometry prediction model, which takes as input a RHEED image from a sample and predicts the stoichiometry.

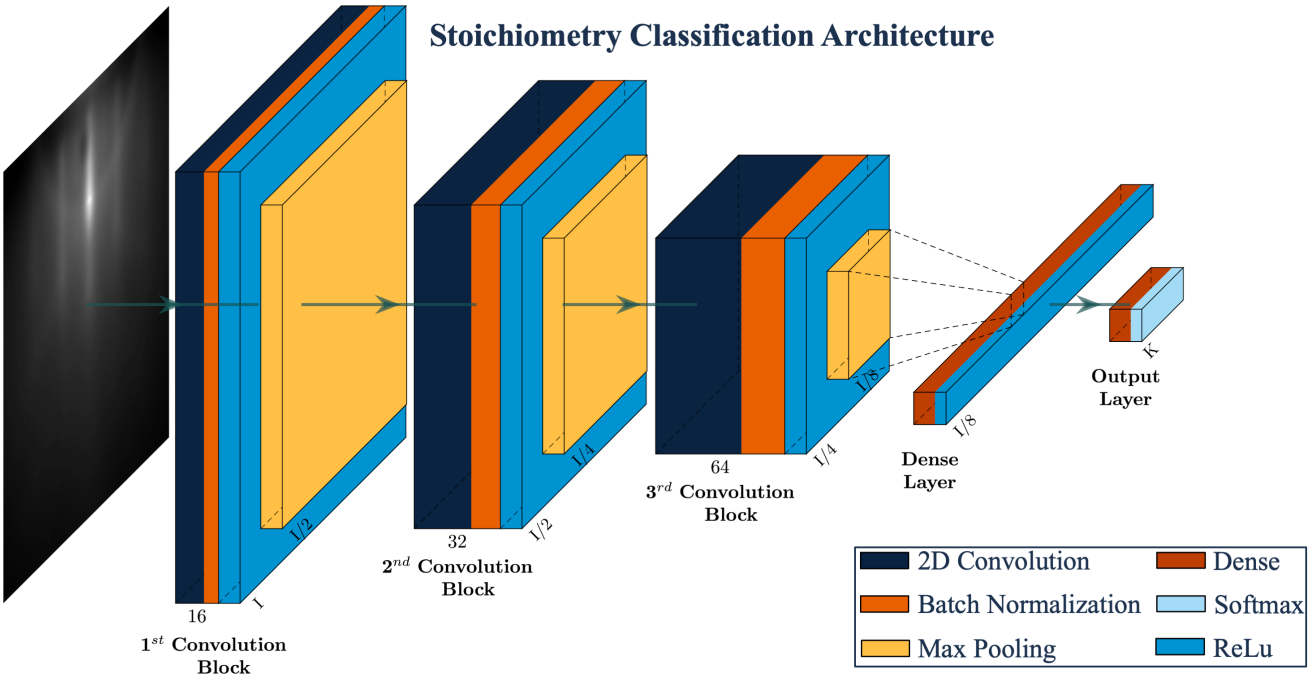

Figure 7.6: CNN model architecture for the classification of sample stoichiometry from RHEED images.

This model consists of a convolution block, four residual blocks, a pooling layer, two dense layers, and an output layer. The convolution block consists of a 2D convolutional layer with 16 filters, a batch normalization layer, and a 2D ReLu layer. Each residual block sends a copy of the output of the previous layer through two different paths. The residual path consists of two 2D convolutional layers and batch normalization layers with a ReLU activation layer between them. The shortcut path has a single convolution and batch normalization layer. The convolutional layers in each path possess the same number of filters; however, the residual path has a kernel size of 3×3, while the shortcut has a kernel size of 1×1. Thus the shortcut path passes on a direct copy of the output data from the previous layer. The results from the residual and shortcut paths are then summed and passed through a ReLu activation. The number of convolutional filters doubles with each successive residual block, with the first block having 32 filters. The first convolutional layer in each residual path and each shortcut path has a stride of 2×2, resulting in the input being down sampled by a factor of 2 in both the x and y dimension. The adaptive pooling layer averages the output across the different filters

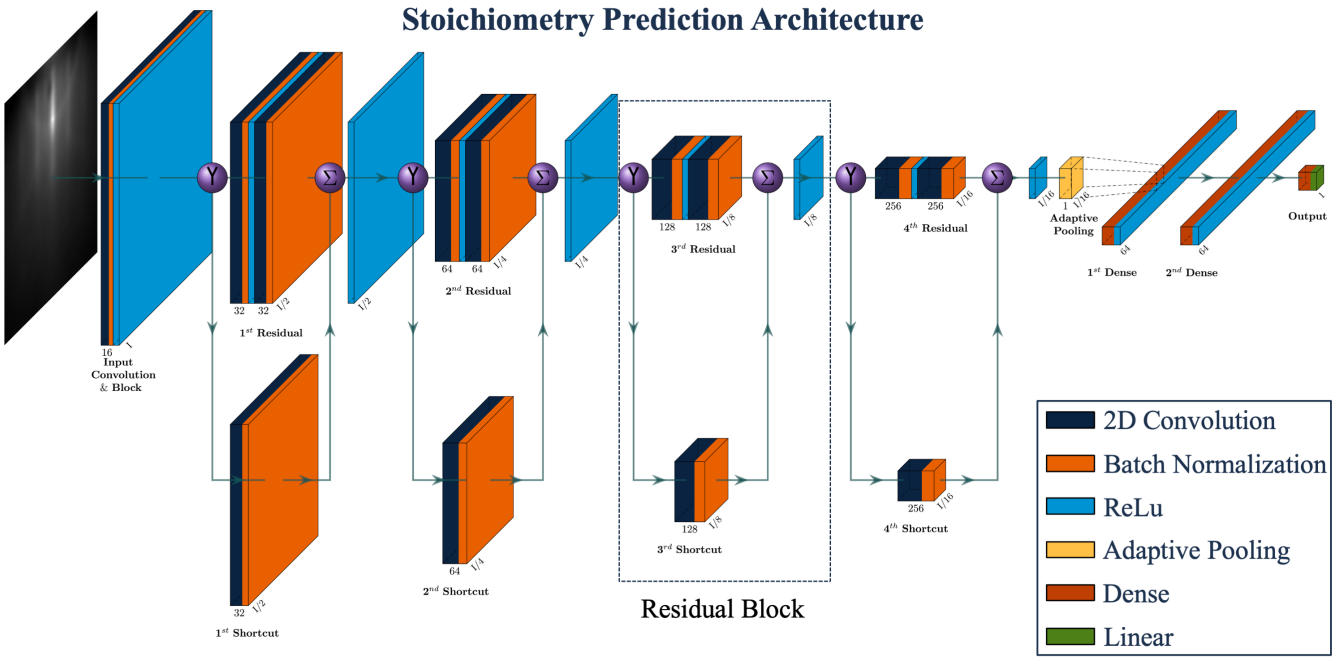

Figure 7.7: CNN model architecture for the prediction of sample stoichiometry from RHEED images.

and outputs data in the shape $\frac{I_X}{16} \times \frac{I_Y}{16}$, where I_X and I_Y are the initial width and height of the image, respectively. The output is then flattened and passed through two dense layers with ReLu activation functions and output sizes of 64. Finally, the data reaches the output layer with a linear activation function and size 1.

This model was programmed in Python using PyTorch and was run on cloud computing resources at the Center for Nanophase Materials Sciences (CNMS). The available samples were broken into training and test sets with sizes 22 and 9, respectively. For each sample, the last frame of growth was used. Prior to training, images were down sampled from 540×740 to 135×185. The model used a root mean squared error (RMSE) loss function and a stochastic gradient descent optimizer with learning rate 0.001.

7.3.3 Stoichiometry Classification Results

Figure 7.8 shows the results of the stoichiometry classification model. The bin labels correspond to the lower bound of the bin, with each bin being 5.3% wide. A width

of 5.3% is a logical choice since the uncertainty in RHEED stoichiometry is on the order of 5%. The values of the bin labels represent the percentage Sr of the sample, where a stoichiometric sample having a 1:1 ratio of Sr to Ti would be represented by 50%. As can be seen from the diagonalized training confusion matrix, the model was able to fully adapt to the training dataset. From the accuracy vs. epoch graph, we see that the model achieved 100% accuracy by 10 epochs, indicating the model learned rapidly. The test data set follows the same trend and also stops improving after 10 epochs. The test confusion matrix shown corresponds to the model weights which yielded the highest accuracy, 75.6%, during training. The test confusion matrix shows that the model is able to accurately classify the majority of images; additionally, all but 19 of the misclassified images were classified in bins adjacent to the correct bin.

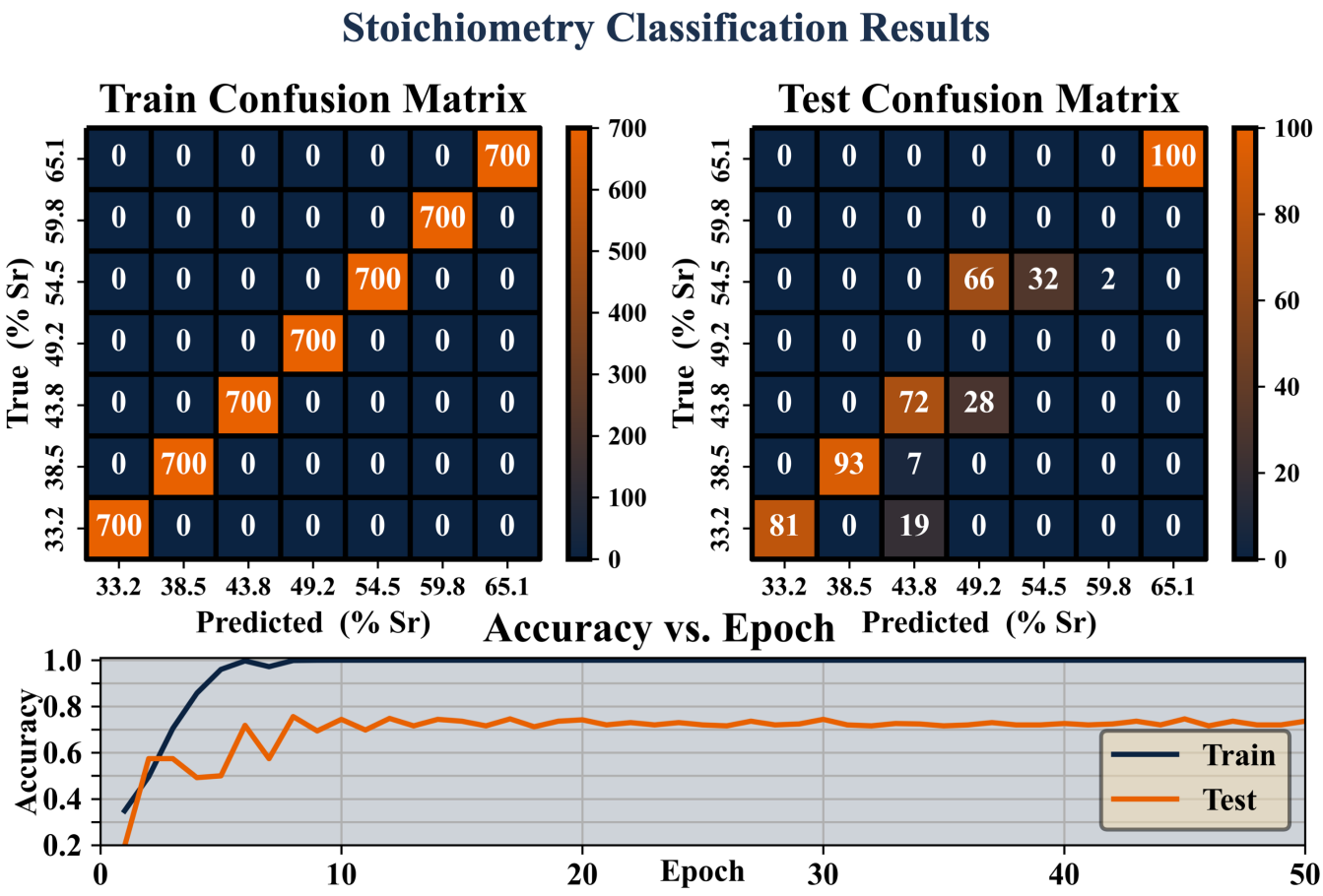

Figure 7.8: Results of the stoichiometry classification model. (Left) Training confusion matrix at final epoch. (Right) Test confusion matrix at final epoch. (Bottom) Accuracy vs. Epoch.

Thus, even when the model is incorrect, the mean error is typically within 10%. This result clearly shows that convolutional neural networks are able to discern the difference between the stoichiometries of samples using RHEED images; however, the model's accuracy is sufficiently high that a film grower would be able to consistently draw useful conclusions.

7.3.4 Stoichiometry Prediction Results

Figure 7.9 and Figure 7.10 show the results of the stoichiometry prediction model. Figure 7.9 shows the RMSE vs. epoch and the coefficient of determination (R^2) vs. epoch. The loss reduces rapidly for the first 75 epochs, and then begins to improve more slowly until plateauing beyond 350 epochs. The R^2 value shows a similar trend, though notably, the R^2 curve of the training data diminishes in variance while the RMSE curve of the training data continues to vary more from epoch to epoch. In both plots we see that the test data follows the same trends as the training data, but does not reach the same loss or R^2 values. Figure 7.10 shows a plot of the true vs. predicted stoichiometry values. This data comes from when the model achieves the highest R^2

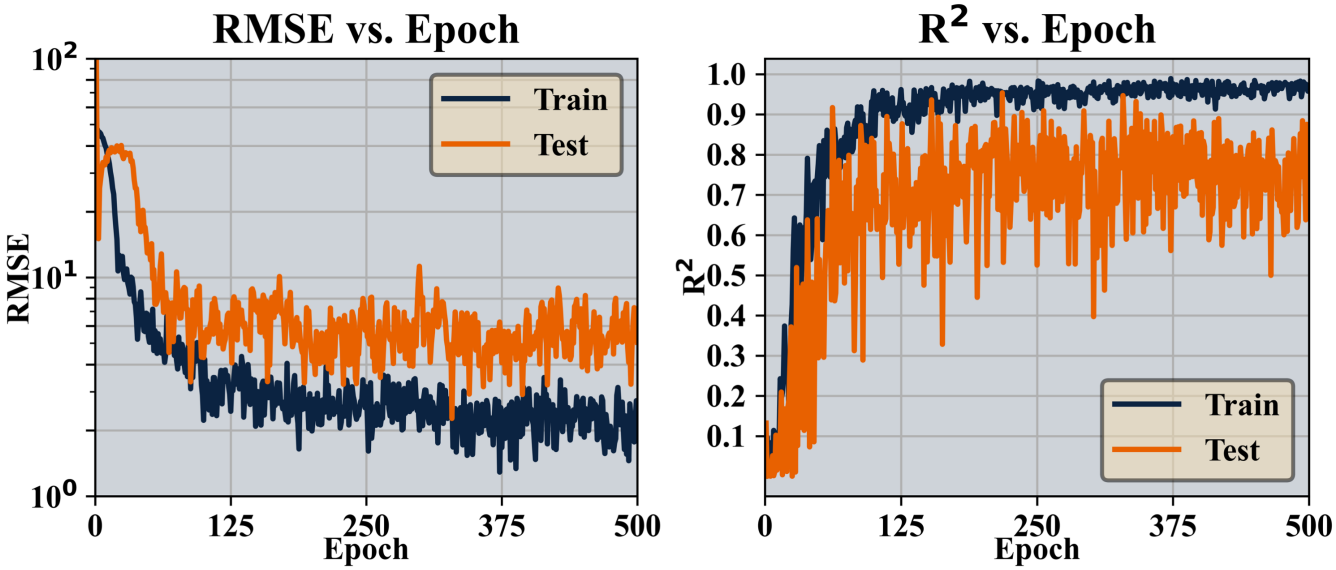

Figure 7.9: Results of the stoichiometry prediction model. (Left) The RMSE loss vs. Epoch. (Right) The R^2 value vs. Epoch.

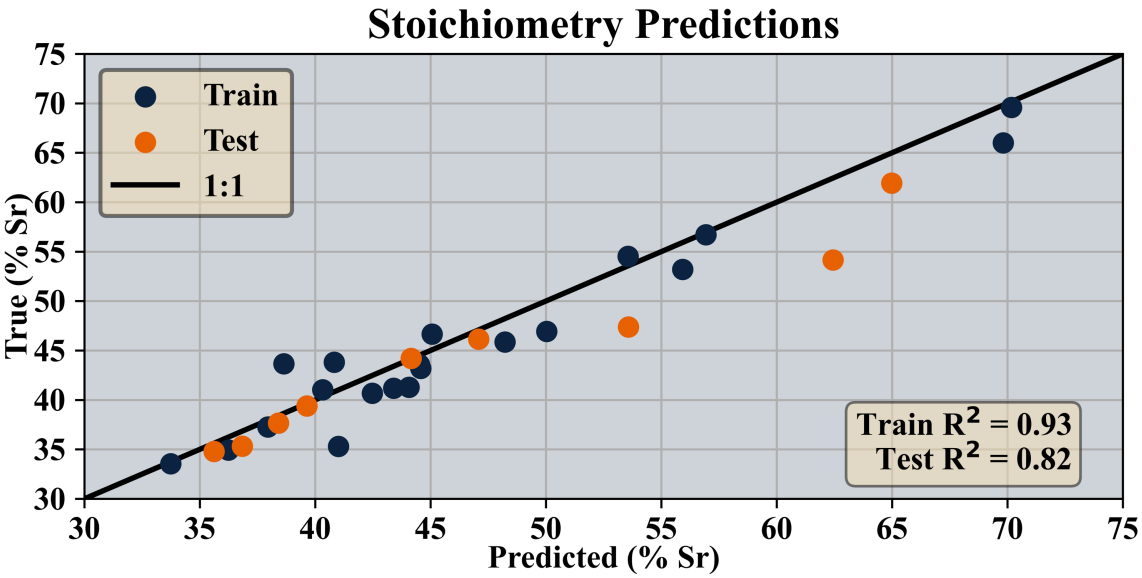

Figure 7.10: A plot of the correlation between the true and predicted values resulting from the stoichiometry prediction model.

for the test dataset. As we can see, the model is able to successfully learn to predict the stoichiometries of both the training and test datasets, resulting in R^2 values of 0.93 and 0.82, respectively. The mean absolute error for the training and test sets were 2.25% and 2.43%, respectively, while the max errors were 5.71% and 8.28% for the training and test sets, respectively. It is clear that the model learned better for samples that were more Ti rich and struggled more with samples that were Sr rich. This is likely due to the distribution of the sample data which had more Ti rich samples, as seen in Figure 7.5. As more data points are collected, the model will likely improve in accuracy in the Sr rich regime.

7.4 Conclusion

Although random forests can offer benefits in understanding what features are significant in data correlation, the model's inability to handle image data and reliance on data descriptors proved too limiting for the purpose of predicting stoichiometry. However, CNN models proved highly successful at interpreting RHEED images. The material classification model was able to achieve an accuracy of 97% when identifying substrate materials based on their RHEED images. The stoichiometry classification model was

able to attain 75% accuracy when classifying sample stoichiometry into narrow regimes. Both of these results proved the concept that CNN models are capable of differentiating between the fine differences RHEED patterns better than most researchers can. However, it is the success of the stoichiometry prediction model that is most impactful. The model was able to achieve an R^2 value of 0.82 and a mean error of 2.43%, with a training set of just 22 samples. This model can serve as the basis for new tools that predict stoichiometry in real time based off small datasets collected on the same system. This development will allow for greater and more accurate control of film synthesis and is a major step towards the effective automation of film synthesis in both research and industry labs.

Chapter 8

Conclusion & Future Work

We successfully demonstrated the epitaxial growth of SHO films on GSO and TSO substrates using the TEMAH metal-organic precursor in (hMBE). We achieved the first synthesis of SHO with -3% biaxial in-plane strain, as confirmed by RSM and STEM measurements. The ability of SHO to remain strained under compressive conditions, along with its insulating properties, highlights its potential as an ideal material for capping layers in perovskite oxide films and heterostructures. Despite previous DFT predictions suggesting the polar P4mm phase may be realized under compressive strain, SHG measurements identified no response, ruling out the P4mm phase and supporting the absence of polar distortions. This is in agreement with prior first-principles studies and contrasts with some previous findings that reported the P4mm phase in fully relaxed SHO-STO films. Furthermore, XAS spectra and 4D-STEM mappings ruled out the presence of the Pnma and $Pm\bar{3}m$ phases and, along with DFT modeling, suggest the phase of the SHO-TSO and SHO-GSO films is I4/mcm.

We have shown that PCA on recordings of RHEED patterns can extract valuable information about the evolution of the film that is not available through traditional analysis methods. By analyzing the change in eigenvalues over the growth process, we identified new patterns such as weak spot oscillations that were previously unrecognized. Additionally, we found that using k-means clustering to analyse the eigenvalues created by PCA results in quantitatively significant clusters that distinguish between different segments of the growth, providing a clear timeline of the film's surface evolution. This advancement offers film growers a more detailed and quantitative tool for analyzing the evolution of a film's surface during growth.

We explored the capabilities of various machine learning architectures to analyzing RHEED images and extract significant results. We found that while random forests

showed limitations in handling image data and were unable to reliably predict stoichiometry, CNN models proved highly successful. The material classification model achieved 97% accuracy in identifying substrate materials, and the stoichiometry classification model attained 75% accuracy in classifying sample stoichiometry into narrow regimes. Most notably, the stoichiometry prediction model was able to achieve a mean error of 2.43% with a small set of 22 samples. These successes pave the way for more complex and advanced models to be developed and the creation of tools that can predict stoichiometry in real time during film synthesis.

While the epitaxial growth of 3% compressively strained SHO did not result in the predicted P4mm phase, it is possible that compressive strain is a necessary but not sufficient condition to synthesize this phase. Future work can investigate the effects of constructing super lattices of alternating layers of STO and SHO, which may result in the STO stabilizing the P4mm phase in the SHO layers.

The success of the machine learning techniques demonstrated that there are significant benefits in augmenting existing data analysis techniques with machine learning methods. Since it has been shown that RHEED images contain sufficient information to inform on sample stoichiometry, future work can investigate the links between RHEED and other data. Since RHEED is surface sensitive and sensitive to changes in the crystal lattice, possible links between atomic force microscopy images and XRD spectra could be researched. While automated synthesis is coming closer to fruition, additional work to create tools that link sample data and system controls is needed. In order to construct a more robust and detailed model of film growth that is needed for automated synthesis, future models for predicting stoichiometry or other film qualities should also attempt to incorporate system data and conditions, such as substrate temperature, oxygen pressure, and effusion cell temperatures.

References

[1] Jermey N. A. Matthews. “Semiconductor industry switches to hafnium-based transistors”. In: *Physics Today* 61.2 (Feb. 2008), pp. 25–26. ISSN: 0031-9228. DOI: 10.1063/1.2883902.

[2] K. Momma and F. Izumi. “VESTA 3 for three-dimensional visualization of crystal, volumetric and morphology data”. In: *J. Appl. Crystallogr.* 44 (2011), pp. 1272–1276.

[3] Anubhav Jain et al. “Commentary: The Materials Project: A materials genome approach to accelerating materials innovation”. In: *APL Materials* 1.1 (July 2013), p. 011002. ISSN: 2166-532X. DOI: 10.1063/1.4812323.

[4] A. Ohtomo and H. Y. Hwang. “A high-mobility electron gas at the LaAlO3/SrTiO3 heterointerface”. In: *Nature* 427.6973 (2004), pp. 423–426. ISSN: 1476-4687. DOI: 10.1038/nature02308.

[5] Changjiang Liu et al. “Two-dimensional superconductivity and anisotropic transport at KTaO¡sub¿3¡/sub¿ (111) interfaces”. In: *Science* 371.6530 (2021), pp. 716–721. DOI: 10.1126/science.aba5511.

[6] Omor F. Shoron et al. “BaTiO3/SrTiO3 heterostructures for ferroelectric field effect transistors”. In: *Applied Physics Letters* 110.23 (June 2017), p. 232902. ISSN: 0003-6951. DOI: 10.1063/1.4985014.

[7] J Haeni et al. “Room-temperature ferroelectricity in strained SrTiO3”. In: *Nature* 430 (2004), pp. 758–761. DOI: 10.1038/nature02773.

[8] Z. Q. Mao, Y. Mori, and Y. Maeno. “Suppression of superconductivity in Sr_2RuO_4 caused by defects”. In: *Phys. Rev. B* 60 (1 July 1999), pp. 610–614. DOI: 10.1103/PhysRevB.60.610.

[9] Peter Rudolph. “Fundamentals and engineering of defects”. In: *Progress in Crystal Growth and Characterization of Materials* 62.2 (2016). Special Issue: Recent Progress on Fundamentals and Applications of Crystal Growth; Proceedings of the 16th International Summer School on Crystal Growth (ISSCG-16), pp. 89–110. ISSN: 0960-8974. DOI: https://doi.org/10.1016/j.pcrysgrow.2016.04.004.

[10] Andrés-Felipe Castro-Méndez, Juanita Hidalgo, and Juan-Pablo Correa-Baena. “The Role of Grain Boundaries in Perovskite Solar Cells”. In: *Advanced Energy Materials* 9.38 (2019), p. 1901489. DOI: https://doi.org/10.1002/aenm.201901489.

[11] J W Christian and V Vítek. “Dislocations and stacking faults”. In: *Reports on Progress in Physics* 33.1 (Jan. 1970), p. 307. DOI: 10.1088/0034-4885/33/1/307.

[12] R. Pentcheva et al. “Termination control of electronic phases in oxide thin films and interfaces: $LaAlO_3/SrTiO_3(001)$”. In: *Philosophical Transactions of the Royal Society A: Mathematical, Physical and Engineering Sciences* 370.1977 (2012), pp. 4904–4926. DOI: 10.1098/rsta.2012.0202.

[13] T. Shimizu et al. “Comparative study of phase transitions in BaTiO3 thin films grown on (001)- and (110)-oriented SrTiO3 substrate”. In: *Journal of Physics: Condensed Matter* 25.13 (Apr. 2013), p. 132001. DOI: 10.1088/0953-8984/25/13/132001.

[14] Yunzhong Chen and Robert J. Green. “Progress and Perspectives of Atomically Engineered Perovskite Oxide Interfaces for Electronics and Electrocatalysts”. In: *Advanced Materials Interfaces* 6.15 (2019), p. 1900547. DOI: https://doi.org/10.1002/admi.201900547.

[15] Tingjun Wu et al. “Application of Perovskite-Structured Materials in Field-Effect Transistors”. In: *Advanced Electronic Materials* 5.12 (2019), p. 1900444. DOI: https://doi.org/10.1002/aelm.201900444.

[16] Xiaolong Liu and Mark C. Hersam. “Interface Characterization and Control of 2D Materials and Heterostructures”. In: *Advanced Materials* 30.39 (2018), p. 1801586. DOI: https://doi.org/10.1002/adma.201801586.

[17] Pavlo Zubko et al. “Interface Physics in Complex Oxide Heterostructures”. In: *Annual Review of Condensed Matter Physics* 2.Volume 2, 2011 (2011), pp. 141–165. ISSN: 1947-5462. DOI: https://doi.org/10.1146/annurev-conmatphys-062910-140445.

[18] G B Stringfellow. “Epitaxy”. In: *Reports on Progress in Physics* 45.5 (May 1982), p. 469. DOI: 10.1088/0034-4885/45/5/001.

[19] Yusuke Ota. “Silicon molecular beam epitaxy”. In: *Thin Solid Films* 106.1 (1983), pp. 1–136. ISSN: 0040-6090. DOI: https://doi.org/10.1016/0040-6090(83)90180-3.

[20] Yu B Bolkhovityanov and O P Pchelyakov. “GaAs epitaxy on Si substrates: modern status of research and engineering”. In: *Physics-Uspekhi* 51.5 (May 2008), p. 437. DOI: 10.1070/PU2008v051n05ABEH006529.

[21] Rajendra Paudel et al. “Band-engineered LaFeO3–LaNiO3 thin film interfaces for electrocatalysis of water”. In: *Journal of Vacuum Science & Technology A* 41.6 (Oct. 2023), p. 063207. ISSN: 0734-2101. DOI: 10.1116/6.0002987.

[22] Sumner B. Harris et al. “Deep learning with plasma plume image sequences for anomaly detection and prediction of growth kinetics during pulsed laser deposition”. In: *npj Computational Materials* 10.1 (2024), p. 105. DOI: 10.1038/s41524-024-01275-w.

[23] Jan-Otto Carlsson and Peter M. Martin. “Chapter 7 - Chemical Vapor Deposition”. In: *Handbook of Deposition Technologies for Films and Coatings (Third Edition)*. Ed. by Peter M. Martin. Third Edition. Boston: William Andrew Publishing, 2010, pp. 314–363. ISBN: 978-0-8155-2031-3. DOI: https://doi.org/10.1016/B978-0-8155-2031-3.00007-7.

[24] Richard W. Johnson, Adam Hultqvist, and Stacey F. Bent. "A brief review of atomic layer deposition: from fundamentals to applications". In: *Materials Today* 17.5 (2014), pp. 236–246. ISSN: 1369-7021. DOI: https://doi.org/10.1016/j.mattod.2014.04.026.

[25] W. Zulehner. "Czochralski growth of silicon". In: *Journal of Crystal Growth* 65.1 (1983), pp. 189–213. ISSN: 0022-0248. DOI: https://doi.org/10.1016/0022-0248(83)90051-9.

[26] D. J. P. Morris et al. "Crystal-to-stripe reordering of sodium ions in Na_xCoO_2 ($x \geq 0.75$)". In: *Phys. Rev. B* 79 (10 Mar. 2009), p. 100103. DOI: 10.1103/PhysRevB.79.100103.

[27] Darrell G. Schlom et al. "Strain Tuning of Ferroelectric Thin Films". In: *Annual Review of Materials Research* 37 (2007), pp. 589–626. ISSN: 1545-4118. DOI: https://doi.org/10.1146/annurev.matsci.37.061206.113016.

[28] H. Rached et al. "Full-potential calculation of the structural, elastic, electronic and magnetic properties of XFeO3 (X=Sr and Ba) perovskite". In: *Physica B: Condensed Matter* 405.17 (2010), pp. 3515–3519. ISSN: 0921-4526. DOI: https://doi.org/10.1016/j.physb.2010.05.060.

[29] Jun He et al. "Control of Octahedral Tilts and Magnetic Properties of Perovskite Oxide Heterostructures by Substrate Symmetry". In: *Phys. Rev. Lett.* 105 (22 Nov. 2010), p. 227203. DOI: 10.1103/PhysRevLett.105.227203.

[30] J Haeni et al. "Room-temperature ferroelectricity in strained SrTiO3". In: *Nature* 430 (2004), pp. 758–761. DOI: 10.1038/nature02773.

[31] L.W. Martin, Y.-H. Chu, and R. Ramesh. "Advances in the growth and characterization of magnetic, ferroelectric, and multiferroic oxide thin films". In: *Materials Science and Engineering: R: Reports* 68.4 (2010), pp. 89–133. ISSN: 0927-796X. DOI: https://doi.org/10.1016/j.mser.2010.03.001.

[32] P Richard and JJV Vinci. “Mechanical behavior of thin films”. In: *Annu. Rev. Mater. Sei* 26 (1996), pp. 431–62.

[33] R. Klockenkämper and A. von Bohlen. “Determination of the critical thickness and the sensitivity for thin-film analysis by total reflection X-ray fluorescence spectrometry”. In: *Spectrochimica Acta Part B: Atomic Spectroscopy* 44.5 (1989), pp. 461–469. ISSN: 0584-8547. DOI: https://doi.org/10.1016/0584-8547(89)80051-5.

[34] A. H. Harker S. C. Jain and R. A. Cowley. “Misfit strain and misfit dislocations in lattice mismatched epitaxial layers and other systems”. In: *Philosophical Magazine A* 75.6 (1997), pp. 1461–1515. DOI: 10.1080/01418619708223740.

[35] M. A. Peña and J. L. G. Fierro. “Chemical Structures and Performance of Perovskite Oxides”. In: *Chemical Reviews* 101.7 (2001). PMID: 11710238, pp. 1981–2018. DOI: 10.1021/cr980129f.

[36] Kai Wang et al. “Perovskite Oxide Catalysts for Advanced Oxidation Reactions”. In: *Advanced Functional Materials* 31.30 (2021), p. 2102089. DOI: https://doi.org/10.1002/adfm.202102089.

[37] Suresh Thapa et al. “Surface stability of SrNbO3+δ grown by hybrid molecular beam epitaxy”. In: *APL Materials* 10.9 (Sept. 2022), p. 091112. ISSN: 2166-532X. DOI: 10.1063/5.0097699.

[38] P. Bezdicka et al. “Preparation and characterization of Fully stoichiometric SrCoO3 by electrochemical oxidation”. In: *Zeitschrift für anorganische und allgemeine Chemie* 619.1 (1993), pp. 7–12. DOI: https://doi.org/10.1002/zaac.19936190104.

[39] K. Agilandeswari and A. Ruban Kumar. “Synthesis, characterization, microstructure, optical and magnetic properties of strontium cobalt carbonate precursor and Sr2Co2O5 oxide material”. In: *Superlattices and Microstructures* 68 (2014), pp. 27–37. ISSN: 0749-6036. DOI: https://doi.org/10.1016/j.spmi.2014.01.002.

[40] R. B. van Dover et al. “Effect of oxidation on the magnetic properties of unprotected TbFe thin films”. In: *Journal of Applied Physics* 59.4 (Feb. 1986), pp. 1291–1296. ISSN: 0021-8979. DOI: 10.1063/1.336519.

[41] S. Thapa et al. “Probing surfaces and interfaces in complex oxide films via in situ X-ray photoelectron spectroscopy”. In: *Journal of Materials Research* (2020), pp. 1–26. DOI: 10.1557/jmr.2020.261.

[42] M. L. Trudeau, A. Tschope, and J. Y. Ying. “XPS investigation of surface oxidation and reduction in nanocrystalline CeXLa1-XO2-Y”. In: *Surface and Interface Analysis* 23.4 (1995), pp. 219–226. DOI: https://doi.org/10.1002/sia.740230405.

[43] Vitaly L Ginzburg, Vitaly Lazarevich Ginzburg, and LD Landau. *On the theory of superconductivity*. Springer, 2009.

[44] Dirk van Delft and Peter Kes. “The discovery of superconductivity”. In: *Physics Today* 63.9 (Sept. 2010), pp. 38–43. ISSN: 0031-9228. DOI: 10.1063/1.3490499.

[45] J. Bardeen. “Theory of the Meissner Effect in Superconductors”. In: *Phys. Rev.* 97 (6 Mar. 1955), pp. 1724–1725. DOI: 10.1103/PhysRev.97.1724.

[46] Myron Strongin et al. “Surface Superconductivity in Type I and Type II Superconductors”. In: *Phys. Rev. Lett.* 12 (16 Apr. 1964), pp. 442–444. DOI: 10.1103/PhysRevLett.12.442.

[47] W.V. Pogosov and M. Combescot. “From one to N Cooper pairs, step by step”. In: *Physica C: Superconductivity* 471.19 (2011), pp. 566–576. ISSN: 0921-4534. DOI: https://doi.org/10.1016/j.physc.2011.07.007.

[48] J. Bardeen, L. N. Cooper, and J. R. Schrieffer. “Theory of Superconductivity”. In: *Phys. Rev.* 108 (5 Dec. 1957), pp. 1175–1204. DOI: 10.1103/PhysRev.108.1175.

[49] Jun Nagamatsu et al. “Superconductivity at 39 K in magnesium diboride”. In: *Nature* 410.6824 (2001), pp. 63–64. DOI: 10.1038/35065039.

[50] G. R. Stewart. “Unconventional superconductivity”. In: *Advances in Physics* 66.2 (2017), pp. 75–196. DOI: 10.1080/00018732.2017.1331615.

[51] A. Schilling et al. “Superconductivity above 130 K in the Hg–Ba–Ca–Cu–O system”. In: *Nature* 363.6424 (1993), pp. 56–58. ISSN: 1476-4687. DOI: 10.1038/363056a0.

[52] Chan Park and Robert L. Snyder. “Structures of High-Temperature Cuprate Superconductors”. In: *Journal of the American Ceramic Society* 78.12 (1995), pp. 3171–3194. DOI: https://doi.org/10.1111/j.1151-2916.1995.tb07953.x.

[53] V Jovanovic et al. “Magnetoresistance and Hall effect in e-doped superconducting SrLaCuO thin films”. In: *Journal of Physics: Conference Series* 150.5 (Mar. 2009), p. 052086. DOI: 10.1088/1742-6596/150/5/052086.

[54] M. Roger et al. “Patterning of sodium ions and the control of electrons in sodium cobaltate”. In: *Nature* 445.7128 (2007), pp. 631–634. ISSN: 1476-4687. DOI: 10.1038/nature05531.

[55] Paul H Lissberger. “Optical applications of dielectric thin films”. In: *Reports on Progress in physics* 33.1 (1970), p. 197.

[56] JG Simmons. “Conduction in thin dielectric films”. In: *Journal of Physics D: Applied Physics* 4.5 (1971), p. 613.

[57] D Dimos and CH Mueller. “Perovskite thin films for high-frequency capacitor applications”. In: *Annual Review of Materials Science* 28.1 (1998), pp. 397–419.

[58] Sonali Saha, T P Sinha, and Abhijit Mookerjee. “Structural and optical properties of paraelectric SrTiO3”. In: *Journal of Physics: Condensed Matter* 12.14 (Apr. 2000), p. 3325. DOI: 10.1088/0953-8984/12/14/309.

[59] N. Setter et al. “Ferroelectric thin films: Review of materials, properties, and applications”. In: *Journal of Applied Physics* 100.5 (Sept. 2006), p. 051606. ISSN: 0021-8979. DOI: 10.1063/1.2336999.

[60] Zi-lin Yuan et al. “A review of ultra-thin ferroelectric films”. In: *Journal of Physics: Condensed Matter* 33.40 (2021), p. 403003.

[61] Radislav A. Potyrailo et al. “Battery-free Radio Frequency Identification (RFID) Sensors for Food Quality and Safety”. In: *Journal of Agricultural and Food Chemistry* 60.35 (2012). PMID: 22881825, pp. 8535–8543. DOI: 10.1021/jf302416y.

[62] C. Rossel et al. “SrHfO3 as gate dielectric for future CMOS technology”. In: *Microelectronic Engineering* 84.9 (2007). INFOS 2007, pp. 1869–1873. ISSN: 0167-9317. DOI: https://doi.org/10.1016/j.mee.2007.04.029.

[63] C. Rossel et al. “Field-effect transistors with SrHfO3 as gate oxide”. In: *Applied Physics Letters* 89.5 (Aug. 2006), p. 053506. ISSN: 0003-6951. DOI: 10.1063/1.2236464.

[64] Thomas Mikolajick et al. “Ferroelectric hafnium oxide for ferroelectric random-access memories and ferroelectric field-effect transistors”. In: *MRS Bulletin* 43.5 (2018), pp. 340–346. DOI: 10.1557/mrs.2018.92.

[65] Garrett Birkhoff and Erwin Kreyszig. “The establishment of functional analysis”. In: *Historia Mathematica* 11.3 (1984), pp. 258–321. ISSN: 0315-0860. DOI: https://doi.org/10.1016/0315-0860(84)90036-3.

[66] N. A. Neef. “Current research on functional analysis methodologies: An introduction”. In: *Journal of Applied Behavior Analysis* 27.2 (1994), pp. 211–214. DOI: 10.1901/jaba.1994.27-211.

[67] Libero J Bartolotti and Ken Flurchick. “An introduction to density functional theory”. In: *Reviews in computational chemistry* (1996), pp. 187–216.

[68] G. Kresse and J. Furthmüller. In: *Phys. Rev. B* 54 (1996), p. 11169.

[69] G. Kresse and J. Hafner. In: *Phys. Rev. B* 49 (1994), p. 14251.

[70] G. Kresse and J. Furthmüller. In: *Comput. Mat. Sci.* 6 (1996), p. 15.

[71] P Giannozzi et al. “Advanced capabilities for materials modelling with QUANTUM ESPRESSO”. In: *Journal of Physics: Condensed Matter* 29.46 (2017), p. 465901.

[72] Paolo Giannozzi et al. “QUANTUM ESPRESSO: a modular and open-source software project for quantum simulations of materials”. In: *Journal of Physics: Condensed Matter* 21.39 (2009), 395502 (19pp).

[73] Paolo Giannozzi et al. “Quantum ESPRESSO toward the exascale”. In: *The Journal of Chemical Physics* 152.15 (2020), p. 154105. DOI: 10.1063/5.0005082.

[74] Burak Himmetoglu et al. “Hubbard-corrected DFT energy functionals: The LDA+U description of correlated systems”. In: *International Journal of Quantum Chemistry* 114.1 (2014), pp. 14–49. DOI: https://doi.org/10.1002/qua.24521.

[75] Chikio Hayashi. *What is Data Science ? Fundamental Concepts and a Heuristic Example*. Ed. by Chikio Hayashi et al. Tokyo: Springer Japan, 1998, pp. 40–51. ISBN: 978-4-431-65950-1.

[76] Longbing Cao. “Data Science: A Comprehensive Overview”. In: *ACM Comput. Surv.* 50.3 (June 2017). ISSN: 0360-0300. DOI: 10.1145/3076253.

[77] Dr. Ravindra D. Sarode Ku. Chhaya A. Khanzode. “Advantages and Disadvantages of Artificial Intelligence and Machine Learning: A Literature Review”. In: (Apr. 2022). DOI: 10.17605/OSF.IO/GV5T4.

[78] Rama K. Vasudevan et al. “Big-Data Reflection High Energy Electron Diffraction Analysis for Understanding Epitaxial Film Growth Processes”. In: *ACS Nano* 8.10 (2014). PMID: 25268549, pp. 10899–10908. DOI: 10.1021/nn504730n.

[79] Sydney R. Provence et al. “Machine learning analysis of perovskite oxides grown by molecular beam epitaxy”. In: *Phys. Rev. Mater.* 4 (8 Aug. 2020), p. 083807. DOI: 10.1103/PhysRevMaterials.4.083807.

[80] Stefania Tentoni et al. “Birthweight by gestational age in preterm babies according to a Gaussian mixture model”. In: *BJOG: An International Journal of Obstetrics & Gynaecology* 111.1 (2004), pp. 31–37.

[81] Marco Sarich, Jan-Hendrik Prinz, and Christof Schütte. “Markov Model Theory”. In: *An Introduction to Markov State Models and Their Application to Long Timescale Molecular Simulation*. Ed. by Gregory R. Bowman, Vijay S. Pande, and Frank Noé. Dordrecht: Springer Netherlands, 2014, pp. 23–44. ISBN: 978-94-007-7606-7. DOI: 10.1007/978-94-007-7606-7_3.

[82] Kaixuan Sun, Jingsheng Chen, and Xiaobing Yan. “The Future of Memristors: Materials Engineering and Neural Networks”. In: *Advanced Functional Materials* 31.8 (2021), p. 2006773. DOI: https://doi.org/10.1002/adfm.202006773.

[83] E. Fortunato et al. “Recent advances in ZnO transparent thin film transistors”. In: *Thin Solid Films* 487.1 (2005). International Conference on Polycrystalline Semiconductors-Materials, Technologies, Device Applications, pp. 205–211. ISSN: 0040-6090. DOI: https://doi.org/10.1016/j.tsf.2005.01.066.

[84] Guijun Yang and Soo-Jin Park. “Deformation of Single Crystals, Polycrystalline Materials, and Thin Films: A Review”. In: *Materials* 12.12 (2019). ISSN: 1996-1944. DOI: 10.3390/ma12122003.

[85] H.Y. Li et al. “Bendability of single-crystal Si MOSFETs investigated on flexible substrate”. In: *IEEE Electron Device Letters* 27.7 (July 2006), pp. 538–541. ISSN: 1558-0563. DOI: 10.1109/LED.2006.876301.

[86] Fernando Rinaldi. “Basics of molecular beam epitaxy (MBE)”. In: *NIVERSITÄT ULM* 31 (2002).

[87] Secondo Franchi. “Chapter 1 - Molecular beam epitaxy: fundamentals, historical background and future prospects”. In: *Molecular Beam Epitaxy*. Ed. by Mohamed Henini. Oxford: Elsevier, 2013, pp. 1–46. ISBN: 978-0-12-387839-7. DOI: https://doi.org/10.1016/B978-0-12-387839-7.00001-4.

[88] Suresh Thapa. “Surface and Interfacial Studies of Perovskite Oxides Grown by Hybrid Molecular Beam Epitaxy”. PhD thesis. Auburn, Alabama: Auburn University, May 2022.

[89] B.A. Joyce. “Growth and perfection of chemically-deposited epitaxial layers of Si and GaAs”. In: *Journal of Crystal Growth* 3-4 (1968), pp. 43–59. ISSN: 0022-0248. DOI: https://doi.org/10.1016/0022-0248(68)90100-0.

[90] J. R. Arthur and J. J. LePore. “GaAs, GaP, and GaAsxP1-x Epitaxial Films Grown by Molecular Beam Deposition”. In: *Journal of Vacuum Science and Technology* 6.4 (July 1969), pp. 545–548. ISSN: 0022-5355. DOI: 10.1116/1.1315677.

[91] Tom Foxon. “History of MBE”. In: *Molecular Beam Epitaxy: Materials and Applications for Electronics and Optoelectronics* (2019), p. 1.

[92] A. Y. Cho. “Morphology of Epitaxial Growth of GaAs by a Molecular Beam Method: The Observation of Surface Structures”. In: *Journal of Applied Physics* 41.7 (June 1970), pp. 2780–2786. ISSN: 0021-8979. DOI: 10.1063/1.1659315.

[93] A. Y. Cho. “GaAs Epitaxy by a Molecular Beam Method: Observations of Surface Structure on the (001) Face”. In: *Journal of Applied Physics* 42.5 (Apr. 1971), pp. 2074–2081. ISSN: 0021-8979. DOI: 10.1063/1.1660490.

[94] K. Ploog et al. “MBE-grown insulating oxide films on GaAs”. In: *Journal of Vacuum Science and Technology* 16.2 (Mar. 1979), pp. 290–294. ISSN: 0022-5355. DOI: 10.1116/1.569929.

[95] Jean-Pierre Locquet. “In-situ MBE growth of epitaxial CuO films with a source of activated oxygen”. In: *Journal of the Less Common Metals* 164-165 (1990), pp. 300–306. ISSN: 0022-5088. DOI: https://doi.org/10.1016/0022-5088(90)90226-A.

[96] M. W. Ruckman, R. C. Budhani, and S. L. Qui. “Oxygenation and possible etching of high Tc superconducting films by oxygen plasma”. In: *AIP Conference Proceedings* 200.1 (Jan. 1990), pp. 114–121. ISSN: 0094-243X. DOI: 10.1063/1.39052.

[97] Bharat Jalan et al. “Analysis of carbon in SrTiO3 grown by hybrid molecular beam epitaxy”. In: *Journal of Vacuum Science & Technology A* 27.6 (Oct. 2009), pp. 1365–1368. ISSN: 0734-2101. DOI: 10.1116/1.3253355.

[98] V.M. Mecea et al. “Development and testing of a high temperature quartz crystal microbalance”. In: *Vacuum* 46.7 (1995), pp. 691–694. ISSN: 0042-207X. DOI: https://doi.org/10.1016/0042-207X(94)00147-2.

[99] S. Majumdar et al. “Development of multilayer oxidation resistant coatings on niobium and tantalum”. In: *Surface and Coatings Technology* 200.12 (2006), pp. 3713–3718. ISSN: 0257-8972. DOI: https://doi.org/10.1016/j.surfcoat.2005.01.034.

[100] K. Y. Cheng. “Development of molecular beam epitaxy technology for III–V compound semiconductor heterostructure devices”. In: *Journal of Vacuum Science & Technology A* 31.5 (Aug. 2013), p. 050814. ISSN: 0734-2101. DOI: 10.1116/1.4816932.

[101] W. Nunn et al. “Novel synthesis approach for ”stubborn” metals and metal oxides”. In: *Proceedings of the National Academy of Sciences of the United States of America* 118.32 (Aug. 2021), e2105713118. DOI: 10.1073/pnas.2105713118.

[102] M. B. Panish. “Molecular Beam Epitaxy of GaAs and InP with Gas Sources for As and P”. In: *Journal of The Electrochemical Society* 127.12 (Dec. 1980), p. 2729. DOI: 10.1149/1.2129580.

[103] E. Veuhoff et al. “Metalorganic CVD of GaAs in a molecular beam system”. In: *Journal of Crystal Growth* 55.1 (1981), pp. 30–34. ISSN: 0022-0248. DOI: 10.1016/0022-0248(81)90267-0.

[104] N Vodjdani, A Lemarchand, and H Paradan. “Parametric studies of GaAs growth by metalorganic molecular beam epitaxy”. In: *Le Journal de Physique Colloques* 43.C5 (1982), pp. C5–339.

[105] Eisuke TOKUMITSU and Kiyoshi TAKAHASHI. “Ultra-thin semiconductor films”. In: *Nihon Kessho Gakkaishi* 28.2 (1986), pp. 124–132.

[106] Bharat Jalan et al. “Growth of high-quality SrTiO3 films using a hybrid molecular beam epitaxy approach”. In: *Journal of Vacuum Science & Technology A* 27.3 (Mar. 2009), pp. 461–464. ISSN: 0734-2101. DOI: 10.1116/1.3106610.

[107] Bharat Jalan, Pouya Moetakef, and Susanne Stemmer. “Molecular beam epitaxy of SrTiO3 with a growth window”. In: *Applied Physics Letters* 95.3 (July 2009), p. 032906. ISSN: 0003-6951. DOI: 10.1063/1.3184767.

[108] Suresh Thapa et al. “Correlating surface stoichiometry and termination in SrTiO3 films grown by hybrid molecular beam epitaxy”. In: *Journal of Vacuum Science & Technology A* 39.5 (July 2021), p. 053203. ISSN: 0734-2101. DOI: 10.1116/6.0001159.

[109] Dow Chemical Company. *Syltherm^{TM} XLT Heat Transfer Fluid*. Accessed: 2024-05-22. 2024.

[110] Matthew Brahlek et al. “Frontiers in the Growth of Complex Oxide Thin Films: Past, Present, and Future of Hybrid MBE”. en. In: *Advanced Functional Materials* 28.9 (Feb. 2018), p. 1702772. ISSN: 1616-3028. DOI: 10.1002/adfm.201702772.

[111] H. Brune. “Growth Modes”. In: *Encyclopedia of Materials: Science and Technology, Sect. 1.9, Physical Properties of Thin Films and Artificial Multilayers*. Record Appears in: Scientific production and competences ¿ SB - School of Basic Sciences ¿ IPHYS - Institute of Physics ¿ LNS - Laboratory of Nanostructures at Surfaces, Peer-reviewed publications, Work produced at EPFL, Book chapters, Published. Pergamon, 2001, pp. 3683–3693.

[112] Frederick Charles Frank and Jan H. van der Merwe. “One-dimensional dislocations. I. Static theory”. In: *Proceedings of the Royal Society of London. Series A. Mathematical and Physical Sciences* 198.1053 (1949), pp. 205–216.

[113] Martin Volmer and A Weber. “Keimbildung in übersättigten Gebilden”. In: *Zeitschrift für physikalische Chemie* 119.1 (1926), pp. 277–301.

[114] I. N. Stranski and L. Krastanov. “Theory of orientation separation of ionic crystals”. In: *Berichte der Akademie der Wissenschaften in Wien* 146 (1938), p. 797.

[115] Wolfgang Braun. *Applied RHEED: Reflection High-Energy Electron Diffraction during Crystal Growth*. English. Vol. 154. Includes bibliographical references (p. [201]-210) and index. Berlin ; New York: Springer, 1999.

[116] Z. Mitura. “RHEED from epitaxially grown thin films”. In: *Surface Review and Letters* 06.03n04 (1999), pp. 497–516. DOI: 10.1142/S0218625X99000470.

[117] Łukasz Kokosza et al. “Simplified Determination of RHEED Patterns and Its Explanation Shown with the Use of 3D Computer Graphics”. In: *Materials* 14.11 (2021). ISSN: 1996-1944. DOI: 10.3390/ma14113056.

[118] *Creative Common Attribution 4.0 International (CC BY 4.0)*. Accessed: 2024-05-22. 2024.

[119] John E. Mahan et al. “A review of the geometrical fundamentals of reflection high-energy electron diffraction with application to silicon surfaces”. In: *Journal of Vacuum Science & Technology A* 8.5 (Sept. 1990), pp. 3692–3700. ISSN: 0734-2101. DOI: 10.1116/1.576481.

[120] Nassim Derriche et al. “Reflection High-Energy Electron Diffraction”. In: *Energy* 8.100keV (2019), 10–100eV.

[121] Yusuke Mizuno et al. “Flux growth of Sr2Ta2O7 crystals and subsequent nitridation to form SrTaO2N crystals”. In: *CrystEngComm* 15 (40 2013), pp. 8133–8138. DOI: 10.1039/C3CE41315B.

[122] Rajendra Paudel. “Band Engineering of Perovskite Ferrite Epitaxial Thin Films for OER Catalysis”. PhD Dissertation. Auburn, Alabama: Auburn University, Aug. 2022.

[123] M Dabrowska-Szata. “Analysis of RHEED pattern from semiconductor surfaces”. In: *Materials Chemistry and Physics* 81.2 (2003), pp. 257–259. ISSN: 0254-0584. DOI: https://doi.org/10.1016/S0254-0584(02)00569-2.

[124] Miles Blanchet. “Synthesis and Characterization of Mn-based Spinels Grown by Molecular Beam Epitaxy”. PhD thesis. Auburn, Alabama: Auburn University, May 2022.

[125] H. Hertz. “Ueber einen Einfluss des ultravioletten Lichtes auf die electrische Entladung”. In: *Annalen der Physik* 267.8 (1887), pp. 983–1000. DOI: https://doi.org/10.1002/andp.18872670827.

[126] Hiroyuki Matsuda, László Tóth, and Hiroshi Daimon. “Variable-deceleration-ratio wide-acceptance-angle electrostatic lens for two-dimensional angular and energy analysis”. In: *Review of Scientific Instruments* 89.12 (2018).

[127] I. Niedermaier et al. “Dual analyzer system for surface analysis dedicated for angle-resolved photoelectron spectroscopy at liquid surfaces and interfaces”. In: *Review of Scientific Instruments* 87 (2016), p. 045105.

[128] S. Karkare et al. “Development of a 3-D energy-momentum analyzer for meV-scale energy electrons”. In: *Review of Scientific Instruments* 90 (2019), p. 053902.

[129] M.P. Seah and W.A. Dench. “Quantitative electron spectroscopy of surfaces: A standard data base for electron inelastic mean free paths in solids”. In: *Surface and Interface Analysis* 1.2 (1979), p. 2.

[130] Peter M.A. Sherwood. “Rapid evaluation of the Voigt function and its use for interpreting X-ray photoelectron spectroscopic data”. In: *Surface and Interface Analysis* 51.2 (2019), pp. 254–274. DOI: https://doi.org/10.1002/sia.6577.

[131] Varun Jain, Mark C. Biesinger, and Matthew R. Linford. “The Gaussian-Lorentzian Sum, Product, and Convolution (Voigt) functions in the context of peak fitting X-ray photoelectron spectroscopy (XPS) narrow scans”. In: *Applied Surface Science* 447 (2018), pp. 548–553. ISSN: 0169-4332. DOI: https://doi.org/10.1016/j.apsusc.2018.03.190.

[132] N. Fairley, A. Carrick, and N. Fairley. *Recipes for XPS Data Processing*. Knutsford: Acolyte Science, 2005.

[133] D. R. Baer et al. “Practical Guides for X-Ray Photoelectron Spectroscopy: First Steps in Planning, Conducting, and Reporting XPS Measurements”. In: *Journal of Vacuum Science & Technology A* 37.3 (2019), p. 031401. DOI: 10.1116/1.5065501.

[134] D. Briggs and J.T. Grant. *Surface Analysis by Auger and X-Ray Photoelectron Spectroscopy*. Chichester, West Sussex, U.K.: IM Publications, 2003.

[135] Sharad Mahatara et al. “High Mobility Two-Dimensional Electron Gas at the BaSnO3/SrNbO3 Interface”. In: *ACS Applied Materials & Interfaces* 14.39 (2022). PMID: 36149756, pp. 45025–45031. DOI: 10.1021/acsami.2c12195.

[136] A. Segmüller, I. C. Noyan, and V. S. Speriosu. “X-Ray Diffraction Studies of Thin Films and Multilayer Structures”. In: *Progress in Crystal Growth and Characterization* 18 (1989), p. 21.

[137] Nicodemus Edwin Widjonarko. “Introduction to Advanced X-ray Diffraction Techniques for Polymeric Thin Films”. In: *Coatings* 6.4 (2016). ISSN: 2079-6412. DOI: 10.3390/coatings6040054.

[138] E. Chason and T. M. Mayer. “Thin film and surface characterization by specular X-ray reflectivity”. In: *Critical Reviews in Solid State and Materials Sciences* 22.1 (1997), pp. 1–67. DOI: 10.1080/10408439708241258.

[139] G. E. M. Jauncey. “The Scattering of X-Rays and Bragg’s Law”. In: *Proceedings of the National Academy of Sciences of the United States of America* 10 (1924), p. 57.

[140] Chu Ryang Wie. “High resolution x-ray diffraction characterization of semiconductor structures”. In: *Materials Science and Engineering: R: Reports* 13.1 (1994), pp. 1–56. ISSN: 0927-796X. DOI: https://doi.org/10.1016/0927-796X(94)90008-6.

[141] D. K. G. de Boer, A. J. G. Leenaers, and W. W. van den Hoogenhof. “Glancing-Incidence X-Ray Analysis of Thin-Layered Materials: A Review”. In: *X-Ray Spectrometry* 24 (1995), p. 91.

[142] Paul F. Fewster. “Reciprocal space mapping”. In: *Critical Reviews in Solid State and Materials Sciences* 22.2 (1997), pp. 69–110. DOI: 10.1080/10408439708241259.

[143] Mario Birkholz. *Thin Film Analysis by X-ray Scattering*. John Wiley & Sons, 2006.

[144] Grant S. Henderson, Frank M.F. de Groot, and Benjamin J.A. Moulton. “X-ray Absorption Near-Edge Structure (XANES) Spectroscopy”. In: *Reviews in Mineralogy and*

Geochemistry 78.1 (Jan. 2014), pp. 75–138. ISSN: 1529-6466. DOI: 10.2138/rmg.2014.78.3.

[145] David J. Griffiths and Darrell F. Schroeter. *Introduction to Quantum Mechanics*. 3rd ed. Cambridge University Press, 2018.

[146] Junko Yano and Vittal K. Yachandra. "X-ray absorption spectroscopy". In: *Photosynthesis Research* 102.2-3 (Nov. 2009), pp. 241–254. DOI: 10.1007/s11120-009-9473-8.

[147] G. Lüpke. "Characterization of semiconductor interfaces by second-harmonic generation". In: *Surface Science Reports* 35.3 (1999), pp. 75–161. ISSN: 0167-5729. DOI: https://doi.org/10.1016/S0167-5729(99)00007-2.

[148] Joachim Mayer et al. "TEM Sample Preparation and FIB-Induced Damage". In: *MRS Bulletin* 32.5 (2007), pp. 400–407. DOI: 10.1557/mrs2007.63.

[149] C.J. Humphreys. "Fundamental concepts of stem imaging". In: *Ultramicroscopy* 7.1 (1981), pp. 7–12. ISSN: 0304-3991. DOI: https://doi.org/10.1016/0304-3991(81)90017-6.

[150] S.J. Pennycook. "Seeing the atoms more clearly: STEM imaging from the Crewe era to today". In: *Ultramicroscopy* 123 (2012). Albert Victor Crewe Memorial Issue, pp. 28–37. ISSN: 0304-3991. DOI: https://doi.org/10.1016/j.ultramic.2012.05.005.

[151] Michiyoshi Tanaka and Kenji Tsuda. "Convergent-beam electron diffraction". In: *Journal of Electron Microscopy* 60.suppl_1 (Aug. 2011), S245–S267. ISSN: 0022-0744. DOI: 10.1093/jmicro/dfr038.

[152] Patrick Cordier. "Dislocations and Slip Systems of Mantle Minerals". In: *Reviews in Mineralogy and Geochemistry* 51.1 (Jan. 2002), pp. 137–179. ISSN: 1529-6466. DOI: 10.2138/gsrmg.51.1.137.

[153] Karen C. Bustillo et al. “4D-STEM of Beam-Sensitive Materials”. In: *Accounts of Chemical Research* 54.11 (2021). PMID: 33979131, pp. 2543–2551. DOI: 10.1021/acs.accounts.1c00073.

[154] Bartosz Michalski and Małgorzata Plechawska-Wójcik. “Comparison of LeNet-5, AlexNet and GoogLeNet models in handwriting recognition”. In: *Journal of Computer Sciences Institute* 23 (June 2022), pp. 145–151. DOI: 10.35784/jcsi.2919.

[155] Jun-Yan Zhu et al. “Unpaired Image-to-Image Translation Using Cycle-Consistent Adversarial Networks”. In: *2017 IEEE International Conference on Computer Vision (ICCV)*. 2017, pp. 2242–2251. DOI: 10.1109/ICCV.2017.244.

[156] Alex Belianinov et al. “Big data and deep data in scanning and electron microscopies: deriving functionality from multidimensional data sets”. In: *Advanced Structural and Chemical Imaging* 1.1 (May 2015), p. 6. ISSN: 2198-0926. DOI: 10.1186/s40679-015-0006-6.

[157] Alex Belianinov et al. “Big data and deep data in scanning and electron microscopies: deriving functionality from multidimensional data sets”. In: *Advanced Structural and Chemical Imaging* 1.1 (May 2015), p. 6. ISSN: 2198-0926. DOI: 10.1186/s40679-015-0006-6.

[158] Sergei V. Kalinin et al. “Big, Deep, and Smart Data in Scanning Probe Microscopy”. In: *ACS Nano* 10.10 (2016). PMID: 27676453, pp. 9068–9086. DOI: 10.1021/acsnano.6b04212.

[159] Evgheni Strelcov et al. “Deep Data Analysis of Conductive Phenomena on Complex Oxide Interfaces: Physics from Data Mining”. In: *ACS Nano* 8.6 (2014). PMID: 24869675, pp. 6449–6457. DOI: 10.1021/nn502029b.

[160] Rama K. Vasudevan et al. “Big data in reciprocal space: Sliding fast Fourier transforms for determining periodicity”. In: *Applied Physics Letters* 106.9 (Mar. 2015), p. 091601. ISSN: 0003-6951. DOI: 10.1063/1.4914016.

[161] Kevin Kaufmann et al. “Crystal symmetry determination in electron diffraction using machine learning”. In: *Science* 367.6477 (2020), pp. 564–568. DOI: 10.1126/science.aay3062.

[162] Steven B. Torrisi et al. “Random forest machine learning models for interpretable X-ray absorption near-edge structure spectrum-property relationships”. In: *npj Computational Materials* 6.1 (July 2020), p. 109. ISSN: 2057-3960. DOI: 10.1038/s41524-020-00376-6.

[163] Keisuke Takahashi and Lauren Takahashi. “Creating Machine Learning-Driven Material Recipes Based on Crystal Structure”. In: *The Journal of Physical Chemistry Letters* 10.2 (2019), pp. 283–288. DOI: 10.1021/acs.jpclett.8b03527.

[164] K.K. Lee et al. “Using neural networks to construct models of the molecular beam epitaxy process”. In: *IEEE Transactions on Semiconductor Manufacturing* 13.1 (2000), pp. 34–45. DOI: 10.1109/66.827338.

[165] Salvador García et al. “Big data preprocessing: methods and prospects”. In: *Big Data Analytics* 1.1 (Nov. 2016), p. 9. DOI: 10.1186/s41044-016-0014-0.

[166] V. Çetin and O. Yıldız. “A comprehensive review on data preprocessing techniques in data analysis”. In: *Pamukkale Üniversitesi Mühendislik Bilimleri Dergisi* 28.2 (2022), pp. 299–312.

[167] Svante Wold, Kim Esbensen, and Paul Geladi. “Principal component analysis”. In: *Chemometrics and Intelligent Laboratory Systems* 2.1 (1987). Proceedings of the Multivariate Statistical Workshop for Geologists and Geochemists, pp. 37–52. ISSN: 0169-7439. DOI: https://doi.org/10.1016/0169-7439(87)80084-9.

[168] Michael Greenacre et al. “Principal component analysis”. In: *Journal of Physics D: Applied Physics* 2.1 (Dec. 2022). DOI: 10.1038/s43586-022-00184-w.

[169] Hervé Abdi and Lynne J. Williams. “Principal component analysis”. In: *WIREs Computational Statistics* 2.4 (2010), pp. 433–459. DOI: https://doi.org/10.1002/wics.101.

[170] Michael E. Wall, Andreas Rechtsteiner, and Luis M. Rocha. “Singular Value Decomposition and Principal Component Analysis”. In: *A Practical Approach to Microarray Data Analysis*. Ed. by Daniel P. Berrar, Werner Dubitzky, and Martin Granzow. Boston, MA: Springer US, 2003, pp. 91–109. ISBN: 978-0-306-47815-4. DOI: 10.1007/0-306-47815-3_5.

[171] Hong Jiang and Kent M. Eskridge. “Bias in Principal Components Analysis Due to Correlated Observations”. In: *Conference on Applied Statistics in Agriculture* (2000). DOI: 10.4148/2475-7772.1247.

[172] Shi Na, Liu Xumin, and Guan Yong. “Research on k-means Clustering Algorithm: An Improved k-means Clustering Algorithm”. In: *2010 Third International Symposium on Intelligent Information Technology and Security Informatics*. 2010, pp. 63–67. DOI: 10.1109/IITSI.2010.74.

[173] Wan-Lei Zhao, Cheng-Hao Deng, and Chong-Wah Ngo. “k-means: A revisit”. In: *Neurocomputing* 291 (2018), pp. 195–206. ISSN: 0925-2312. DOI: https://doi.org/10.1016/j.neucom.2018.02.072.

[174] Steven J. Rigatti. “Random Forest”. In: *Journal of Insurance Medicine* 47.1 (Jan. 2017), pp. 31–39. ISSN: 0743-6661. DOI: 10.17849/insm-47-01-31-39.1.

[175] Yaoshiang Ho and Samuel Wookey. “The Real-World-Weight Cross-Entropy Loss Function: Modeling the Costs of Mislabeling”. In: *IEEE Access* 8 (2020), pp. 4806–4813. DOI: 10.1109/ACCESS.2019.2962617.

[176] Zhou Wang and Alan C. Bovik. “Mean squared error: Love it or leave it? A new look at Signal Fidelity Measures”. In: *IEEE Signal Processing Magazine* 26.1 (2009), pp. 98–117. DOI: 10.1109/MSP.2008.930649.

[177] Bjoern H. Menze et al. “A comparison of random forest and its Gini importance with standard chemometric methods for the feature selection and classification of spectral data”. In: *BMC Bioinformatics* 10.1 (July 2009), p. 213. ISSN: 1471-2105. DOI: 10.1186/1471-2105-10-213.

[178] Te Han et al. “Comparison of random forest, artificial neural networks and support vector machine for intelligent diagnosis of rotating machinery”. In: *Transactions of the Institute of Measurement and Control* 40.8 (2018), pp. 2681–2693. DOI: 10.1177/0142331217708242.

[179] Anna Bosch, Andrew Zisserman, and Xavier Munoz. “Image Classification using Random Forests and Ferns”. In: *2007 IEEE 11th International Conference on Computer Vision*. 2007, pp. 1–8. DOI: 10.1109/ICCV.2007.4409066.

[180] Giacomo Indiveri and Shih-Chii Liu. “Memory and Information Processing in Neuromorphic Systems”. In: *Proceedings of the IEEE* 103.8 (Aug. 2015), pp. 1379–1397. ISSN: 1558-2256. DOI: 10.1109/JPROC.2015.2444094.

[181] Kevin Gurney. *An Introduction to Neural Networks*. 1st. CRC Press, 1997. DOI: 10.1201/9781315273570.

[182] Aurelien Geron. *Hands-On Machine Learning with Scikit-Learn, Keras, and TensorFlow: Concepts, Tools, and Techniques to Build Intelligent Systems*. 2nd. O’Reilly Media, Inc., 2019. ISBN: 1492032646.

[183] Andrea Apicella et al. “A survey on modern trainable activation functions”. In: *Neural Networks* 138 (2021), pp. 14–32. ISSN: 0893-6080. DOI: https://doi.org/10.1016/j.neunet.2021.01.026.

[184] Saad Hikmat Haji and Adnan Mohsin Abdulazeez. “Comparison of Optimization Techniques Based on Gradient Descent Algorithm: A Review”. In: *PalArch’s Journal of Archaeology of Egypt / Egyptology* 18.4 (Feb. 2021), pp. 2715–2743.

[185] Shibani Santurkar et al. “How Does Batch Normalization Help Optimization?” In: *Advances in Neural Information Processing Systems*. Ed. by S. Bengio et al. Vol. 31. Curran Associates, Inc., 2018.

[186] Jin Xu et al. “Reluplex made more practical: Leaky ReLU”. In: *2020 IEEE Symposium on Computers and Communications (ISCC)*. 2020, pp. 1–7. DOI: 10.1109/ISCC50000.2020.9219587.

[187] Yann LeCun et al. “Handwritten Digit Recognition with a Back-Propagation Network”. In: *Advances in Neural Information Processing Systems*. Ed. by D. Touretzky. Vol. 2. Morgan-Kaufmann, 1989.

[188] Haris Iqbal. *HarisIqbal88/PlotNeuralNet v1.0.0*. Version v1.0.0. Dec. 2018. DOI: 10.5281/zenodo.2526396.

[189] Glority Global Group Ltd. *PictureThis - Plant Identifier*. App Store [iOS]. Accessed: 2024-05-22. 2024.

[190] baeldung. *What Is the Purpose of a Feature Map in a Convolutional Neural Network*. Accessed: May 24, 2023. 2023.

[191] Zijun Zhang. “Improved Adam Optimizer for Deep Neural Networks”. In: *2018 IEEE/ACM 26th International Symposium on Quality of Service (IWQoS)*. June 2018, pp. 1–2. DOI: 10.1109/IWQoS.2018.8624183.

[192] Koby Crammer, Alex Kulesza, and Mark Dredze. “Adaptive regularization of weight vectors”. In: *Machine Learning* 91.2 (May 2013), pp. 155–187. ISSN: 1573-0565. DOI: 10.1007/s10994-013-5327-x.

[193] W. M. P. van der Aalst et al. “Process mining: a two-step approach to balance between underfitting and overfitting”. In: *Software & Systems Modeling* 9.1 (Jan. 2010), pp. 87–111. ISSN: 1619-1374. DOI: 10.1007/s10270-008-0106-z.

[194] Zhun Wei and Xudong Chen. “Physics-Inspired Convolutional Neural Network for Solving Full-Wave Inverse Scattering Problems”. In: *IEEE Transactions on Antennas and Propagation* 67.9 (Sept. 2019), pp. 6138–6148. ISSN: 1558-2221. DOI: 10.1109/TAP.2019.2922779.

[195] Han Gao, Luning Sun, and Jian-Xun Wang. “Super-resolution and denoising of fluid flow using physics-informed convolutional neural networks without high-resolution labels”. In: *Physics of Fluids* 33.7 (July 2021), p. 073603. ISSN: 1070-6631. DOI: 10.1063/5.0054312.

[196] Shengze Cai et al. “Physics-Informed Neural Networks for Heat Transfer Problems”. In: *Journal of Heat Transfer* 143.6 (Apr. 2021), p. 060801. ISSN: 0022-1481. DOI: 10.1115/1.4050542.

[197] T. Sakamoto et al. “Well defined superlattice structures made by phase-locked epitary using RHEED intensity oscillations”. In: *Superlattices and Microstructures* 1.4 (1985), pp. 347–352. ISSN: 0749-6036. DOI: https://doi.org/10.1016/0749-6036(85)90097-7.

[198] Michael Griebel and Helmut Harbrecht. “Singular value decomposition versus sparse grids: refined complexity estimates”. In: *IMA Journal of Numerical Analysis* 39.4 (July 2018), pp. 1652–1671. ISSN: 0272-4979. DOI: 10.1093/imanum/dry039.

[199] Xin Liu, Zaiwen Wen, and Yin Zhang. “Limited Memory Block Krylov Subspace Optimization for Computing Dominant Singular Value Decompositions”. In: *SIAM Journal on Scientific Computing* 35.3 (2013), A1641–A1668. DOI: 10.1137/120871328.

[200] Y. Eren Suyolcu et al. “Engineering ordered arrangements of oxygen vacancies at the surface of superconducting La2CuO4 thin films”. In: *Journal of Vacuum Science & Technology A* 40.1 (Dec. 2021), p. 013214. ISSN: 0734-2101. DOI: 10.1116/6.0001473.

[201] Halid Mulaosmanovic et al. “Ferroelectric field-effect transistors based on HfO2: a review”. In: *Nanotechnology* 32.50 (2021), p. 502002.

[202] M. Sousa et al. “Optical properties of epitaxial SrHfO3 thin films grown on Si”. In: *Journal of Applied Physics* 102.10 (Nov. 2007), p. 104103. ISSN: 0021-8979. DOI: 10.1063/1.2812425.

[203] Brendan J. Kennedy, Christopher J. Howard, and Bryan C. Chakoumakos. “High-temperature phase transitions in $SrHfO_3$”. In: *Phys. Rev. B* 60 (5 Aug. 1999), pp. 2972–2975. DOI: 10.1103/PhysRevB.60.2972.

[204] K. Black et al. “SrHfO3 Films Grown on Si(100) by Plasma-Assisted Atomic Layer Deposition.” In: *Chemistry of Materials* 23.10 (2011), pp. 2518–2520. DOI: 10.1021/cm200315u.

[205] Hosein Shahmirzaee and Reza Mardani. “Enhancement of piezoelectricity of tetragonal P4mm SrHfO3 under uniaxial stress: A first principle study”. In: *Computational Condensed Matter* 14 (2018), pp. 46–48. ISSN: 2352-2143. DOI: https://doi.org/10.1016/j.cocom.2017.12.006.

[206] Lauren M. Garten et al. “Theory-Guided Synthesis of a Metastable Lead-Free Piezoelectric Polymorph”. In: *Advanced Materials* 30.25 (2018), p. 1800559. DOI: https://doi.org/10.1002/adma.201800559.

[207] R. Vali. “Structural phases of SrHfO3”. In: *Solid State Communications* 148.1 (2008), pp. 29–31. ISSN: 0038-1098. DOI: https://doi.org/10.1016/j.ssc.2008.07.018.

[208] Safari Amisi. “First-principles study of structural and vibrational properties of SrHfO3 compared to SrZrO3”. In: *Computational Condensed Matter* 20 (2019), e00383. ISSN: 2352-2143. DOI: https://doi.org/10.1016/j.cocom.2019.e00383.

[209] Megha Acharya et al. “Exploring the $Pb_{1-X}Sr_XHfO3$ System and Potential for High Capacitive Energy Storage Density and Efficiency”. In: *Advanced Materials* 34.1 (2022), p. 2105967. DOI: https://doi.org/10.1002/adma.202105967.

[210] A. M. Glazer. “The classification of tilted octahedra in perovskites”. In: *Acta Crystallographica Section B* 28.11 (Nov. 1972). DOI: 10.1107/S0567740872007976.

[211] A. M. Glazer. “Simple ways of determining perovskite structures”. In: *Acta Crystallographica Section A* 31.6 (Nov. 1975). DOI: 10.1107/S0567739475001635.

[212] Raphaël Aeschlimann et al. “A Living-Dead Magnetic Layer at the Surface of Ferrimagnetic DyTiO3 Thin Films”. In: *Advanced Materials* 30.29 (2018), p. 1707489. DOI: https://doi.org/10.1002/adma.201707489.

[213] Shaked Caspi et al. “Effect of capping layers on the near-surface region of SrVO3 films”. In: *Journal of Vacuum Science & Technology A* 40.1 (Dec. 2021), p. 013208. ISSN: 0734-2101. DOI: 10.1116/6.0001419.

[214] Zhicheng Zhong and Philipp Hansmann. “Band Alignment and Charge Transfer in Complex Oxide Interfaces”. In: *Phys. Rev. X* 7 (1 Mar. 2017), p. 011023. DOI: 10.1103/PhysRevX.7.011023.

[215] Gaurab Rimal and Ryan B Comes. “Advances in complex oxide quantum materials through new approaches to molecular beam epitaxy”. In: *Journal of Physics D: Applied Physics* 57.19 (2024), p. 193001.

[216] Kate M. Adkison et al. “Suitability of binary oxides for molecular-beam epitaxy source materials: A comprehensive thermodynamic analysis”. In: *APL Materials* 8.8 (Aug. 2020), p. 081110. DOI: 10.1063/5.0013159.

[217] Dennis M. Hausmann et al. “Atomic Layer Deposition of Hafnium and Zirconium Oxides Using Metal Amide Precursors”. In: *Chemistry of Materials* 14.10 (2002), pp. 4350–4358. DOI: 10.1021/cm020357x.

[218] Suresh Thapa et al. “Probing surfaces and interfaces in complex oxide films via in situ X-ray photoelectron spectroscopy”. en. In: *Journal of Materials Research* 36.1 (Jan. 2021), pp. 26–51. ISSN: 2044-5326. DOI: 10.1557/s43578-020-00070-9.

[219] G. Kresse and J. Furthmüller. “Efficiency of ab-initio total energy calculations for metals and semiconductors using a plane-wave basis set”. In: *Computational Materials Science* 6.1 (1996), pp. 15–50. ISSN: 0927-0256. DOI: https://doi.org/10.1016/0927-0256(96)00008-0.

[220] G. Kresse and J. Furthmüller. “Efficient iterative schemes for ab initio total-energy calculations using a plane-wave basis set”. In: *Phys. Rev. B* 54 (16 Oct. 1996), pp. 11169–11186. DOI: 10.1103/PhysRevB.54.11169.

[221] John P. Perdew, Kieron Burke, and Matthias Ernzerhof. “Generalized Gradient Approximation Made Simple”. In: *Phys. Rev. Lett.* 77 (18 Oct. 1996), pp. 3865–3868. DOI: 10.1103/PhysRevLett.77.3865.

[222] P. E. Blöchl. “Projector augmented-wave method”. In: *Phys. Rev. B* 50 (24 Dec. 1994), pp. 17953–17979. DOI: 10.1103/PhysRevB.50.17953.

[223] G. Kresse and D. Joubert. “From ultrasoft pseudopotentials to the projector augmented-wave method”. In: *Phys. Rev. B* 59 (3 Jan. 1999), pp. 1758–1775. DOI: 10.1103/PhysRevB.59.1758.

[224] Benjamin H Savitzky et al. “py4DSTEM: A Software Package for Four-Dimensional Scanning Transmission Electron Microscopy Data Analysis”. In: *Microscopy and Microanalysis* 27.4 (Aug. 2021). DOI: 10.1017/S1431927621000477.

[225] Deok-Yong Cho, Hyung-Suk Jung, and Cheol Seong Hwang. “Structural properties and electronic structure of HfO 2-ZrO 2 composite films”. In: *Physical Review B—Condensed Matter and Materials Physics* 82.9 (2010), p. 094104.

[226] S.J. Pennycook and D.E. Jesson. “High-resolution Z-contrast imaging of crystals”. In: *Ultramicroscopy* 37.1 (1991), pp. 14–38. ISSN: 0304-3991. DOI: https://doi.org/10.1016/0304-3991(91)90004-P.

[227] D. Cherrad and D. Maouche. “Structural, electronic and optical properties of SrHfO3 (I4/mcm, Imma, Cmcm, P4/mbm and P4mm) phases”. In: *Physica B: Condensed Matter* 405.18 (2010), pp. 3862–3868. ISSN: 0921-4526. DOI: https://doi.org/10.1016/j.physb.2010.06.018.

[228] J. G. Connell et al. “Preparation of atomically flat SrTiO3 surfaces using a deionized-water leaching and thermal annealing procedure”. In: *Applied Physics Letters* 101.25 (Dec. 2012), p. 251607. ISSN: 0003-6951. DOI: 10.1063/1.4773052.

[229] D. J. Groenendijk and S. Gariglio. “Sequential pulsed laser deposition of homoepitaxial SrTiO3 thin films”. In: *Journal of Applied Physics* 120.22 (Dec. 2016), p. 225307. ISSN: 0021-8979. DOI: 10.1063/1.4971865.

[230] A. Herklotz et al. “Stoichiometry control of complex oxides by sequential pulsed-laser deposition from binary-oxide targets”. In: *Applied Physics Letters* 106.13 (Apr. 2015), p. 131601. ISSN: 0003-6951. DOI: 10.1063/1.4916948.

Appendix

In addition to the DFT model described in the main paper, 2 additional models were investigated. These subsequent models followed the same process and calculations as the first, with the only difference being how the ϵ_{33} value was determined. For the first model, ϵ_{33} was calculated using $\epsilon_{33} = \frac{-\nu}{1-\nu}(\epsilon_{11} + \epsilon_{22})$ where ν is the Poisson's ratio calculated from our experimental data. For the second model, ϵ_{33} was held constant at 0.0 while ϵ_{11} and ϵ_{22} varied. For the third model, ϵ_{33} was calculated such that the unit cell volume was held constant as ϵ_{11} and ϵ_{22} varied.

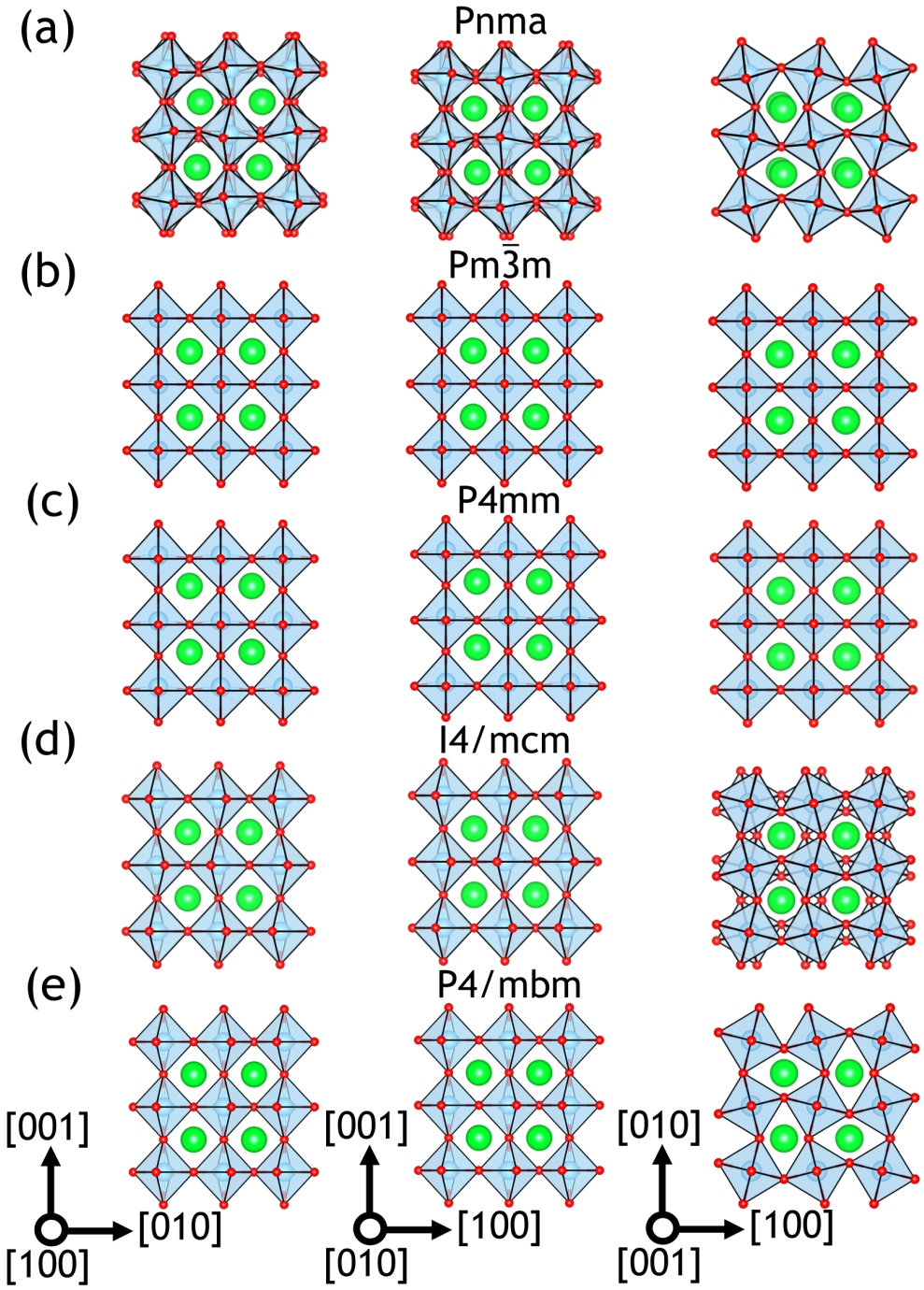

Figure A.1: (a) Pnma, (b) Pm$\bar{3}$m, (c) P4mm, (d) I4/mcm, and (e) P4/mbm crystal structures with 3% in-plane strain along with the respective crystallographic orientations. The crystallographic orientations correspond to a pseudocubic unit cell.

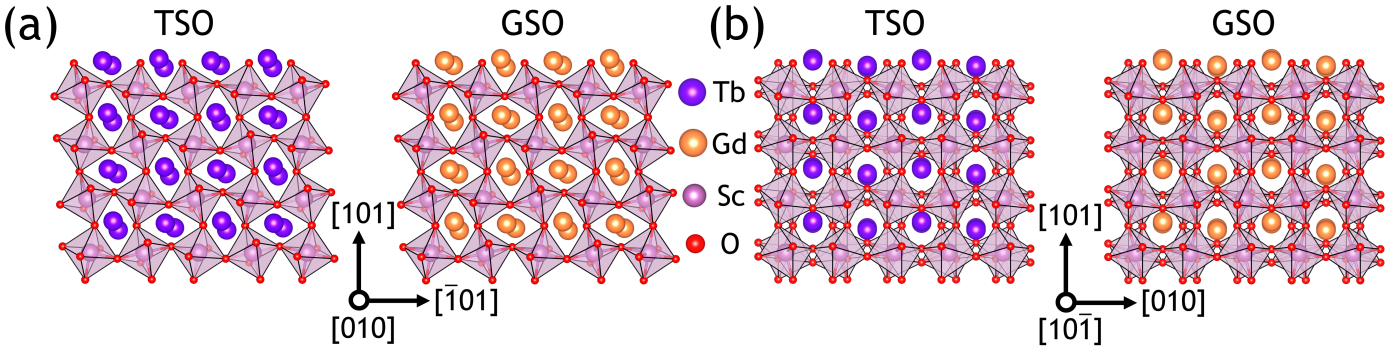

Figure A.2: Atomic models showing the TSO and GSO substrate orientations used for SHO growth along (a) [010] and (b) [10$\bar{1}$].

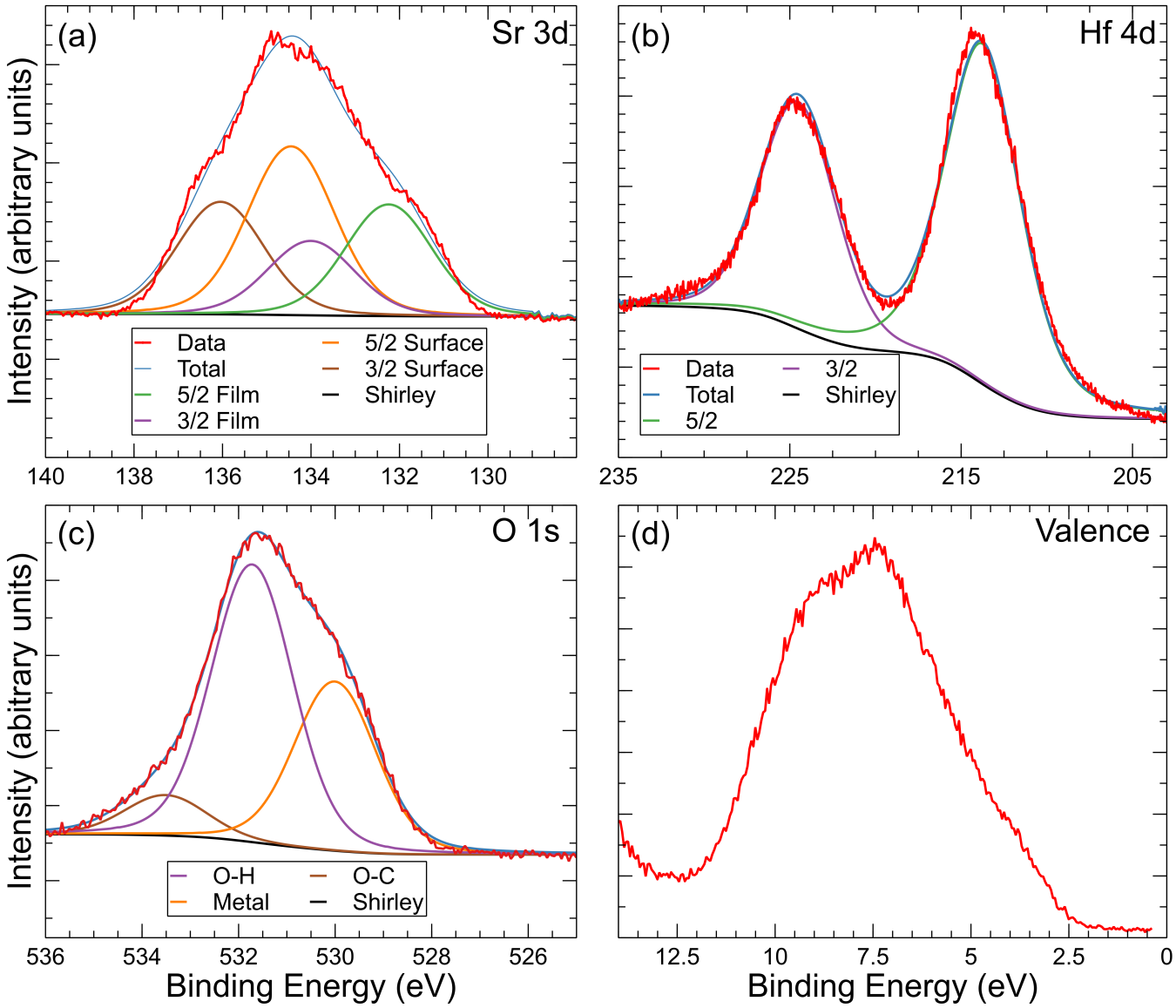

Figure A.3: (a-c) XPS data from a SHO-TSO sample for Sr 3d, Hf 4d, and O 1s transitions. The Sr 3d (a) and O 1s (b) spectra contain additional peaks consistent with oxidation of the top Sr mono layer. (d) Valence band spectra for the same sample.

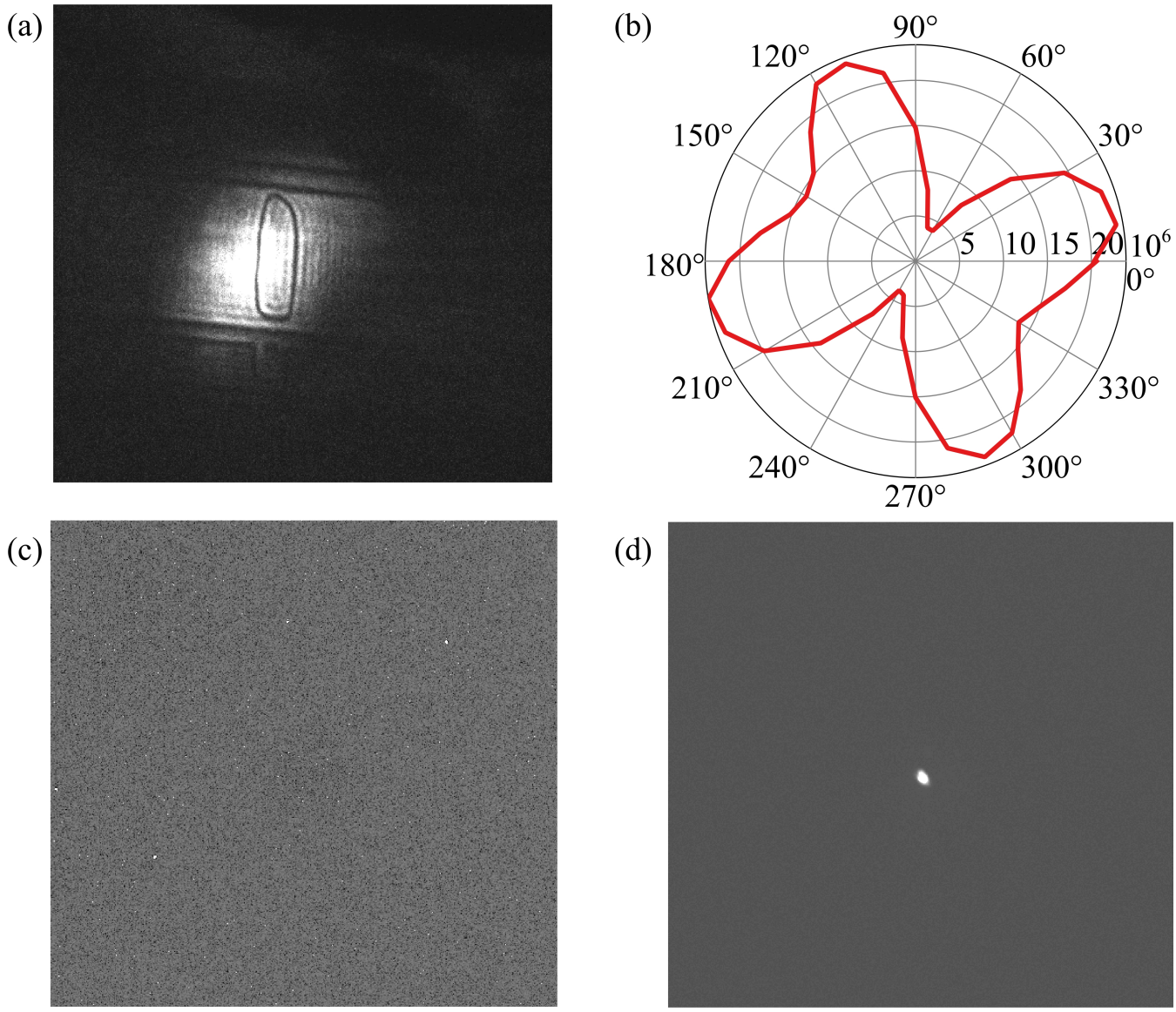

Figure A.4: (a) EMCCD camera image of BaTiO3 SHG pattern. (b) SHG signal for BaTiO3. (c) EMCCD camera image of SHO-TSO showing no SHG signal. (d) EMCCD camera of direct beam signal.

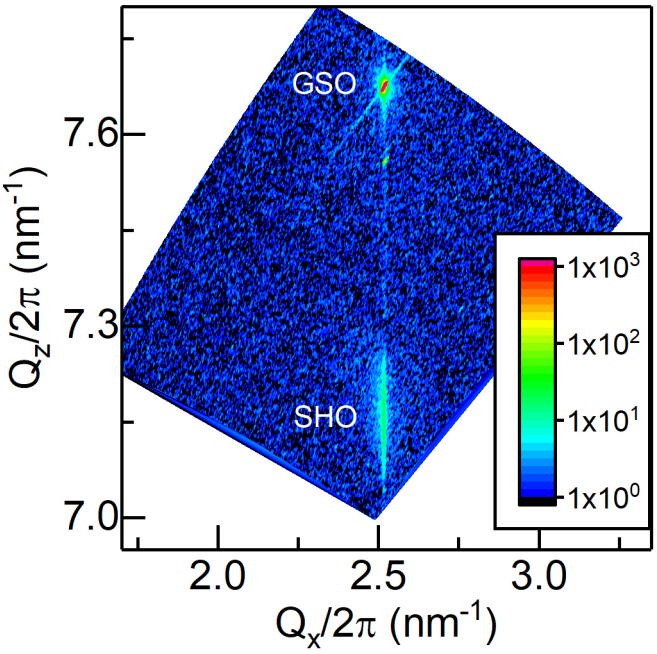

Figure A.5: RSM of an SHO-GSO sample showing the SHO film is not relaxed and has the same in plane lattice parameter as the GSO substrate.

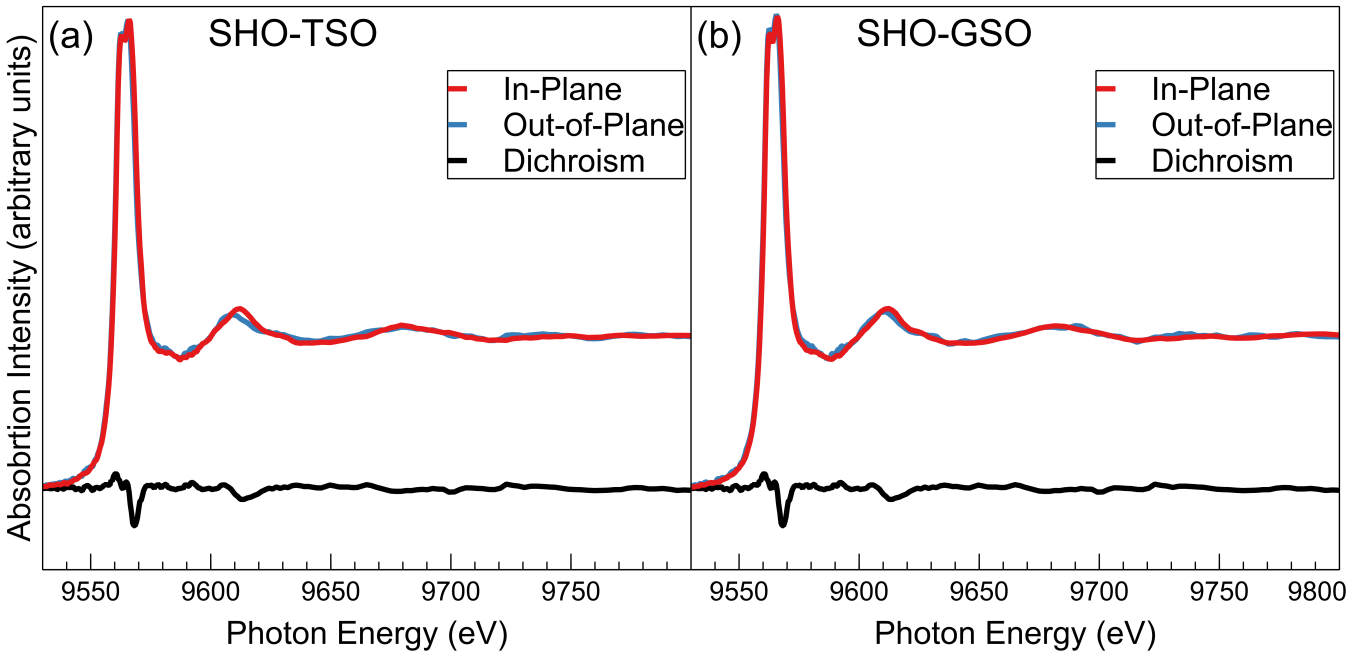

Figure A.6: Wide view of the XAS data shown in the main paper.

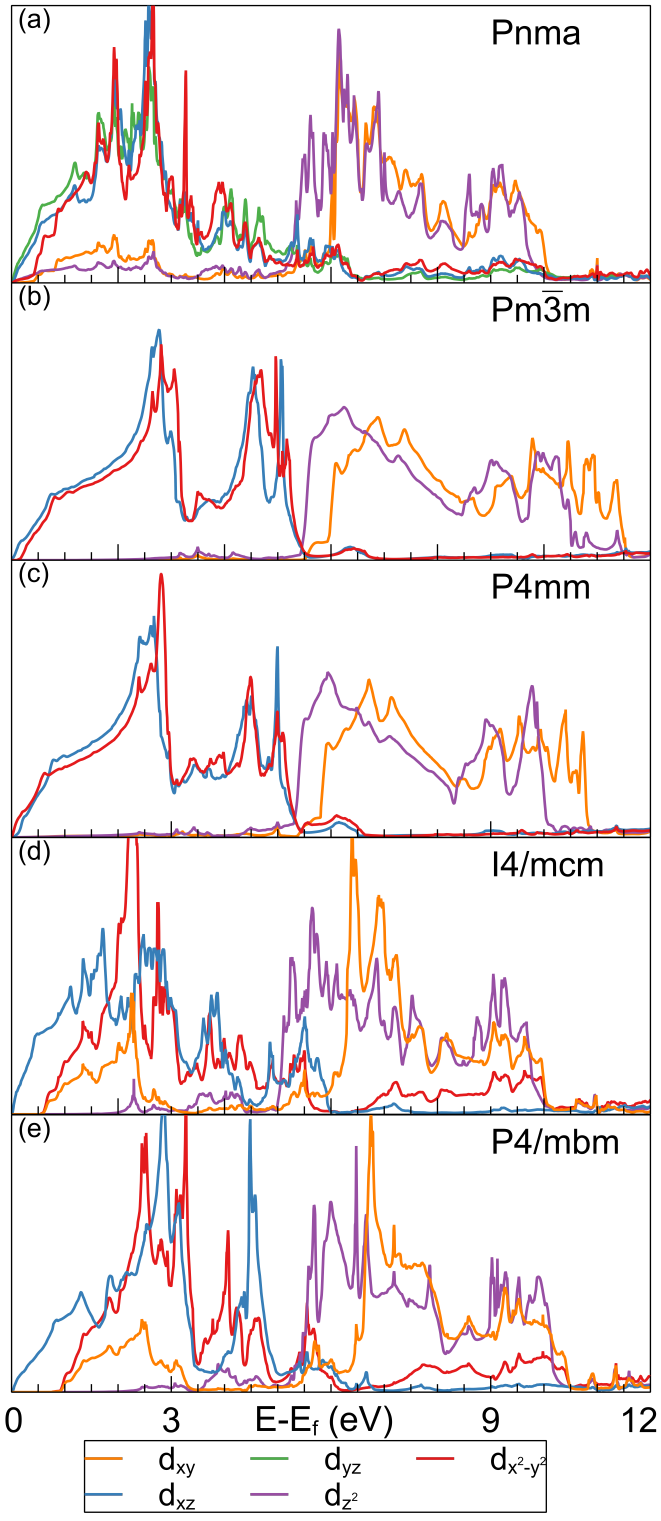

Figure A.7: The eDOS for the Pnma, Pm$\bar{3}$m, P4mm, I4/mcm, and P4/mbm phases for the DFT model where ϵ_{33} was held constant at 0.0.

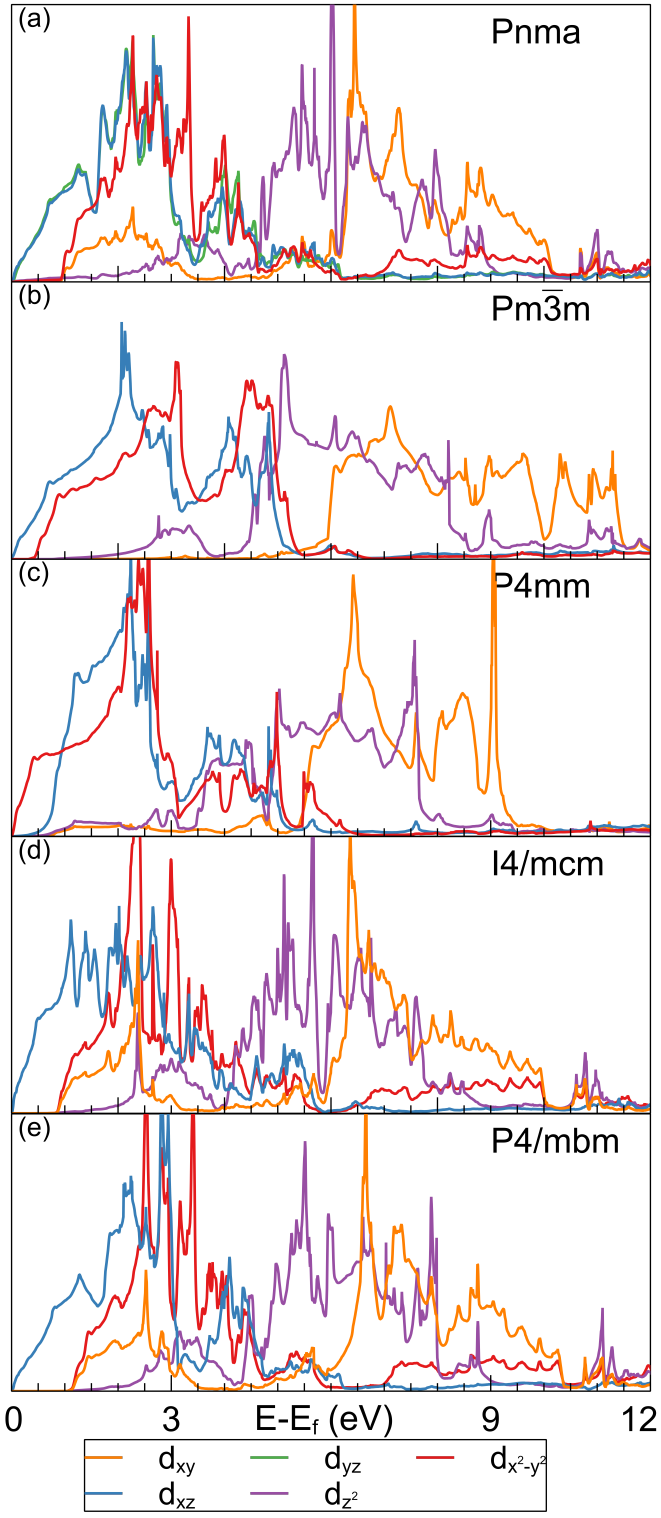

Figure A.8: The eDOS for the Pnma, Pm$\bar{3}$m, P4mm, I4/mcm, and P4/mbm phases for the DFT model where the unit cell volume was held constant.

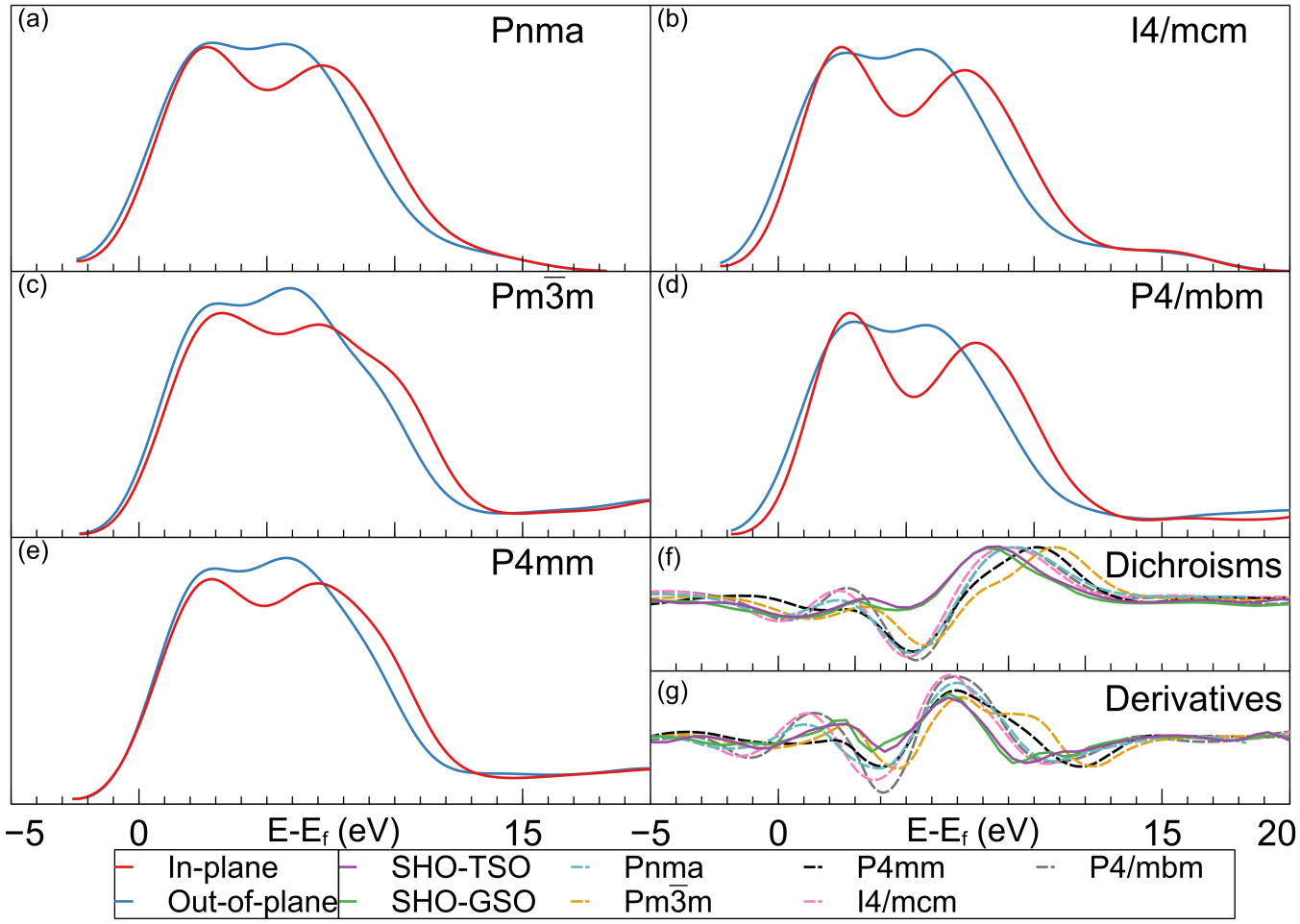

Figure A.9: (a-e) Gaussian convolutions of the eDOS for the 5 phases of SHO modeled by DFT where ϵ_{33} was calculated using Poisson's ratio. (f),(g) The dichroisms and the first derivative of the dichroisms, respectively, for the 5 phases modeled with DFT and the XAS data.

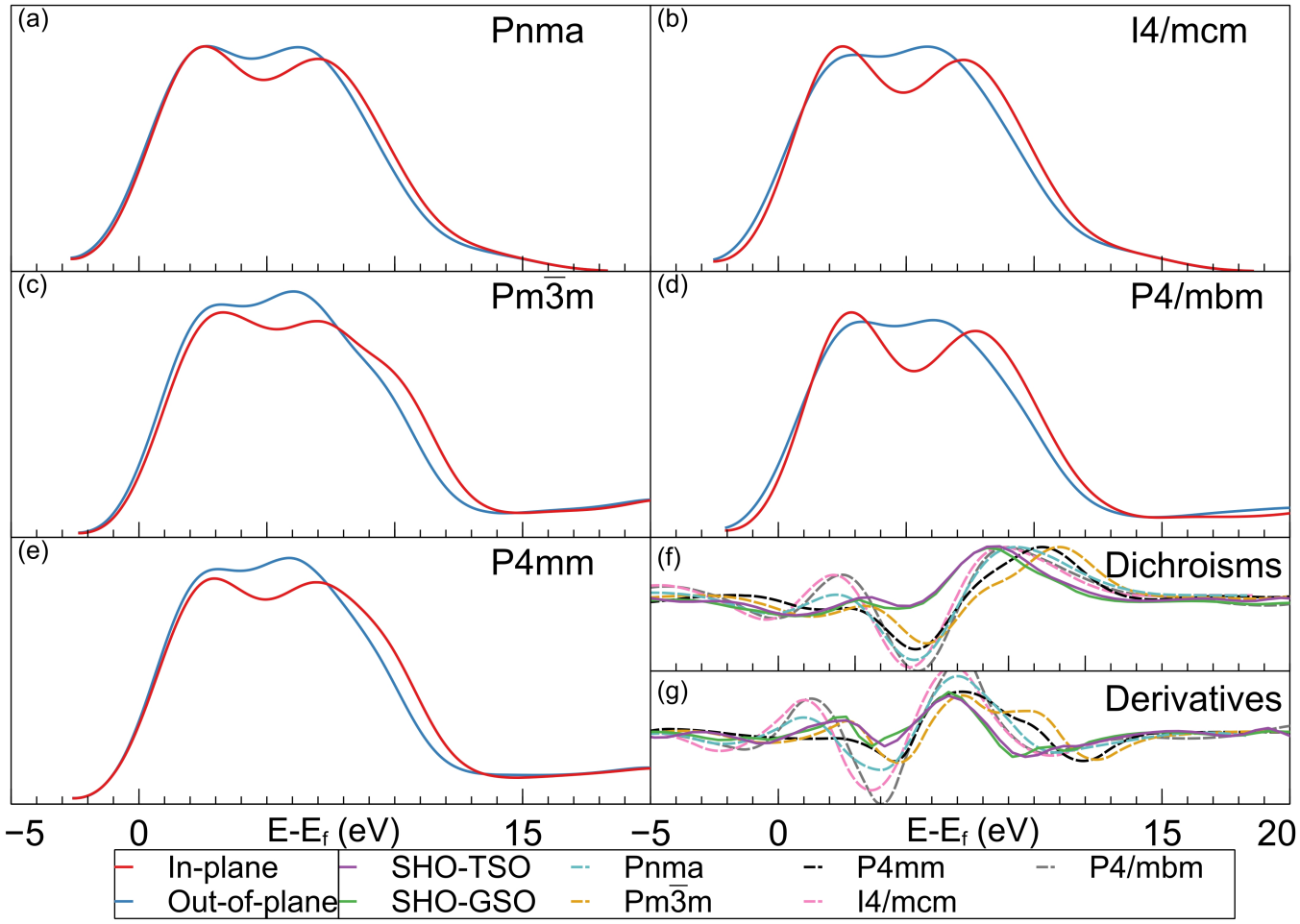

Figure A.10: (a-e) Gaussian convolutions of the eDOS for the 5 phases of SHO modeled by DFT where ϵ_{33} was held constant at 0.0. (f),(g) The dichroisms and the first derivative of the dichroisms, respectively, for the 5 phases modeled with DFT and the XAS data.

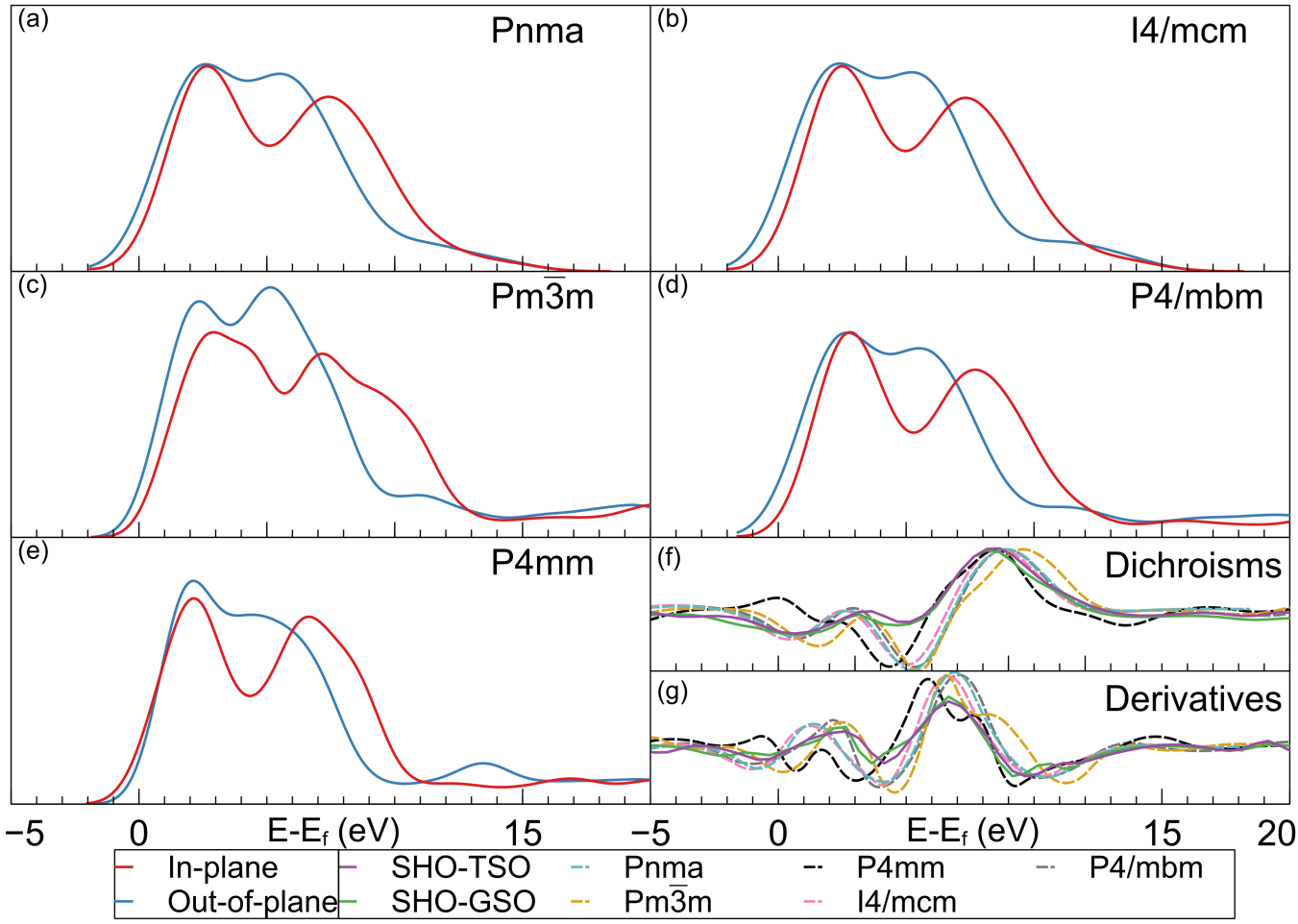

Figure A.11: (a-e) Gaussian convolutions of the eDOS for the 5 phases of SHO modeled by DFT where ϵ_{33} was calculated to hold the volume of the unit cell constant. (f),(g) The dichroisms and the first derivative of the dichroisms, respectively, for the 5 phases modeled with DFT and the XAS data.

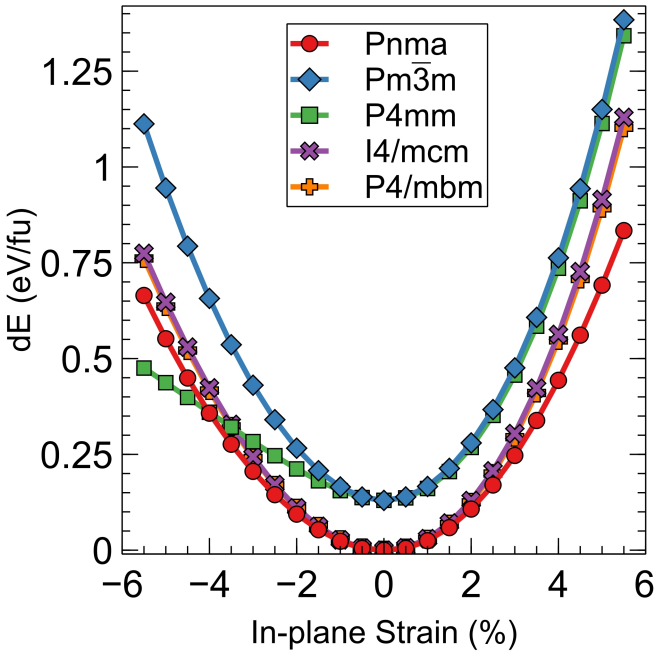

Figure A.12: Plot of the change in energy from the ground state for SHO as a function of in-plane strain for the 5 phases modeled with DFT where ϵ_{33} was calculated to hold the volume of the unit cell constant.

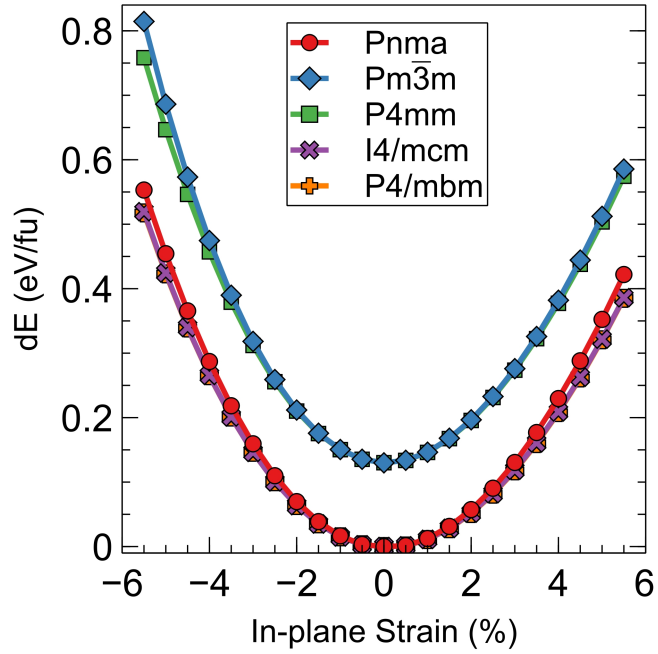

Figure A.13: Plot of the change in energy from the ground state for SHO as a function of in-plane strain for the 5 phases modeled with DFT where ϵ_{33} was held constant at 0.0.

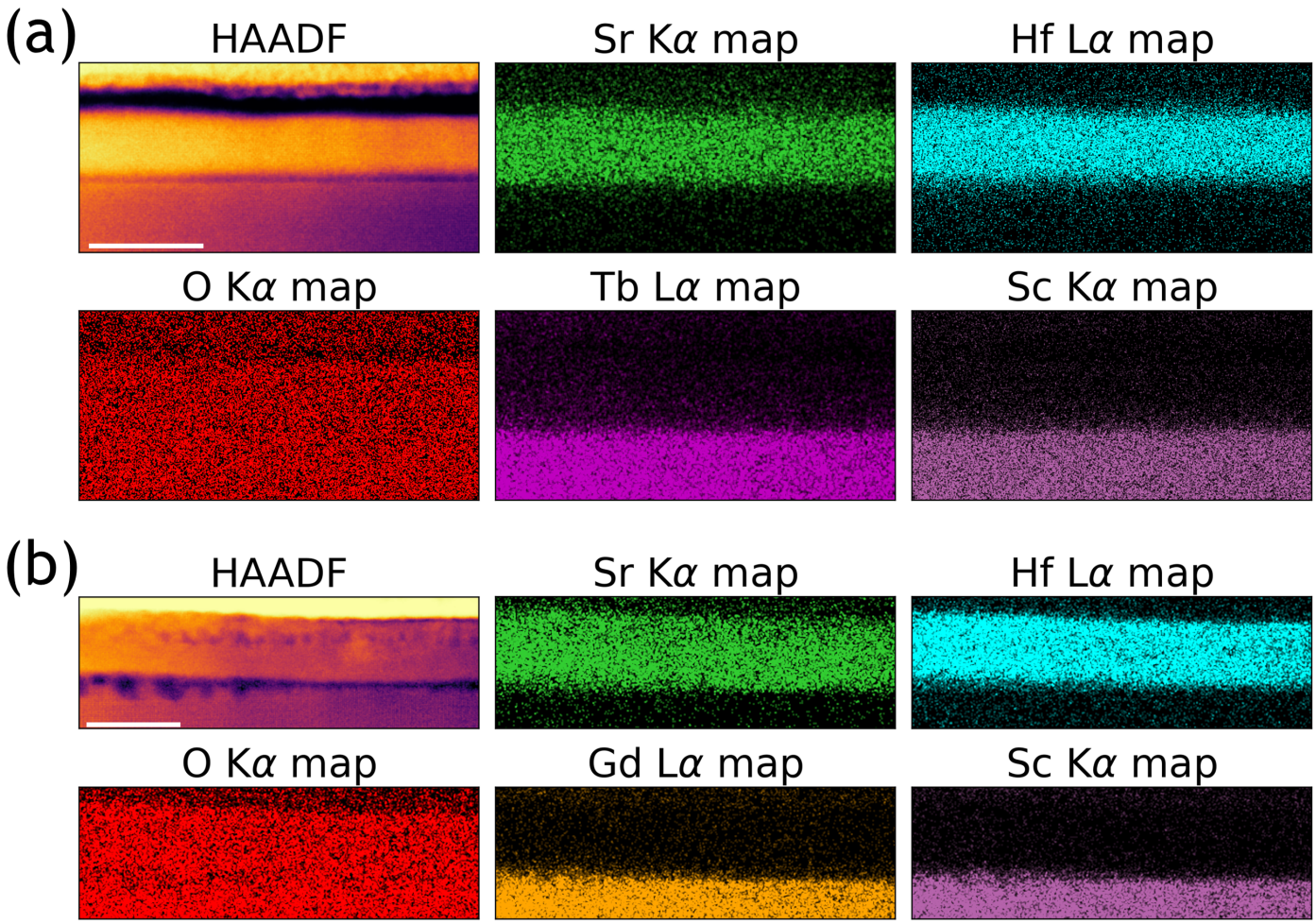

Figure A.14: HAADF images and EDS chemical maps showing the chemical distribution of (a) SHO-TSO and (b) SHO-GSO samples. Scale bars correspond to 20 nm.

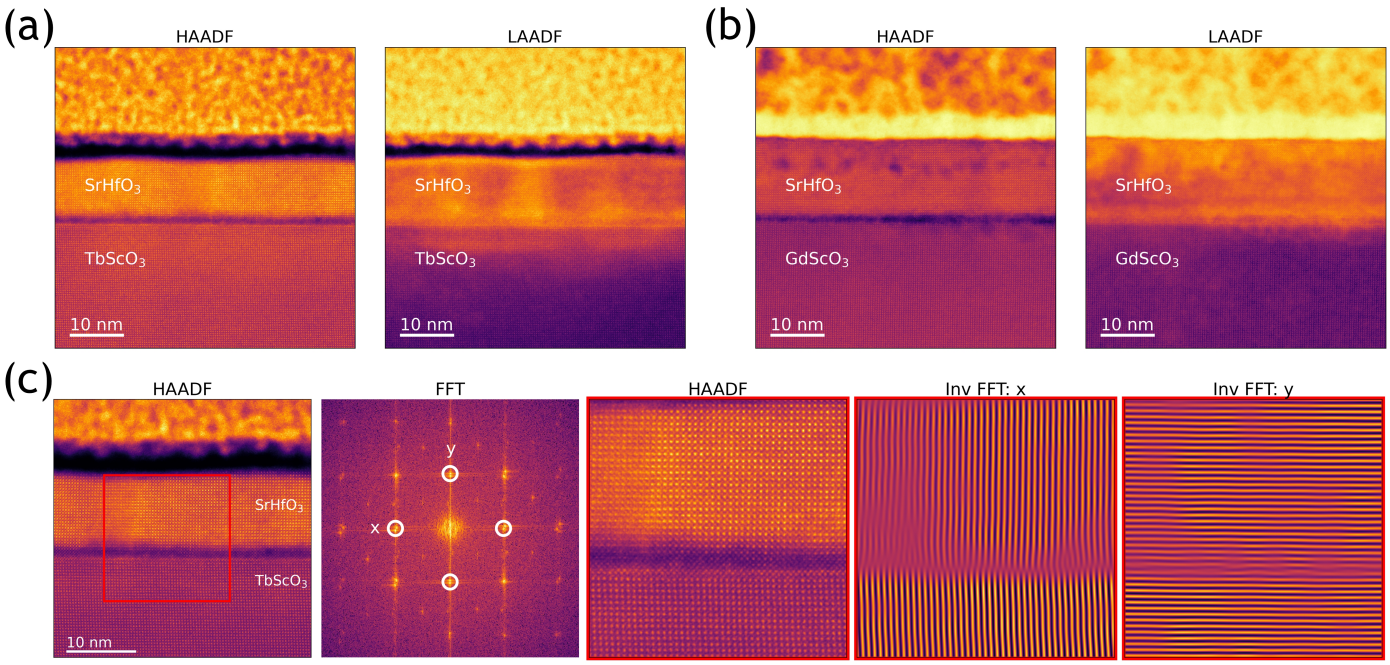

Figure A.15: Wide field-of-view HAADF and LAADF images for (a) SHO-TSO and (b) SHO-GSO samples. (c) HAADF image along with the FFT pattern for SHO-TSO sample. The HAADF image and inverse FFT patterns, for the region highlighted as red box. The spots chosen for generating inverse FFT patterns are highlighted as white open circles in the FFT pattern.

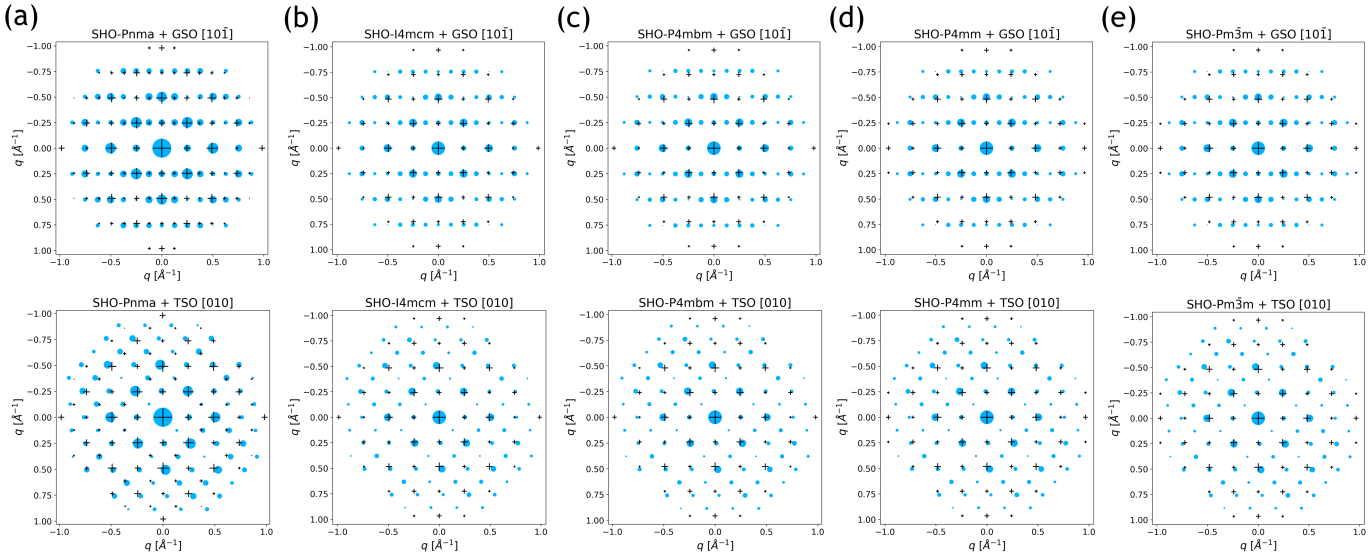

Figure A.16: Simulated electron diffraction pattern for SHO (black-cross) and GSO/TSO (blue-dots). The SHO and GSO/TSO comparison is shown for all the potential SHO phases, (a) Pnma, (b) I4/mcm, (c) P4/mbm, (d) P4mm, (e) Pm$\bar{3}$m. The top panel corresponds to SHO-GSO [10$\bar{1}$] and the bottom panel corresponds to SHO-TSO[010].